

UNIVERSITÉ SORBONNE PARIS CITÉ



UNIVERSITÉ PARIS DIDEROT
École doctorale des Sciences de la Terre et de l'Environnement
et Physique de l'Univers, Paris - ED 560
Laboratoire Astroparticule et Cosmologie (APC)

Optical and noise studies for Advanced Virgo and filter cavities for quantum noise reduction in gravitational-wave interferometric detectors

Eleonora Capocasa

Thèse de doctorat de Physique de l'Univers
dirigée par Matteo Barsuglia et Raffaele Flaminio

présentée et soutenue publiquement le 13 novembre 2017
devant un jury composé de :

Danièle Steer	Professeur - Université Paris Diderot	<i>Présidente du jury</i>
Antonie Heidmann	Directeur de recherche - CNRS	<i>Rapporteur</i>
David Shoemaker	Senior scientist - MIT	<i>Rapporteur</i>
Giovanni Losurdo	Chercheur - INFN	<i>Examinateur</i>
Matteo Barsuglia	Directeur de recherche - CNRS	<i>Directeur de thèse</i>
Raffaele Flaminio	Professeur - Université de Tokyo	<i>Co-directeur de thèse</i>



Abstract

Gravitational-wave astronomy has started in September 2015 with the first detection of a binary black-hole merger by LIGO. Since then, several black-hole mergers and a binary neutron star merger have been observed. Advanced Virgo joined the two LIGO detector in the observation run, in August 2017, highly increasing the localization capabilities of the network. In order to fully exploit the scientific potential of this new-born field, a huge experimental effort is needed to bring the instruments at their design sensitivity and to further improve them. This thesis, developed in this context, it is composed of two parts. The first is about Advanced Virgo : we have developed an automatic noise budget for the laser frequency noise and we have performed optical characterization measurements for the kilometric arm cavities. Round trip losses as low as 80 ppm have been measured. They are among the lowest ever measured for beams of these size. The second part is about the design and development of a 300 m filter cavity, a prototype to demonstrate the frequency dependent squeezing production with properties needed for a broadband quantum noise reduction in the future upgrades of KAGRA, Advanced Virgo and Advanced LIGO. We have contributed to the design and integration phases of the project. We have first made the optical design of the cavity, including the the specifications for the main cavity optics and a detailed estimation of the squeezing degradation sources . We have then developed a local control system for the mirrors, assembled the suspensions, and finally aligned and brought the cavity in resonance with the laser light.

Keywords: gravitational waves detection, gravitational astronomy, Advanced Virgo, interferometers, optical cavities, laser frequency stabilization, quantum noise, filter cavities, frequency dependent squeezing.

Resumée

L'astronomie gravitationnelle a débuté en septembre 2015 avec la première détection de la fusion de deux trous noirs par LIGO. Depuis lors, plusieurs fusions de trous noirs et une fusion d'étoiles à neutrons ont été observées. Advanced Virgo a rejoint les deux observatoires LIGO dans la prise de données en août 2017, augmentant fortement les capacités de localisation du réseau. Afin d'exploiter pleinement le potentiel scientifique de ce nouveau domaine, un énorme effort expérimental est nécessaire pour améliorer la sensibilité des interféromètres. Cette thèse, développée dans ce contexte, est composée de deux parties. La première concerne Advanced Virgo: nous avons développé un budget de bruit automatique pour le bruit de fréquence du laser et nous avons effectué des mesures de caractérisation optique pour les cavités de bras kilométriques. Des pertes aller-retour aussi faibles que 80 ppm ont été mesurées. Elles sont parmi les plus basses jamais mesurées avec un faisceau de cette taille. La deuxième partie concerne la conception et le développement d'une cavité de filtrage de 300 m, un prototype pour démontrer la production de lumière squeezing dépendante de la fréquence avec les propriétés nécessaires pour une réduction du bruit quantique à large bande dans KAGRA, Advanced Virgo et Advanced LIGO. Nous avons contribué à la fois aux phases de conception et d'intégration du projet. Nous avons d'abord fait le design optique de la cavité, y compris les spécifications pour l'optique de la cavité et une estimation détaillée des sources de dégradation pour le squeezing. Nous avons donc développé un système de contrôle pour les miroirs, assemblé les suspensions et finalement aligné et mis la cavité en résonance avec la lumière laser.

Mots-clés: détection des ondes gravitationnelles, astronomie gravitationnelle, Advanced Virgo, interféromètres, cavités optiques, stabilisation en fréquence du laser, bruit quantique, cavités de filtrage, lumière squeezed dépendante de la fréquence.

Acknowledgments

When I started my PhD, three years ago, I didn't expect it to be such an exciting experience. This was partly due to the luck of witnessing an epochal discovery such as the first detections of gravitational waves, and mostly due to the chance of working with many caring people who transmitted me their enthusiasm and their knowledge. Their help supported me during these years, and to all of them I would like to express my gratitude.

To Antoine Heidmann and David Shoemaker, for accepting to be referees of this work, for their careful review of the manuscript, and for the useful comments they provided. To Giovanni and Danièle, for participating in the jury and for patiently examining this thesis.

To Matteo, for sharing with me not only his knowledge, but also his many inspiring ideas and questions. He always guided my work with care and with his positive attitude towards difficulties. He taught me to ask myself questions, and to aim to see "the big picture". He has always found the time to discuss with me and his enthusiasm made me enjoy science as never before.

To Raffaele, for opening the doors of TAMA to me, and for the countless hours he spent with me there, trying to change me into an experimental physicist. For all the times he welcomed me in his office, answering my too many questions, and for encouraging me far beyond my expectations. The deep passion he transmits about this work has been a great source of motivation for me and pushed me to always do better.

To my colleagues at APC, and in particular to Matteo Tacca, for helping me since the first day and for all the time we spent working together in many different countries, to Donatella, for her warm friendship, to Eric, for the wise advices he gave me in more than one occasion, to Agata, for her kind support in these last days, and to Pierre Prat, for his precious help with the electronics. I also want to thank also all the people in the administration for their valuable support and for their kindness.

To all my PhD mates: Léa, Thibault, Camille, Pierros, Dimitri, Gayathri, Leandro, Jean-Baptiste, Yann, Simon, Ranajoy, Lucille, Andrea, Tuan, Alessandro, Thuong, Cyrille and all the other with whom I sheared lunches, coffees, ideas, beers, projects and concerns. They made every day life at APC so pleasant that it will be very sad to leave. A special thanks is due to Philippe for every time he corrected my

drafts in French.

To all the people on Virgo site: Paolo, Maddalena, Eric, Bas, Gabriel, Antonino, Irene, Dan, Diego, Fjodor, Annalisa, Julia, Lucia, Federico, Henrich, Ettore, Jérôme, Massimo, Franco, Gary and all the others... Most of this work would not have been possible without their constant help not only when I was on site. I want to thank them for all the rides, the noise injections and the lock-unlocks they did for me and for always taking the time to teach me.

To Giancarlo Cella, who gave me the possibility to do this work in the first place and who keeps answering all the difficult questions. To Francesco, who is still my best officemate despite the distance.

To the members of the mythical TAMA team: Yuefan, Manuel and Marc, for the many hours we spent together checking picomotors, aligning the cavity and for all the “one last thing” done before going to dinner. To Shibo, Matteo and all the people who passed through TAMA and made my stays at NAOJ so enriching and pleasant. A special thanks goes to Agnes for being always so caring and supportive.

To all my friends, and in particular to Annina, Chiara, Costanza, Giulia, Sara and Veronica. For more than ten years they have been at my side, making my life lighter and cheerful.

To my family, for their unconditional love and for being my reference point no matter how far I am.

Finally, to Marco, for providing nice pictures and much more.

Contents

1 Direct detection of gravitational waves	5
1.1 The gravitational radiation	7
1.1.1 Wave solution of the linearised Einstein equations	7
1.1.2 Production and sources of gravitational waves	9
1.1.3 Astrophysical sources of gravitational waves	10
1.1.3.1 Compact binary coalescence	11
1.1.3.2 Core collapse supernovae	11
1.1.3.3 Pulsars	12
1.1.3.4 Stochastic Background	13
1.1.4 Why do we care about detecting gravitational waves?	13
1.1.4.1 Physics with gravitational waves	14
1.1.4.2 Astrophysics with gravitational waves	14
1.1.4.3 Cosmology with gravitational waves	15
2 Interferometric gravitational waves detectors	17
2.1 Interferometer working principle	17
2.2 Sensitivity limits of interferometers	19
2.2.1 Shot noise	20
2.2.2 Radiation pressure noise	22
2.2.3 Seismic Noise	23
2.2.4 Newtonian Noise	24
2.2.5 Thermal Noise	25
2.2.6 Other noise sources	28
2.3 Improved interferometer configuration	29
2.3.1 Fabry-Perot cavities	29
2.3.2 Power recycling	33
2.3.3 Signal recycling	34
3 First detection of gravitational waves	37
3.1 Initial network of ground-based GW detectors	37
3.2 Second generation of ground-based GW detection	40

3.2.1	Advanced LIGO	40
3.2.2	KAGRA	41
3.2.3	Advanced Virgo	41
3.3	First detections: beginning of the gravitational astronomy	43
3.3.1	The observations	43
3.3.2	Binary black hole mergers	45
3.3.3	Estimation of the source parameters	46
3.3.4	GW170814: first three-detector BBH merger observation	48
3.3.5	Test of general relativity	49
3.3.6	Merging rate and astrophysical implications	50
3.3.7	GW170817: first binary neutron star merger observation	51
II	Optical and noise studies for Advanced Virgo	55
4	The Advanced Virgo detector	59
4.1	Injection system	59
4.1.1	Laser source	59
4.1.2	External injection bench	60
4.1.3	Suspended Injection benches	60
4.1.4	Input mode cleaner	61
4.1.5	The reference cavity	62
4.2	Optical configuration	63
4.3	Mirror suspensions and control	64
4.4	Noise budget and design sensitivity	66
5	Injection system noise analysis	69
5.1	Frequency pre-stabilization loops	70
5.1.1	PDH signal calibration	73
5.1.2	Open loop transfer functions	74
5.2	Sensing noise	75
5.2.1	Shot noise	76
5.2.2	Dark and ADC noise	77
5.3	Classical radiation pressure noise	77
5.4	Quantum radiation pressure noise	78
5.5	Thermal noise	79
5.5.1	Pendulum thermal noise	79
5.5.2	Coating thermal noise	80
5.6	RFC length noise	80
5.7	Angular control noise	82
5.8	Beam pointing control (BPC) noise	85
5.9	The "real" frequency noise	87

5.10	Noise budget automation	90
5.11	Frequency noise improvement and conclusions	90
6	Optical Characterization of the arm cavities	93
6.1	Finesse	94
6.2	Round trip losses	98
6.3	G-factor	105
6.4	Mismatching and misalignment	106
III	Filter cavity for frequency dependent squeezing production	111
7	Frequency dependent squeezing in the two-photon formalism	117
7.1	Quantization of the electromagnetic field	117
7.2	Quantum states of light	118
7.2.1	Fock states	118
7.2.2	Coherent states	119
7.2.3	Squeezed state	120
7.3	Two-photon formalism	121
7.4	Homodyne detection of squeezed states of light	123
7.5	Input output relations	124
7.5.1	Filter cavity in the two-photon formalism	127
7.5.2	Squeezing degradation due to optical losses	128
8	Filter cavity optical design	131
8.1	Choice of cavity parameters	132
8.2	Requirements on mirror quality	134
8.3	Squeezing degradation budget	142
8.4	Motivations for using long filter cavities	146
8.5	Frequency dependent squeezing with EPR entanglement	150
8.6	Improvement in KAGRA sensitivity	153
9	Filter cavity experiment integration	157
9.1	Production of frequency independent squeezing	158
9.2	Input telescope	159
9.3	Mirrors control	164
9.4	Mirror position readout	165
9.5	Optical levers implementation	168
9.5.1	PSD position accuracy	170
9.5.2	Optical lever tuning	172
9.6	Feedback loop implementation	177
9.7	Local controls performance	178
9.8	Mirrors preparation and installation	181

CONTENTS

9.9 Cavity alignment	183
9.10 Lock and optical characterization	184
9.10.1 Servo preparation	185
9.10.2 Lock characterization	186
9.10.3 Conclusion and future plans	191
10 Conclusions and perspectives	195
A Electromagnetic field in Fabry-Perot cavities	197
B Round trip losses from reflectivity	203
C Injection telescope design	205
C.1 Beam astigmatism	205
C.2 Spherical aberrations	207
C.3 Losses due to mirror defects	207
D Local control: transfer functions computation	209
E Filter cavity optical gain and transfer functions	213
Bibliography	221

Introduction

Gravitational waves are perturbations of the space-time which propagate at the speed of light and which are emitted by accelerating masses. Their existence has been predicted by Einstein in 1916 as a consequence of his theory of General Relativity.

In September 2015, almost one century after Einstein's prediction, gravitational waves have been directly detected for the first time. The discovery arrived after more than 50 years of experimental efforts motivated by the great scientific potential of this new tool to observe the Universe.

The two Advanced LIGO interferometers observed for the first time a gravitational wave (GW) produced by the fusion of two black-holes at a distance of about 400 Mpc, by measuring a strain of only 10^{-18} m over a distance of 4 km.

Advanced Virgo, a 3 km interferometer located in Italy, joined Advanced LIGO in August 2017, participating in the first three detectors observation of a BBH merger (the fourth seen by LIGO) and in the first observation of a binary neutron stars (BNS) merger, where for the first time also an electromagnetic counterpart associated to the gravitational signal has been detected.

The scientific payoff of this achievement is dramatic: with these first observations alone, it has been possible, just to give a few examples, to prove the existence of binary black holes (BBH) and the possibility for these objects to merge, to identify the BNS merging as progenitors of short gamma ray bursts and to have an independent measurement of the Hubble constant.

The network of second generation gravitational-wave detectors is expected to enlarge in the next future: a Japanese kilometric scale detector, KAGRA, is currently being assembled in Kamioka mine and it is expected to become operational in a few years. Future upgrades of this second generation network are already planned in order to further increase their sensitivity and better exploit the scientific potential of gravitational waves.

The first part of this manuscript describes the activities I have done in the context of Advanced Virgo commissioning, that is the phase between the end of the integration and the beginning of the data taking. The goal is to tune the interferometer and to reduce the noise sources as much as possible in order to reach a sensitivity interesting for the data taking.

The first part of the interferometer to be commissioned is the laser source and the so

CONTENTS

called *injection system*, composed of all the active and passive systems used to stabilize the laser light. Among the properties of the laser light, the frequency stability is crucial to acquire and maintain the lock of the arm cavities: if the laser frequency is not stable enough, the control system driving the mirror position is not able to put the cavity on resonance.

My first activity in the context of AdVirgo commissioning was to perform a noise budget for the frequency noise, in order to understand which are the main noises limiting the laser frequency stability and possibly reduce them. For my analysis, I have investigated the possible sources of frequency noise and for all of them I have estimated (or measured when possible) a projection of their effects on the frequency noise. The ultimate goal of this activity is to bring the frequency noise level below 1 Hz RMS, the requirement set for the arm lock acquisition.

The second activity in the context of AdVirgo commissioning was to participate to the optical characterization on the interferometer arm cavities. The goal of this work was to check if the optical properties of the cavities were those required to make the interferometer work properly. The main quantities measured were the cavity finesse, the round trip losses, the g-factor (which is related to the curvature radius of the mirrors) and the mismatching between the injected beam and the mode which resonates inside the cavity. The measurement of the round trip losses is particularly interesting for a more general purpose: as we will see in details in the third part of this thesis, they play a key role when squeezed light is used and for this reason it is important to have a full understanding and a reliable strategy to measure them.

The sensitivity of second generation GW detectors will be limited in a large fraction of the spectrum by the quantum nature of the light. The use of squeezed quantum states of light with modified noise features is being deeply investigated as a strategy to reduce quantum noise. These states are actually vacuum states of light, whose amplitude and phase uncertainties (which are equal in ordinary vacuum) are respectively increased and reduced using non-linear crystals. They can be represented as ellipses in the amplitude-phase plane. In order to reduce quantum noise in the whole interferometer bandwidth this squeezing ellipses has to be rotated of an angle which depends on the frequency. Such frequency dependence can be achieved by reflecting a frequency-independent squeezed state by a high finesse detuned cavity, called *filter cavity*. The rotation of the squeezing angle has been experimentally demonstrated in the MHz region and, more recently, in the kHz region. The second part of this work concerns the design and development of a full scale filter cavity prototype, implemented in the former TAMA interferometer infrastructure, at the National Astronomical Observatory of Japan (NAOJ). The goal of this experiment is to demonstrate for the first time the production of frequency dependent squeezing with a rotation angle of ~ 70 Hz, which is the frequency required for an optimal quantum noise reduction in second generation GW interferometers.

First, I have contributed to the optical design of the cavity. Since squeezed states

are easily degraded by optical losses, it is important to design the cavity in order to reduce as much as possible all the loss sources. Since mirror defects are responsible for most of the light scattered out of the cavity, the requirement on the mirror flatness is a crucial parameter to be set. I used FFT simulations of the cavity with realistic mirrors map in order to set a requirement for the mirror flatness. Along with this analysis, I have performed a squeezing degradation budget taking into account possible sources of squeezing degradation other than cavity losses.

In the last part of this manuscript I describe all the experimental work done in order to achieve the lock of the cavity: the installation of the suspensions system, the preparation and installation of the mirrors both of the cavity and the injection telescope, the development of mirrors local controls and the preparation of the analog electronic needed for the lock of the cavity.

This thesis is divided into three parts, each composed of three chapters. In the following an outline of the structure is presented:

- **PART I - Direct detection of gravitational waves**

- **Chapter 1** We recall the basis of GW theory, their production mechanism and most promising sources. Finally we briefly discuss the scientific interest of GW detection.
- **Chapter 2** We illustrate the principle of the GW detection with Michelson interferometers, discussing their noise limitation and strategies to improve their configuration.
- **Chapter 3** We present the first network of interferometers and their results, then we describe the main upgrades which brought to the second generation network and to the first gravitational-wave detections. We present the observations performed and we summarize their scientific implications.

- **PART II - Optical and noise studies for advanced Virgo**

- **Chapter 4** We illustrate the main features of AdVirgo, with particular attention to its injection system and we discuss its design sensitivity.
- **Chapter 5** We present the work performed to estimate the frequency noise budget of the pre-stabilized laser. We detail the procedure done to automate the noise budget and the improvement history of the frequency noise.
- **Chapter 6** We describe the techniques used for the arm cavity characterization and the main results obtained.

- **PART III - Filter cavity for frequency dependent squeezing production**
 - **Chapter 7** We introduce a suitable formalism to describe squeezed states and we use it to compute the quantum noise of the interferometer and its potential reduction by using frequency dependent squeezing.
 - **Chapter 8** We present the optical design of the 300 m filter cavity in TAMA including the simulations done to set requirements on the mirror quality and the squeezing degradation budget. We describe the motivation for using long filter cavity and compare their performances with those of a technique recently proposed which uses EPR entanglement.
 - **Chapter 9** We describe the filter cavity installation and commissioning.

This work has been carried out from October 2014 to October 2017. The commissioning activity has been performed partly on the Virgo site and at APC, for the analysis of the data. The work on the filter cavity experiment has been carried out during 9 months spent at NAOJ, while some preparatory works has been done at APC.

Part I

Direct detection of gravitational waves

CHAPTER 1

The gravitational radiation

In this chapter, gravitational waves (GW) are introduced in the context of General Relativity as solutions of linearized Einstein equations. Then, their production mechanisms are presented as well as the most promising sources for Earth-based detectors. In the last section we try to point out the scientific interest of their detection, showing that the potential of this unprecedented tool certainly rewards the long quest towards their detection.

1.1 Wave solution of the linearised Einstein equations

In the Einstein theory of special relativity [1], the space-time is described as a 4-dimensional manifold where the distance between two neighboring events is

$$ds^2 = \eta_{\mu\nu} dx^\mu dx^\nu \quad (1.1)$$

where $\eta_{\mu\nu}$ is the Minkowski metric, describing flat space, which in cartesian coordinate is

$$\eta = \begin{pmatrix} -1 & 0 & 0 & 0 \\ 0 & 1 & 0 & 0 \\ 0 & 0 & 1 & 0 \\ 0 & 0 & 0 & 1 \end{pmatrix}$$

In General Relativity [2] this distance assumes a more general form:

$$ds^2 = g_{\mu\nu} dx^\mu dx^\nu \quad (1.2)$$

Here the metric is no longer flat and $g_{\mu\nu}$ accounts for the curvature of the space-time. This representation allows to encode the effect of gravitation, which is no longer regarded as a force but as a modification of the space-time geometry.

General relativity also provides a relation between the space-time curvature and the

matter and energy distribution which produces it: the Einstein field equations:

$$G_{\mu\nu} = \frac{8\pi G}{c^4} T_{\mu\nu} \quad (1.3)$$

where c is the speed of light, G is the Newton's gravitational constant, $G_{\mu\nu}$, is the Einstein tensor, a non linear function of the metric $g_{\mu\nu}$ and its derivatives and $T_{\mu\nu}$ is the stress-energy tensor, accounting for the matter and energy distribution. In many cases, as in the vicinity of the Earth, the deviation from the flat metric induced by the presence of a matter-energy distribution is small enough to allow the metric tensor $g_{\mu\nu}$ to be written in the form

$$g_{\mu\nu} = \eta_{\mu\nu} + h_{\mu\nu} \quad (1.4)$$

where $h_{\mu\nu}$ is a small quantity describing the deviation from the flat Minkowski metric $\eta_{\mu\nu}$, thus encoding the effect of gravitation.

In this *weak field* approximation the Einstein equations become linear. Moreover, it is possible to choose an opportune set of coordinates such that, in the absence of sources, they assume the form:

$$\left(\nabla^2 - \frac{1}{c^2} \frac{\partial^2}{\partial t^2} \right) h_{\mu\nu} = 0 \quad (1.5)$$

This is a wave equation for the space-time perturbation $h_{\mu\nu}$ and its solution is a *gravitational wave*:

$$h_{\mu\nu}(\vec{x}, t) = \epsilon_{\mu\nu} \exp i(2\pi f t - \vec{k} \cdot \vec{x}) \quad (1.6)$$

where f is the frequency of the waves, \vec{k} is the wave vector and $\epsilon_{\mu\nu}$ is the polarization tensor.

This means that perturbations propagate at the speed of light in the space-time, modifying its metric. It can be shown that these waves have only two independent polarizations, orthogonal to the propagation direction. A general solution for a wave propagating in the z-direction is

$$\epsilon_{\mu\nu} = (h_+ \epsilon_{\mu\nu}^+ + h_\times \epsilon_{\mu\nu}^\times) \exp i(2\pi f t - \vec{k} \cdot \vec{z}) \quad (1.7)$$

where $\epsilon_{\mu\nu}^+$ and $\epsilon_{\mu\nu}^\times$ are a basis for the polarization tensor $\epsilon_{\mu\nu}$ and writes:

$$\epsilon_{\mu\nu}^+ = \begin{pmatrix} 0 & 0 & 0 & 0 \\ 0 & 1 & 0 & 0 \\ 0 & 0 & -1 & 0 \\ 0 & 0 & 0 & 0 \end{pmatrix} \quad \epsilon_{\mu\nu}^\times = \begin{pmatrix} 0 & 0 & 0 & 0 \\ 0 & 0 & 1 & 0 \\ 0 & 1 & 0 & 0 \\ 0 & 0 & 0 & 0 \end{pmatrix}$$

These two polarizations are usually referred to as *plus* and *cross*, according to the shape of the equivalent force fields that they produce. This points out a peculiar

feature of the gravitational wave radiation, which has been exploited for its detection: it modifies the space-time in a differential way. In fact, the distance between test masses changes at the wave frequency, with opposite sign in orthogonal directions. The relative change in the distance, the strain amplitude, is the amplitude h of the gravitational wave. The effect of the passage of a gravitational radiation on a set of test masses is shown in Fig. 1.1 for the two polarizations.

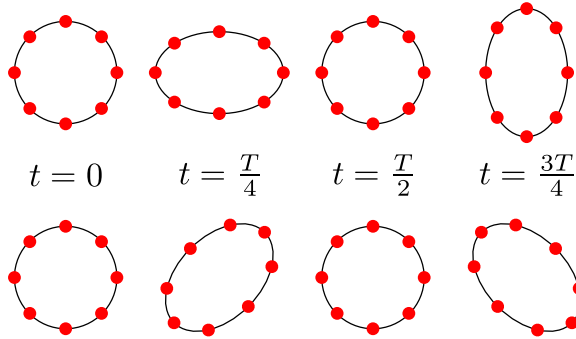


Figure 1.1: The effect of the passage of a gravitational radiation on a set of test masses for the plus polarization (upper line) and cross polarization (lower line). The propagation direction is assumed orthogonal to the page.

1.2 Production and sources of gravitational waves

In analogy with electromagnetic waves, which are produced by the acceleration of charges, gravitational waves are produced by the acceleration of masses. Also in this case, an exact description of the wave emission can be given using retarded potentials [3] but if the size of the source is small with respect to the wavelength, the radiation can be usefully approximated with a multipole expansion. The energy conservation laws (as the charge conservation for the electromagnetic radiation) makes the monopole term vanish. The linear and angular momentum conservation do the same for the electric and magnetic dipole terms. The first non zero term of the expansion is then the quadrupole one. Einstein found that the gravitational wave strain h at a distance r generated by the quadrupole moment of a system is:

$$h_{ij}(t) = \frac{2G}{r c^4} \ddot{Q}_{ij}(t - r/c) \quad (1.8)$$

The traceless mass quadrupole moment is defined as a function of the source mass density $\rho(\vec{x}, t)$

$$Q_{ij} = \int d^3x \rho(x_i x_j - \frac{1}{3} r^2 \delta_{ij}) \quad (1.9)$$

where δ_{ij} is the Kronecker delta. The quadrupole moment of an object of dimension R , mass M , and an asymmetry in the mass distribution quantified by ϵ , can be

approximated as $Q \simeq \epsilon R^2 M$. If T is the characteristic timescale of the quadrupole moment variation, and we define v a characteristic speed for the mass distribution elements $v = R/T$, Eq. 1.8 can be rewritten as

$$h \simeq \epsilon \frac{G}{c^2} \frac{M}{r} \left(\frac{v}{c} \right)^2 \quad (1.10)$$

The multiplicative factor $G/c^2 \simeq 10^{-29}$ m/Kg is so small to make impossible the production of detectable gravitational waves on Earth. An instructive calculation reported in [4] estimates that the strain produced by a pair of masses of 1 tonne each, connected by a rod of 2 m rotating at a frequency of 1 kHz, at a distance of one GW wavelength ($\lambda = 300$ km) is about $\simeq 10^{-39}$ which is several order of magnitude lower than the sensitivity achievable by current and next generation GW detectors. Gravitational waves are carrying energy away from their sources. The rate at which this energy is carried away, that is, the luminosity is written in terms of the quadrupole moment as

$$\dot{E}_{GW} = \frac{c^3}{16\pi G} \int |\dot{h}|^2 dS = \frac{1}{5} \frac{G}{c^5} \ddot{Q}_{ij} \ddot{Q}_{ij} \quad (1.11)$$

the integral is computed over a sphere of radius r and the quantity on the right-hand side must be averaged over several periods.

Using the approximated formula for the quadrupole momentum and writing the mass as a function of the Swartzschild radius $R_{\text{Sch}} = 2GM/c^2$ the luminosity can be cast in the form

$$\dot{E}_{GW} = \epsilon \frac{c^5}{G} \left(\frac{v}{c} \right)^6 \left(\frac{R_{\text{Sch}}}{R} \right)^2 \quad (1.12)$$

from which it is evident that more compact sources, with more asymmetric mass distribution and higher velocity are emitting energy in the form of gravitational radiation at a higher rate.

1.3 Astrophysical sources of gravitational waves

According to previous considerations, it is clear that only astrophysical sources are capable of producing detectable gravitational waves. The expected amplitude and frequency of the emitted radiation for different sources can be predicted after calculating the evolution of their quadrupole moment. In order to detect a gravitational signal its amplitude should be above the detector sensitivity at the frequency of the gravitational wave. Another important parameter to be considered is the expected occurrence rate of the source. Signals can be divided, according to their time duration with respect to the observation time, into transient signals and continuous signals. In the following are reported the most promising astrophysical sources for the earth based GW detectors.

1.3.1 Compact binary coalescence

A compact binary system can be composed by two neutron stars (NS-NS), two black holes (BH-BH) or a neutron star and a black hole (BH-NS). Gravitational radiation is the main mechanism through which they loose energy. The strain amplitude of the gravitational waves at a distance r from the source is:

$$h \simeq 10^{-21} \cdot \left(\frac{\mathcal{M}}{M_{\odot}} \right)^{5/6} \left(\frac{f}{100 \text{ Hz}} \right)^{5/6} \left(\frac{r}{15 \text{ Mpc}} \right)^{-1} \quad (1.13)$$

Where f is the GW frequency (which is the double of the orbital frequency) \mathcal{M} is the chirp Mass defined as a function of the reduced mass $\mu = \frac{m_1 m_2}{m_1 + m_2}$ and the total mass $M = m_1 + m_2$ as

$$\mathcal{M} = \mu^{2/3} M^{2/5} \quad (1.14)$$

The energy loss makes the orbit shrink with time, while the frequency increases and so does the wave amplitude, according to Eq. 1.13. The wave frequency increases with time as

$$f = \frac{5}{8\pi} \left(\frac{c^3}{G\mathcal{M}} \right)^{5/8} (t_c - t)^{-3/8} \quad (1.15)$$

The two compact objects will eventually merge in a single one at the time t_c .

The rate of NS-NS mergers is estimated on the observed BNS systems and on theoretical models of their formation and evolution. It has been updated using the information on the first BNS merging detection to $1540^{+3200}_{-1220} \text{ Gpc}^{-3} \text{ yr}^{-1}$ [5]. The rate of BBH mergers estimated after the first three detections were $12 - 213 \text{ Gpc}^{-3} \text{ yr}^{-1}$. While the lack of detection of NS-BH during the fist LIGO observation run allowed to set an upper limit of $3600 \text{ Gpc}^{-3} \text{ yr}^{-1}$.

1.3.2 Core collapse supernovae

The collapse of the core of a massive star, also known as Supernova Type II event, is supposed to produce a strong gravitational waves emission. Stars with masses larger than $8 M_{\odot}$ are able to fuse elements with increasing atomic mass up to Iron. Fusion of higher atomic mass elements is energetically unfavourable and for that reason the core becomes inert. When it exceeds the Chandrasekhar mass of about $1.4 M_{\odot}$, electron degeneracy pressure is no longer able to compensate for the gravitational compression: the core matter is transformed in neutrons and the star begins to collapse. When the density increases too much, neutron degeneracy makes the collapse turns into a bounce (which can be followed by many others depending on the damping degree). If the collapsing is not symmetric the change in the quadrupole moment of the mass will give rise to a burst of gravitational waves. Since the physics of the process is extremely complicated and still not well understood, it is difficult to have precise estimations for the evolution of the quadrupole moment of the system. More recent models predict a gravitational wave strain of order of $10^{-23} - 10^{-20}$ for a core collapse

event at 10 kpc, signal durations between 1 ms and few s, frequencies between 1 and few 1 kHz and total emitted energy between $10^{-12} - 10^{-7} M_{\odot}c^2$. If such predictions are true, detection of core-collapse events by second-generation GW detector will be limited to our galaxy and the Small and to Large Magellanic Clouds. The expected rate of core collapse supernovae in the Milky Way is $(0.6 - 10.5) \cdot 10^{-2} \text{ yr}^{-1}$ and it is $(1.9 - 4.0) \cdot 10^{-3} \text{ yr}^{-1}$ in the combined Magellanic Clouds [6].

1.3.3 Pulsars

Pulsars are rotating neutron stars emitting a beam of electromagnetic radiation. The emission is originated by the presence of a misalignment between the rotation and the magnetic axes of the star at the expenses of their rotational energy. The beam is emitted in correspondence of the magnetic pole of the pulsar and is pointing toward Earth once every period, giving the pulsed appearance to the radiation. After the first observation of a pulsar made by Hewish and Bell in 1967 [7], more than 2000 pulsars have been discovered. Most of them emit at radio frequencies. In order to be a source of gravitational waves they have to show a certain degree of asymmetry, to allow the quadrupole moment to vary with time. The expected gravitational wave strain is [4]

$$h \simeq 3 \cdot 10^{-25} \cdot \left(\frac{\epsilon}{10^{-6}} \right) \left(\frac{I}{10^{-38} \text{ kg} \cdot \text{m}^2} \right) \left(\frac{f}{1 \text{ kHz}} \right)^2 \left(\frac{10 \text{ kpc}}{R} \right) \quad (1.16)$$

were I is the moment of inertia and ϵ , the equatorial ellipticity, accounts for the asymmetry of the system. Such asymmetry can have different origins, as a non-symmetric residual strain from the star birth or a strong internal magnetic field not aligned to the rotation axis [8]. Despite the low expected strain the fact that the signal is continuous and can be integrated for a long time increases the SNR and thus the chances of detection. Moreover, if the source parameters (position, frequency, spin-down) are well identified, a targeted search can be performed. The frequency of emitted GW is expected to be twice that rotation frequency. Many targeted searches have been carried out on data from first-generation detectors allowing to put upper limits on the amplitudes of the generated GW and thus on their structure asymmetry [9, 10]. Since GW emission brings to a loss of rotational energy and decreases the spin frequency, the observation of such a spin-down can be used to place an indirect upper limit on its gravitational wave emission, known as *spin-down limit*. The most recent research for signals from the Crab and Vela pulsars conducted on Virgo VSR4 produced a strain upper limit for Crab of $6.9 \cdot 10^{-25}$ about a factor of 2 below the spin-down limit. The corresponding upper limit on star ellipticity is about $3.7 \cdot 10^{-4}$ [11].

1.3.4 Stochastic Background

A stochastic background of gravitational radiation is a random GW signal produced by the superposition of many weak, independent, unresolved sources. These sources can be astrophysical such as those discussed above: unresolved compact binary coalescences of black holes and neutron stars, rotating neutron stars, supernovae or can be associated with stochastic processes in the early Universe: cosmic strings, inflationary models, phase transitions and the pre-Big Bang scenario. In analogy to the cosmic microwave background, the cosmological stochastic background is expected to be stationary, gaussian, unpolarized and isotropic while this is not the case for the astrophysical stochastic background since the distribution of galaxies with distances up to 100 Mpc is not isotropic and if the interval between events is short with respect to the duration, the integrated signal may result in continuous, "popcorn noise" background [12]. A rough computation reported in [13], based on the statistic obtained by the BBH mergers observed [14], estimates that the total rate of binary black hole mergers is between ~ 1 per minute and a few per hour. Assuming for each signal a duration between a few tenths of a second to ~ 1 second, the fraction of time that the signal is not present in the data is $\ll 1$. On one hand, from this background it could be possible to extract information on compact objects physics such as the star formation history. On the other hand it could be a "foreground" that would conceal the stochastic background of cosmological origin.

1.4 Why do we care about detecting gravitational waves?

Started in the 1960s, the quest for gravitational waves has been one of the longest in the history of science. The huge effort done to detect the extremely faint effects of the gravitational radiation are not only motivated by the will to confirm Einstein predictions. So far most of the information we had about the Universe has been extrapolated from the electromagnetic radiation coming from it. Gravitational radiation shows complementary features with respect to the electromagnetic one:

- EM radiation is emitted by accelerated charged particles and due to the fact that the matter is generally neutral, it is likely to encode information of small regions of the source (and have small wavelength). On the other hand GW radiation, being produced by acceleration of large masses can bring information of the overall motion of the object (and have a longer wavelength).
- Since EM radiation interacts strongly with matter it is easier to be detected but at the same time it is easily scattered or absorbed during its path from the source to the observer. Conversely GW radiation interacts very weakly with the matter and, despite the fact it is harder to detect, it is able to convey uncorrupted information from remote sources.

Thus gravitational waves represent a completely new tool to observe the Universe and can address open questions in fundamental physics, astrophysics and cosmology. The scientific payoffs in each of these fields are remarkable and will increase with the number and the strength of detected events.

1.4.1 Physics with gravitational waves

Despite the fact that General Relativity (GR) is a "simple" and effective way to describe gravity and its predictions have proven to be consistent with all the experimental observations so far, alternative theories have been proposed over the years. The main motivations were the attempt to quantize gravity and more recently to address cosmological issues associated with dark matter and dark energy. Proposed alternative theories give predictions which contradicts those of general relativity only in the strong field regime. Observing compact binary coalescence will allow to study the two-body motion of a compact-object in highly nonlinear regime, providing data for accurately testing strong-field dynamics of general relativity, allowing to confront and possibly rule out different theories of gravity [15].

The search for non-standard polarizations, predicted by alternative theories could contribute to these investigations. Constrain of the speed of GW waves, which can be determined comparing the arrival time on earth of a possible electromagnetic counterpart provides an additional test of GR.

1.4.2 Astrophysics with gravitational waves

Detection of GW from inspiralling binary of neutron-stars can be used to obtain physical information such as mass, spin, radius and Equation of State (EoS) of their components. As the two body approach each other their orbits start to be perturbed by the tidal forces thus the waveform emitted encodes information on the neutron star structure and EoS of the nuclear matter [16].

We will see how the coincident observation of GW170817, the first gravitational wave radiation detected from a BNS coalescence, with gamma ray burst (GRB) could confirm that such events are progenitors of at least some of the short-duration, hard-spectrum GRB observed. Moreover a network of gravitational wave detectors can provide a good localization of the BNS mergers, allowing for an effective EM-follow up, as it happened with GW170817.

Gravitational waves from merging of BBH contains the information on the spin of the two black holes, which is an important hint to discriminate between different formation mechanisms.

In case of a supernovae, detection of the associated GW, originated in its core, would provide information on the general degree of asymmetry of its dynamics. Moreover it can inform on the explosion mechanism, on the evolution of the proto-neutron star,

the rotation rate of the collapsed core and the nuclear EoS [6].

Observation of continuous GW signals from pulsar would directly inform on the source parameters and in particular on their ellipticity, while upper-limits on this can be set also in case of non-detection. Studying relationship between the GW emission frequency and the rate of EM pulses would possibly give information on the mechanisms responsible for this asymmetry. It will be also useful to investigate possible phase discontinuities and their relations with changes in the crust stresses. Moreover, since not all the spinning neutron stars are supposed to emit EM radiation, GW could be the only way to observe EM-silent neutron stars.

1.4.3 Cosmology with gravitational waves

Since the observation of a GW from a merger of compact object with a network of detectors will allow a direct measurement of the source distance, these events can be used as *standard sirens* to independently calibrated distances. If the redshift of the source it is also known, these two informations can be combined to measure cosmological parameters such as the Hubble constant [17]. However, since a redshifting of frequency is indistinguishable from a rescaling of the masses, the source redshift has to be obtain in an independent way. A first option is to use the presence of an EM counterpart from which to deduce the host galaxy of the event and thus the redshift. This method has been successfully used with GW170817 and its EM counterpart [18]. The possibility to extract the redshift with other means has been explored in order to allow the measurements of cosmological parameters with GW observation alone. The main proposed methods are:

- By using statistical approach on many observations, using error regions on the sky derived from observations from a network of detectors to limit the possible number of host galaxies [17, 19].
- By measuring tidal effects in binary NS-NS or BH-NS merger which depends on the rest-frame mass (assuming to know the EoS) [20].
- By using information encoded in the postmerger signal which, according to numerical simulations, consists in a short burst with a characteristic frequency depending of the rest-frame mass of the sources [21].
- By exploiting the narrowness of the mass distribution of the neutron star population [22]: neutron star masses are expected to lie in a narrow range, once the shape is known the measured (redshifted) masses can be compared with expected ones to infer the redshift.

While through cosmic microwave background we can observe the Universe back to roughly 300.000 years after Big Bang, detection of cosmological GW background will provide a unique chance to observe the Universe at its origins up to $\sim 10^{-27}$ s

after the Big Bang [23]. The amplitude and frequency dependence of the expected spectrum of this background radiation is subjected to considerable uncertainty according to the models used to predict it. Standard inflation model predicts a nearly flat spectrum over a very wide frequency range but there are alternatives which foresee both increasing or decreasing with frequency. Being able to detect them will be a test for the early universe cosmology as it will help to investigate possible competitive mechanisms able to generate primordial GW radiation.

CHAPTER 2

Interferometric gravitational waves detectors

In this chapter we will present the working principle of a Michelson interferometer as a detector of gravitational waves, illustrating the features which makes it particularly suitable for this extremely precise measurement. In the following we list and describe the noises which limit the sensitivity of this instrument. In the last section we discuss improvement from the simple Michelson scheme, such as the integration of resonant cavities in the arms and addition of power and signal recycling mirrors, as strategies to increase the detector sensitivity.

2.1 Interferometer working principle

In the previous chapter we have seen that gravitational waves modify spacetime curvature. The most direct way to observe a gravitational wave is to measure the change that its passing induces in the time taken by the light to travel between two free-falling masses. Recalling that for a light-like interval $ds^2 = 0$, if the metric is slightly perturbed by the presence of a gravitational wave, we have

$$cdt^2 = (\eta_{\mu\nu} + h_{\mu\nu})dx^\mu dx^\nu \quad (2.1)$$

Assuming to have two suspended mirrors, the time taken by the light to go from the input to the end mirror will be

$$\int_0^{\tau_e} dt = \frac{1}{c} \int_0^L \sqrt{1 - h_{11}(t)} dx \simeq \int_0^L (1 - \frac{1}{2}h_{11}(t)) dx \quad (2.2)$$

where we took a first order approximation. Moreover, for the sake of simplicity, we assumed the mirrors to be along the x -axis and the gravitational wave to be plus-polarized with an amplitude small enough to take only the second order of the square root Taylor expansion. Assuming $h_{11} = h \cdot e^{2\pi i f_{GW} t}$, with the substitution $t = L/c^1$, Eq. 2.2 becomes

¹We can neglect the effect of the gravitational wave on this relation.

$$\int_0^{\tau_e} dt = \frac{L}{c} + \frac{h}{4\pi f_{\text{GW}}} (e^{2\pi i f_{\text{GW}} \frac{L}{c}} - 1) \quad (2.3)$$

The same calculation can be done for the time taken by the light to come back to the input mirror, with the substitution $t = (2L-x)/c$. The round trip time becomes:

$$\int_0^{\tau_{rt}} dt = \frac{2L}{c} + \underbrace{\frac{h}{4\pi f_{\text{GW}}} (e^{2\pi i f_{\text{GW}} \frac{2L}{c}} - 1)}_{\Delta\tau_{rt}} \quad (2.4)$$

The second term, $\Delta\tau_{rt}$, represents the round trip time variation due to the gravitational-wave perturbation. In case the GW frequency is small with respect to the round trip time, i.e. $f_{\text{GW}} \ll L/c$, $\Delta\tau_{rt}$ can be approximated at the first order as:

$$\Delta\tau_{rt} = \frac{2L}{c} \frac{h}{2} \quad (2.5)$$

This means that the round trip time variation induced by a gravitational wave is a fraction $h/2$ of the unperturbed round trip time and it corresponds to a length variation of

$$\frac{\Delta L}{L} = \frac{h}{2} \quad (2.6)$$

If we use a continuous laser of frequency f , the phase delay given by GW is:

$$\Delta\phi = 2\pi f_{\text{laser}} \cdot \Delta\tau_{rt} \quad (2.7)$$

From Eq. 2.7, it is clear that a change in the frequency causes also a phase shift, which is indistinguishable from a time delay induced by the gravitational wave. Using a Michelson interferometer, which compares the phase of the beams having travelled in orthogonal arms, it is possible to cancel out frequency fluctuations as long as the arms are symmetric. Moreover, in the presence of Fabry-Perot cavities in the arms, it is possible to use the common length of the arms as a reference to stabilize the laser.² In addition the differential effect of the gravitational wave is exploited to gain a factor of two in the signal. In fact Eq. 2.4 can be written, for a beam propagating in the y direction, simply by considering that $h_{11} = -h_{22}$. Assuming again a plus polarization, we find a round trip time difference between the two arms of

$$\Delta\tau_{\text{itf}} = \frac{h}{2\pi i f_{\text{GW}}} (e^{i2\pi f_{\text{GW}} 2L/c} - 1) = h \frac{2L}{c} \text{sinc}\left(\frac{2Lf_{\text{GW}}}{c}\right) e^{2\pi f_{\text{GW}} L/c} \quad (2.8)$$

where $\text{sinc } \alpha = \frac{\sin \alpha}{\alpha}$.

The corresponding phase-shift, obtained by substituting $\Delta\tau_{\text{itf}}$ in Eq. 2.7, is

²Alternative configurations can stabilize the laser using a cavity as a reference and detect GW by measuring length changes of the other cavity using the stabilized laser.

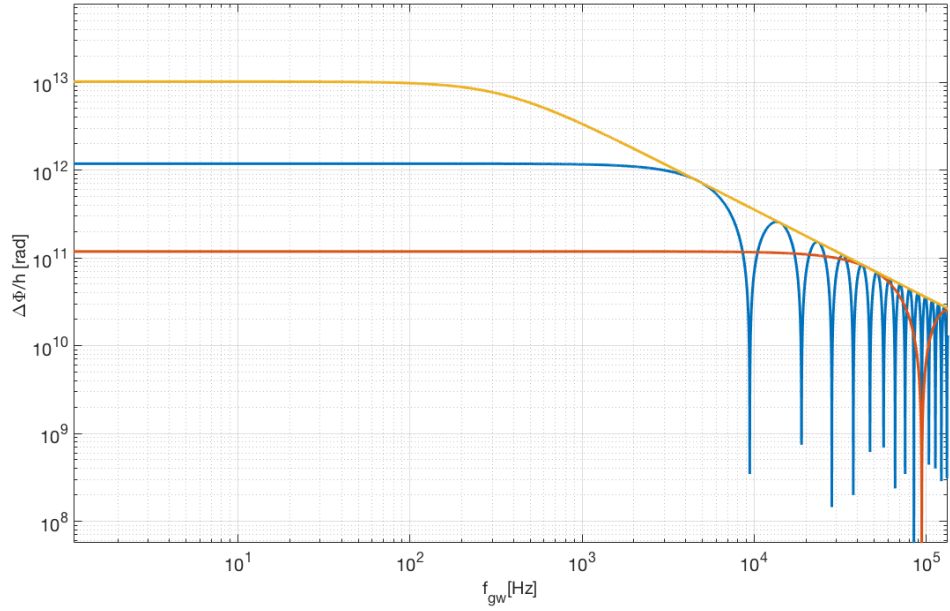


Figure 2.1: Frequency response of a simple Michelson interferometer with arm length of 100 km (blue line), 10 km (red line) and a Michelson interferometer with Fabry-Perot cavities of 3 km and with a finesse of 450 (yellow line).

plotted in Fig. 2.1 for a simple Michelson interferometer with arm length of 100 km (blue line) and 10 km (red line). We remark that:

- When $f_{\text{GW}} \ll 2L/c$ the amplitude of the effect increases with the length of the arms.
- When the frequency becomes comparable with the round trip time, the effect starts to decay as $1/f_{\text{GW}}$.
- When f_{GW} is an integer multiple of the round trip time $c/2L$ no signal is generated.

2.2 Sensitivity limits of interferometers

In order to be able to detect gravitational waves, we must ensure that the signal produced by their passing is larger than the random variation of the output in the absence of gravitational waves. This random variation, usually called *noise*, can be regarded as a random time series $s(t)$ and can be characterized by its single side Power Spectral Density defined as

$$S(f) = \lim_{T \rightarrow \infty} \frac{2}{T} \left| \int_{-T}^{+T} s(t) e^{-2i\pi ft} dt \right| \quad (2.9)$$

which measures the amount of time variation in the time series, occurring at frequency f [4]. Unlike the Fourier transform, the power spectrum doesn't keep the information of the phase of the sinusoidal components, which has no relevance for a random time series. The amplitude spectral density is defined as

$$\tilde{S}(f) = \sqrt{S(f)} \quad (2.10)$$

2.2.1 Shot noise

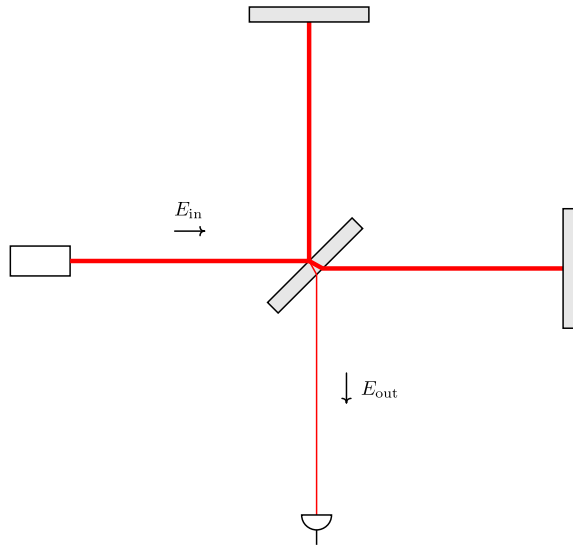


Figure 2.2: Optical scheme of a Michelson interferometer.

A Michelson interferometer, as the one sketched in Fig. 2.2 can convert a differential change in its arms length into a change in the power exiting from the anti-symmetric port. An evident limit to the sensitivity is thus set by the smallest power change that we are able to detect. It can be easily shown that for a simple Michelson interferometer, where for simplicity we took a 50:50 beamsplitter, the power at the dark port is given by

$$P_{\text{out}} = \frac{P_{\text{in}}}{4} (R_1 + R_2)(1 + C \cos \phi) \quad (2.11)$$

where R_1 and R_2 are the end mirrors power reflectivities and C is the contrast of the interferometer defined as

$$C = \frac{2r_1 r_2}{R_1 + R_2} \quad (2.12)$$

with r_1 and r_2 end mirrors amplitude reflectivities.

The phase difference ϕ is composed by a static part ϕ_{sta} and a part induced by the passing of the gravitational wave ϕ_{gw} . If we assume $R_1 = R_2 = 1$ and $\phi_{\text{gw}} \ll \phi_{\text{sta}}$, keeping only the first order term we obtain

$$P_{\text{out}} = \frac{P_{\text{in}}}{2} [1 + C \cos(\phi_{\text{sta}}) - C \sin(\phi_{\text{sta}})\phi_{\text{gw}}] \quad (2.13)$$

The change in power originated by the passing of a gravitational wave is

$$\delta P_{\text{gw}} = \frac{P_{\text{in}}}{2} C \sin(\phi_{\text{sta}})\phi_{\text{gw}} \quad (2.14)$$

Its maximum, as a function of the static phase ϕ_{sta} , occurs when $\phi_{\text{sta}} = \pi/2$, which corresponds to the mid-fringe condition for P_{out} .

In the following we present a semiclassical description of the noise due to quantum nature of light, a complete quantum description, which will be essential for describing the use of squeezed light as a mitigation technique for this noise, will be given in the third part of the thesis.

The arrival of photons on a photodetector are discrete independent events, thus described by a Poissonian distribution. The probability to count N events in an interval of time when we have an average of \bar{N} is

$$P(N) = \frac{\bar{N}^N e^{-\bar{N}}}{N!} \quad (2.15)$$

If $\bar{N} \gg 1$, the standard deviation of the distribution σ is equal to $\sqrt{\bar{N}}$. Given P_{out} , the average number of photons \bar{N} impinging on a photodiode with quantum efficiency η in a time interval δT is

$$\bar{N} = \frac{\eta P_{\text{out}} \delta T}{\hbar \omega} \quad (2.16)$$

thus the power fluctuation associated with the Poissonian statistics will be

$$\delta P_{\text{shot}} = \sqrt{\bar{N}} \frac{\hbar \omega}{\eta \delta T} = \sqrt{\frac{P_{\text{out}} \hbar \omega}{\eta \delta T}} \quad (2.17)$$

The ratio between the change in power originated by the gravitational wave (the signal) and that originated by the indetermination in the arrival time of photons (the shot noise) is

$$\frac{\delta P_{\text{gw}}}{\delta P_{\text{shot}}} = \sqrt{\frac{\eta P_{\text{in}} \delta T}{\hbar \omega}} \frac{C \sin \phi}{\sqrt{(1 + C \cos \phi)}} \phi_{\text{gw}} \quad (2.18)$$

This time the ratio is maximized when $\cos \phi = \frac{-1 + \sqrt{1 - C^2}}{C}$, which is close to the dark fringe condition. Under this condition, the minimum detectable phase change is found imposing $\delta P_{\text{gw}} = \delta P_{\text{shot}}$

$$\delta \phi_{\min} = \sqrt{\frac{\hbar \omega}{\eta P_{\text{in}} \delta T}} \quad (2.19)$$

This corresponds to an amplitude spectral density of

$$h_{\text{shot}} = \frac{\lambda}{2\pi L} \sqrt{\frac{\hbar\omega}{\eta P_{\text{in}}}} \simeq 5 \cdot 10^{-21} \left[\frac{1}{\sqrt{\text{Hz}}} \right] \quad (2.20)$$

assuming $\lambda = 1064 \text{ nm}$, $L = 3 \text{ km}$, $P_{\text{in}} = 20 \text{ W}$.

2.2.2 Radiation pressure noise

The fact that photons arrive not equally spaced in time and that they carry a non-zero momentum causes a fluctuating radiation pressure force on the test masses which reflect the light. This is responsible for a displacement noise of the test masses limiting the sensitivity of the interferometer. The fluctuation in the radiation pressure force exerted on a perfectly reflecting mirror is related to the power fluctuation of the light impinging on it as

$$\delta F = \frac{2\delta P}{c} \quad (2.21)$$

As before, the power fluctuation are generated by the non constant arrival time of the photons on the mirror and the corresponding amplitude spectral density for the force fluctuations is

$$F(f) = \sqrt{\frac{8\pi\hbar P}{c\lambda}} \quad (2.22)$$

which in turn corresponds to a displacement spectrum for each mass of

$$x(f) = \frac{F(f)}{M(2\pi f)^2} = \frac{1}{M(2\pi f)^2} \sqrt{\frac{2\pi\hbar P}{c\lambda}} \quad (2.23)$$

where M is the mirror mass. The radiation pressure noise will be

$$h_{\text{rp}}(f) = \frac{2}{L} x(f) \quad (2.24)$$

where the factor 2 comes from the fact that fluctuations in the two arms are anti-correlated.³ The quantum noise is given by the sum of these two contributions:

$$h_{\text{qn}} = \sqrt{h_{\text{shot}}^2 + h_{\text{rp}}^2} \quad (2.25)$$

As can be seen in Fig. 2.3, at low frequency it is dominated by the radiation pressure which scales as $1/f^2$, while at high frequency it is dominated by the shot noise, which is independent of the frequency. Given a frequency f , it is possible to find a value for the power that minimizes h_{qn} . The locus of all this minima, called *standard quantum limit*, is

$$h_{\text{SQL}} = \frac{1}{\pi f L} \sqrt{\frac{\hbar}{M}} \quad (2.26)$$

³Even if this semiclassical description brings to correct results, the complete quantum picture proposed by Caves [24], presented in the following, will relate radiation pressure noise only to the vacuum fluctuations entering the ITF darkport.

Given an interferometer with arms length L and mirror masses M , the standard quantum limit (SQL) seems to represents a lower limits for the sensitivity achievable. Although connected to the fundamental uncertainty principle of quantum mechanics, SQL is not a fundamental limit itself. We will see how the use of quantum states of light with modified noise features, so called squeezed light, will allow to circumvent this limit.

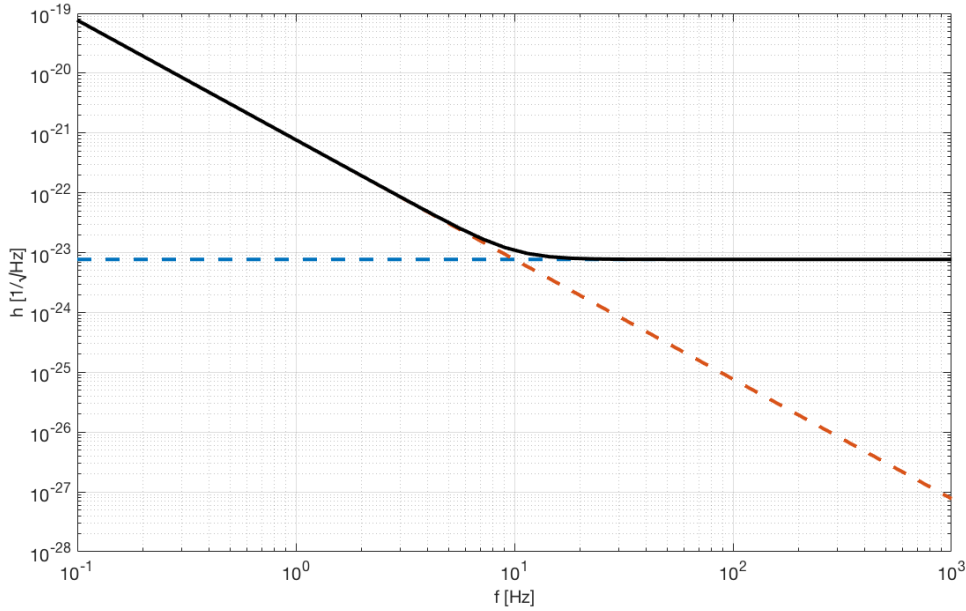


Figure 2.3: The strain equivalent quantum noise is plotted for an interferometer with $M = 50$ kg, $L = 3$ km, $P = 10$ MW. The two contribution of radiation pressure noise and shot noise are shown in blue and red respectively.

2.2.3 Seismic Noise

Everywhere on Earth the ground is subjected to a persistent vibration originated by different factors referred to as *seismic noise*. Low frequencies (below 1 Hz) are mainly due to natural factors and in particular to ocean waves. The peak between 0.1 and 0.3 Hz, known as *microseismic peak*, is expected to be generated by pairs of ocean wave trains of opposing propagation directions with half the seismic frequency [25]. At high frequency (above 1 Hz), seismic noise is mainly produced by human activities. A typical vibration spectrum above 1 Hz is given by [26]

$$x_s = 10^{-7} \left(\frac{1\text{Hz}}{f} \right)^2 \frac{m}{\sqrt{\text{Hz}}} \quad (2.27)$$

To reach a sensitivity of 10^{-23} at 100 Hz such noise need to be attenuated of more than 10 orders of magnitude. Interferometers exploit the filtering behavior of the

pendulum in order to isolate their test masses from seismic noise. The equation of motion of a mass m suspended to a wire of length l writes $m\ddot{x} = -(mg/l)(x - x_{\text{sus}})$, thus the transfer function between the mass motion and the motion of the suspension point is given by

$$\frac{x}{x_{\text{sus}}} = \frac{f_0^2}{f_0^2 - f^2} \quad (2.28)$$

where $f_0 = \frac{1}{2\pi}\sqrt{\frac{g}{L}}$ is the pendulum resonance frequency. Above the resonance frequency the transfer function can be approximated as:

$$\frac{x}{x_{\text{sus}}} \simeq -\frac{f_0^2}{f^2} \quad (2.29)$$

This shows that the pendulum acts as a second order lowpass filter and that combining a cascade of pendulums an arbitrary level of attenuation can be obtained. Nevertheless there are physical limitations to the number of pendulums we can use and on how low their frequency resonance can be pushed. Pendulum-like seismic noise attenuators used for suspending mirrors in second generation gravitational wave detectors, are conceived to have resonance frequencies lower than 1 Hz. Below this frequency detectors sensitivity is limited by seismic noise.

2.2.4 Newtonian Noise

The change in the gravitational field in the vicinity of the interferometer produces a displacement noise for the test masses which is not possible to shield. Such a change is caused by a variation of the mass distribution induced by seismic waves in the ground and density fluctuations in the atmosphere. According to [27], given a ground motion spectrum x_g , the equivalent strain noise is

$$h_{\text{nn}} = \frac{G}{\sqrt{3\pi}} \frac{\rho}{L} \frac{x_g}{f^2} \quad (2.30)$$

where L is the arm length, G is the gravitational constant and ρ is the ground density near the instrument.

The seismic contribution, together with the atmospherical one that has a similar magnitude [28], are expected to limit the sensitivity of second and third generation gravitational wave detectors below 20 Hz. Since there is no means to isolate test masses from such disturbance, the strategy is, at first, to locate the instrument in a quiet place. It has also been observed that the effects of the newtonian noise are reduced of about one order of magnitude by going underground. For this reason the Japanese detector KAGRA is being installed in Kamioka mine and Einstein Telescope, the European third generation gravitational waves detector is also planned to be built underground. The possibility to measure independently the newtonian noise and subtract it from the data has been successfully tested [29]. Seismic arrays have been installed around Advanced LIGO and are being currently installed in

Advanced Virgo at this scope.

2.2.5 Thermal Noise

Thermal noise is due to the fact that each vibration mode of the mirrors and of their suspensions is randomly excited with an energy proportional to the temperature T of the system. In practice, this consists in a vibration of the atoms of the system which results in a displacement noise for the test mass. The fluctuation-dissipation theorem states that there is a relation between the response of a driven dissipative system and the spontaneous fluctuations of a generalized variable of the system in equilibrium [30]. From this relation is possible to deduce the power spectral density of a dissipative force F_{th} acting on a system where $x(t)$ is the position of a mass and $\dot{x}(t) = v(t)$ is its velocity. The equation of motion for the system in frequency domain can always be written as

$$F_{th}(\omega) = Z(\omega) \tilde{v}(\omega) \quad (2.31)$$

where $Z(\omega)$ is the impedance. By defining the admittance of the system as $Y(\omega) = Z^{-1}(\omega)$ and recalling that in frequency domain $\tilde{v}(\omega) = i\omega x(\omega)$, the relation above can be rewritten as

$$x(\omega) = Y(\omega) \frac{F_{th}(\omega)}{i\omega} \quad (2.32)$$

According to the fluctuation-dissipation theorem, power spectrum of the thermal fluctuation force $S_F(\omega)$ is given by

$$S_F(\omega) = 4k_b T \operatorname{Re}[Z(\omega)] \quad (2.33)$$

where k_b is the Boltzmann constant and T is the temperature of the system. This relation, together with Eq 2.32, allows us to compute the power spectral density for the mass position

$$S_x = |Y| \frac{S_F}{\omega^2} = \frac{4k_b T}{\omega^2} \operatorname{Re}[Y(\omega)]$$

In our systems, the dissipative forces causing thermal noise are mainly due to internal damping of the material composing the mirrors and their suspensions. An effective model to describe this effect is an extension of Hooke law [31]:

$$F = k [1 + i\phi(\Omega)] x \quad (2.34)$$

where the imaginary coefficient ϕ , the *loss angle*, accounts for the dissipation of the system, introducing a delay between the force applied and the displacement. The

corresponding spectral density is

$$S_x = \frac{4k_b T k \phi}{\phi^2 k^2 + \omega (k - M\omega^2)^2} \quad (2.35)$$

which, above the resonance, can be approximated as

$$S_x = \frac{4k_b T \phi \omega_0^2}{M \omega^5} \quad (2.36)$$

where ω_0 is the angular frequency at resonance.

2.2.5.1 Pendulum thermal noise

We used this model to compute the pendulum thermal noise spectrum for a suspended mirror. The elastic constant of the pendulum is the sum of the lossless constant provided by gravity

$$k_g = \frac{Mg}{L}$$

(where M is the mirror mass and L is the wire length) and a smaller constant which originates from the wire elasticity and is affected by losses

$$k_{el} = \frac{N_w \sqrt{T_w EI}}{2L^2} (1 + i\phi_w)$$

with N_w number of wire, E wire material Young module, L wire length, I moment of inertia of the wire cross section, T_w tension of each wire and ϕ_w is the loss angle of the wire. Since $k_g \gg k_{el}$ we have

$$k_{tot} \approx k_g \left(1 + i \frac{k_{el}}{k_g} \phi_w \right)$$

The loss angle is

$$\phi_p = \frac{k_{el}}{k_g} \phi_w = \frac{N_w \sqrt{T_w EI}}{2gLM} \phi_w$$

The ratio, $\frac{k_{el}}{k_g}$ usually referred to as *dilution factor*, is a measure of the loss reduction achieved using a pendulum instead of a spring made of a material with the same loss angle ϕ_w of the pendulum wire and this is due to the fact that gravity is not subjected to dissipation.

The thermal spectrum above resonance is obtained by substituting the pendulum loss angle ϕ_p in Eq. 2.36:

$$S_x = \frac{4k_b T \phi_p \omega_0^2}{M \omega^5} \quad (2.37)$$

Typical value of ϕ_p for the steel wires used in Virgo where $\sim 10^{-6}$ (intrinsic losses of steel wires and dilution factor are $\sim 10^{-3}$). Silica fibers used in second

generation detectors instead of steel wires has much lower intrinsic loss of $\sim 10^{-7}$, even with a larger dilution factor $\sim 10^{-2}$ (required by a larger uncertainty on the fiber strength), the resulting value of ϕ_p is $\sim 10^{-9}$. The equivalent strain noise due pendulum thermal noise for Advanced Virgo is plotted in Fig. 4.4.

2.2.5.2 Coating thermal noise

Starting from the fluctuation-dissipation theorem, the mirror thermal noise can be computed by means of a direct approach [32]. The observable affected by thermal noise $x(t)$ is defined as the displacement of the mirror surface $u(r,t)$ as sensed by the impinging laser beam whose intensity, in our case, has a Gaussian profile $I(r)$.

$$x(t) = \int I(r)u(r,t)dS \quad (2.38)$$

To compute the thermal noise spectrum we could imagine to apply on the mirror, for each frequency, a sinusoidal force $F(r,t)$ with the same intensity distribution of the laser beam. The admittance of this system Y is

$$Y(\omega) = \frac{i\omega x(\omega)}{F(\omega)} = \frac{v(\omega)}{F(\omega)}$$

its real part will account for the dissipation of the system

$$Re[Y] = Re \left[\frac{v(\omega)F^*}{F(\omega)^2} \right] = \frac{W_{diss}(\omega)}{F(\omega)^2}$$

Thanks to the fluctuation dissipation theorem, the spectrum of the mirror surface motion induced by thermal noise is found to be

$$S_x = \frac{4k_bT}{\omega^2} Re[Y] = \frac{4k_bT}{\omega^2} \frac{W_{diss}(\omega)}{F(\omega)^2} \quad (2.39)$$

where W_{diss} is the dissipated energy. For a mirror with loss angle ϕ the dissipated energy is given by

$$W_{diss} = \omega\phi U_{max} \quad (2.40)$$

where U_{max} is the maximum energy stored in the mirror during an oscillation. This corresponds to

$$U_{max} = \frac{1 - \sigma^2}{2\sqrt{\pi}E_0w} F(\omega)^2 \quad (2.41)$$

where σ is the Poisson ratio, E_0 the mirror Young modulus and w the laser beam radius. Finally we can find the mirror thermal noise spectrum

$$S_x = \frac{4k_bT}{\omega} \frac{(1 - \sigma^2)}{2\sqrt{\pi}E_0w} \phi \quad (2.42)$$

It has been observed that the main contribution to the mirror total thermal noise is due to the tiny reflective coating layer on the mirror surface. The reasons are that at present the loss angle of the coating (which are composed of alternating layer of high and low refraction indices) are much higher than that of the mirror substrate ($\sim 10^{-4}$ respect with $\sim 10^{-9}$) and that such losses are concentrated on the mirror surface. Moreover the fraction of the energy U_{\max} stored in the surface due to the application of a Gaussian force (see computation above) is larger than that on the substrate, thus losses on the surface has a stronger impact with respect to the others. The coating thermal noise is given by the following expression [33]:

$$S_x = \frac{8k_b T}{\omega} \frac{(1 + \sigma)(1 - 2\sigma)t}{\pi E_0 w^2} \phi_c$$

where t is the coating thickness.

Coating thermal noise for Advanced Virgo is plotted in Fig. 4.4, where it can be seen that it is expecting to limit the sensitivity between 30 Hz and 100 Hz.

2.2.6 Other noise sources

There are many other noise sources that affect the detection operation whilst not limiting the design sensitivity. Among them we mention

- **Scattering from residual gas** - Interferometers operate in vacuum to avoid phase fluctuations induced by scattering from the residual gas. The equivalent strain for a single species of molecule is

$$S_{\text{vac}} = \frac{(4\pi\alpha)^2 \rho}{v_0 L^2} \int_0^L \frac{\exp[-2\pi f \omega(z)/v_0]}{\omega(z)} dz \quad (2.43)$$

where α is the polarizability, ω the beam radius, L the arm length, ρ is the number density and v_0 is the most probable speed of the particle.

- **Laser noises** - fluctuations in the laser frequency, power and direction fluctuations can couple with the asymmetry of the arm and affect the sensitivity. As we will see in detail in the following chapters, frequency stabilization is an important issue to be tackled and is eventually reduced by locking the laser frequency on the common mode of the interferometers. Classical power fluctuations are reduced before entering the interferometer as well as jitter noise which is filter by the input mode cleaner.
- **Scattered light** - As we will see in detail in Sec. 8.2, mirror imperfections produce scattering of the incident beam. Scattered photons by ITF mirrors or auxiliary optics are likely to hit vacuum pipes, chambers or other mechanical parts and get their phase modulated by their vibrations. If they recombine with the main laser, they produce a phase noise. Light absorbers, known as

baffles, are placed along the vacuum pipe, near the mirrors and in other sensible places, preventing scattered photons to recombine with the main laser beam.

- **Cosmic rays** - Mirrors are crossed every second by thousands of particle (mainly muons) which transfer energy to them. The equivalent strain spectrum of low energy (less than 100 GeV) muons is [34]

$$S_{\text{muons}} = 10^{-26} - 10^{-27} \left(\frac{100\text{Hz}}{f} \right) \quad (2.44)$$

and is a factor 100 lower than the design sensitivity of second generation detectors. Spurious signals generated by higher energy particles are expected to be very rare and can be ruled out by comparing data of two interferometers far from each other.

- **Technical noises** - The interferometers is kept at its working point by means of many feedback loops. Numerous error signal are extracted and used, after being opportunely filtered, to drive the actuators. Many of the noises mentioned above can contaminate error signals and are reintroduced in the system by the actuators. Both sensors and actuators are also affected by electronic noise. One of the goals of the commissioning activity is to optimize feedback loops in order to reduce these technical noises below the expected sensitivity level.

2.3 Improved interferometer configuration

We have seen in Eq. 2.20 that the sensitivity of a simple Michelson interferometer limited by the shot noise can be increase by using longer arms and more powerful laser. Since there are technical limitations to the maximum arm length as well as on the maximum laser power available, the simple Michelson interferometer has been modified adding Fabry-Perot cavities in their arms to increase the optical path and a technique, known as *power recycling*, has been developed in order to increase the power in the interferometer without increasing the input one.

Finally the possibility to shape the detector sensitivity has been made possible by placing an additional mirror, called *signal recycling*, between the ITF dark port and the detection. In the section a detailed description of these three modifications to the standard Michelson configuration is present.

2.3.1 Fabry-Perot cavities

We have seen that the interferometer sensitivity benefits from longer arms.⁴ Since, for earth based interferometers the arm length so far has been limited to few kilometers by technical issues, an effective way to increase the optical path is to replace the

⁴If we not consider technical issues, the only drawback of having long arms is the reduction of the bandwidth shown in Fig. 2.1.

arms with Fabry-Perot cavities.

A Fabry-Perot cavity is composed of two mirrors separated by a distance L . With reference to the Fig. 2.4, the beams inside and outside the cavity are related as:

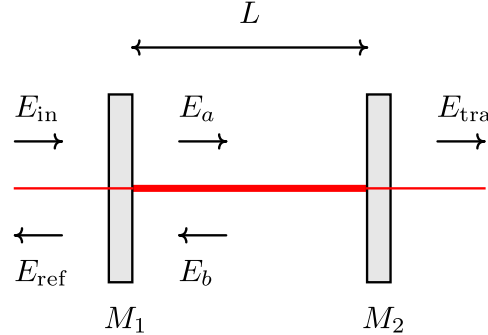


Figure 2.4: Fields in a Fabry-Perot cavity

$$E_a = t_1 E_{\text{in}} + r_1 E_b \quad (2.45)$$

$$E_b = r_2 e^{-i\phi} E_a \quad (2.46)$$

$$E_{\text{tra}} = t_2 e^{-i\phi/2} E_a \quad (2.47)$$

$$E_{\text{ref}} = -r_1 E_{\text{in}} + t_1 E_b \quad (2.48)$$

where $\phi = 2L\omega_{\text{laser}}/c$ and r, t are the amplitude reflectivity and transmissivity of the mirror 1 (input mirror) and 2 (end mirror). These values, together with the round trip phase shift ϕ , determine respectively the transmissivity, reflectivity and gain of the cavity:

$$t_{\text{cav}} = \frac{E_{\text{tra}}}{E_{\text{in}}} = \frac{t_1 t_2 e^{-i\phi/2}}{1 - r_1 r_2 e^{i\phi}} \quad (2.49)$$

$$r_{\text{cav}} = \frac{E_{\text{ref}}}{E_{\text{in}}} = -r_1 + \frac{r_1 t_1^2 e^{-i\phi}}{1 - r_1 r_2 e^{i\phi}} \quad (2.50)$$

$$g_{\text{cav}} = \frac{E_a}{E_{\text{in}}} = \frac{t_1}{1 - r_1 r_2 e^{i\phi}} \quad (2.51)$$

The circulating, transmitted and reflected power are defined as the absolute square of their respective amplitudes.

The transmitted power reads:

$$T_{\text{cav}}(\phi) = |t_{\text{cav}}(\phi)|^2 = \frac{t_1^2 t_2^2}{1 + r_1^2 r_2^2 - 2r_1 r_2 \cos(\phi)} \quad (2.52)$$

It is a periodic function of the round trip phase shift ϕ and is maximized when the condition $\phi/(2\pi) = \text{integer}$ is met. In this case the input beam E_{in} interferes constructively with the beam inside the cavity and it is said to be resonant with the cavity. The separation between two consecutive resonances is called *free spectral range*.

range and can be expressed as a length in terms of the wavelength of the laser λ

$$\Delta L_{\text{FSR}} = \frac{\lambda}{2} \quad (2.53)$$

or as a frequency in terms of the cavity length

$$\Delta\nu_{\text{FSR}} = \frac{c}{2L} \quad (2.54)$$

The cavity reflectivity at the resonance (assuming lossless input mirror, i.e. $t^2 + r^2 = 1$) can be approximated as:

$$r_{\text{cav}} \simeq \frac{r_2 - r_1}{1 - r_1 r_2} \quad (2.55)$$

According to the relative value of r_1 and r_2 , three cases can be distinguished:

- *Under-coupled cavity* ($r_1 > r_2$), the promptly reflected part of the incoming beam dominates the beam leaking out of the cavity. In the limit where r_1 approaches the unity the cavity is completely decoupled from the incoming beam.
- *Over-coupled cavity* ($r_1 < r_2$), the beam leaking out of the cavity dominates the promptly reflected one. Since in this condition the phase of the reflected beam changes across the resonance more significantly, working in over-coupled condition is necessary when we are interested in measuring changes in the cavity length.
- *Optimally coupled cavity* ($r_1 = r_2$), the power gain is maximized but there is no reflected beam and the incident beam is fully transmitted.

Circulating, transmitted and reflected power, for the there cases, are show in Fig. 2.5 for a cavity with a finesse of 60. Over-coupled cavities are more suitable for gravitational waves detectors as they allow for a larger circulating power, better exploiting the resonance effect of the cavity. Moreover the phase change of the reflected field at the resonance, which keeps the important information about a change in the cavity length, is larger than in under-coupled cavities.⁵

Given a Fabry-Perot cavity we can compute its *linewidth*, usually expressed as the *full width at half maximum* (FWHM) of the circulating power, while the *half width at half maximum* (HWHM) is known as pole frequency. It reads

$$\text{Linewidth(FWHM)} = 2f_p = \frac{2\text{FSR}}{\pi} \arcsin \left(\frac{1 - r_1 r_2}{2\sqrt{(r_1 r_2)}} \right) \quad (2.56)$$

⁵The largest change in the reflected phase is find for optimally coupled cavities but in that case the reflected amplitude vanishes.

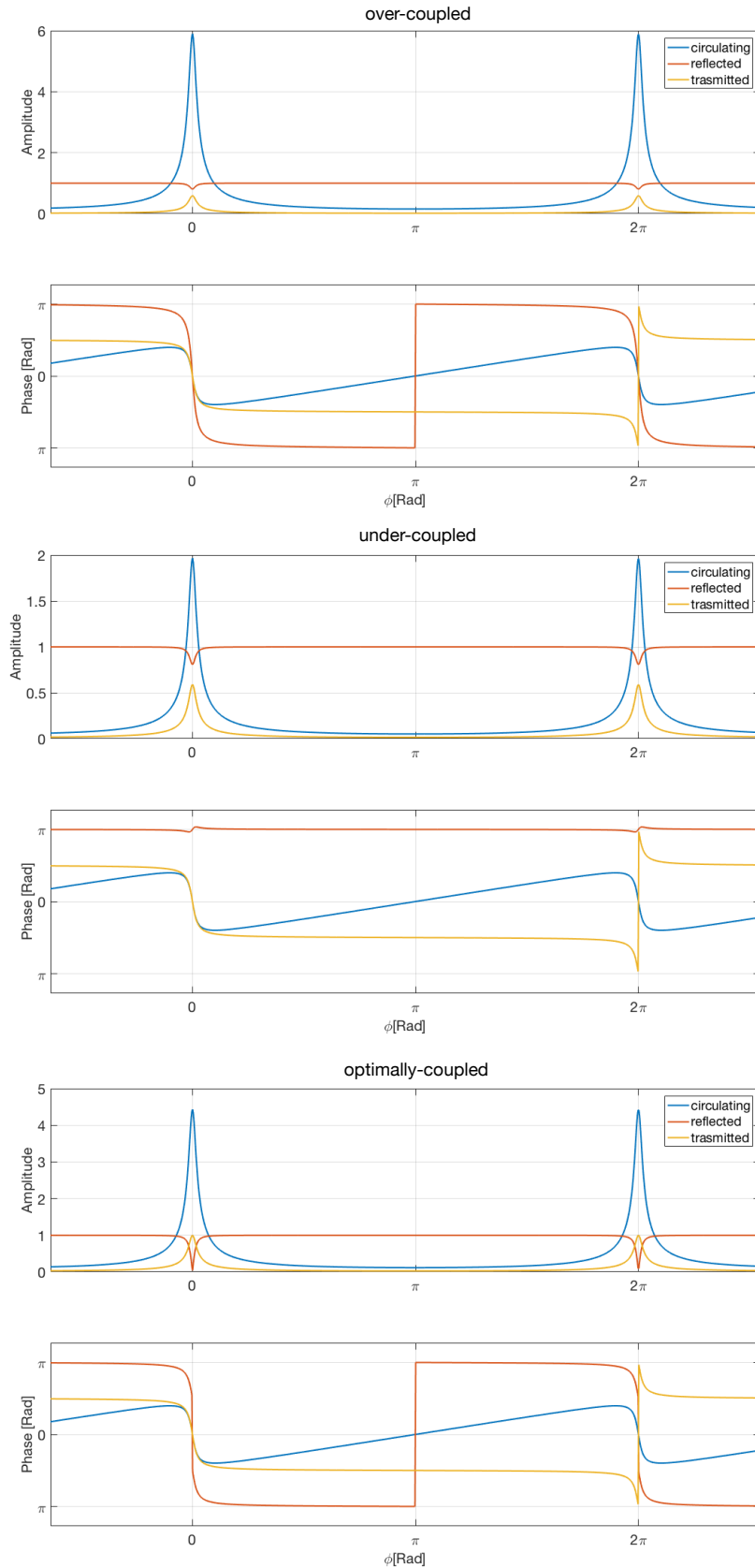


Figure 2.5: Circulating, trasmitted and reflected fields (amplitude and phase) are plotted for a Fabry-Perot cavity with a finesse of 60. The reflectivities of the two cavity mirrors are set in order to have a over-coupled cavity in the first plot, an under-coupled cavity in the second plot and an optimally-coupled cavity in the third plot.

The ratio between the linewidth and the FSR is called finesse and accounts for the sharpness of the resonance. It is also connected to the effective number of bounces of the light in the cavity as

$$N_{\text{bounces}} = \frac{2F}{\pi} \quad (2.57)$$

If the finesse is high (r_1, r_2 close to 1) it can be approximated as

$$F = \frac{\text{FSR}}{\text{FWHM}} \simeq \frac{\pi\sqrt{r_1 r_2}}{1 - r_1 r_2} \quad (2.58)$$

As can be seen in Fig. 2.5, a small detuning from the resonance produces a change in the phase of the reflected field which is larger if the cavity is over-coupled. If the finesse is much larger than one, the slope can be approximated as

$$\frac{d \arg(r_{\text{cav}})}{d\phi} \simeq \frac{2F}{\pi} \quad (2.59)$$

This means that a phase change, possibly caused by the passing of a gravitational wave, is amplified by a factor proportional to the finesse, which is actually the number of bounces in the cavity reported in Eq. 2.57.

Frequency response

The effect on the cavity mirrors produced by the passing of a gravitational waves can be modeled as a sinusoidal motion of the end mirror, where the amplitude of the oscillation, is usually much smaller than the laser wavelength λ . Such a motion causes an additional dephasing of the reflected beam, resulting in the generation of two acoustic sidebands at a distance of $\pm f_{gw}$ from the carrier. The amplitude of these effects is proportional to the amplitude of the oscillation and to the amplitude of the field resonating in the cavity. In the condition where $f_{gw} \ll c/L$, it can be shown that the frequency response of the ITF with Fabry-Perot cavities reads:

$$\Delta\phi = h \frac{F}{\text{FSR}} \frac{2\pi c}{\lambda} \frac{1}{\sqrt{1 + (\frac{f_{gw}}{f_p})^2}} \quad (2.60)$$

We see that the low frequency response increases with the Finesse and the cavity behaves as a simple pole with the cut-off frequency f_p , thus reducing the sensitivity for $f_{gw} > f_p$.

2.3.2 Power recycling

Since the end mirrors are almost totally reflecting and arm cavity losses are small (as we will see in Sec. 6.2), when the interferometer is set near the dark fringe, all the light is sent back towards the laser. The interferometer is then seen from the bright port as a mirror with a very high reflectivity (equal to the average of the arm

cavity reflectivities). By placing an additional mirror along the path between the laser and the beam splitter it is possible to create an additional resonant cavity in order to increase the circulating power inside the ITF, without increasing the input power. The recycling gain of this *power recycling cavity* can be computed simply substituting in Eq. 2.51 the reflectivity of the power recycling mirror and that of the arms cavity. The maximum is achieved when the cavity is optimally-coupled, that is when the reflectivity of the power recycling mirror is chosen to be equal to that of the arm cavities (assuming negligible losses).

It is interesting to notice that, unlike the arm cavities, the power recycling cavity does not affect the bandwidth of the interferometer. This can be explained by the fact that sidebands generated by the gravitational waves, because of their differential nature, exit directly from the asymmetric port of the beam splitter without being recycled and possibly filtered by the power recycling cavity. On the other hand their amplitude, being proportional to the power circulating in the cavity, benefits from the presence of the power recycling. In Advanced Virgo assuming (arm cavity finesse of 450 and arm round trip losses of 75 ppm) maximum power recycling gain achievable is about 48. Transmission of the PR mirror has been chosen to be $\sim 5\%$, corresponding to a lower power recycling gain of 37.5, with respect to optimal coupling it allows to increase the strength of signals in reflection from the ITF used for the power recycling cavity alignment and to reduce the effects of optical aberrations.

2.3.3 Signal recycling

In analogy to the power recycling technique, a mirror can be placed after the beam splitter dark port, creating a cavity that affects only the differential signals [35]. It will form a cavity referred to as *signal recycling cavity*. The presence of this mirror will have negligible effects on the carrier, as it is not reaching the dark port. The sidebands generated inside the cavity by the gravitational wave will see a double cavity, made by the Fabry-Perot mirrors and the signal recycling. The effect of this double cavity depends on the microscopic position of the SR mirror which is usually characterized by the phase ϕ that the carrier field would acquire while propagating inside it. If $\phi = 0$, the bandwidth of the detector is increased but the sensitivity before the cut-off frequency is reduced (broadband configuration). Conversely when $\phi = \pi/2$, the bandwidth is reduced but the sensitivity is increased (tuned configuration). For the intermediate values (detuned configurations) there is a peak frequency, depending on ϕ . The sensitivity below the peak is comparable to the broadband one, while the high frequency is worse than it. To get an intuitive motivation of such a behavior it is useful to think at the SR mirror and the input cavity mirror as an equivalent mirror (with transmission and reflection coefficients which depend on ϕ) forming a Fabry-Perot cavity together with the end mirror. For different ϕ we have

- $\phi = 0$. The reflectivity of the equivalent mirror is the lowest possible. The

sidebands will see a cavity with reduced finesse, thus the bandwidth is enlarged at the expenses of the low frequency sensitivity.

- $\phi = \pi/2$. The reflectivity of the equivalent mirror is the highest possible, The sidebands will see a cavity with increased finesse producing the opposite effect.
- $0 < \phi < \pi/2$. In this case, the equivalent mirror introduces an additional dephasing⁶ in reflection with respect to the only input mirror which normally will push them out of resonance. There exists one particular frequency for which the additional dephasing can compensate exactly those acquired inside the arm cavities. This causes a peak on the sensitivity accounting for the resonance of this particular frequency which depends on ϕ .

The changes in the detector response according to different tuning of the signal recycling mirror is shown in Fig. 2.6.

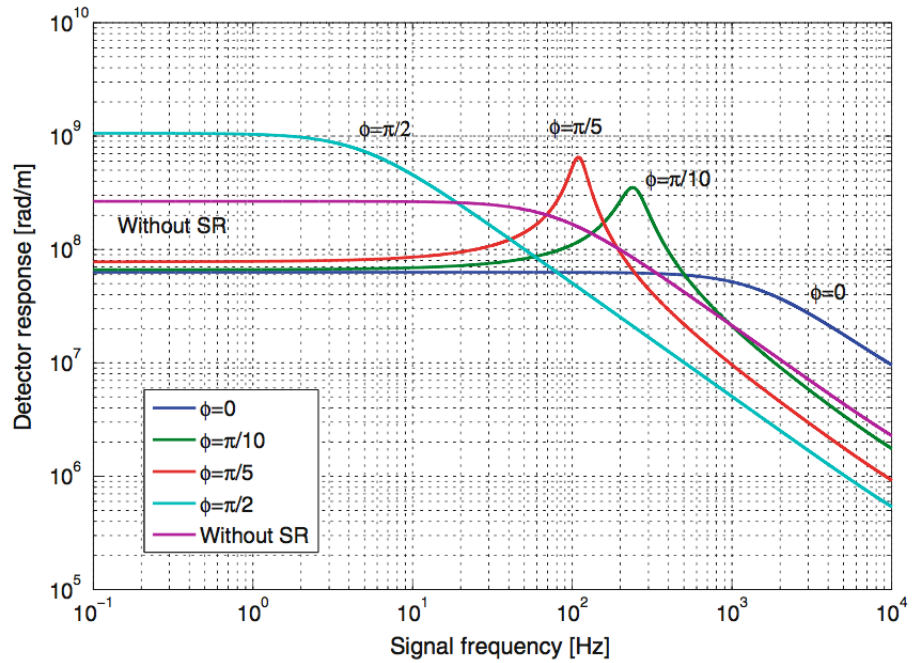


Figure 2.6: Detector response for different tuning of the signal recycling mirror. Plot from [36].

⁶Since the length of the signal recycling cavity is much shorter than the wavelength signal, we can neglect the phase accumulated by the propagation inside it and consider this additional dephasing as independent of the signal frequency.

CHAPTER 3

First detection of gravitational waves

In this chapter we will recall the path which brought to the first direct detections of gravitational waves. In the first section the initial network of GW detectors is presented together with the scientific results of their observation. Even if no GWs have been observed, interesting upper limit have been set on rate and amplitude of several possible sources. In the second section we present the second generation GW detectors, with a short summary of the major upgrades performed from the first generation ones, which allowed to gain an order of magnitude in the sensitivity. Finally in the third section we present the first gravitational-waves detections: fours binary black hole mergers and a binary neutron star merger. We briefly describe the signal search, the information we could extract about the source and the physical and astrophysical implication of the observations.

3.1 Initial network of ground-based GW detectors

The experimental effort to detect gravitational waves started in the 1960s with Weber's resonant bars [37]. In the same period, the use of interferometers was proposed for the first time. It was followed by a long period of prototyping and theoretical analysis of their possible performances and scientific potential which led to proposals to build long base-line interferometers [38].

The first generation of gravitational-wave detectors consisted of the two LIGO (4 km), located in Livingston and in Hanford, Virgo (3 km), near Pisa in Italy, GEO (600 m) near Hannover in Germany and TAMA (300 m) near Tokyo in Japan. The installation started in late 1990s and was followed by many years of commissioning activities alternated with periods of joint data taking between 2002 and 2011. This intense activity provided a deep knowledge of the interferometer performances and limits. After undergoing some major improvements, LIGO and Virgo obtained a final sensitivity close to the initial design sensitivity. The best sensitivity achieved by the first generation interferometers is respectively $1.5 \cdot 10^{-21}/\sqrt{\text{Hz}}$ (TAMA),

$2 \cdot 10^{-22}/\sqrt{\text{Hz}}$ (GEO), $6 \cdot 10^{-23}/\sqrt{\text{Hz}}$ (Virgo), $2 \cdot 10^{-23}/\sqrt{\text{Hz}}$ (LIGO) [39]. The four detectors have similar optical schemes composed by a power recycled interferometers, all of them with the exception of GEO made use of Fabry-Perot cavities to increase the optical path of the light. In turn GEO was the only one using signal recycling [40]. Test masses, fused silica mirrors of diameters between 10 cm (TAMA) and 35 cm (VIRGO), were suspended with chains of pendulums providing isolation from seismic noise. The laser power stored ($\lambda = 1064$ nm) was going from 1 kW (TAMA) up to 50 kW (LIGO) [39]. Fig. 3.1 shows the best sensitivity achieved by first generation GW detectors.

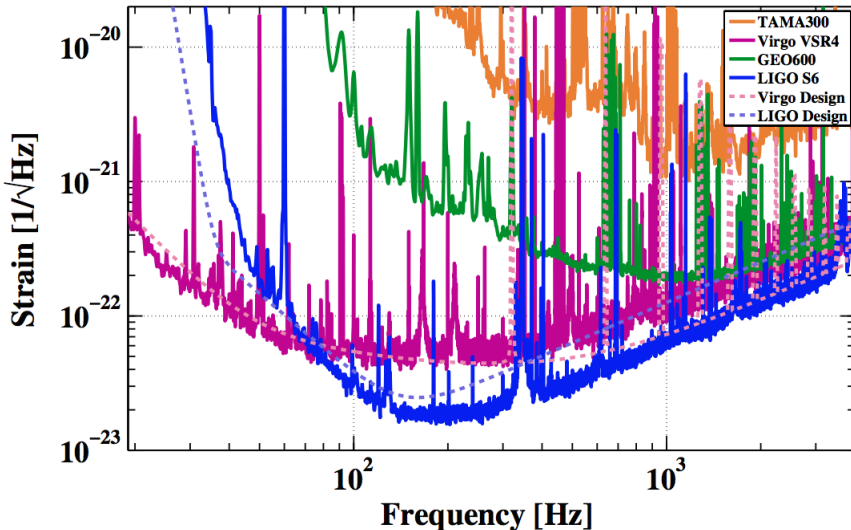


Figure 3.1: Best sensitivity achieved by first generation gravitational wave detectors [39]

Observation results

Even if no gravitational wave detection has been reported from the data taken by first generation detectors, the analysis of the data allowed to put upper limits on the rate of coalescence of compact objects and on the amplitude of signal from pulsars, stochastic background and of events that could have taken place in coincidence with some external trigger (e.g. gamma ray burst).

The data collected by LIGO and Virgo between July 2009 and October 2010 were analyzed looking for signals from binary neutron stars (NS-NS), binary black holes (BH-BH), and binaries of a black hole and neutron star (NS-BH) with total mass between 2 and $25M_\odot$. The sensitivity range for binary neutron stars was 40 Mpc and further for BH-BH and NS-BH binaries.¹. The upper limits found for NS-NS,

¹The BNS range is defined as the sky location and source orientation averaged distance at which the coalescence of a pair of $1.4 M_\odot$ neutron stars gives a matched filter signal-to-noise ratio of 8 in

NS-BH and BH-BH were respectively $1.3 \cdot 10^{-4}$, $3.1 \cdot 10^{-5}$ and $6.4 \cdot 10^{-6} \text{ Mpc}^{-3} \text{ yr}^{-1}$ [41]. An upper limit of $3.3 \cdot 10^{-7} \text{ Mpc}^{-3} \text{ yr}^{-1}$ has been set also on the rate of heavier BH-BH binaries with nonspinning components having total mass between 19 and 28 M_\odot [42].

For what concerns the search for unmodeled signals, an upper limit on the rate of 1.3 events/year has been set for signals having $h_{\text{rss}}^2 5 \cdot 10^{-22} - 5 \cdot 10^{-20} \text{ Hz}^{-1/2}$ (the search targeted signal shorter than 1 s, in a frequency bandwidth of 64–5000 Hz) [43].

The lack of gravitational wave detection in the presence of an external trigger has been used to rule out some hypothesis on the galaxy hosting a gamma ray burst (GRB). It was the case of GRB 070201, a short-duration, hard-spectrum GRB, electromagnetically localized in the direction of M31 (Andromeda Galaxy). Possible progenitor events such as NS-NS or NS-BH binary coalescences or soft GRB repeaters can also emit gravitational waves. The absence of a gravitational signal recorded in an interval of 180 s about the time of the trigger³ ruled out the coalescence of compact binary with masses in the range $1M_\odot < m_1 < 3M_\odot$ and $1M_\odot < m_2 < 40M_\odot$ in the Andromeda Galaxy, as a progenitor of GRB 070201. Assuming the GRB 070201 had a binary neutron star merger as a progenitor, then it should have happened at a distance $D > 3.5 \text{ Mpc}$ (assuming random inclination) [44].

Also the search for continuous signal, although it did not detect any gravitational signal, was useful to set interesting upper limits on pulsar GW emissions. The most stringent upper limit for Crab was of $6.9 \cdot 10^{-25}$, about a factor of 2 below the spin-down limit. It corresponds to an upper limit on star ellipticity of about $3.7 \cdot 10^{-4}$. These results were obtained from the analysis on Virgo VSR4 data. [11].

A stochastic background appears in a single detector as random fluctuations of the output power which is indistinguishable from noise. Even if its level is expected to be lower than the detector noise floor, unlike the noise it is supposed to be coherent between different detectors and can be revealed by cross-correlating data from pairs of interferometers of the network. This has been done by correlating data from the two LIGO detectors acquired during the S5-VSR1. No signature of gravitational wave background has been found but the analysis set an upper limit for the energy density of the stochastic gravitational-wave background (normalized by the critical energy density of the Universe), at 100 Hz of $6.9 \cdot 10^{-6}$ [45].

a single detector. The BBH range considers black holes of $30M_\odot$. The horizon, instead, assumes an optimally oriented source.

²The amplitude of the signal is expressed in terms of the root-sum-square strain amplitude h_{rss} arriving at the Earth, defined as in the range $h_{\text{rss}} = \sqrt{\int |h_+(t)|^2 + |h_\times(t)|^2}$.

³At the trigger time only LIGO Hanford detector was taking data. The presence of a network of detectors can be exploited in case of external trigger to increase the sensitivity in a specific direction, by imposing conditions on the relative time delay and the signal amplitude recorded by different detectors.

3.2 Second generation of ground-based GW detection

After a few years of data taking without detections, an, already planned, second generation network of interferometers started to be integrated. The goal was to increase the sensitivity of about one order of magnitude, increasing the volume of the observable universe by a factor of 1000 in order to detect gravitational waves on a regular basis, opening the way to gravitational astronomy. This second generation network includes the two detector of Advanced LIGO, Advanced Virgo and the Japanese detector KAGRA.

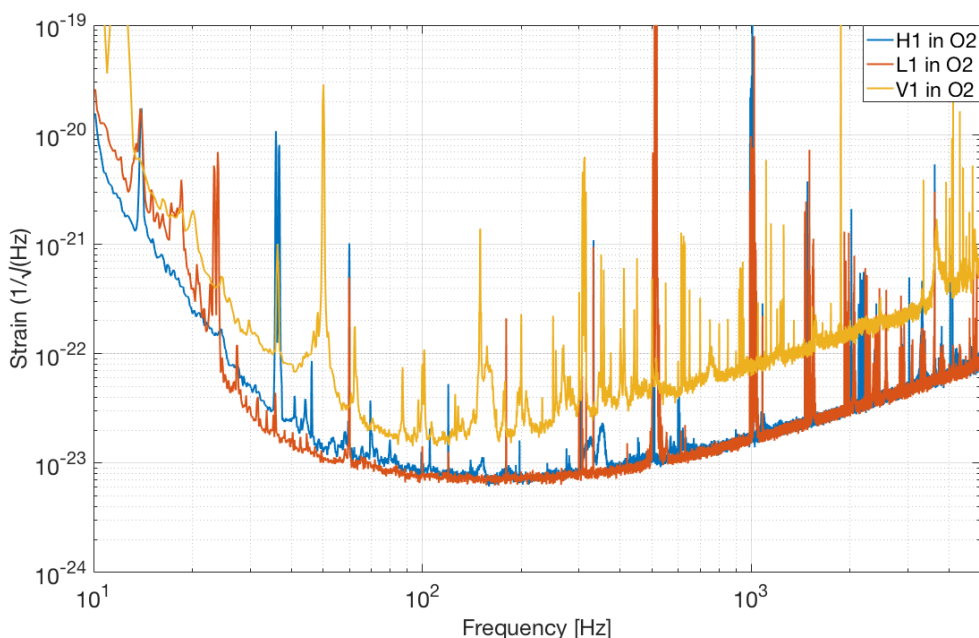


Figure 3.2: Sensitivity of the two Advanced LIGO and Advanced Virgo during the second observation run O2.

3.2.1 Advanced LIGO

Advanced LIGO project has been approved by the National Science Foundation in 2008. The installation, started in 2011, has been completed in few years and followed by a commissioning period from mid 2014 to mid 2015, leading to the first observation run O1 which lasted from September 2015 to January 2016 [46]. Design sensitivity for the BNS inspiral range is 190 Mpc. The sensitivity of Advanced LIGO in O1 at 100 Hz was $8 \cdot 10^{-24} \text{ } \text{1}/\sqrt{\text{Hz}}$, the BBH range was 1.3 Gpc and the BNS one about 75 Mpc. This represented an increase of about a factor 3-4 with respect to the best sensitivity achieved by initial LIGO. The second observation run O2 started at the end of November 2016 and lasted until the end of August 2017. Advanced Virgo joined the run for the last month of observation.

3.2.2 KAGRA

KAGRA (KAmioka GRAvitational wave detector) is a 3 km interferometer located in the mine of Kamioka, in Japan. The project was approved in 2010 and the integration, which officially started in January 2012, is still ongoing. A preliminary run in a simple Michelson configuration (iKAGRA) was performed in March 2016. In the final configuration, the KAGRA test masses will be cooled down to 20K. The cryogenic technology, which is devised to reduce thermal noise of sapphire mirrors has been tested on CLIO, an underground 100 m interferometer (also located in Kamioka mine) used as a test facility for KAGRA [47]. KAGRA is expected to start its cryogenic operation in 2018 and to reach its final configuration before 2020, joining the second generation network. The presence of a fourth detector, with comparable sensitivity, will bring an essential contribution to gravitational wave observations: it will not only improve the sources' localization, but also increase the detection rate of almost a factor 2, by improving the network duty cycle and by allowing coherent data analysis to reduce the spurious instrumental coincident background [48]. Moreover it will allow for a more accurate parameter estimation [49].

3.2.3 Advanced Virgo

Advanced Virgo [50] has been approved by INFN and CNRS at the end of 2009. The target BNS range (with signal recycling tuned in the optimal configuration) is about 135 Mpc. Installation works started in 2012 and were completed by the end of 2016. After some months of commissioning in August 2017 Advanced Virgo joined the two LIGO detectors for the last month of the second observation run O2 with a sensitivity of about 27 Mpc. The following is a list of the main upgrades concerning the technology and the configuration of second generation gravitational wave detectors which were performed in order to improve their sensitivity of an order of magnitude.

- **Dual recycling** - The possibility to shape the frequency response of the interferometer by adding a semireflecting mirror on the path between the beam splitter dark port and the detection will be exploited by second generation detectors. GEO was the only first generation interferometer that successfully tested this technology [40].⁴ As explained in Sec. 2.3.3, by microscopically adjusting the mirror position, it is possible to tune the sensitivity in order to target specific astrophysical sources. Advanced LIGO was operated in the first two observation runs in a broadband resonant sideband extraction configuration. Both Advanced Virgo and KAGRA planned, in their design configuration, to make use of a detuned signal recycling to be more sensitive to BNS coalescence. At present, signal recycling has not yet been installed in Advanced Virgo, which

⁴We remark that the overall configuration is different since GEO does't have Fabry-Perot cavities in their arms.

has started its operation in a Fabry-Perot Michelson configuration with power recycling.

- **Improved mirrors** - Better quality mirrors have been used both in Advanced Virgo and Advanced LIGO [51]. Mirror weight has been doubled (42 kg) in Advanced Virgo to reduce the effect of the radiation pressure noise. Since a non negligible optical absorption in the mirrors of first generation detectors resulted in thermal lensing effect and significant distortions of the mirror surface, the requirement for mirror absorption is less than 1 ppm/cm. Deviations from perfect spherical surfaces (flatness and microroughness depending on the spatial frequency of the defects) are responsible for scattering losses (see 8.2 for more details). The flatness RMS is less than 0.5 nm for advanced Virgo mirrors while the requirement was 8 nm for initial Virgo. Improvements in coating losses allowed for a reduction of mirror thermal noise which is however limiting the detector sensitivity between 50 and 300 Hz.
- **More powerful laser** - In order to improve the shot noise limited high frequency sensitivity, advanced detectors are designed to store from 0.5 to 1 MW in their arms cavities. This increase of a factor 10-50 with respect to the first generation will require suitable optics to avoid thermal lensing and heavier mirrors to reduce the effect of radiation pressure noise. Particular attention has to be payed to reduce classical power fluctuations as at this high power level such fluctuations move the mirrors and can affect the differential signal in the presence of an asymmetry in the arm finesse.
- **Monolithic suspensions** - Thermal noise of the steel wires used to suspend the mirrors was limiting the sensitivity of first generation detector at low frequency. This was in part due to the intrinsic dissipation of the steel. In second generation detectors, the steel wire have been replaced with fused silica fiber (sapphire for KAGRA) with an intrinsic dissipation which is about a factor 1000 lower than steel. This technique was first successfully tested in GEO and in an upgrade of Virgo [52]. Then, an intense activity of R&D has followed in order to adapt the suspension design to the new optics. Despite the great advantage in terms of noise reduction, fused silica fibers are very fragile and can easily break if they come into contact with external bodies. The presence of projectile particles accelerated by the vacuum pumps was responsible for the repeated break of the fibers in Advanced Virgo. As a temporary solution, steel wires were used for suspending the mirrors in order to allow the commissioning to continue while investigating the problem. The reinstallation of monolithic suspensions is one of the planned activity for the commissioning period between the second and the third observation run.
- **Arm cavities configuration** - In order to allow for larger beams and re-

duce the effect of quantum noise Advanced Virgo switched from plano-concave Fabry-Perot cavities to bi-concave ones. The finesse of the arm cavities have also been increased from ~ 50 to ~ 450 .

- **Thermal compensation** - The planned increase of the circulating power will cause a temperature gradient inside the optics. This produces a thermoelastic deformation resulting in a change of the radius of curvature of the mirrors and in a non uniformity of the optical path of the light inside the mirror which is acting as a lens (thermal lensing effect). The installation of a ring heater around the mirrors allows to compensate for the change in the radius of curvature. In order to cope with the thermal lens effect, a CO_2 laser in a ring shape will be shined on a compensation plate suspended in front of the input test masses (in the recycling cavity side).
- **Vibration isolation** - Advanced LIGO performed other two major changes in its configuration. It replaced the previous vibration isolation system formed by a bench laying on a stack of isolating layers of rubber and metal with a three-stage hybrid active-passive system [53]. Virgo was already equipped with an isolation system, the *superattenuator*, which was already compliant with second generation requirements.
- **Optical configuration** - For what concerned the optical configuration in first generation interferometers, power recycling cavity was marginally stable. This was an effect of the combined necessity of a short cavity and a large beam. Thermal distortion, mirrors defects and misalignment can make high order modes resonate in such cavities, reducing the optical gain of the fundamental mode and making the control more difficult. For first generation thermal compensation systems were used to reduce these effects. Advanced LIGO and KAGRA opted for a different configuration with long folded stable recycling cavities. For planning and budget reasons, Advanced Virgo has kept marginally stable cavity configuration, relying on a more performant thermal compensation system and an increased mirror surface quality.

3.3 First detections: beginning of the gravitational astronomy

3.3.1 The observations

After a few days from the beginning of their stable operation, on September 14, 2015, the two LIGO interferometers detected for the first time a signal (GW150914) compatible with the gravitational radiation emitted by the merging of two black holes with masses of about $36 M_\odot$ and $29 M_\odot$, at an estimated distance between 230



Figure 3.3: Network of second generation gravitational waves detectors. From top right, clockwise: Advanced LIGO Hanford, KAGRA (artistic view), Advanced Virgo, Advanced LIGO Livingston.

and 570 Mpc. The event had a signal-to-noise (SNR) ratio of 24. This was the first direct gravitational-wave detection and was followed by other three observations of binary black hole mergers. The second one, on December 26, 2016 (GW151226) was identified as the coalescence of two black holes with masses respectively of $14.2 M_{\odot}$ and $7.5 M_{\odot}$ at a distance between 250 and 620 Mpc, with a SNR of 13. The third observation, on January 4, 2017, performed during the second observation run O2, concerned two black holes with masses of $31.2 M_{\odot}$ and $19.4 M_{\odot}$ respectively and a SNR of 13. The estimated distance was between 490 and 1330 Mpc. The fourth published observation, on August 14, 2017 concerned again two black holes with masses of $30.5 M_{\odot}$ and $25.3 M_{\odot}$ at a distance between 330 and 670 Mpc, but this time, for the first time, the merging has been observed by a network of three detectors. As we will detail in the following this allowed a major improvement in the localization of the source and gave the possibility to perform some preliminary test on the nature of gravitational-wave polarization. Lastly on August 17, 2017 the network detected, for the first time, a gravitational-wave signal emitted by the merging of two neutron stars with masses between $1.17 M_{\odot}$ and $1.6 M_{\odot}$ at a distance of about 40 Mpc. For the first time an electromagnetic counterpart has been detected in association with the gravitational wave signal. Only with this one event, marking the beginning of multimessenger astronomy, a wealth of relevant discoveries have been done. A summary of them is presented in the following.

3.3.2 Binary black hole mergers

3.3.2.1 A simple proof that GW150914 was a black hole binary coalescence

As a first step in order to better visualize the signal, the raw strain data $h(t)$ are filtered using a band-pass filter to keep only the frequencies inside LIGO bandwidth (30 - 350 Hz) and using a notch-filter to removing some particular frequencies known to be part of the instrumental noise. After this operation, the presence of a signal, shown in Fig. 3.4, was clear enough to be recognizable by eye⁵. The same is true for the time frequency representation, which shows the typical increase of the frequency over time expected from gravitational emission of two coalescing masses. A signal with this kind of frequency behavior is known as *chirp*. In GW150914, the frequency increased from 35 to 150 Hz in 0.2 s. Its time evolution, at the leading order, can be used to find the chirp mass of the system by using the relation

$$\mathcal{M} = \frac{(m_1 m_2)^{3/5}}{(m_1 + m_2)^{1/5}} = \frac{c^3}{G} \left[\frac{5}{96} \pi^{-8/3} f^{-11/3} \dot{f} \right] \quad (3.1)$$

where G is gravitational constant, c is the speed of light and f and \dot{f} are the frequency and its time derivative measured in any moment of the inspiral phase.⁶ From the measured chirp mass $\mathcal{M} = 30 M_\odot$ we can set a lower limit on the total mass of the system $M = m_1 + m_2 \geq 70 M_\odot$ corresponding to a Schwarzschild radius greater than 105 km. The fact that the computed chirp mass is constant up to the merging and that the amplitude of the oscillation increases with time are in agreement with what we expect from a binary merging. The frequency at which the amplitude is maximum, $f \sim 150$ Hz, corresponds to the double of the orbital frequency of the two masses. From this information, simply applying the third Kepler's law, we can infer that the separation of the two masses at the maximum of the frequency was only 350 km. This small value, combined with the lower limit that we have on the masses, leads to the conclusion that the two compact objects can only be black holes.

3.3.2.2 The signal search

In order to detect the presence of a gravitational waves transient in the data, two types of search are used: one, specific for finding signals from compact binary coalescences and the other to detect transient signals without any assumption on their waveform. Events detected in both observatories with a consistent time delay are assigned a detector statistics values quantifying their SNR. The significance of an event is estimated by comparing its detection statistic value with the background, that is the rate at which the noise in the detectors produces an event with the same

⁵With respect to GW150914, the second detected signal GW151226 lasted for a longer time but with a lower strain amplitude which made indispensable the use of matched filtering to identify it.

⁶The equation can be integrated, removing the dependence from the derivative, to find Eq. 1.15.

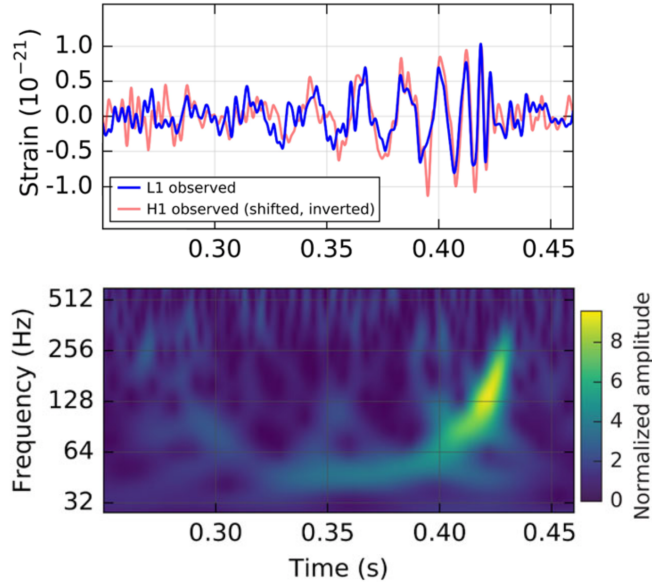


Figure 3.4: Top row: time-series data from gravitational-wave event GW150914 observed by the LIGO Hanford and Livingston. Data are filtered with a 35–350 Hz bandpass filter and band-reject filters to remove the known instrumental spectral lines. The Hanford strain has been shifted back in time by 6.9 ms and inverted. Bottom row: a representation of the strain-data as a time-frequency plot. The increase in signal frequency is well visible. Both images are taken from [54]

(or higher) detector statistic. Background is estimated by looking for coincident events in the two detectors obtained by shifting SNR maxima of one detectors by an amount of time longer than the propagation time between the two observatories (which is about 10 ms). In the case of binary coalescence search, this procedure has been repeated about 10^7 times, in order to have an equivalent background analysis time of 608 000 years. The GW150914 was found to have a detection statistic of 23.1, which is larger than any other background event. For this reason it was possible to put only an upper limit on the false alarm rate of 1 in 203 000 years⁷. Considering 16 days of observation, this corresponds to a false alarm rate lower than $2 \cdot 10^{-7}$.

3.3.3 Estimation of the source parameters

The difference in the arrival time of the signal in the two detectors allowed to localize the event in a ring in the sky with an area of about 600 deg^2 . The amplitude at the two detectors and relative phase of the signal can be used to further improve the localization and infer the distance to the source and the binary orientation. A coherent Bayesian analysis is applied on the data from both detectors to estimate the source parameters. The gravitational waveform is determined by the masses $m_{1,2}$ and

⁷Both candidates and background events are divided into three search groups according to their template length in order to account for the varying background noise.

angular momentum $S_{1,2}$ of the binary components, their location and orientation, the time and phase of coalescence and the eccentricity of the system. [55]. The angular momentum is related to the magnitude of the dimensionless spin as

$$a_{1,2} = \frac{c}{Gm_{1,2}^2} |S_{1,2}| \quad (3.2)$$

The components of the spin aligned with the orbital angular momentum, defined as

$$\chi_{1,2} = \frac{c}{Gm_{1,2}^2} S_{1,2} \cdot \hat{L} \quad (3.3)$$

are the only affecting the phase evolution of the inspiral. Following the post-Newtonian (PN) theory, phase evolution is expanded in powers of the orbital velocity v/c . Aligned-spin components don't affect the signal at leading order (which is dominated by chirp mass) and for this reason they can be only weakly constrained. The most meaningful parameter for describing the spin effect on the binary phasing is the mass-weighted combination of the orbit-aligned spins

$$\chi_{\text{eff}} = \frac{m_1 \chi_1 + m_2 \chi_2}{M} \quad (3.4)$$

which enters in the successive order of the PN expansion together with the mass ratio. The non aligned components of the spin χ_p are responsible for a precession of the orbital plane. For the parameter estimation of GW150914 and GW151226 two kinds of model of waveform covering the inspiral, merger, and ringdown phases were used: one assumes the spins aligned with the angular orbital momentum, the other does not have this constraint and allows for a precession of the orbital plane. The two give similar results [14]. For similar mass binary coalescences, the spin of the final black hole is determined by the orbital angular momentum of the system at the merging time. As expected, similar values around 0.7 are found for the spin of the final black hole for the three detections. The radiated energy can be inferred by measuring the difference between the initial and the final mass. The estimated emitted energy in gravitational waves for GW150914 is about $3 M_\odot c^2$ with a maximum instantaneous luminosity of $200 M_\odot c^2 s^{-1}$. This is the most luminous known phenomenon in the Universe: at its peak as much power as that of 10^{23} suns was emitted [56]. Peak luminosity for equal mass binaries is independent of their mass components and for this reason they can be used as standard sirens. The source luminosity distance is inferred from the signal amplitude. Such amplitude scales inversely with the distance but it also depends on the orbit plane inclination. The information on the orientation is kept in the two polarizations of the wave. In the presence of only two detectors, almost aligned, it is difficult to infer information on the polarizations and thus on the orbit inclination. This degeneracy results in a great uncertainty on the distance. The redshift cannot be measured only from the gravitational-wave signal and it is

	GW150914	GW151226	GW170104	GW170814
Primary BH mass	$36.2^{+5.2}_{-3.8} M_{\odot}$	$14.2^{+8.3}_{-3.7} M_{\odot}$	$31.2^{+8.4}_{-6.0} M_{\odot}$	$30.5^{+5.7}_{-3.0} M_{\odot}$
Secondary BH mass	$29.1^{+3.7}_{-4.4} M_{\odot}$	$7.5^{+2.3}_{-2.3} M_{\odot}$	$19.4^{+5.3}_{-5.9} M_{\odot}$	$25.3^{+2.8}_{-4.2} M_{\odot}$
Chirp mass	$28.1^{+1.8}_{-1.5} M_{\odot}$	$8.9^{+0.3}_{-0.3} M_{\odot}$	$21.1^{+2.4}_{-2.7} M_{\odot}$	$24.1^{+1.4}_{-1.1} M_{\odot}$
Total mass	$65.3^{+4.1}_{-3.4} M_{\odot}$	$21.8^{+5.9}_{-1.7} M_{\odot}$	$50.7^{+5.9}_{-5} M_{\odot}$	$55.9^{+3.4}_{-2.7} M_{\odot}$
Final BH mass	$62.3^{+3.7}_{-3.1} M_{\odot}$	$20.8^{+6.1}_{-1.7} M_{\odot}$	$48.7^{+5.7}_{-4.6} M_{\odot}$	$53.2^{+3.2}_{-2.5} M_{\odot}$
Radiated energy	$3^{+0.5}_{-0.5} M_{\odot} c^2$	$1^{+0.1}_{-0.2} M_{\odot} c^2$	$2^{+0.6}_{-0.7} M_{\odot} c^2$	$2.7^{+0.4}_{-0.3} M_{\odot} c^2$
Peak Luminosity	$3.6^{+0.5}_{-0.4} 10^{56} \frac{\text{erg}}{\text{s}}$	$3.3^{+0.8}_{-1.6} 10^{56} \frac{\text{erg}}{\text{s}}$	$3.1^{+0.7}_{-1.3} 10^{56} \frac{\text{erg}}{\text{s}}$	$3.7^{+0.5}_{-0.5} 10^{56} \frac{\text{erg}}{\text{s}}$
Effective inspiral spin	$-0.06^{+0.14}_{-0.14}$	$0.21^{+0.20}_{-0.10}$	$-0.12^{+0.21}_{-0.30}$	$0.06^{+0.12}_{-0.12}$
Final BH spin	$0.68^{+0.05}_{-0.06}$	$0.74^{+0.06}_{-0.06}$	$0.64^{+0.09}_{-0.20}$	$0.7^{+0.07}_{-0.05}$
Luminosity distance	$420^{+150}_{-180} \text{ Mpc}$	$440^{+180}_{-190} \text{ Mpc}$	$880^{+450}_{-390} \text{ Mpc}$	$540^{+130}_{-210} \text{ Mpc}$
Source redshift	$0.09^{+0.029}_{-0.036}$	$0.09^{+0.03}_{-0.04}$	$0.18^{+0.08}_{-0.07}$	$0.11^{+0.03}_{-0.04}$

Table 3.1: Comparison between the properties of the four detected BH-BH coalescence. The masses are reported in the source-frame. They have to be multiplied by $(1 + z)$ to be converted in the detector frame. The redshift assumes a flat cosmology with Hubble parameter $H_0 = 67.9 \text{ km s}^{-1} \text{Mpc}^{-1}$ and density parameter $\Omega_m = 0.3065$

computed assuming standard cosmology⁸. A summary of the parameter estimation results for the four binary black hole coalescences detected so far is shown in Tab. 3.3.3.

3.3.4 GW170814: first three-detector BBH merger observation

Two weeks after Advanced Virgo joined O2, it recorded together with the two LIGO a signal produced by the coalescence of a binary black hole [57]. Fig. 3.5 (top line) shows the time series of the SNR produced by shifting the best-matched template and computing the SNR at each time. The SNR are 13.7 for LIGO-Livingston, 7.3 for LIGO-Hanford and 4.4 for Virgo and the total three-detector network matched-filter signal-to-noise ratio of 18. The probability that the peak observed in Virgo SNR is due to noise has been estimated to be 0.3%.

Localization

As expected [58, 59], the main contribution to the source parameter estimation provided by the presence of Virgo (even if with a sensitivity between a factor 2 and 3 lower than the two LIGO) consisted in a substantial improvement of the source localization. This is computed starting from the differences in the arrival time, phase and amplitude of the signal in the three sites [58]. The 90% credible region of 1160 deg^2 individuated using only the two LIGO data was reduced to 60 deg^2 by adding Virgo data. A plot of the sky localization of the four BBH mergers detected is shown

⁸As show in Sec. 1.4.3 this is not always true, as in case the signal has a EM counterpart.

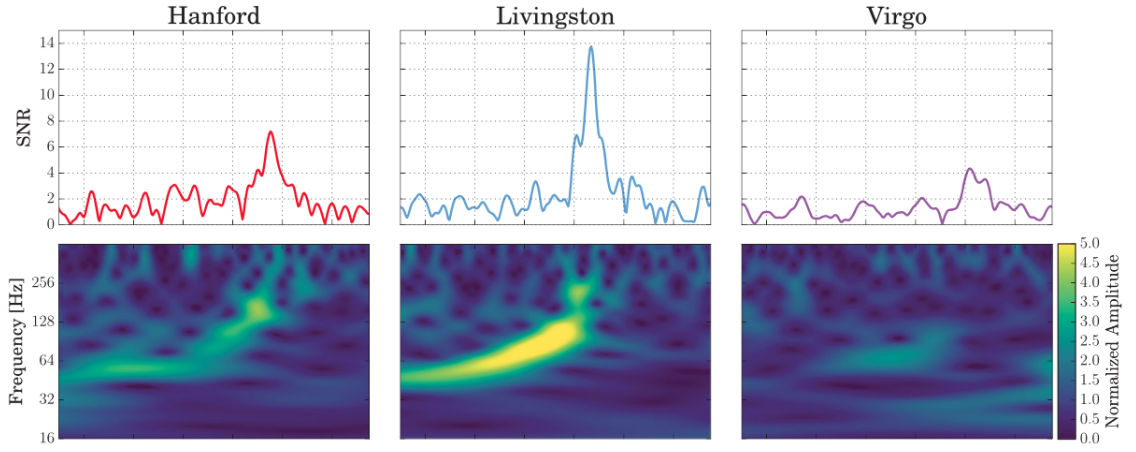


Figure 3.5: GW170814 event observed by LIGO Hanford, LIGO Livingston, and Virgo. Top row: SNR time series. Bottom row: Time- frequency representation of the strain. The plot is taken from [57]

in Fig. 3.6: the improvement due to the presence of a third detector is evident. In general, one of the main payoffs of this improvement is that a smaller localization region allows for a more effective EM follow-up. In the specific case of BBH merger, we have seen in Sec. 1.4.3 that a better localization can be used to individuate probable host galaxies and possibly constrain Hubble constant H_0 even in the absence of an EM counterpart.

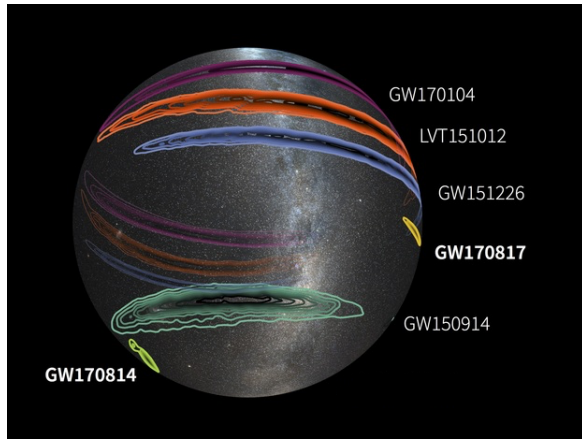


Figure 3.6: Sky-localization of all the GW sources detected up to now. The contours represent the 90% credible regions. Credit: LIGO/Caltech/MIT/Leo Singer (Milky Way image: Axel Mellinger)

3.3.5 Test of general relativity

The observation of a binary black hole coalescence provided for the first time the possibility to study two-body motion in the large-velocity, highly non-linear regime

of gravity. Many investigations have been done in order to verify the consistency of the observed signal with a binary black-hole merger in General Relativity (GR) [60]. At first, the amount of residual signal found in the data after having subtracted the most-probable waveform according to GR has been used to bound possible violations of the theory which are not predicting the same parameters for the system.

By comparing the mass and spin parameters of the final black hole inferred from the binary's inspiral signal with those obtained from the merger and ringdown signal it was possible to check the consistency of the results.

A search for evidence of a modified gravitational-wave dispersion relation allowed to put a lower limit on the Compton wavelength of the graviton of $\lambda_g > 1.6 \cdot 10^{13}$ corresponding to an upper limit on the graviton mass of $7.7 \cdot 10^{-23} eV/c^2$. In the post-Newtonian approximation, the gravitational-wave phase can be expressed as power series. From general relativity we can deduce the coefficients of such expansion. Deviation from nominal values of these coefficients can be compared with data in order to check to what extent they are still compatible with observations and set constraints on their deviation. No evidence of violations of general relativity was observed.

Polarization test

GR predicts that the metric perturbation induced by a gravitational waves has only two polarizations among the six allowed by a generic metric theories of gravity. For GW170814, the presence of Virgo, whose arms are not aligned with those of the two LIGO (which are almost coaligned), provided a way to test this prediction by projecting the GW onto the detector network. Even if in principle a generic theory of gravity can present a combination of all the 6 polarization (2 tensor, 2 vector and 2 scalar polarization) only a simplified test has been performed, where only models with pure scalar, pure vector and pure tensor polarization have been considered [61]. By repeating the coherent Bayesian analysis performed to compute the source parameter estimation and replacing the standard antenna pattern response with those relative to pure scalar or vector polarization it has been found that the pure tensor polarization is strongly preferred with respect to the pure vector and the pure scalar ones [57].

3.3.6 Merging rate and astrophysical implications

Up to the first detection, BH-BH rates predictions were only based on population-synthesis models [62], with upper limits provided by the lack of detections from first generation detectors. The first detections revealed a population of stellar-mass black hole mergers and provided data to constrain their rate and their mass distributions. The most up-to-date merging rate has been computed after the third detection (GW170104). The computation has been done assuming two different source distri-

bution models [62]. The rate, found including the results for the two models, is $12 - 213 \text{ Gpc}^{-3}\text{yr}^{-1}$. Such results are especially useful to the study of black hole binary formation by providing constraints on different astrophysical models [63, 64]. Two formation channels are proposed to explain the origin of stellar black hole binaries: isolated evolution or dynamical process in dense stellar systems. In alternative, binaries can be formed by primordial black holes. Information on the spin can also be used to constrain different formation models: binaries originated from dynamical processes (of both stellar and primordial black holes) are expected to have a isotropic distribution of spin. Isolated binary black hole models are supposed to have small spin misalignment. From the three observations, misaligned spins seem to be preferred [65]. The consistent number of detections expected in the next few years will improve the precision of such constraints, better informing us on black hole astrophysics.

3.3.7 GW170817: first binary neutron star merger observation

On August 17, 2016, 8 days before the end of O2, the gravitational wave emitted during the inspiral and merging of a binary neutron star has been detected by the two LIGO interferometer and Virgo, for the first time [5]. Such signal lasted in the detector for about 100 s. It was observed with a combined SNR of 32.4 and is the loudest GW signal ever recorded. As already mentioned, thanks to the identification of an electromagnetic counterpart, it has been possible to extract an impressive amount of relevant scientific results. A summary of them and some interesting points of this detection are given in the following.

Can we be sure that we are observing a binary neutron star?

The fact that the binary system merging has been associated with a EM counterpart demonstrate the presence of matter and ruled out the case of a BBH. The possibility of having a neutron star-black hole system cannot be excluded but it is inconsistent with the observed masses of black holes in binary systems. In fact, the binary component masses of GW170817 have been estimated to be between 1.17 and 1.6 M_{\odot} .⁹ The incertitude is mainly due to a degeneracy in the effect on the waveform of the mass ratio and the orbit-aligned spins of the two objects.¹⁰ Components of BNS observed so far have masses in a range between 1.17 and 1.6 M_{\odot} , while stellar mass black observed in our galaxy are larger than $5M_{\odot}$. For these mass consistency considerations the binary system which produced GW170817 has been confidently claimed to be formed by two neutron stars.

⁹These values are given restricting the spin magnitude below 0.05, consistently with the values of the observed population of binary neutron stars.

¹⁰Such constraint for the masses has been found assuming a dimension less spin below than 0.05, according to the spins value observed so far.

Equation of states and tidal effects

Neutron stars have an extreme high density, comparable with that of the atomic nucleus that is $\sim 3 \cdot 10^{17} \text{ kg/m}^3$. Since this value is hardly reproducible in laboratory, GWs produced in a binary coalescence represent a valuable way to access the matter behavior in such extreme conditions.

Investigation on the equation of state of neutron stars is one of the first scientific target of the gravitational wave detection from a BNS merger. The GW waveform starts to be affected from the internal structure of the binary components when the orbit size becomes comparable with that of the two stars. This effect increases the quadrupole momentum variation, accelerating the merging.

Each star is characterized by a parameter, known as deformability, which, given the equation of state, depends only on its mass. The waveform is affected by a combination of the deformability of the two stars. From the waveform observed, has been possible to find constraints on the deformability of the two stars, thus disfavoring equations of state which predict less probable deformabilities. In particular it was possible to discard equations of state leading to less compact stars, since the corresponding deformabilities fall outside the 90% probability region [5].

Coincident gamma ray burst

For many years binary neutron star mergers have been considered possible progenitors of short, hard-spectrum GRBs. Recent GR numerical simulation demonstrated that binary neutron star mergers induce the formation of a relativistic jet-like and ultrastrong magnetic field able to produce short GRBs [66]. In correspondence with the GW signal, a GRB, named 1701717A, was observed independently by the Gamma-ray telescopes Fermi and INTEGRAL. The major astrophysics result of such joint observation (whose probability of having occurred by chance has been estimated to be $5 \cdot 10^{-8}$) is the confirmation that at least some of the observed SGRBs are originated by the coalescence of compact objects [67].

The measured time delay of $+1.74 \pm 0.05$ s between the GW and EM signal allowed to set upper limits on the difference between the speed of the two signals between $-3 \cdot 10^{-15}$ and $7 \cdot 10^{-16}$ times the speed of light.¹¹ It also allowed to constrain the violation of the Lorentz invariance and test the equivalence principle [67].

The kilonova and other EM transients

The accurate localization ($\simeq 29 \text{ deg}^2$ at a distance of $40_{-14}^{+8} \text{ Mpc}$) provided by a three detectors observation of the GW signal allowed for an effective search of EM counterparts by ground and space based telescopes. About 10 h after the merger, a bright optical transient has been independently identified in the galaxy NGC 4993

¹¹It has been assumed that the EM radiation could have been emitted in a interval which goes from the peak of the GW emission to 10 s after it.

by many telescopes [68]. The initial UV-blue emission faded within 48 hours while optical and infrared emission showed an evolution toward red and started to fade after roughly a week. The observed EM counterpart is compatible with the so called *kilonova*: an electromagnetic transient which originated by a rapid neutron capture (r-process) nucleosynthesis [69, 70, 71, 72]. During the merger phase a small part of neutron-rich material composing the neutron stars is supposed to be ejected and to provide a site for nucleosynthesis of heavy elements via r-process. Kilonova is a visible/near-infrared emission which is powered by the decay of unstable nuclei resulting from the r-process. Its occurrence, usually searched in correspondence of GRBs, has proved that BNS coalescences are one of the process at the origin of heavy nuclei formation in the Universe.

About respectively 9 and 16 days after the merger also X-ray and radio emissions were detected. These late emissions are though not to be originated from the same physical process that generated the ultraviolet, optical and near-infrared emissions [68].

Also searches for neutrinos or ultra-high-energy GRB have been performed but no events associated with the BNS merger have been detected [73].

Remnant

The nature of the merger remnant depends on the masses of the binary components and on their state equation. Different possibilities have been proposed, among them there are long-lived neutron stars or short-lived ones, collapsing in a black hole after about 1 s. The amplitude of the gravitational radiation expected from these model is at least one order of magnitude lower than the present detector sensitivity, therefore the lack of GW observation cannot rule out any scenario [74].

Hubble constant measurement

For distances below 50 Mpc the local "Hubble flow" velocity of a source is directly proportional to its proper distance:

$$v_H = H_0 d \quad (3.5)$$

The proportionality constant, known as Hubble constant H_0 , is a measurement of the mean expansion rate of the Universe. Thanks to the joint detection of a GW signal and its EM counterpart it has been possible to estimate H_0 independently of any cosmic distance ladder. The EM transient has been used to identify the galaxy hosting the BNS merger and thus its Hubble flow velocity, while the distance d has been extract from the GW signal. The resulting Hubble constant is $H_0 = 70_{-8}^{+12} \text{ km s}^{-1} \text{ mpc}^{-1}$ [18], which is consistent with the previous measurements.

BNS merging rete

The inferred merging rate of BNS computed on the basis of this only observation in O2, using O1 upper limit as a prior, is $1540^{+3200}_{-1220} \text{Gpc}^{-3}\text{yr}^{-1}$. This value is consistent with that derived from BNS system observed in our Galaxy. The astrophysical background produced by unresolved BNS coalescences has a magnitude comparable with that originated by BBH coalescence. A search for these two backgrounds has not yet been performed on the O2 data, but it is expected to be detectable in the next observation runs [75].

Part II

Optical and noise studies for Advanced Virgo

Context and motivations

During the installation Advanced Virgo, which took place from 2012 to 2016, some preliminary commissioning activities have been carried on on the different subsystems progressively installed in order to speed up the commissioning of the full interferometer. Part of my thesis work has been dedicated to this activities.

At the end of 2014 the Injection system was already operational and a pre-stabilization of the laser frequency was put in place using the input mode cleaner and a rigid reference cavity. My first contribution to the Advanced Virgo commissioning was to investigate the noises of such system and develop a noise budget for the laser frequency noise. The main goal of this activity was to contribute to the noise hunting activity in order to reduce the residual laser frequency noise below the threshold set by the lock acquisition of the arm cavities.

In May 2016 the Fabry-Perot cavity in the north arm was locked for the first time, followed by the west arm in August of the same year. I contributed to the optical characterization of the cavities by measuring relevant parameters such as the round trip losses, the mismatching and the g-factor, in order to check the proper operation of the system and point out potential issues.

This second part of the thesis, focused on the commissioning activity of Advanced Virgo, is divided in three chapters: an introductory one, where the main features of Advanced Virgo are presented to complete the description given in Sec. 3.2.3 which was mainly focusing on the upgrade from the initial Virgo. In the second chapter I present the work done to produce a noise budget for the frequency stability and to create a code to compute it automatically.

The third chapter is dedicated to the arm's cavity optical characterization. The techniques used for the measurements of the relevant parameters are discussed and the main results are presented.

CHAPTER 4

The Advanced Virgo detector

4.1 Injection system

The role of the so called injection system is to deliver a laser beam whose power, frequency and direction fluctuations are low enough to allow the correct operation of the interferometer. The stability requirements set on Advanced Virgo Technical design report [76] are reported in Tab. 4.1.

Parameter	Requirement
Transmission to the ITF	70% (assuming 175 W on TEM_{00} at injection input)
Power on HOM	< 5%
Intensity noise	$2 \cdot 10^{-9} / \sqrt{\text{Hz}}$
Beam jitter	$< 10^{-9} \text{ rad} / \sqrt{\text{Hz}}$
Frequency noise	1 Hz RMS

Table 4.1: Beam stability requirement.

4.1.1 Laser source

In the AdVirgo design configuration the injection system is supposed to receive 175 W on the fundamental mode at its input from the Prestabilized Laser System. The laser system consists in 1W Nd:YAG laser emitting at 1064, amplified to 200 W by adding coherently two beams of 100 W obtained from two parallel rod amplifiers. Such a system has not yet been implemented and in its initial operation Advanced Virgo is using the same laser source used in Virgo. Such system, able to deliver up to 45 W, has been reinstalled at the beginning of 2014 and it is using the injection-locking technique [77], where an highly stable lower power laser (called master laser) controls the oscillation of a high power laser (called slave laser), in order to obtain a high power beam with good stability performances.

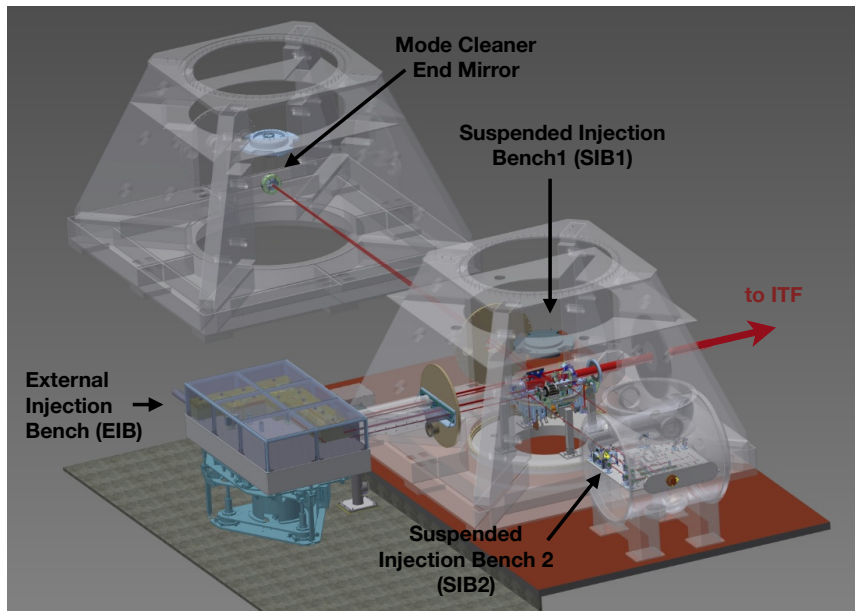


Figure 4.1: Tridimensional representation of towers and benches composing the injection system.

4.1.2 External injection bench

A 3D representation of the injection system optical benches and vacuum tanks containing them is presented in Fig. 4.1 while Fig. 4.2 shows a scheme of the beam path. The external injection bench (EIB) is an in-air non suspended optical table. It hosts Electro-optic modulators providing RF sidebands¹ used for the interferometer control, a Faraday isolator to prevent back reflected light to interfere with the laser, a telescope to match the beam in the Input Mode Cleaner cavity (IMC) and quadrant and single element photodiodes used for its lock and alignment. A Beam Pointing Control (BPC) system, consisting in a set of quadrant photodiode and piezo actuators is also installed to control the beam position and reduce the jitter.

4.1.3 Suspended Injection benches

The Suspended Injection Bench 1 (SIB1) is accommodated in the INJ vacuum tower and it is composed of an upper and a lower part. The upper part hosts the IMC input and output mirrors, which are two flat mirrors at almost 90° held in a monolithic support (dihedron). The beam exiting the IMC is sent by a periscope on the lower part of the bench, here a pick-off is extracted and sent to the a rigid reference cavity (RFC) and on a photodiode used for the power stabilization (Pstab). The beam is sent again in the upper part of the bench where it passes the high power Ultra-High

¹Working principle of this systems is detailed in App. E

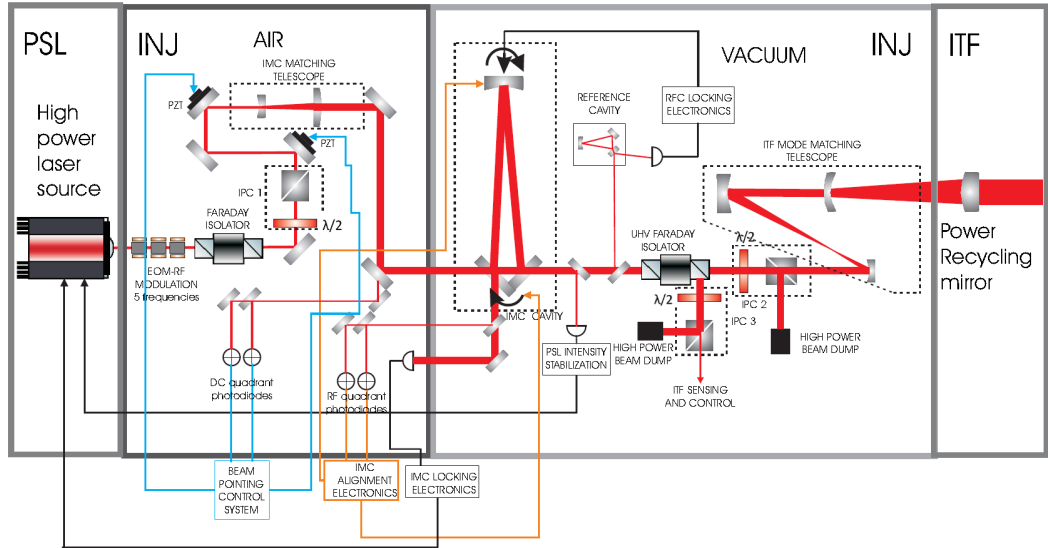


Figure 4.2: Schematic of the beam path in the injection system [78].

Vacuum (UHV) compatible Faraday isolator which isolates the IMC from the ITF reflection. Then it passes through the ITF Mode matching telescope and it is finally injected into the ITF.

The beam reflected by the ITF goes back up to the UHV Faraday isolator and it is sent to the suspended injection bench 2 (SIB2). This bench, suspended inside a smaller vacuum tower, hosts also the beam reflected by the RFC which is sensed by a photodiode for the lock and quadrant photodiodes for the automatic alignment. Photodiodes are also used to monitor the beam reflected by the control of the ITF auxiliary degrees of freedom. The possibility to tune the beam power in different points of its path is provided by a Input Power Control system (IPC) consisting in a half wave plate which can be controlled remotely and a pair of polarizing cubes.

4.1.4 Input mode cleaner

The Input Mode Cleaner (IMC) is a high finesse suspended triangular Fabry-Perot cavity used in transmission. Such configuration has been chosen as it minimizes the back reflected light. As mentioned above, the cavity is composed by two flat mirrors accommodated on SIB1 and a curve mirror at a distance of ~ 144 m which is suspended in a dedicated vacuum chamber. The purposes of this cavity are many:

- **Filtering of spatial modes** - In order to maximize the coupling with the recycling cavity, we want the injected beam to be a TEM_{00} as much as possible. Since the IMC is a non-degenerate cavity, the transmission is maximum for the fundamental mode and decreases for higher order modes (HOM) according to the their frequency separation from it.

- **Filtering of beam jitter** - A shift or a tilt of the beam with respect to the IMC axis is seen as the presence of an HOM [79]. Since the axis of a suspended cavity is very stable for frequencies above few Hz, the beam position fluctuations are filtered and the transmitted TEM₀₀ is stable with respect to that resonating into the interferometer.
- **Filtering of amplitude and frequency fluctuation** - As already observed in Sec. 2.3.1, a Fabry-Perot cavity acts as a first order low pass filter for amplitude and frequency fluctuations above the cavity pole. The attenuation factor is given by

$$G(f) = \frac{1}{\sqrt{1 + \left(\frac{f}{f_0}\right)^2}} \quad (4.1)$$

with $f_0 = c/(4LF)$. The measured mode cleaner finesse is ~ 1000 , therefore the pole is at ~ 520 Hz.

- **Reference for frequency stabilization** - The length of the IMC above few Hz is very stable with respect to the free running laser frequency noise. Therefore it provides a good reference for a frequency pre-stabilisation of the laser, needed to allow the ITF lock acquisition. This active frequency noise reduction is achieved by locking the laser frequency on the IMC. More detail on this pre-stabilisation technique will be given in the following chapter.

The suspended bench and the mode cleaner end mirror position are controlled by using optical levers to reduce their motion to few tenth of μrad and allow to acquire the lock. Once the lock is acquired, a global alignment control which uses wavefront sensor, is engaged. More details on these control system and their effect on the laser frequency stabilization will be given in the following chapter.

4.1.5 The reference cavity

The reference cavity (RFC) is a monolithic triangular cavity of 30 cm used at low frequency as a reference for the frequency stabilization of the beam. In fact, at frequency lower than few Hz, the IMC length is less stable due to the motion of the suspended mirrors. The RFC has a finesse of ~ 920 [80] and it is placed in a small separate vacuum tank in the lower part of SIB1.

4.2 Optical configuration

The Advanced Virgo optical configuration is shown in Fig. 4.3. It consists in a dual recycling Fabry-Perot interferometer:

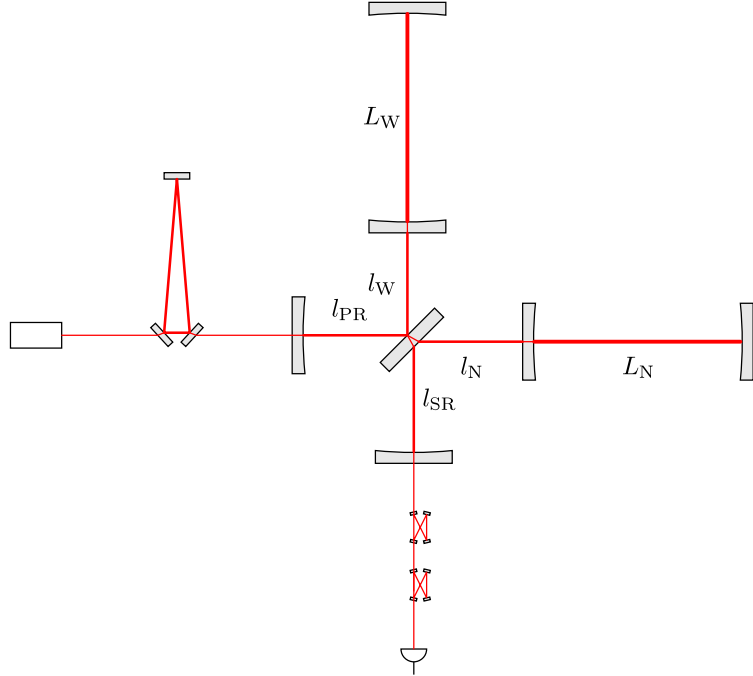


Figure 4.3: Advanced Virgo optical configuration.

- **Fabry-Perot cavities** - With respect to Virgo which used plano-concave cavities, Advanced Virgo arm cavities have a bi-concave geometry. The use of bi-concave cavities allows to increase the beam size on the cavity mirrors thus reducing the impact of the thermal noise. The input and the end mirrors have a RoC of ~ 1420 m and ~ 1683 m, respectively. In this configuration the beam waist is about 9.7 mm and its located almost in the middle of the cavity. The beam size on the mirrors is about 49 mm on the input mirror and 58 mm on the end.

The ends mirrors are almost completely reflective while the transmission of the input beam is set to $\sim 1.4\%$, giving a finesse of ~ 450 . More details on arm's Fabry-Perot cavity will be given in Chap. 6.

- **Recycling cavities** - The power recycling (PR) and signal recycling (SR) mirrors has both a RoC of 1430 and a transmissivity of 5% and 20% respectively. They form, together with the input mirrors, the power recycling and the signal recycling cavity. Such cavities have a length of about ~ 12 m and beam dimension of about 50 mm. They are marginally stable, meaning that the resonance frequencies of the higher order modes are close to that of the fundamental one.

Since RF sidebands do not resonate in the arm cavities they are more affected than the carrier by this degeneracy. A thermal compensation acting in the mirrors has been developed in order to mitigate this effect.

The beam exiting the ITF from the antisymmetric port, before being detected, is filtered by two short and high finesse bow-tie cavities, called Output Mode Cleaners (OMC). They get rid of higher order modes in order to minimize contrast defect.

Degrees of freedom and control

In order to be in the proper working condition, the interferometer has to be on the dark fringe, the arm cavities and recycling cavities have to be on resonance. Low frequency drift and residual mirror motion make impossible to achieve this condition without a global control system able to extract information on mirror position and act on them to keep the detector in its working point. There are five degrees of freedom to be controlled:

- **CARM** (Common Arm Length): it is the sum of the arm cavities length $L_1 + L_2$ and it is used as a reference for the frequency stabilization of the laser.
- **DARM** (Differential Arm Length): which is the difference of the arm cavities length $|L_1 - L_2|$. This is the degree of freedom related to the dark fringe condition and also the one containing the gravitational wave signal.
- **PRCL** (Power Recycling Cavity Length) that is $l_{\text{pr}} + (l_1 + l_2)/2$. It is related to the resonance condition of the power recycling cavity.
- **SRCL** (Signal Recycling Cavity Length) that is $l_{\text{sr}} + (l_1 + l_2)/2$. It is related to the resonance condition of the signal recycling cavity, which is detuned in some configurations.
- **MICH** (Michelson arms difference Length) that is $|l_1 - l_2|$. It is the Michelson differential length. As DARM it is related to the dark fringe condition, even if with a smaller weight.

Residual seismic noise is also responsible for inducing mirror rotations which affect the alignment of the cavities preventing a proper operation. In order to mitigate this effect a global angular control system (known as automatic alignment or AA) is implemented.

4.3 Mirror suspensions and control

The system developed to suspend mirrors in Virgo, known as *superattenuator* [81], has been proven to provide a very high level of isolation from seismic disturbance, which is compliant with the requirement of Advanced Virgo. Since coupling between

different degrees of freedom of the mirrors are likely to appear, such system is conceived to reduce seismic disturbance in the six degrees of freedom of the mirrors. An attenuation factor of more than 10^{-10} above 3 Hz in all the d.o.f. has been achieved. Each superattenuator, shown in Fig. 4.3, is hosted in a 10 m tall vacuum chamber and its composed of three parts:

- **The inverted pendulum** - It consists of three aluminum legs of about ~ 7 m. Each of them is connected to ground through a flexible joint, allowing for pendulum oscillation in the horizontal plane [82]. The tops of the three legs are connected to a mechanical ring (Top Ring) supporting the first seismic filter, called *Filter 0*. The inverted pendulum provides attenuation of the seismic disturbance, for frequencies above its resonant frequency. It reads

$$f_{\text{ip}} = \frac{1}{2\pi} \sqrt{\frac{k}{m} - \frac{g}{L}} \quad (4.2)$$

where k is the stiffness of the flexible joint, L is the length of the leg and m is the mass on its top. For an inverted pendulum of given length we can change the mass to have an arbitrarily low resonance frequency (ultimately limited by the stability of the system), exploiting the anti-spring effect of the gravity. In Virgo the parameters have been chosen in order to have $f_{\text{ip}} \simeq 50$ mHz. Another advantage of this system is that it allows to move the whole suspended chain applying very small forces to correct long term mirror drifts.

The first element of the filter chain is the so called *Filter 0*, surround by the top ring. On a platform on its top a set of sensors and actuators are installed and used to actively damp the inverted pendulum resonances [83].

- **The seismic filter chain** - The chain of seismic filters suspended to the filter 0 is composed of five cylindrical drum shaped mass, of about 100 Kg. The vertical attenuation is provided by a set of triangular cantilever spring blades connecting the each stage to the following one. They filter vertical seismic noise above their resonance frequency which is at about 1.5 Hz. In order to attenuate the excitation of the rotational degrees of freedom, the filters are suspended as close as possible to their center of mass.
- **The last stage** - The last stage of the suspension known as payload is located in a dedicated ultra-high vacuum chamber. It is composed by a mass called *marionette*, suspended to the last seismic filter by a central steel wire, (called *filter 7*), the mirror, suspended to it with four wires and the relative actuators. It also includes devices for the thermal compensation and baffles which are rigidly connect it to the body of the Filter 7. The role of the marionette is to control the mirror position and to allow longitudinal and angular alignment. A set of coils and magnets are used to this purpose. Correction applied a the

level of the marionette (and on the top stage) benefit from the pendulum filter effect which reduces the unavoidable driving noise associated to the actuations. For the same reason if we want to move the mirror at a frequency much higher than the suspension resonant frequency (1-2 Hz), we need to act directly on the mirror. To this purpose mirrors are equipped with a set of magnets which can be pushed and pulled by using coils. Correction to compensate long term thermal drift ($f < 30$ m Hz) are sent to the top the inverted pendulum and can exploit its large dynamic.

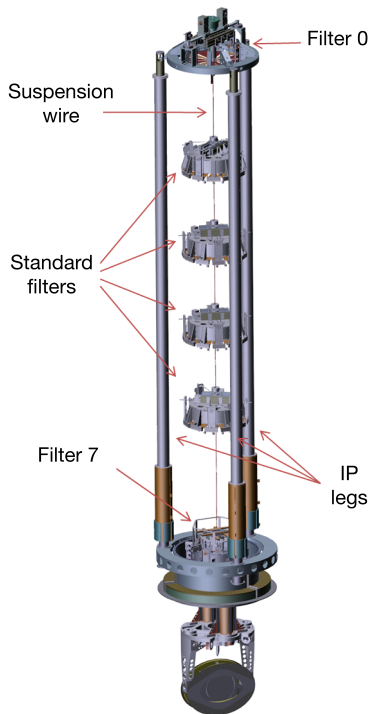


Figure 4.4: Schematic of the superattenuator [50].

4.4 Noise budget and design sensitivity

In Fig. 4.4 the target sensitivity of Advanced Virgo is shown together with the noise sources which contribute to limit it. The sensitivity is estimated assuming an input power of 125 W and the signal recycling in a broadband configuration. It is limited by the seismic noise below 3 Hz.² Between 3 Hz and 20 Hz, it is limited by Newtonian noise and suspension thermal noise. Between 30 Hz and 100 Hz it is limited by mirror coating noise and quantum noise and above 100 Hz it is limited only by quantum noise. The corresponding BNS range is 120 Mpc while the BBH range is 1.18 Gpc.

²It is worth to notice that due to the superattenuator effect the slope of the seismic noise is very steep: it limits the sensitivity to 10^{-12} at 0.1 Hz and to less than 10^{-19} at 3 Hz.

This estimation does not take into account the presence of technical noises such as control noise from feedback loops used for to keep the ITF on the working point and scattered light noise or environmental noises. In Fig. 4.6 a noise budget for the

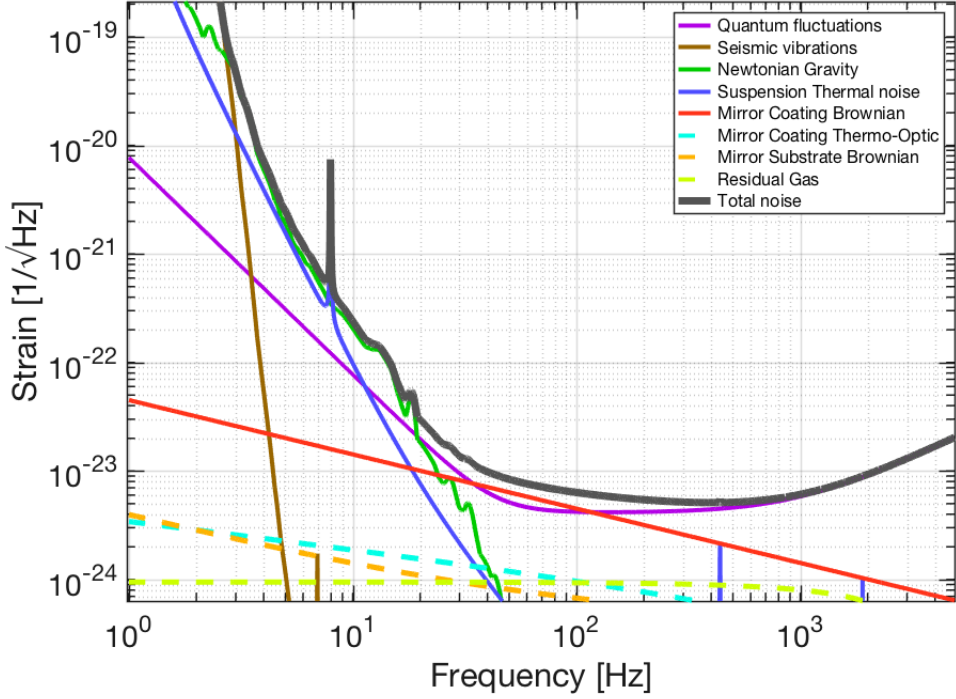


Figure 4.5: Noise budget for Advanced Virgo sensitivity, computed using GWINC with 125 W of injected power and tuned signal recycling (broadband configuration).

AdVirgo sensitivity during O2 is shown (BNS range 27 Mpc and $30M_{\odot}$ BBH range 320 Mpc) [84]. The injected power is 13 W, no signal recycling was installed and the suspension thermal noise was higher than the design one as monolithic suspensions are not yet integrated. It is limited by control noises (ISC) up to about 30 Hz, from thermal noise up to 100 Hz and from quantum noise above. We see that not all the noise contributions have been identified and in some regions the sum of measured and estimated noise does not reproduce perfectly the measured sensitivity. This results in a discrepancy between the BNS inspiral range estimated which is 33 Mpc and that actually measured which is 27 Mpc.

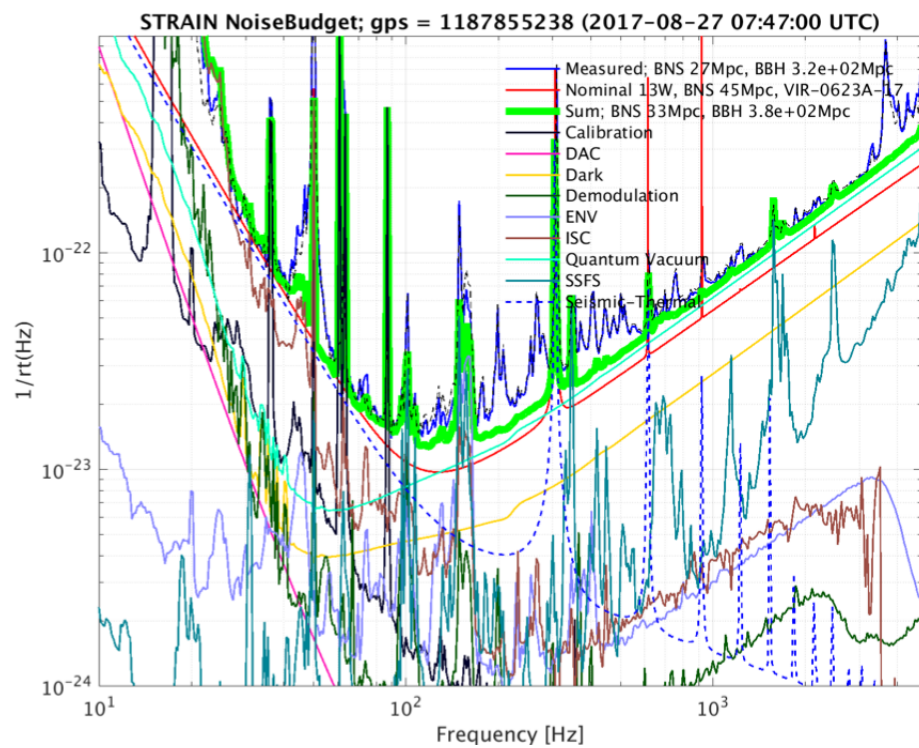


Figure 4.6: Noise budget for the Advanced Virgo sensitivity during O2 [84].

CHAPTER 5

Injection system noise analysis

We have seen that the change in the time taken by the light to perform a cavity round trip (possibly generated by a gravitational wave) can be detected by measuring the change in the light phase from the relation: $\Delta\phi = 2\pi f_{\text{laser}} \Delta\tau_{rt}$. From this relation we see that a noise of the light frequency results in a noise of the measured phase change that limit the precision of our measurement. One of the advantages of the Michelson interferometer configuration is that in principle for perfectly symmetric arms, frequency noise cancels out. However, an asymmetry of about ~ 20 cm, called *Schnupp asymmetry*, between the short Michelson arm is needed for signal read-out purpose. Moreover, other arm cavity parameters, such as finesse and losses, are unavoidable sources of asymmetry. The requirement on the frequency stability is thus determined by the level of asymmetry of the arms.

The spectrum of free running laser noise of Advanced Virgo laser can be approximated as

$$S_{\text{laser}} \frac{10^4}{f} \left[\frac{\text{Hz}}{\sqrt{\text{Hz}}} \right] \quad (5.1)$$

If we require the frequency noise to be a factor 10 below the design sensitivity, considering an arm asymmetry of 1%, the free running laser noise has to be reduced of ~ 9 order of magnitudes. Arms cavities length is stable enough to provide a reference compliant with this requirement. Anyway a first pre-stabilization of the laser is necessary for the lock acquisition. The requirement for that is set to 1 Hz RMS [76], since we want the noise to be much lower than the arm cavity bandwidth (~ 50 Hz). This pre-stabilization is achieved by using the input mode cleaner and the reference cavity as length references.

In this chapter a detailed description of the pre-stabilization strategy is presented together with an analysis of the noise limiting the frequency stability. The goal of this activity was to estimate the frequency stability of the laser after this pre-stabilization and produce a noise budget for the frequency noise in order to contribute to its reduction below the requirement.

5.1 Frequency pre-stabilization loops

The laser frequency pre-stabilization is achieved within the injection system using two loops with different bandwidth (See Fig. 5.1)[85, 86]

- a first fast pre-stabilization loop (~ 200 kHz bandwidth) which locks the laser frequency on the input mode cleaner (IMC) length.
- a second loop (~ 80 Hz bandwidth) which locks the laser frequency on the reference cavity (RFC).

In this way the suspended IMC, which is very stable at high frequency (above few Hz), is used in that region as a length reference while the RFC is used at low frequency. The error signal for the first loop is generated using the Pound-Drever-Hall (PDH) technique in reflection. In the second loop the frequency of the IMC transmitted beam is compared with the RFC length and the PDH signal in reflection is used to control the IMC cavity length acting on its end mirror.

The correction signal applied to the laser frequency is constituted by:

- A thermal correction (up to 50 mHz) acting on the laser crystal temperature.
- A piezo correction (up to more than 10 kHz) acting on the laser crystal length.
- A EOM correction (for higher frequencies) sent to an electro-optic modulator which is able to correct the beam frequency during its propagation.

In Fig. 5.2 a scheme of the two loops is shown. Once the interferometer is locked, a second stage of frequency stabilization (SSFS) is engaged [85]. In this configuration the error signal is provided by using the common arm length (CARM) as reference. In this configuration the RFC is still used as reference at low frequency.

However, our noise analysis is performed on the injection system running in stand-alone configuration. In order to measure the frequency stability of the pre-stabilized laser we measure the PDH error signal in reflection from the RFC which is the result of a comparison between the laser frequency and the RFC length. As we will see in detail in the following section, this is a measure of the actual frequency noise only if it is not limited by the RFC noise or by the loop sensing noise. The first step will be thus to produce a frequency noise budget for the RFC error signal to understand which are the noise noises limiting it. Then we will show how to use this information to estimate the actual frequency noise of the beam injected into the ITF.

In the following noises which affect the RFC error signal are presented and their impact on such signal is obtained. We stated by computed analytically the loop equations to find the projection of each noise on the RFC error signal. We use the following notation:

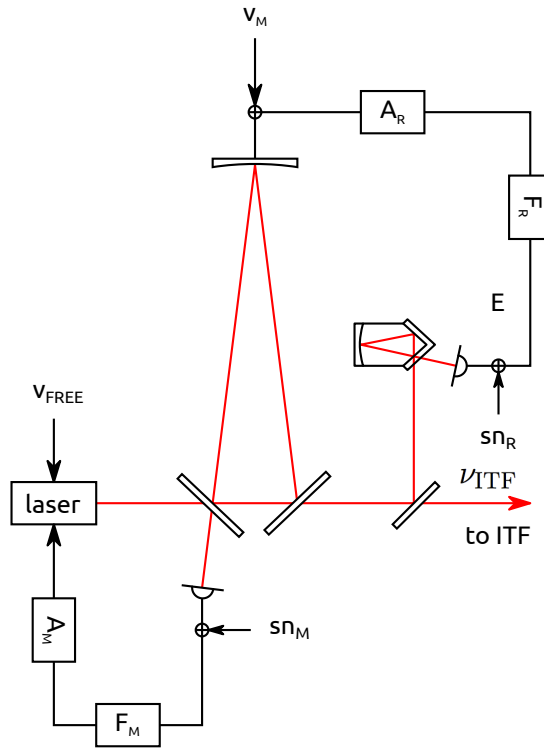


Figure 5.1: Optical scheme of the two frequency stabilization loops.

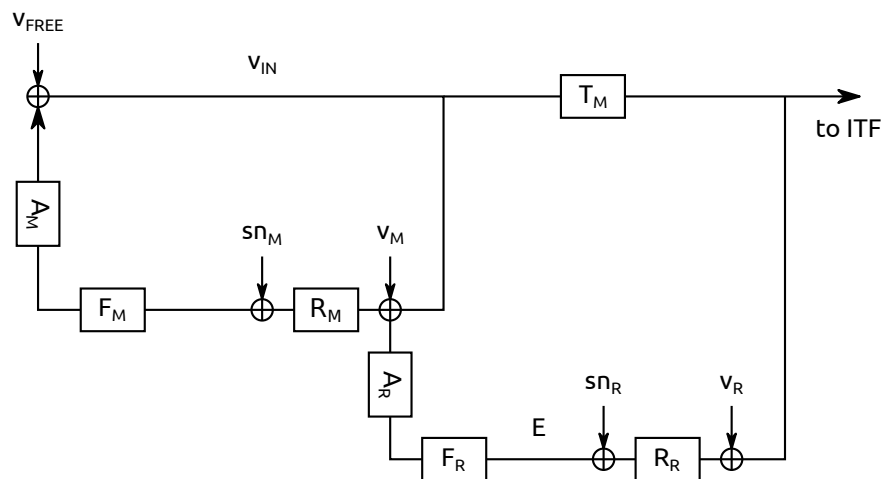


Figure 5.2: Block scheme of the two frequency stabilization loops.

- Noises
 - $\nu_{\text{free}} \left[\frac{\text{Hz}}{\sqrt{\text{Hz}}} \right]$ Free running laser noise
 - $\nu_R \left[\frac{\text{Hz}}{\sqrt{\text{Hz}}} \right]$ RFC length noise (converted to equivalent frequency noise)¹
 - $\nu_M \left[\frac{\text{Hz}}{\sqrt{\text{Hz}}} \right]$ IMC length noise (converted to equivalent frequency noise)
 - $\nu_{\text{ITF}} \left[\frac{\text{Hz}}{\sqrt{\text{Hz}}} \right]$ Frequency noise sent to the interferometer
 - sn_M [V] sensing noise in the IMC reflection error signal
 - sn_R [V] sensing noise in the RFC error signal
- Transfer functions
 - $A_M \left[\frac{\text{Hz}}{\text{V}} \right]$ laser actuator transfer function
 - $F_M \left[\frac{\text{V}}{\text{Hz}} \right]$ IMC electronic filter transfer function
 - $A_R \left[\frac{\text{Hz}}{\text{V}} \right]$ RFC actuator transfer function
 - $F_R \left[\frac{\text{V}}{\text{Hz}} \right]$ RFC electronic filter transfer function
 - $T_M \left[\frac{\text{Hz}}{\text{Hz}} \right]$ optical transfer function for the IMC transmission
 - $R_M \left[\frac{\text{V}}{\text{Hz}} \right]$ transfer function between the noise entering IMC [Hz] and the PDH demodulated error signal [V]. It includes the optical response of the cavity and the PHD calibration factor $\left[\frac{\text{V}}{\text{Hz}} \right]$
 - $R_R \left[\frac{\text{V}}{\text{Hz}} \right]$ transfer function between the noise entering RFC [Hz] and the PDH demodulated error signal [V]. It includes the optical response of the cavity (which can be considered flat for the RFC up to more than 10^5 Hz) and the PHD calibration factor
- E [V]: RFC error signal

From the block diagram 5.2 the following equations can be deduced.

$$E = sn_R + R_R(\nu_R + T_M\nu_{in}) \quad (5.2)$$

$$\nu_{in} = \nu_{\text{free}} + A_M F_M(sn_M + R_M(\nu_M + \nu_{in} + A_R F_R E)) \quad (5.3)$$

then

$$\nu_{in} = \left[\frac{1}{1 - A_M F_M R_M} \right] (\nu_{\text{free}} + A_M F_M sn_M + A_M F_M R_M \nu_M + A_M F_M R_M A_R F_R E)$$

¹When comparing cavity length noise with laser frequency noise we use the relationship $\delta\nu/\nu = \delta L/L$. The conversion factor from m to Hz is $\nu/L = 2 \cdot 10^{12} \text{Hz/m}$

and

$$E = \left[1 - \frac{T_M A_M F_M R_M A_R F_R R_R}{1 - A_M F_M R_M} \right]^{-1} \quad (5.4)$$

$$\cdot \left[s n_R + R_R \nu_R + \left(\frac{T_M R_R}{1 - A_M F_M R_M} \right) (\nu_{free} + A_M F_M s n_M) + A_M F_M R_M \nu_M \right] \quad (5.5)$$

By defining $G_M = A_M F_M R_M$ the pre-stabilization open loop transfer function and $G_R = A_R F_R R_R$ the RFC open loop transfer function, we find

$$E = \left[1 - \frac{T_M G_M G_R}{1 - G_M} \right]^{-1} \left(s n_R + R_R \nu_R + \frac{T_M R_R}{1 - G_M} \nu_{free} + \frac{T_M R_R G_M}{(1 - G_M) R_M} s n_M + \frac{T_M R_R G_M}{1 - G_M} \nu_M \right)$$

Assuming a very high gain for the pre stabilization loop in the frequency region of interest ($f < 10$ kHz), that is, considering $G_M \rightarrow \infty$ the previous relation becomes:

$$E = \left[\frac{1}{1 + T_M G_R} \right] \left(s n_R + \frac{T_M R_R}{R_M} s n_M + R_R \nu_R + T_M R_R \nu_M \right) \quad (5.6)$$

From Eq. 5.6 we read how each noise contributes to the total frequency noise measured by RFC error signal and how the RFC loop affects their projection on the RFC error signal.

5.1.1 PDH signal calibration

This calibration factor needed to convert the RFC error signal from Volt to Hz or meter has been obtained in two different ways:

- As detailed in Sec. E, the PDH signal generated during a scan of the laser frequency, is linear around the point where the cavity crosses the resonance. This part of the signal can be fitted to extract the linear coefficient which gives the calibration (see Fig. 5.3). In order to convert the time on the x-axis into Hz, we used the fact that the RFC Full Width at Half Maximum (FWHM) of the resonance peak is known, and corresponds to:

$$\text{FWHM} = \frac{c}{2LF} = 5.26 \cdot 10^5 \text{Hz} \quad (5.7)$$

where we used the value $L = 0.31$ m and $F = 920$ [80].

- The open-loop transfer function can be modeled as the product of the electronic filter (which is known), the actuator (which has been previously calibrated) and the optical gain which is the only free parameter. The latter can be estimated by comparing this model with the measured open loop transfer function. This method is less direct as it rely on the correct calibration of the actuator. The

values obtained with these two methods are in agreement within 3%.

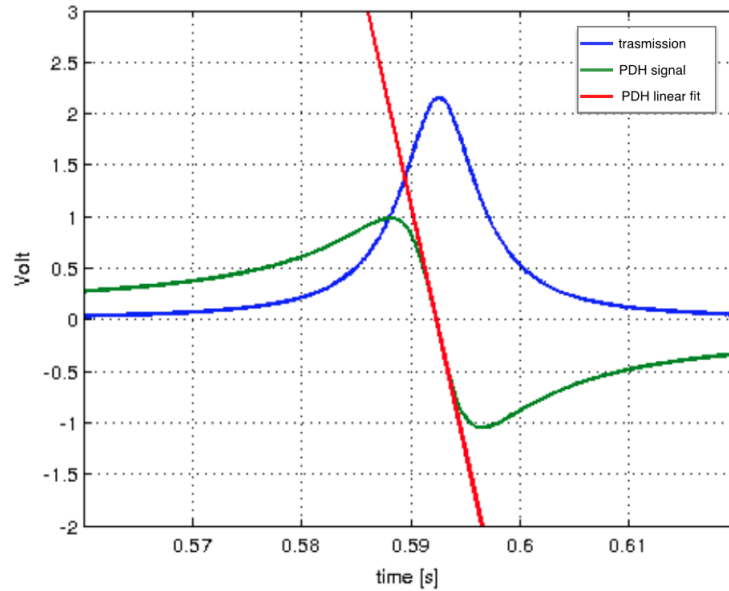


Figure 5.3: PDH signal and its linear fit in the central region, used to calibrate the RFC error signal.

5.1.2 Open loop transfer functions

The open loop transfer function the RFC, G_M has been measured by means of a noise injection between 10 Hz and 500 Hz. It has been compared with the modeled one which, as already said, is composed by the electronic corrector filter F_M , the mechanical response of the actuator A_M , the optical gain R_M and a pure delay due to the digital electronic.

Corrector filter : Unity Gain Frequency: 83 Hz

	Freq	Q
real zero	1	0
real zero	5	0
complex zero	11	0.7
complex zero	11	0.7
complex zero	20.5	2
complex zero	28.4	2
real zero	240	0
real pole	0	0
complex pole	2	2
complex pole	5	3
complex pole	20.5	20
complex pole	28.4	20
real pole	800	0
complex pole	2000	0.8

Actuator mechanical response : gain $16 \cdot 10^{-6} \text{m/V}$ in DC

	Freq	Q
complex pole	0.667	10

Delay : $800 \cdot 10^{-6} \text{s}$

The comparison between the modeled transfer function and the measured one is shown in Fig. 5.4. The two curves agree above 10 Hz where the noise injection has been performed.

5.2 Sensing noise

A noise, known as *sensing noise*, is introduced every time that an optical signal is recorded by a photodiode. It is composed by shot noise, dark noise and ADC noise if the analog signal is converted to a digital one (as in the case of RFC error signal). The mechanisms originating this noise are discussed in the following.

Sensing noises of the photodiodes used to lock the reference cavity and the mode cleaner affect the RFC error signal in the following way (see Eq. 5.6):

$$E = \left[\frac{1}{1 + T_M G_R} \right] (\mathbf{sn}_R + \frac{T_M R_R}{R_M} \mathbf{sn}_M) \quad (5.8)$$

since the optical gain R_R of the reference cavity is much smaller than the optical gain of the mode cleaner R_M , and the two sensing noises are comparable, only the contribution of RFC photodiode \mathbf{sn}_R has been taken into account.

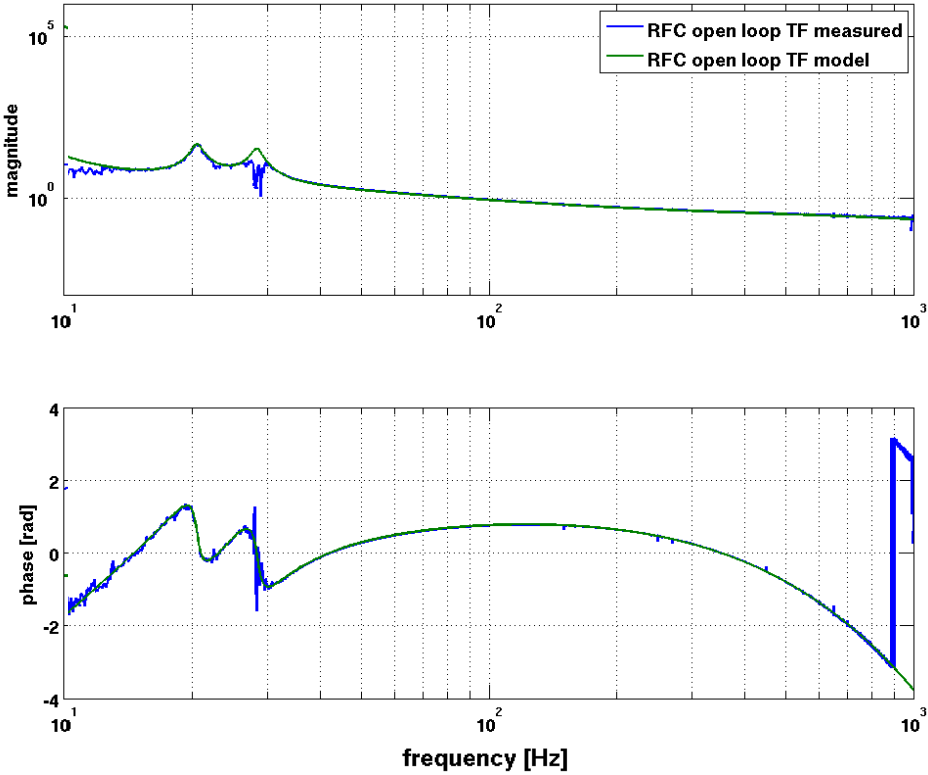


Figure 5.4: Comparison between the RFC transfer function measured and the theoretical model.

In order to compute the sensing noise, we took into account different mechanisms detailed in the following.

5.2.1 Shot noise

Shot noise, already described in Sec. 2.2.1, is a fundamental noise which stems from the discrete nature of the photons causing an uncertainty in their arrival time on a photodetector. Being a counting noise, it is governed by Poissonian statistic and, for a DC signal, it has a flat spectral density given by

$$S_{shot,DC} = \sqrt{2h\nu P_{in,DC}} \left[\frac{W}{\sqrt{Hz}} \right] \quad (5.9)$$

where $P_{in,DC}$ is the DC power impinging on the photodetector. Shot noise is measured as a photocurrent noise at the output of the photodiode and its value in terms of optical power can be recovered knowing the photodiode responsivity.

Here we are interested in computing the shot noise for a modulated signal. An estimation for it can be found considering a white noise with a known spectral density amplitude. If we multiply it by a cosine (in the time domain), the spectrum of the noise will remain flat and its amplitude will result reduced of a factor $\frac{1}{\sqrt{2}}$. Thus the shot noise for a demodulated signal can be approximated as [87]

$$S_{shot,AC} = \sqrt{h\nu P_{in,DC}} \left[\frac{W}{\sqrt{\text{Hz}}} \right] \quad (5.10)$$

We used this formula to estimate the shot noise of the demodulated RFC error signal.

5.2.2 Dark and ADC noise

The demodulated signal is digitized by means of an analog-to-digital converter (ADC) which introduces a white noise. This noise has been found by measuring at ADC output signal when the analog input was disconnected. We obtained:

$$n_{ADC} \simeq 2 \cdot 10^{-7} \left[\frac{V}{\sqrt{\text{Hz}}} \right] \quad (5.11)$$

The dark noise is a voltage at the photodiode amplifier output which if present even if there is no light impinging on it. We measured the sum of the dark noise and the ADC noise looking at the RFC error signal when there was no light reaching the photodiode, under the assumption that these noises are independent of the amount of light reaching the photodiode. The noise measured was $n_{sum} \simeq 4.5 \cdot 10^{-7} \frac{V}{\sqrt{\text{Hz}}}$. Assuming that dark noise and ADC noise are independent, the first can be obtained from the total measured one, knowing the ADC noise:

$$n_{dark} = \sqrt{n_{sum}^2 - n_{ADC}^2} \simeq 4 \cdot 10^{-7} \left[\frac{V}{\sqrt{\text{Hz}}} \right] \quad (5.12)$$

The different contributions to the sensing noise and their sum are plotted in Fig. 5.5 along with the RFC error signal. As shown in Eq. 5.8, in order to compare them, the sensing noise has been divided by $(1 + T_M G_R)$ to take into account the effect of the loop.

5.3 Classical radiation pressure noise

We have seen in Sec. 2.2.2 that light impinging on mirrors exerts on them a force known as radiation pressure force. Classical fluctuations in the beam power cause a fluctuation in the radiation pressure force, by directly moving the mirrors, results in a cavity length noise. Classical radiation pressure has been computed considering that a beam of power P exerts on a mirror a force given by $F = \frac{2P}{c}$; thus the fluctuations in the force are connected to those in the power by $\Delta F = \frac{2\Delta P}{c}$. From the mirror equation of motion in frequency domain $M(-2\pi f^2 + \omega_0^2) \tilde{x} = \tilde{F}$ we can deduce a relation between the spectral density of the mirror motion and the radiation pressure force:

$$S_x(f) = \frac{2}{4\pi^2 c M f_0^2 \left(\left(\frac{f}{f_0} \right)^2 - 1 \right)} \times S_p \quad (5.13)$$

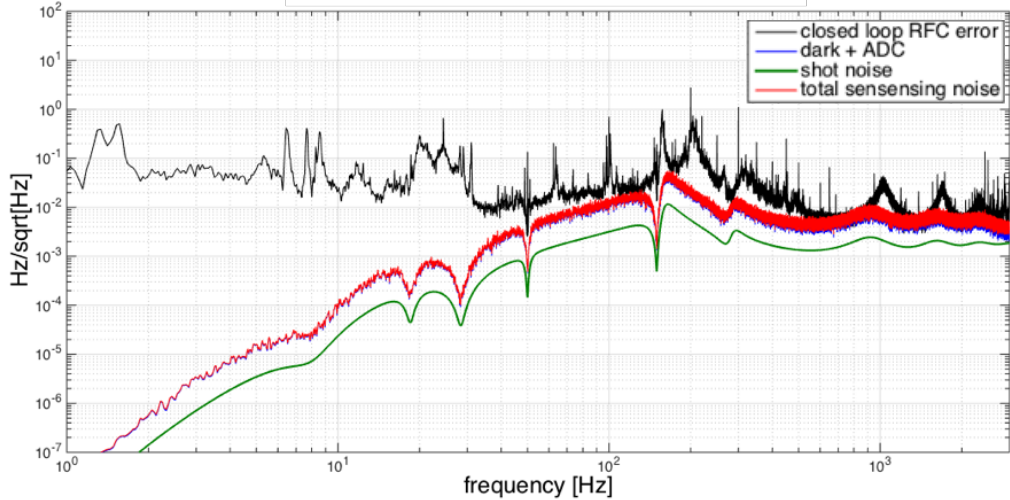


Figure 5.5: Different contributions to sensing noise and their sum compared with the RFC error signal. According to Eq. 5.8, the sensing noise has been divided by $(1 + T_M G_R)$ to take into account the effect of the loop.

where S_p is the spectral density of the intensity fluctuation of the laser, M is the mirror mass and f_0 is the pendulum resonance frequency.

In order to estimate the fluctuations of the power inside the cavity S_p we made the assumption that the laser relative intensity noise (RIN), that is the laser spectral density divided by its mean power, is the same inside and outside the cavity. Therefore in order to find S_p we measured the RIN on the IMC transmitted beam and multiplied it for the estimated value of the power inside the cavity. We used the approximated formula $P_{cav} = \frac{\text{Finesse}}{\pi} \cdot P_{in}$, with a IMC finesse around 1000 [88]. Since the impact of the radiation pressure is inversely proportional to the mass, its effect on the IMC input and output, which are fixed on the suspended injection bench (SIB 1), has been neglected and only its effect on the IMC end mirror have been taken into account. Its spectrum, compared to the RFC error signal, is plotted in Fig. 5.6, where we have used a $M = 3.4$ kg and $f_0 = 0.669$ Hz

5.4 Quantum radiation pressure noise

As observed in Sec. 2.2.2, fluctuations of the power impinging on the mirror can also be due to the quantum fluctuation in the number of incident photons. We have seen that as the shot noise, this is another manifestation of the particle nature of light and this two noises can be shown to be interdependent. We estimate the quantum radiation pressure contribution combining the spectral density of the fluctuating force

5.14

$$S_F(f) = \frac{2}{c} \sqrt{2h\nu P_{cav}} \quad (5.14)$$

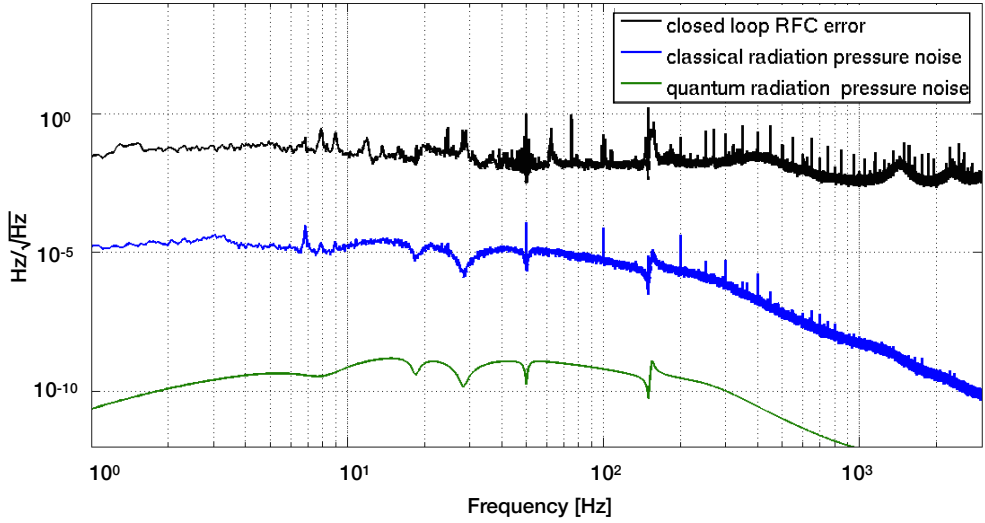


Figure 5.6: Classical and quantum radiation pressure noise compared with the RFC error signal.

As in the classical case, we can take the mirror equation of motion and find the spectral density of its displacement by inserting the spectral density of the fluctuating force:

$$S_x(f) = \frac{2}{4\pi^2 c M f_0^2 \left(\left(\frac{f}{f_0} \right)^2 - 1 \right)} \sqrt{2h\nu P_{cav}}$$

Quantum and classical radiation pressure noise spectra, divided by $(1 + T_M G_R)$, are compared to RFC error signal in Fig. 5.6. We see that both of them are far from being limiting factor for the laser frequency stability.

5.5 Thermal noise

Thermal noise, whose nature has been presented in Sec. 2.2.5, has been estimated both for the IMC suspension and for the coating of its mirrors.

5.5.1 Pendulum thermal noise

In Sec. 2.2.5.1 we obtain an expression to compute suspension thermal noise that writes:

$$S_x = \frac{4k_b T \phi_p \omega_0^2}{M \omega^5} \quad (5.15)$$

where k_b is the Boltzmann constant, M the mass of the mirror and

$$\phi_p = \frac{k_{el}}{k_g} \phi_w = \frac{N_w \sqrt{T_w E I}}{2gLM} \phi_w$$

with N_w number of wire, E wire material Young module, L wire length, I moment of inertia of the wire cross section, T_w tension of each wire and ϕ_w is the loss angle of the wire.

We computed the square root of this quantity for both the IMC end mirror and the suspended injection bench in order to find the amplitude spectral density of the displacement. We used the following parameters:

		SIB1	MC
Weight	M	198 kg	3.4 kg
Number of wires	N_W	3	2
Wire length	L	0.7048 m	0.555 m
Wire's cross section moment of inertia	I	$5.153 \cdot 10^{-13} m^4$	$2.485 \cdot 10^{-17} m^4$
Wire material		Maraging steel 250	C40 steel
Wire material modulus of elasticity	E	$2.1 \cdot 10^{11} Pa$	$2.2 \cdot 10^{11} Pa$
Wire's losses	ϕ_w	$6 \cdot 10^{-5}$	$1.9 \cdot 10^{-4}$

The dilution factors (defined in Sec. 2.2.5.1) of the SIB1 and the MC are $9.2 \cdot 10^{-6}$ and $7.3 \cdot 10^{-4}$, respectively. By multiplying them for the respective material loss angles we find $\phi_p^{IB} = 6 \cdot 10^{-11}$ and $\phi_p^{MC} = 1.4 \cdot 10^{-7}$. The two contributions and their incoherent sum, divided by $(1 + T_M G_R)$, are compared with the RFC error signal in Fig. 5.7.

5.5.2 Coating thermal noise

As already reported in Sec. 2.2.5 the expression of the mirror coating thermal noise is [33]:

$$S_x = \frac{8k_b T}{\omega} \frac{(1+\sigma)(1-2\sigma)t}{\pi E_0 w^2} \phi_c \quad (5.16)$$

where σ is the Poisson ratio, E_0 the mirror Young modulus, w the laser beam radius, t is the coating thickness and ϕ_c is the loss angle

We computed the square root of this quantity for both the IMC end mirror and the injection bench to find the amplitude spectral density of the displacement. We used: $\sigma = 0.17$, $E_0 = 7 \cdot 10^{10} Pa$, $w_{IB} = 0.005 m$, $w_{MC} = 0.01 m$, $\phi_c^{IB} = 4 \cdot 10^{-4}$, $\phi_c^{MC} = 5 \cdot 10^{-4}$, coating thickness $t_{IB} = 1.8 \cdot 10^{-6} m$, coating thickness $t_{MC} = 6.5 \cdot 10^{-6} m$. The total coating thermal noise is compared with the pendulum thermal noise and the RFC error signal in Fig. 5.7. We see that also in this case they are at least four orders of magnitude below the error signal spectrum, therefore they don't limit the frequency stability.

5.6 RFC length noise

The rigid reference cavity, described in Sec. 4.1.5, used to stabilize the laser at low frequencies, is affected by thermal noise inducing fluctuation in its length which projects on the RFC error signal. Some investigations have been done in the past,

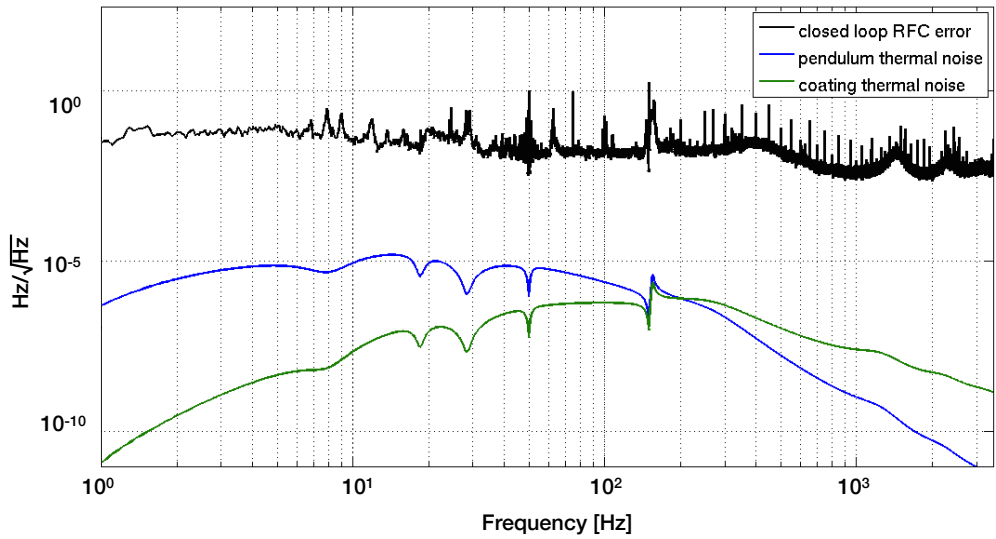


Figure 5.7: Pendulum and coating thermal noise spectrum compared with RFC error signal. The effect of the loop has been taken into account in the comparison.

in order to measure such noise. An upper limit for this noise has been obtained by Bondu in 1996 [86], two RFCs have been used for the measurement: a laser was locked to one of them and the other was used as a reference to measure the frequency stability. The error signal spectrum of the measurement cavity in Fig. 5.8 (blue line) is the sum of the two RFC cavity noises. Another measurement of the RFC noise has been performed by Bondu in 2008 using as reference a laser stabilized on the Virgo arms length [86]. The spectral density for this measurement is plotted in Fig. 5.8 (green line). The two measurements seem to be in agreement.

A theoretical estimation of the RFC length noise has been done by Numata et al. [89]. They assumed that the noise is originates from thermal fluctuations and computed numerically the contribution of the spacer and the mirrors (coating and substrate). Numata's result has been fitted by the function

$$n_{RFC} = \frac{10^{-1}}{\sqrt{f}} \frac{Hz}{\sqrt{Hz}} \quad (5.17)$$

This estimation is plotted in Fig. 5.8 (red line) together with the two measurements by Bondu. The theory shows a good agreement with the floor of both experimental results. We have used the estimation given by Numata as RFC length noise in our noise budget. The projection of this noise on the RFC error signal is shown in Fig. 5.9 and it seems to be the limiting noise in the frequency region between 40 and 150 Hz.

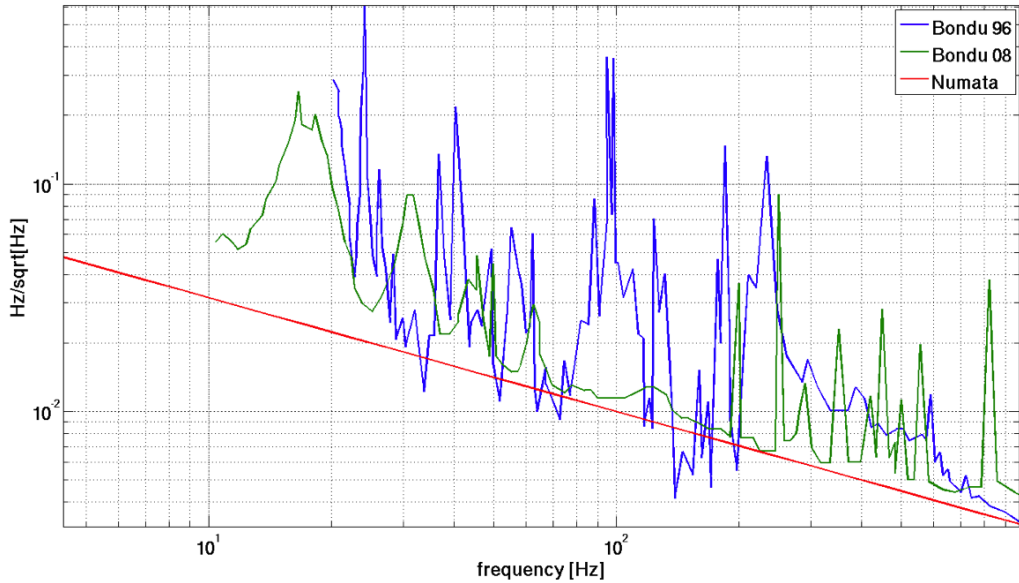


Figure 5.8: Theoretical estimated RFC length noise (red line) is compared with two different experimental measurements

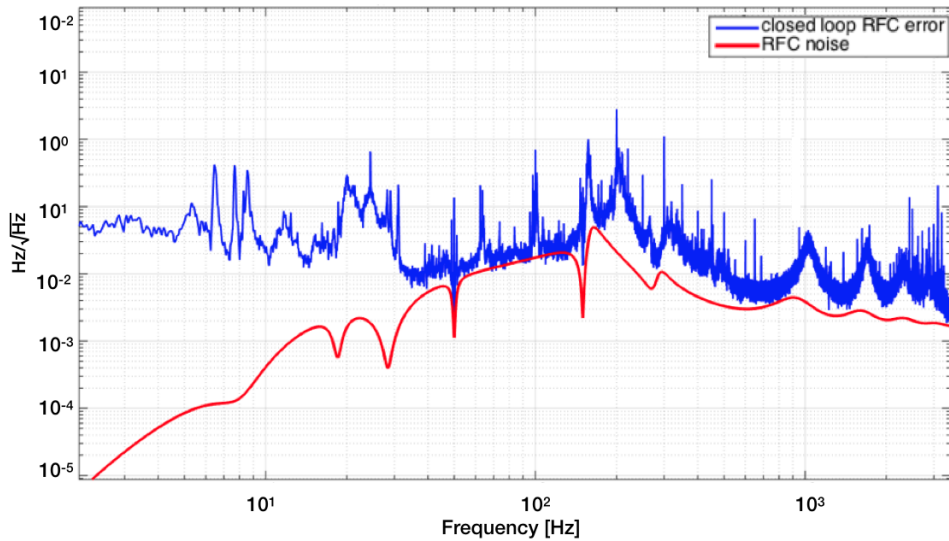


Figure 5.9: RFC length noise projection on the RFC error signal.

5.7 Angular control noise

In order to keep the IMC aligned with respect to the laser, the angular degrees of freedom of the MC end mirror and the suspended injection bench are controlled. Two different techniques are used. The Local Controls (LC) use optical levers as position sensors with respect to the ground. They provide information only on the position

of a mirror with respect to the ground and not on the laser beam position with respect to the mirrors.² Since they use the ground as reference, they are affected by seismic noise. Moreover they are affected by an higher sensing noise. The automatic alignment (AA) based on the wavefront sensing technique, on the other hand, uses the fact that a cavity misalignment generates higher order modes. The amount of higher order modes produced is measured, extracting a demodulated error signal from quadrant photodiodes, and provides information on the cavity alignment. Two quadrant placed in reflection with a Gouy phase shift of 90° , modulated at 22 MHz are used. In addition the signal from a DC quadrant placed in transmission of the IMC end mirror is used. The sensitive degrees of freedom to be controlled are θ_x , θ_y , θ_z for the SIB1 and θ_x , θ_y for the MC. The relation between their values and the quadrant signal is expressed by the optical matrix, measured by injecting monochromatic excitations on the actuators in order to measure the transfer function between each degree of freedom and the quadrant signal.

Local controls are used to stabilize the mirrors during the lock acquisition and to reduce their angular displacement below some tenths of microradians in order to reach the linear regime of the Automatic Alignment error signals. Unlike Automatic alignment, Local control are not compliant with the requirement set on the angular stability for a low noise operation of the interferometer, as their sensor are affected by an higher electronic noise and long term drift [90]. Two different control schemes are possible: a *fast control* which uses only global signal with a bandwidth of tens of Hz and a *drift control* where the global control are used with a control bandwidth of few mHz while at higher frequency local controls are used. In order to measure the noise contribution of the angular control noise to RFC error, we measured the transfer function between the correction applied to the marionette and the RFC error signal. This has been done by means of a noise injection on the marionette. The transfer functions for the three injection bench degrees of freedom θ_x , θ_y , θ_z are shown in Fig. 5.10. The contribution of the angular control noise of the injection bench to RFC error signal is found by multiplying the spectrum of the correction signal in normal condition with the absolute value of the measured transfer function.

$$N_{\text{proj}}(f) = |TF(f)|_{\text{with noise}} \cdot |ASD(f)|_{\text{no noise}} \quad (5.18)$$

As it can be seen in Fig. 5.11 the IB angular control noise represents the limiting noise in the RFC error signal up to 40 Hz. Noise injections on the IMC end mirrors showed a very low coherence with RFC error signal, thus their projection are not included in the noise budget.

²More details on this technique and on its implementation can be found in Sec. 9.3.

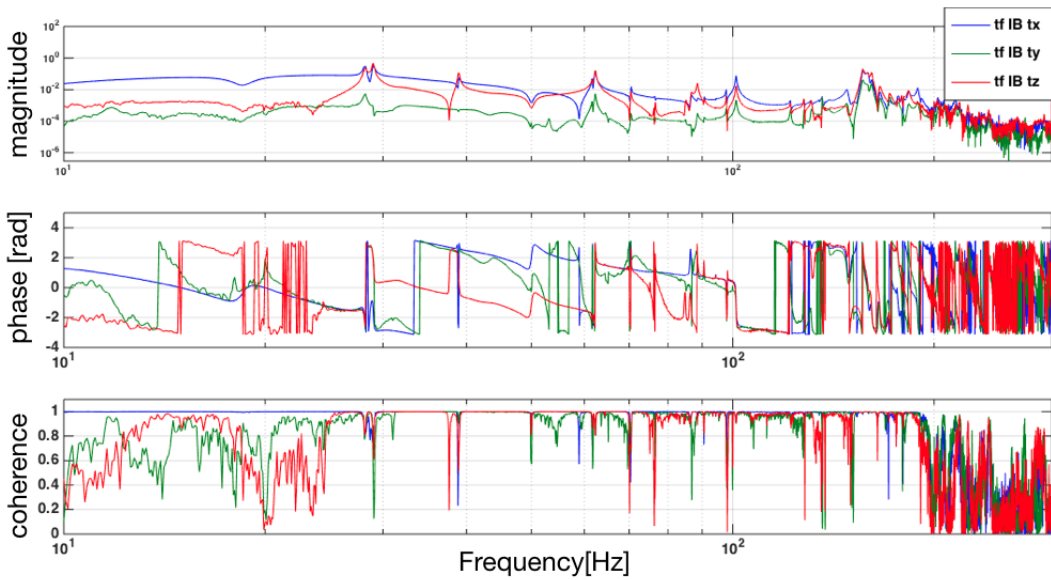


Figure 5.10: Transfer functions between the correction applied to the marionetta and the RFC error signal for the 3 degree of freedom of the injection bench.

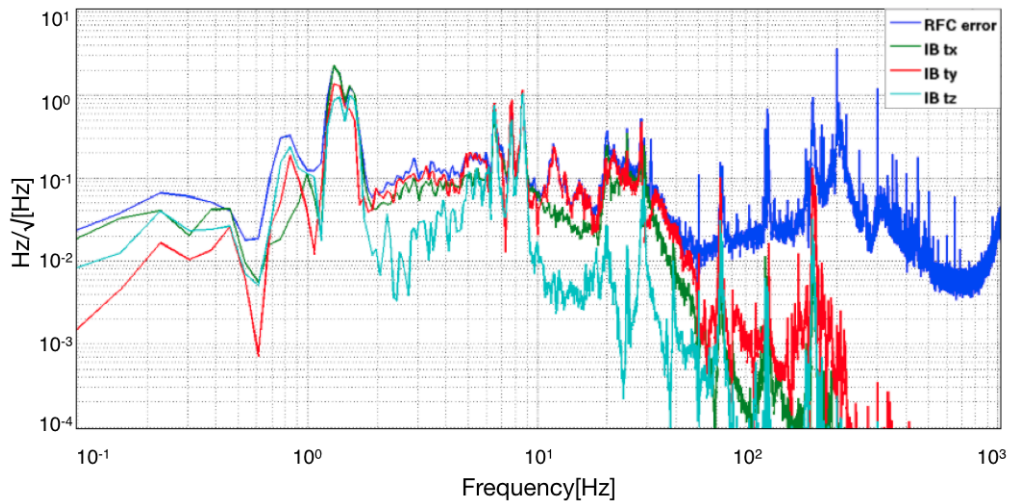


Figure 5.11: Injection Bench angular control noise projections.

5.8 Beam pointing control (BPC) noise

The beam pointing noise, usually referred to as jitter noise, consists in a shift or a tilt of the input beam axis with respect to the IMC cavity axis. A jitter of the beam which enters the interferometer couples with a possible asymmetry between its arms causing a phase noise. For that reason the injection system has to deliver a beam with specific requirements in terms of jitter. A sensing system composed by two quadrant photodiodes is used to monitor the shift and the tilt of the beam at the IMC input [91]. A beam pick-off is taken before the IMC and it is sent to two quadrants which are placed at a distance producing a Gouy phase shift of 90° . In this way each quadrant is sensitive only to one degree of freedom: the pure shift for the so-called Near Field quadrant and the tilt for the Far Field one. These signals are used as error signals in a feedback loop, the Beam Pointing Control (BPC), active in the frequency range up to 10 Hz. The correction obtained filtering the error signal, is sent to the actuators: two tip/tilt piezo mirrors placed as in Fig. 5.12.

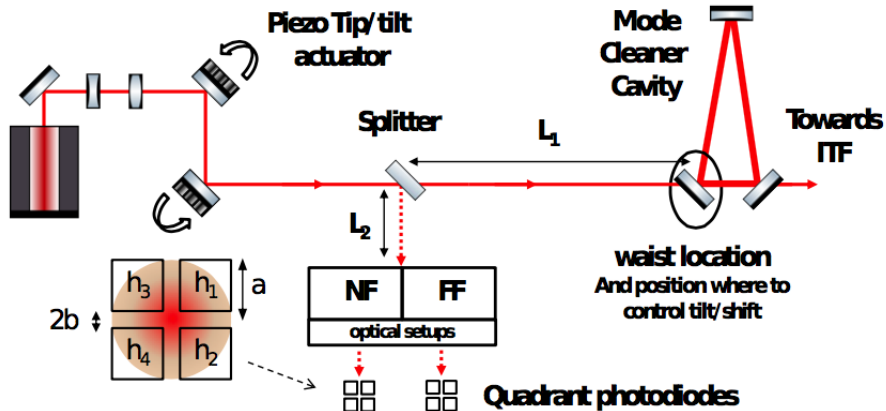


Figure 5.12: Beam pointing control scheme from [91]

As discussed in Sec. 4.1.4 above the bandwidth of the Automatic Alignment loop (~ 1 Hz) the IMC acts as a filter for the beam jitter. The jitter, seen as a misalignment by the cavity, produces higher order modes which cannot resonate and are weakly transmitted. On the other hand, in the region where the Automatic Alignment is active, the cavity is kept aligned following the beam position fluctuation which are transmitted almost unchanged.

The projection on the RFC error signal has been found by injecting noise on the BPC actuators and measuring the transfer function between the jitter and the RFC error signal for all the degree of freedom: shift in x and y and tilt in θ_x and θ_y . The transfer functions have been than multiplied for the jitter signals in normal condition to find the noise projections that are shown in Fig. 5.13. We observe that the RFC

error signal is not limited by such noise.

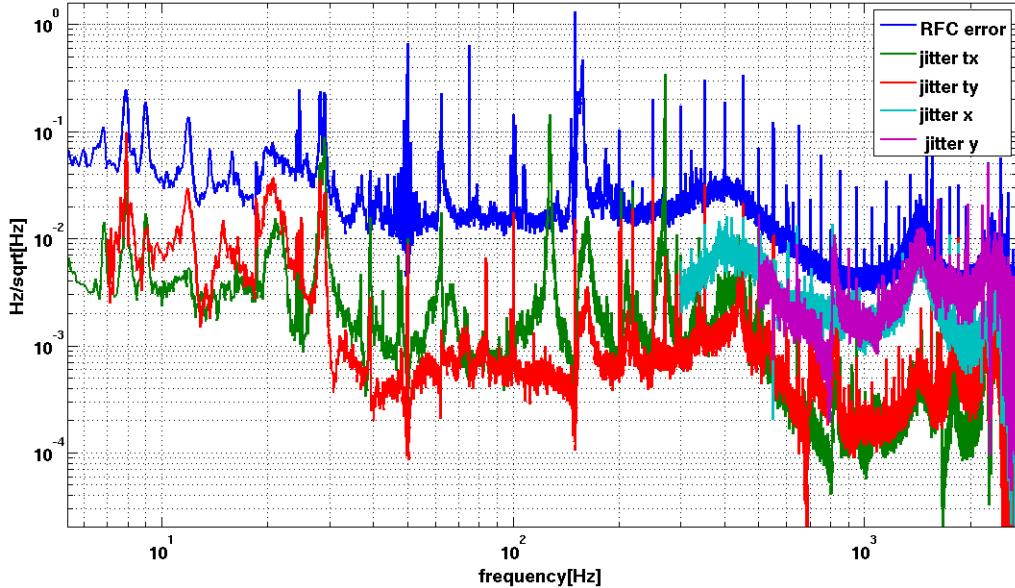


Figure 5.13: Jitter noise projection on the RFC error signal.

The mechanism through which the jitter noise affects the RFC error signal is not straightforward. For example, in the RFC error signal there are peaks around 10 Hz explained by the noise projection of the angular control of the input bench and also seen by the BPC sensors. We found them to have a high coherence with the seismometers of the external injection bench (EIB). Since the AA quadrants on the EIB are supposed to be insensitive to seismic noise at the first order, we suppose that motion of the external injection bench causes a real jitter of the beam which is seen as a misalignment from the AA quadrant and then re-injected as angular control noise by their control loop. However this coupling mechanism through the AA control loop is unlikely to act at high frequency because the AA loop is not active at these frequencies.

From the argument above it is evident that at low frequency, angular control noise and jitter noise can not be considered independent. For that reason they can not be summed in quadrature to obtain the total noise. When summing all the noise sources, a solution to avoid an overestimation of the total noise is to take into account the jitter noise projection obtained from a transfer function measured under local controls.

All the noise projections computed above have been put together to realize a noise budget for the RFC error signal (See Fig. 5.14). In Fig. 5.15, only the most relevant noises are shown: we see that the frequency noise is limited by injection bench angular control noise up to 40 Hz. From RFC thermal noise in the region

between 50 and 120 Hz and by sensing noise above. We remark that there are some bumps (for example at 200 Hz) and some peaks at high frequency which are not explained by the incoherent sum of all the noises considered.

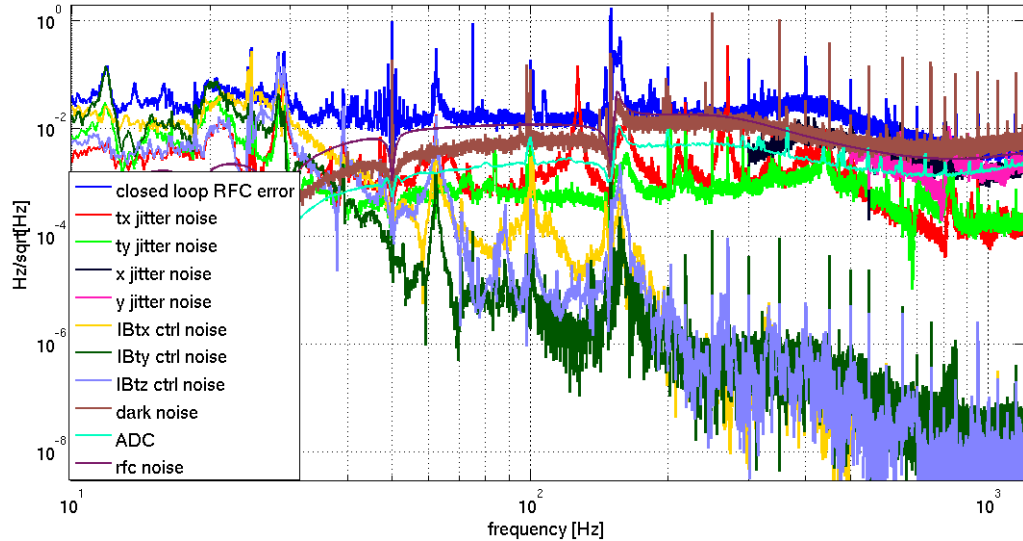


Figure 5.14: Noise budget for the RFC error signal.

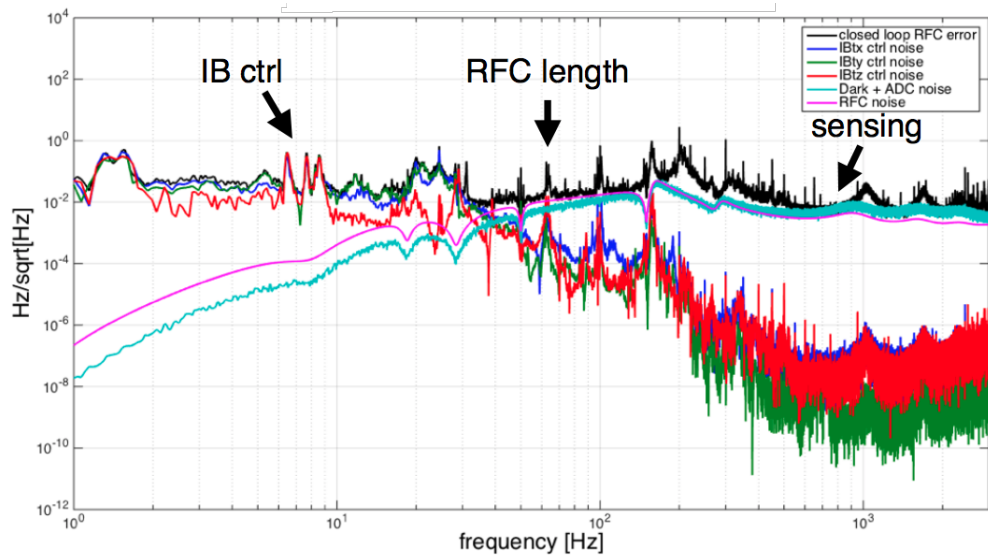


Figure 5.15: Noise budget for the RFC error signal showing only limiting noises.

5.9 The "real" frequency noise

As we have anticipated, our ultimate goal is to estimate the frequency noise of the beam that is sent to the ITF, referred to as ν_{RFC} in Fig. 5.1. Up to now, our

analysis was performed on the RFC error signal and we produced a noise budget showing which are the noises that limit it. Since we found out that both RFC and sensing noise are between the limiting sources, RFC frequency noise cannot be simply considered a measurement of the real frequency noise. The next step will be thus to compute how this signal is related with the real frequency noise in order to reconstruct the latter. A simplified expression in terms of noises which contribute to RFC error signal can be deduced from Eq. 5.6 and reads

$$E = \left[\frac{1}{1+G} \right] (sn_R + ln_R + ln_M) \quad (5.19)$$

Where G is the RFC open loop transfer function, sn_R is the sensing noise, ln_R and ln_M are the length noise of the RFC and IMC respectively. On the other hand, the real frequency noise sent to the ITF is [92]:

$$\nu_{\text{ITF}} = \left[\frac{1}{1+G} \right] (sn_R + ln_R) + \left[\frac{G}{1+G} \right] ln_M \quad (5.20)$$

Where sn_R , ln_R and ln_M are assumed to be converted in Hz. By comparing the two expressions we see that the contribution of IMC length noise is the same, but if we consider the RFC error signal an estimation of the real frequency noise, we underestimate RFC length noise and sensing noise in the frequency region where $G \gg 1$ and at the same time we overestimate them in the frequency region where $G \ll 1$. In Fig. 5.16 the RFC error signal limiting noises have been combined following Eq. 5.20 in order to reconstruct the frequency noise of the beam sent to the ITF. We observed that the RMS of such reconstructed signal is slightly lower than that obtain from the RFC error signal [92]. So we can regard RFC error signal as an upper limit for the frequency noise of the beam sent to the ITF.

Frequency noise measurement using arm cavity

Once the north arm cavity was locked we could perform an independent measurement of frequency noise and compare it with that obtained with the RFC. First we observed that the north arm PDH error signal was highly coherent with the RFC error signal in the region between 50 and 400 Hz. This suggests that the error signal is dominated by the frequency noise in this frequency region. Since the north arm and the RFC give independent measurements of the frequency noise, we have checked whether the two methods give coherent results. Error signal of the arm is connected to frequency noise by the following relation :

$$E_{\text{arm}} = C_{\text{arm}} \frac{\nu_{\text{ITF}}}{\sqrt{1 + \left(\frac{f}{f_0} \right)^2}} \rightarrow \nu_{\text{ITF}} = \frac{E_{\text{arm}}}{C_{\text{arm}}} \cdot \sqrt{1 + \left(\frac{f}{f_0} \right)^2} \quad (5.21)$$

where ν_{ITF} is the frequency noise, E_{arm} is the error signal of the north cavity,

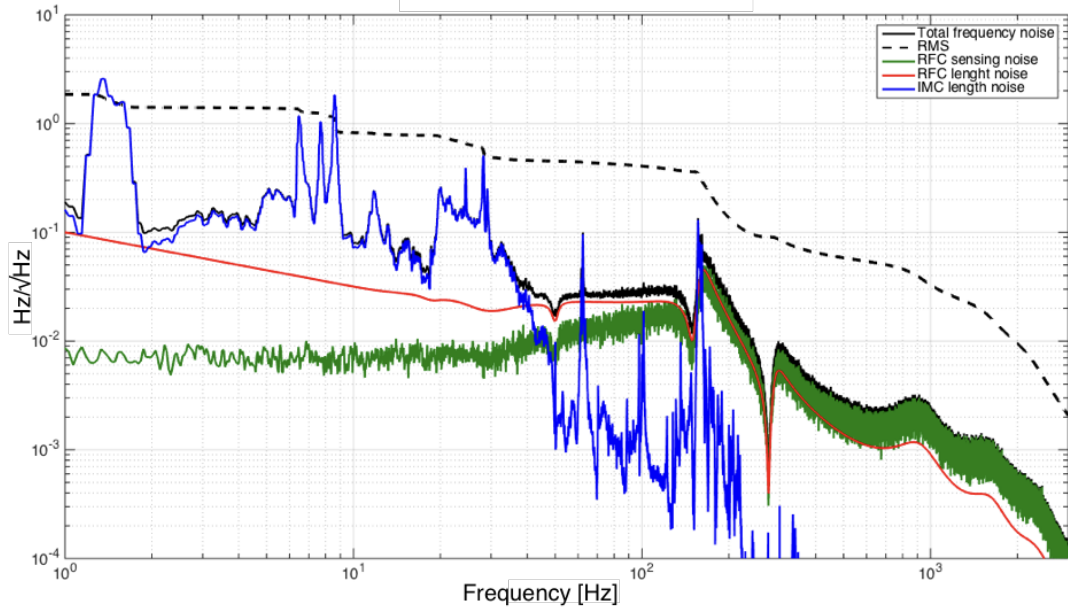


Figure 5.16: The RFC error signal limiting combined following Eq. 5.20 in order to reconstruct the "real" frequency noise sent to the ITF.

$f_0 \simeq 55.5$ Hz is the pole of the arm (assuming a finesse of 450) the C_{arm} is a calibration factor from Hz to Volt. We did not take into account the effect of the arm cavity control loop since at the time of the measurement it had a bandwidth of 15 Hz. According to the analysis presented before, in the region 50-500 Hz, the RFC error signal is limited by the length noise of the RFC and its sensing noise. We have seen that the frequency noise of the laser ν_{ITF} , as measured by the RFC error signal, is related to error signal in the following way:

$$E_{\text{rfc}} = C_{\text{rfc}} \frac{\nu_{\text{ITF}}}{G} \rightarrow \nu_{\text{ITF}} = E_{\text{rfc}} \frac{G}{C_{\text{rfc}}} \quad (5.22)$$

where G is the RFC open loop transfer function of the RFC and C_{rfc} is the RFC error signal calibration factor. In Fig. 5.17 we have superposed the frequency noise ν_{ITF} as measured by the north arm cavity and by the RFC. We observe that the two spectra are in good agreement in the region between 50 and 400 Hz (where the coherence between the two signals is high), showing that the two measurements are consistent.

We remark that this analysis is not highly dependent from the north arm cavity pole. The calibration factor for the north arm has been chosen in order to superpose the two spectra and has been used to estimate the lock accuracy of the cavity. We found $1/C_{\text{rfc}} = 2.7 \cdot 10^4$ Hz/V (or $2.9 \cdot 10^{-7}$ m/V) which corresponds to a lock accuracy of ~ 30 pm. This value has been found to be consistent with the result of an independent calibration of the error signal, thus confirming our analysis.

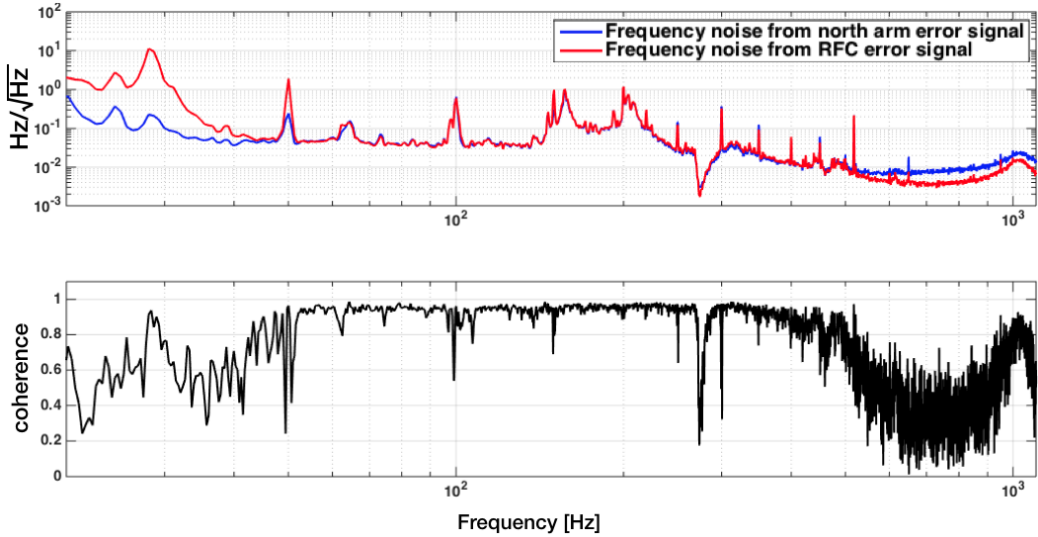


Figure 5.17: Comparison between the frequency noise of the prestabilized laser measured by the RFC and the north arm cavity.

5.10 Noise budget automation

The process to compute the noise budget has been automated and included as a standard procedure in *Metatron*. This is a state machine based code for the automation of Advanced Virgo control [93], which has been adapted from a code developed in LIGO, known as *Guardian* [94]. In Fig. 5.18 the state machine graph for the injection node is shown. A preliminary operation in order to compute the noise budget is to measure the transfer function between the noise in a degree of freedom and the RFC error signal. This is done using a python script which can inject noise of desired amplitude and shape on the IMC angular controls, on the BPC actuators and in the RFC loop. GPS of noise injection are recorded and used by a MATLAB script which computes the transfer functions. Then, another MATLAB script is called: it measures corrections sent to the actuators in stationary conditions and produces the noise budget. As can be observed from the state machine graph, the noise injection is not a necessary preliminary step in the noise budget computation. Since the transfer functions are unlikely to change very often, it is also possible to directly run the noise budget script which in that case will use the latest computed transfer functions.

5.11 Frequency noise improvement and conclusions

Noise budget has proven to be a useful tool in the injection system commissioning, to monitor the frequency noise and identify possible problems in the pre-stabilization

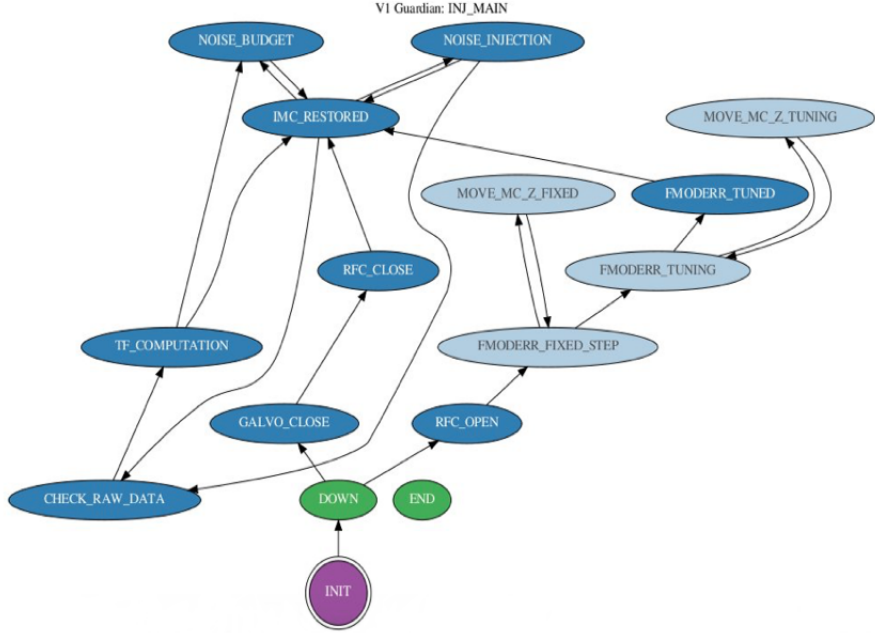


Figure 5.18: The state machine graph for the injection node in Metatron.

loop. In Fig. 5.19 are shown the progress in the reduction of frequency noise achieved over four months of commissioning, which lead to meet the requirement of 1 Hz RMS. The main improvements to reduce the noise consisted in an optimization of the RFC loop filter and the automatic alignment system (tuning of the corrector filters, reducing noise in the quadrant error signal) in the increasing of the power, the use of more performant photodiodes for the RFC loop which were also suspended and put in vacuum and in the replacement of the electronic.

The activity described in this chapter and the main results obtained can be summarized as follows

- We performed for the first time a complete noise budget for the RFC error signal.
- We use it to deduce the real frequency noise of the pre-stabilized laser, injected into the ITF.
- We have automated the noise budget and use for the noise hunting activity, contributing to reduce frequency noise below the requirement
- Once the requirement was achieved we could lock the arm cavities. Then we could confirmed our frequency noise estimation by comparing it to the cavity error signal and finding a good agreement between the two.

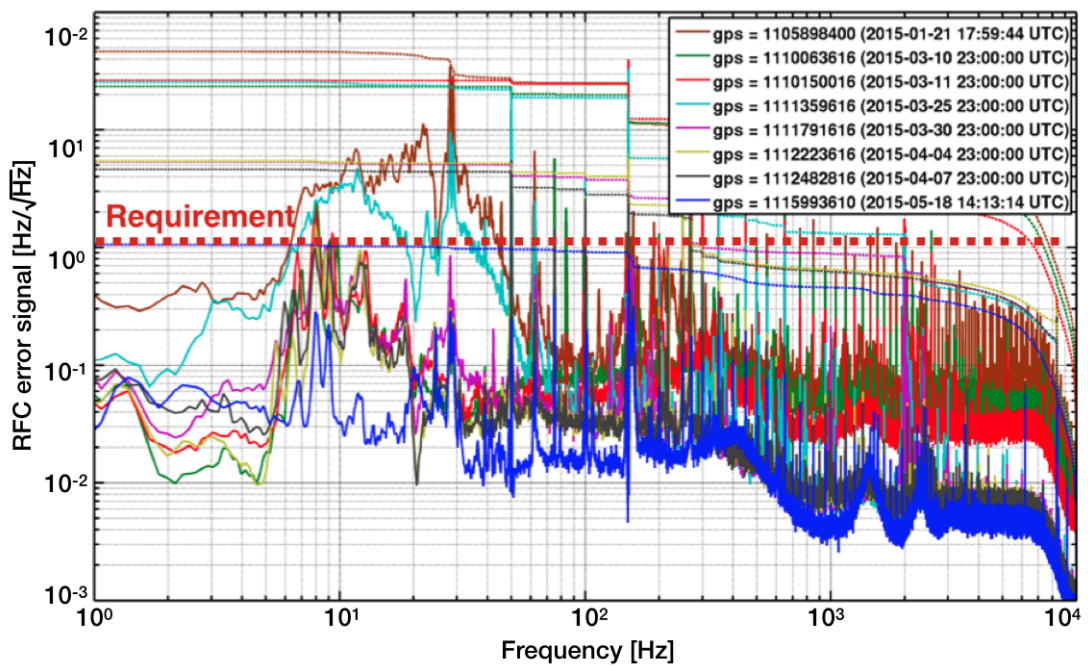


Figure 5.19: Improvement of the RFC error signal up to the requirement of 1 Hz RMS.

CHAPTER 6

Optical Characterization of the arm cavities

In this chapter we present the techniques used to measure optical parameters of the arm cavities and the main results we obtained. The quantity measured are the finesse, the round trip losses (RTL), the cavity g-factor, the misalignment and mismatching. The main goal of this activity is to check that all these parameters are compliant with a proper operation of the interferometer. Moreover, inconsistent results in these measurements have often triggered investigation and point out issues such as beam clipping or alignment problems. We remark that the techniques presented here can be also used for the characterization of the quantum filter cavity presented in the third part of this thesis.

Fig. 6.1 shows the optical scheme of Advanced Virgo and in particular the location

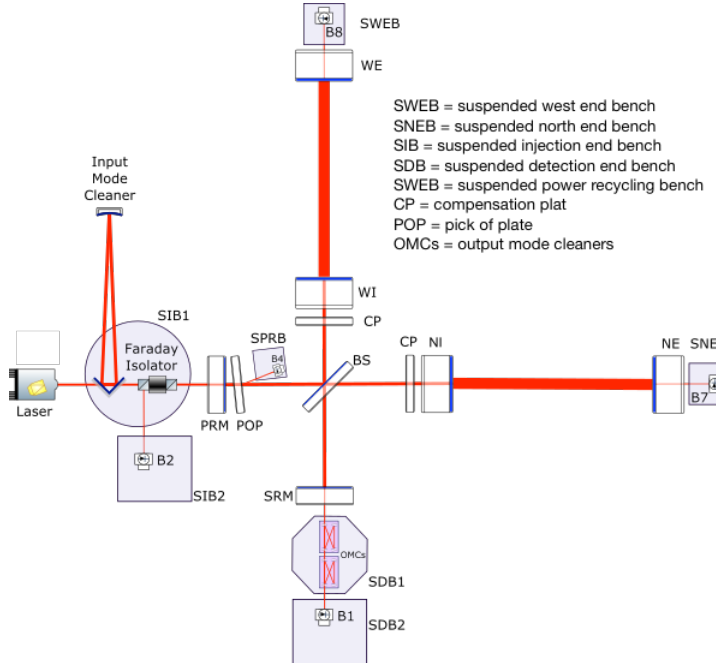


Figure 6.1: Optical scheme of Advanced Virgo with photodiode disposition.

of the photodiodes used for the ITF sensing and control. Each photodiode is actually constituted by two photodiodes and a beamsplitter before them. Cavity mirrors have been polished coated and characterized at LMA. In Tab. 6.1 we report some of the measured parameters of the arm cavity mirrors which have been used in the following computations.

Parameter	North IM [95]	North EM [96]	West IM [97]	West EM [98]
RoC	1424.58 m	1695 m	1424.56 m	1696 m
Transmission HR	$1.377 \pm 0.006\%$	4.4 ± 0.1 ppm	$1.375 \pm 0.007\%$	4.3 ± 0.2 ppm
Reflectivity AR	32 ± 10 ppm	$133 \pm$ ppm	58 ± 9 ppm	155 ± 15 ppm
Absorption	0.19 ± 0.08 ppm	0.24 ± 0.10 ppm	0.22 ± 0.06 ppm	0.24 ± 0.12 ppm
Flatness RMS	0.27 nm	0.5 nm	0.31 nm	0.35 nm

Table 6.1: Measured parameters of the arm cavity mirrors. Transmission and reflectivity are both referred to power.

6.1 Finesse

Finesse has been defined in Eq. 2.58 as the ratio of the free spectral range (FSR) to cavity linewidth (FWHM). The straightforward method to evaluate it consists in measuring the FSR and the linewidth by performing a cavity free swinging. We will see in the following that if the cavity is crossed in a time higher than its storage time, this method is not effective since the Airy peak is distorted by dynamical effects [99]. The expected value of the finesse can be computed, knowing the reflectivity of the mirrors, by using the formula (when r_1 and $r_2 \simeq 1$)

$$F \simeq \frac{\pi\sqrt{r_1 r_2}}{1 - r_1 r_2} \quad (6.1)$$

Using the measured reflectivities reported in Tab. 6.1 we found a Finesse of 453 ± 2 for the north arm and 453.7 ± 2.3 for the west arm.

Etalon effect

The computation above doesn't take into account the effect of the Fabry-Perot cavity constituted by the faces of the input mirrors and known as *etalon effect*. In fact input mirrors are composed of two faces: one with anti-reflectivity (AR) coating and the other with high-reflectivity (HR) coating. They form a Fabry-Perot cavity whose length depends on the substrate temperature, which can affect the arm cavity behavior. The reflectivity of the arm cavity if we take into account the AR face becomes:

$$r_{\text{cav}}^e = \frac{-r_{\text{AR}} + r_{\text{cav}} \exp(-i\beta)}{1 - r_{\text{AR}} r_{\text{cav}} \exp(-i\beta)} \quad (6.2)$$

where r_{AR} is the reflectivity of the AR face and β is the phase acquired after a round-trip inside the input mirror. It can be shown that at the resonance the reflectivity, computed taking into account the etalon effect r_{cav}^e , is connected to the standard one by the relation [86]

$$r_{\text{cav}}^e = r_{\text{cav}} \left(1 + r_{\text{AR}} \cos(\beta) \frac{1 - r_{\text{cav}}^2}{r_{\text{cav}}} \right) \quad (6.3)$$

The reflectivity variation is small (< 10 ppm) since in our case $(1 - r_{\text{cav}}^2) \ll 1$ and $r_{\text{AR}} \ll 1$.

We can then compute the change in the cavity pole and in the finesse due to the etalon effect finding [86]

$$f_p^e = f_p \left(1 + r_{\text{AR}} \cos(\beta) \frac{2r_{\text{cav}}^2 + r_{\text{cav}} - 1}{r_{\text{cav}}} \right) \quad (6.4)$$

$$F^e = F \left(1 - r_{\text{AR}} \cos(\beta) \frac{2r_{\text{cav}}^2 + r_{\text{cav}} - 1}{r_{\text{cav}}} \right) \quad (6.5)$$

We see that in this case the change is more relevant. The reason for this is that the cavity reflectivity (in over-coupled cavities) is much less dependent on the input mirror transmissivity than the finesse or the cavity pole and thus it is less affected by the etalon effect.

By using the values reported in Tab. 6.1 we found that the etalon effect can induce a variation on the finesse and the cavity pole up to 1.1% for the north arm and 1.5% for the west arm. It is important to remark that even if we can measure the finesse with a very small statistic error, the etalon has to be considered as a systematic error of the measurement.

Decay time

The finesse can be computed measuring the cavity storage time which is connected to it by the relation

$$F = \pi \cdot \text{FSR} \cdot \tau_{\text{sto}} \quad (6.6)$$

The storage time can be measured by quickly extinguishing the light entering a cavity on resonance. The power inside the cavity is expected to decrease exponentially as [100]

$$P_{\text{cav}}(t) = \frac{P_0 T_1}{(1 - r_1 r_2)^2} \exp(-2t/\tau_{\text{sto}}) \quad (6.7)$$

where P_0 is the power stored in the cavity when it is locked.

A key factor to perform a good measurement is to extinguish the beam as quickly as possible. The easiest way to do it is to unlock the IMC. In Fig. 6.2 the power decay due to the IMC unlock is shown for the IMC transmitted power, the transmitted and the reflected power of the arm cavity. In order to fit the transmitted power and find

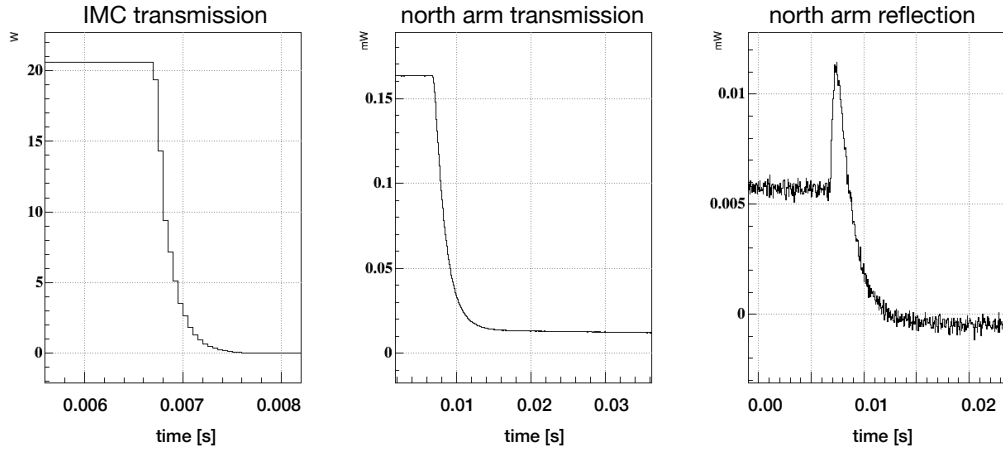


Figure 6.2: Power decay due to the IMC unlock for the IMC transmitted power, the transmitted (B7) and the reflected power (B4) of the north arm cavity. The bump in the reflected power is due to the fact that, when the input beam is cut, the light exiting the cavity and coming back toward the laser is not anymore destructively interfering with the input light.

τ_{sto} we had to take into account the effect of the IMC time decay (even if it is much shorter than that of the cavity) and a much longer time decay due to the response of the photodiode pre-amplifier.¹.

The result of the fit, done by F. Sorrentino, gave a storage time $\tau_{\text{sto}} = 2.88$ ms for both the cavities. The estimated systematic error is about 1%. The finesse, computed from Eq. 6.6 was found to be 452 ± 5 for the two cavities. In Fig. 6.3 the results of this measurement (and its systematic error) have been compared with the expected finesse computed from the measured mirror reflectivities. The error bars, in this case, account for the etalon effect. The two show a good agreement for both the arms.

Ringing effect

The decay time can also be extracted from the *ringing effect*. As anticipated, this effect arises if the cavity decay time (also referred to as cavity storage time) is longer than the time taken to cross the resonance

$$t_{\text{cross}} = \frac{\lambda}{2vF} \quad (6.8)$$

In this condition, the light does not have enough time to completely fill the cavity and the incoming field beats with the evolving stored field in the cavity producing an oscillatory behavior, referred to as ringing. The threshold velocity for observing

¹This effect has been observed and quantified by closing the shutter of the photodiode

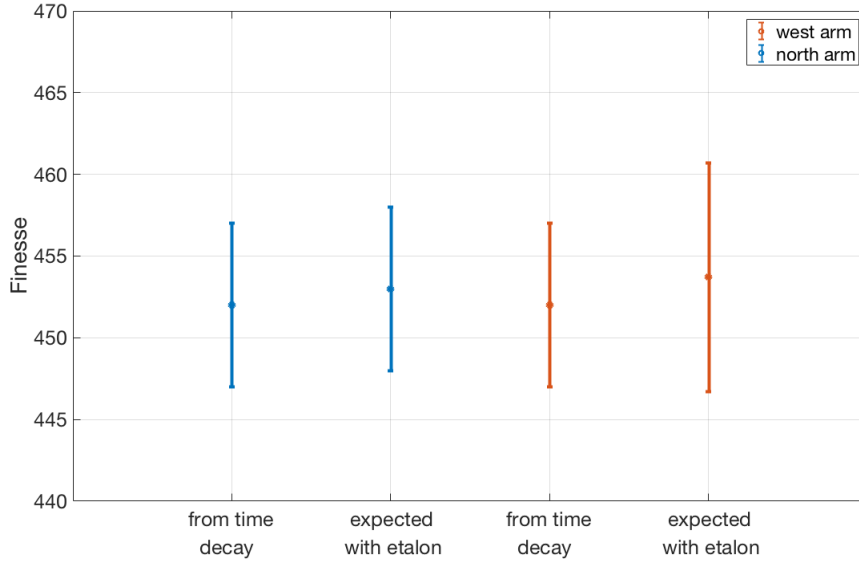


Figure 6.3: Comparison of the finesse measured from the decay time and that computed from mirrors reflectivities (considering also the etalon effect).

it is obtained when $t_{\text{sto}} = t_{\text{cross}}$. For Advanced Virgo arm cavities we have

$$v_{\text{thre}} = \frac{\pi \lambda c}{4F^2 L} \simeq 0.4 \mu\text{m/s} \quad (6.9)$$

An analytical expression for the behaviour of the field in the cavity is [101]

$$E(t) = D(t)\Theta(t) \quad (6.10)$$

where $D(t)$ and $\Theta(t)$ are defined as

$$D(t) = (i\pi/\alpha)^{\frac{1}{2}} t_1 A e^{-i\beta^2/\alpha} \quad (6.11)$$

$$\Theta(t) = (\alpha/i\pi)^{\frac{1}{2}} \sum_{n=0}^{\infty} e^{i\alpha(n-\beta\alpha)^2} \quad (6.12)$$

and the parameters α and β are defined as

$$\alpha = \frac{kv}{\text{FSR}} \quad (6.13)$$

$$\beta = kvt - i \frac{L}{c\tau_{\text{sto}}} \quad (6.14)$$

$$(6.15)$$

where $k = 2\pi/\lambda$ and v is the speed of the mirror.

The measured transmitted power when the cavity crosses the resonance (in Fig. 6.4) shows clearly the ringing effect. Data have been fitted with the model of Eq. 6.10,

showing a very good agreement. From the fit, it was possible to infer the speed of the cavity and the storage time. The finesse has been obtained from the storage time using Eq. 6.6. The decay time for the north arm extrapolated from the fit in Fig. 6.4 is 0.0029 s corresponding to a finesse of 455.5 which is in agreement with what expected. The cavity speed was $2.37 \mu\text{m/s}$, which, as expected is above the threshold to observe the ringing effect.

The commissioning team on site have performed a similar analysis on a large number

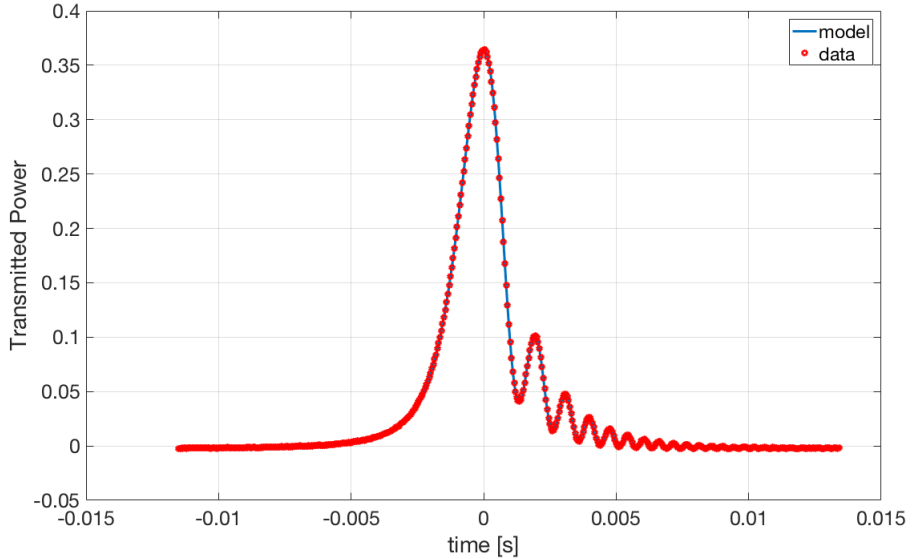


Figure 6.4: Transmitted power when the cavity crosses the resonance showing an evident ringing effect. Data are perfectly fitted by the model presented in Eq. 6.10

of peaks for both the arms finding a value of 467 ± 3 and 466 ± 3 (respectively for the north and west arm), where the error is the standard deviation of the measurements. This value is slightly above the error bar of the expected value (considering the etalon effect) and that obtained from the decay time measured.

6.2 Round trip losses

Photons traveling back and forth in the arm cavities can be absorbed by the mirrors, can fall out of the mirror if it is not large enough with respect to the beam or can be scattered by mirrors defects. The round trip losses in a Fabry-Perot cavity are defined via the energy conservation as [102]:

$$\Lambda_{rt}^2 = \frac{P_{in} - P_r - P_t}{P_{circ}} \quad (6.16)$$

where P_{in} is the input power, P_{circ} , P_t , P_r are the powers circulating in the cavity, transmitted and reflected, respectively. Losses should be as low as possible as they

reduce the Fabry-Perot reflectivities and the recycling gain accordingly. Moreover, an asymmetry between RTL of the two arms couples with frequency noise, resulting in a noise at the ITF output. The interest of performing RTL measurement goes beyond the simple verification that they are compliant with the requirement. As we will see in the third part of this thesis, RTL play a key role when squeezed light is used and strategies to precisely measures this quantity have been the subject of recent investigations. [100, 103].

Mirrors defects, responsible for most of the lost light are usually characterized by their spatial frequency.² Long-range surface defects are expected to couple the TEM₀₀ to higher-order modes. This kind of losses on the fundamental mode are not taken into account by the RTL definition given in Eq. 6.16, anyway differences between this formula and the round trip loss defined on the TEM₀₀ are expected to be negligible for Advanced Virgo mirrors as low order aberrations are extremely small [104].

Virgo RTL have been estimated to be about 330 ppm [105] while the requirement for Advanced Virgo has been set to 75 ppm.

How to measure round trip losses

Round trip losses affect different optical parameters such as the decay time, the finesse and the cavity reflectivity and in principle they can be extrapolated from them.

A practical way to extract losses from these quantities starts from the assumption that losses can be considered numerically equivalent to an increase in the end mirror transmission (which in our case is below 5 ppm) [106]:

$$r_2 = \sqrt{1 - T_2 - L} \simeq \sqrt{1 - L} \quad (6.17)$$

Since we are expecting to measure very low loss level the limiting factor in this kind of measurement is represented by the precision we can obtain.

For example in the case of finesse and decay time we have seen that the etalon effect is producing a variation up to 1.5% of their values. We can see from Fig. 6.5 that it corresponds to the variation induced by about 300 ppm of round trip losses and it is clear that a precise measurement of RTL below 100 ppm is not possible.

However we have shown in the previous section that the cavity reflectivity is slightly affected by the etalon effect and then it can be a good quantity from which to extract the losses.

The reflectivity of a the cavity at the resonance, with the approximation of Eq. 6.17 reads:

$$P_{\text{res}_n} = R_{\text{cav}} = \left[\frac{r_1 - r_2}{1 - r_1 r_2} \right]^2 \simeq \left[\frac{r_1 - \sqrt{1 - L}}{1 - r_1 \sqrt{1 - L}} \right]^2 \quad (6.18)$$

²Details about mirror defects characterization and their impact on RTL can be found in Sec. 8.2.

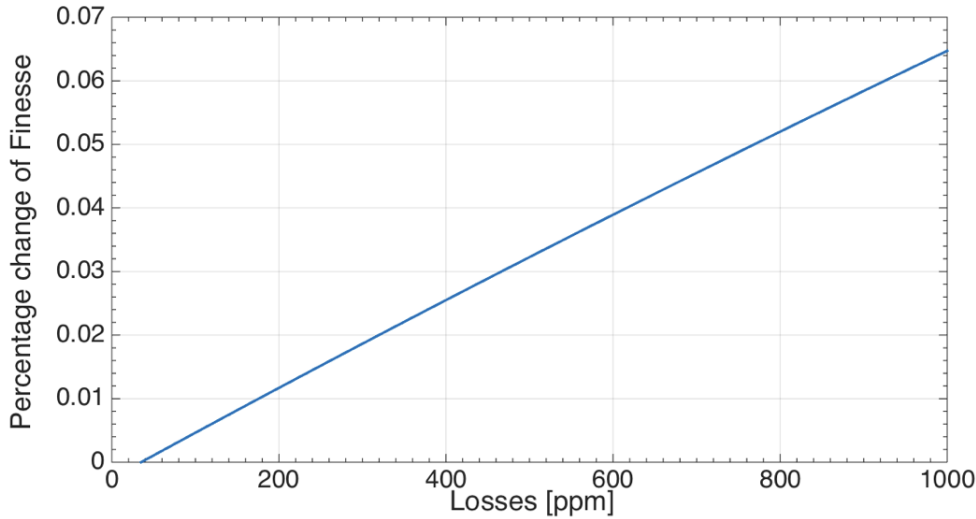


Figure 6.5: Percentage change in the Finesse induced by a change in RTL

where P_{res_n} is the reflected power on resonance normalized by the incident power P_{in} .

$$P_{\text{res}_n} = \frac{P_{\text{res}}}{P_{\text{in}}} \quad (6.19)$$

The incident power P_{in} can be measured in two ways:

- by measuring the reflected power when the cavity is out of resonance (since $T_2 \sim 0$).
- by misaligning the cavity end mirror and measuring the power reflected from the input mirror whose reflectivity is known.

The expected change in the cavity reflectivity induced by losses in Advanced Virgo cavities is plotted in Fig. 6.6. We see that for example a reduction of 3% in the reflectivity corresponds to 100 ppm of losses.

The equation 6.18 can be inverted and approximated to find

$$L = \frac{T_1}{2} \frac{1 - P_{\text{res}_n}}{1 + P_{\text{res}_n}} \quad (6.20)$$

The losses are measured by unlocking the cavities and recording the change in the reflected power. As can be seen from the optical scheme in Fig. 6.1 the reflected power is sensed by different photodiodes. The measurement is performed one arm at time, while the other is misaligned in order to avoid interference due to Michelson Fringes.

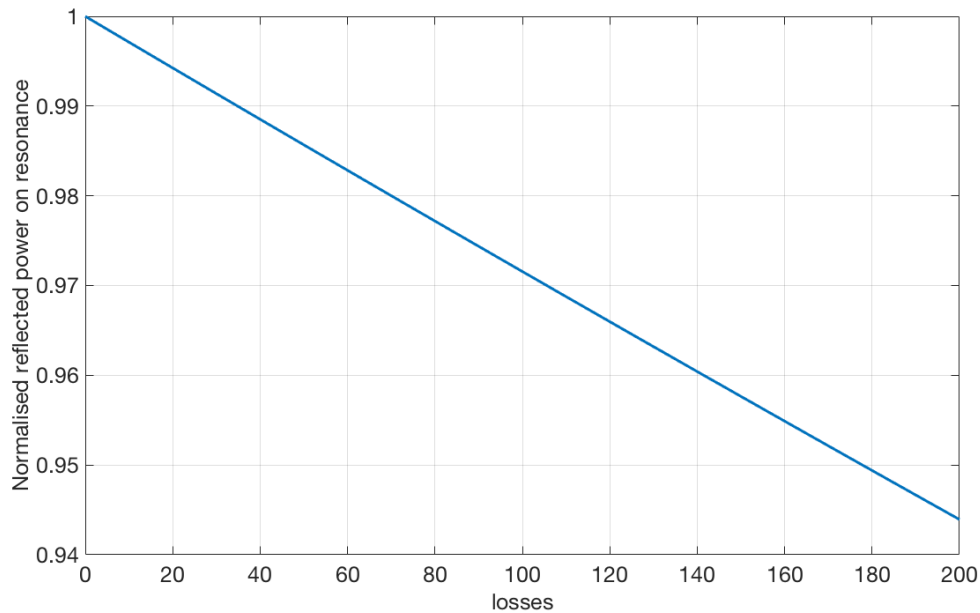


Figure 6.6: Change in the cavity reflectivity as a function of the round trip losses.

Possible issues affecting the measurement

If a part of the incoming power does not couple with the cavity (usually in presence of mismatching, misalignment or sidebands) it will be promptly reflected and will not experience losses. As a consequence, the reflectivity of the cavity on resonance will increase and the measured losses are reduced.

This effect has been confirmed by simulations but it is often unacknowledged. In fact, there is a general belief that the presence of mismatching or misalignment would increase the losses. This is probably due to the reasonable observation that a poor alignment will cause the beam to be not optimally centered on the mirrors and it will be more affected by clipping losses.

We have observed that a tilt and a shift of the beam with respect to the cavity axis, producing 20% of misalignment, bring to a displacement of the beam on the mirror of less than 3 cm and it corresponds to about 1 ppm of clipping losses. Thus we conclude that this effect is negligible [107].

Assuming that RTL associated to a cavity are those measured in perfect alignment and matching condition, we are interested in compensating the effect of not coupled power in our reflectivity measurement. In this general case, assuming that a fraction γ of the incoming power does not couple with the cavity, the reflected power at

resonance can be rewritten as:

$$P_{\text{res}}^\gamma = R_{\text{cav}} P_{\text{in}} (1 - \gamma) + \gamma P_{\text{in}} \quad (6.21)$$

$$\frac{P_{\text{res}}^\gamma}{P_{\text{in}}} = P_{\text{res}_n}^\gamma = R_{\text{cav}} (1 - \gamma) + \gamma \quad (6.22)$$

From the equation above we find:

$$\frac{P_{\text{res}_n}^\gamma - \gamma}{(1 - \gamma)} = R_{\text{cav}} \quad (6.23)$$

By comparing Eq. 6.23 and Eq. 6.18 we see that in presence of a fraction γ of non coupled incident power, the measured reflected power $P_{\text{res}_n}^\gamma$ has to be corrected before being used in Eq. 6.20 to compute the RTL, according to the following relation

$$P_{\text{res}_n} = \frac{P_{\text{res}_n}^\gamma - \gamma}{(1 - \gamma)} \quad (6.24)$$

Fig. 6.7 shows the deviation of the extrapolated losses from the real ones as a function of the mismatching, where the losses have been computed using simply the reflected power and the corrected reflected power, respectively. The plot has been obtained by simulating the arm cavity with the software *Finesse* and adding a known level of losses and mismatching. We see that using the corrected reflected power we can recover the true loss value.

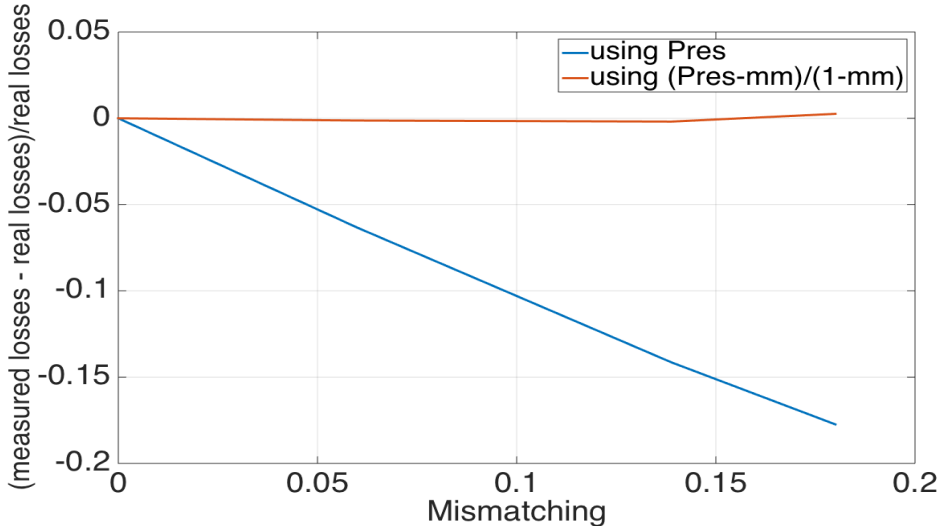


Figure 6.7: Difference between extrapolated losses and real ones as a function of the mismatching. Losses have been computed using the simple reflected power and the corrected reflected power, respectively. The plot has been obtained by simulating the arm cavity with the software *Finesse* and adding a known level of losses and mismatching.

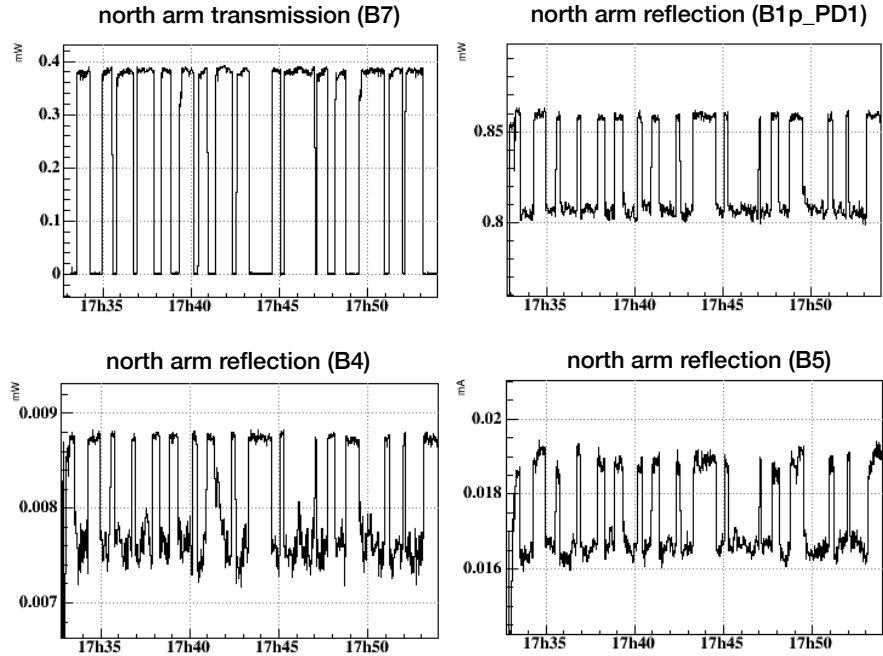


Figure 6.8: Set of lock-unlocks performed on the north arm, done to investigate a presumed excess of losses. B7 photodiode (top left plot) measures the transmission. The other photodiodes measure the reflection. Their disposition is shown in Fig. 6.1.

In practice, before performing the measurement the mismatching, misalignment and amplitude of sidebands are estimated (see Sec. 6.4) and their sum is used to correct the measured reflected power and infer the real loss value.

Measurements results

Arm cavity RTL have been measured four times, between 2016 and July 2017, each time by performing a series of lock-unlock. During the first measurement an excess of losses on the north arm was observed. It confirms the presence of a dust contamination on the north input mirror which was observed by eye as the scattered light recorded by a camera was much more intense than that scattered by other cavity mirrors [108]. The mirror has been dismounted, cleaned at LMA and resuspended. The change in reflectivity during the set of lock-unlock relative to this measurement are shown in Fig. 6.8. A summary of the results found is show in Tab. 6.2. The photodiodes used for the measurement, shown in Fig. 6.1, are

- **B1p** - located on the detection bench collects the reflection from the first face of the beam splitter.
- **B5** - located on the detection bench collects the reflection from the second face of the beam splitter (it sees only the north arm reflection).

PD	02/10/16		21/11/16		05/02/17		05/07/17	
	NArm (ppm)	WArm (ppm)	NArm (ppm)	WArm (ppm)	NArm (ppm)	WArm (ppm)	NArm (ppm)	WArm (ppm)
B1p (PD1)	210±15	75±6	76±5	81±5	63±3	69±3	N/A	N/A
B1p (PD2)	190±9	60±6	74±5	79±5	61±2	59±2	56±5	61±5
B4 (PD1)	490±50	200±100	248±35	256±35	N/A	N/A	N/A	N/A
B5 (PD1)	440±28	N/A	91±7	N/A	311±8	N/A	230±10	N/A

Table 6.2: Summary of the loss measurements seen from different photodiodes. Only the losses measured by B1p photodiodes are consistent with the upper limits set from the recycling gain measurement.

- **B4** - located on the suspended power recycling bench (SPRB) collects a pick-off of the reflected beam just before the power recycling mirror.

Normally each of them is composed of two photodiodes (PD1 and PD2) after a beam splitter but, at the time of the measurements, only B1p has the two photodiodes available.

We observed that results from different photodiodes are often not in agreement between each other.

Our conclusion are:

- Since an upper limit for the losses of 100 ppm has been set by the measurement of the recycling gain, photodiodes showing losses higher than this value have been considered not reliable.
- Photodiodes of B1p are the only ones showing consistent results over time, which are also compatible with upper limits. Therefore we tend to trust their results and conclude that the losses are in a range of 65-75 ppm, thus compliant with Advanced Virgo requirements.
- The origin of the discrepancy between observation from different photodiodes is not really understood. We suspect that it can be due to a not perfect centering of the beam on the photodiode combined with a change of the shape and the position of the beam between the lock and unlock state.

Comparison with expected losses

FFT simulation performed with measured mirror maps predicted a loss value between 10-15 ppm, as we will see in detail in Chap. 8 such simulations does not consider light scattered at angle larger than few mrad, which are induced by higher spatial frequency defects non included in the maps. Losses due to higher frequency spatial defects (usually known as *roughness*) can be measured from a scattering angle of few

degree and have been estimated to be ~ 10 ppm per mirror. Additional 5 ppm are added to account for mirror absorption and transmission. The total value for the expected losses is of about 35-40 ppm. That is roughly half of the measured losses. The same discrepancy between measured and expected losses has been observed in Advanced LIGO, which seems to confirm that some loss source is being neglected in our theoretical budget. Losses due to scattering at angles between mrad and a few degrees are being investigated as a possible cause of these differences[109].

6.3 G-factor

Mirror RoCs are chosen in order to have a stable cavity. The stability condition reads [110]

$$0 < \left(1 - \frac{L}{R_1}\right) \left(1 - \frac{L}{R_2}\right) < 1 \quad (6.25)$$

where the first and the second factor, indicated as g_1 and g_2 are referred to as *g-parameters*. The product $g = g_1 \cdot g_2$ determines the optical mode spectrum of the cavity, i.e the frequency (or length) separation between between the fundamental and the higher order modes:

$$\Delta L_{(m+n)} = \frac{FSR}{\pi} \arccos \sqrt{g} \quad (6.26)$$

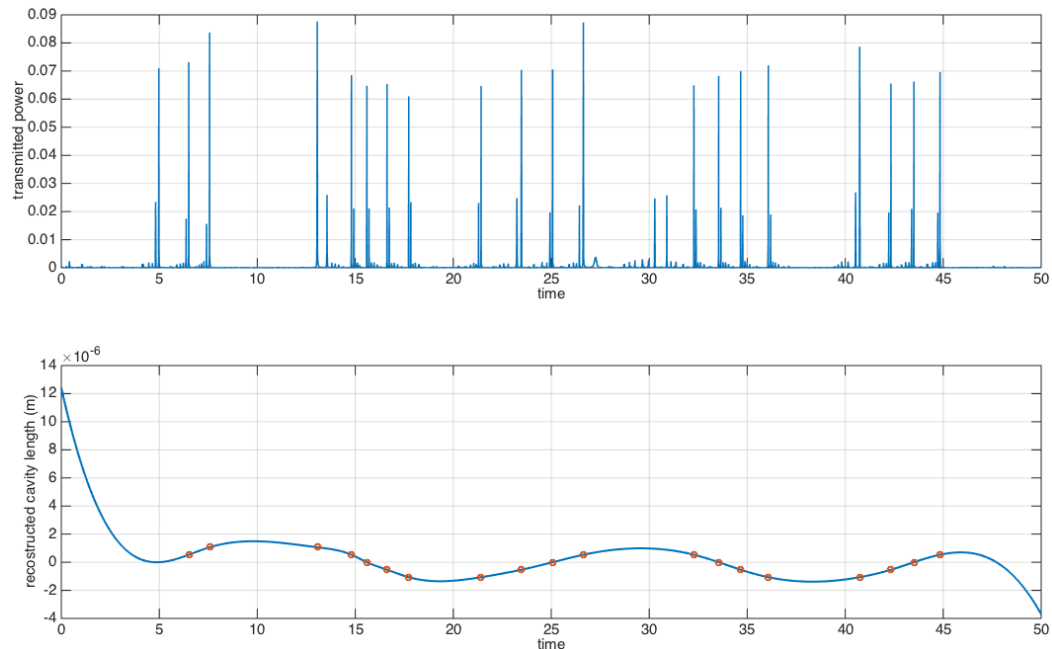


Figure 6.9: Transmitted power during a free swinging of the cavity shows the cavity optical spectrum (top plot). The evolution of the cavity length in time is reconstructed from the free swinging (bottom plot).

Fig. 6.9 shows a free swinging of the cavity (top plot) from which the cavity length variation has been reconstructed (bottom plot). We obtained the cavity g-factor by measuring the length difference between the fundamental and first higher order mode. For the north arm we found:

$$g_{na} = \left(\cos \left(\frac{\Delta L_1}{FSR} \right) \pi \right)^2 = 0.895 \pm 0.057 \quad (6.27)$$

which is consistent with the expected value of 0.851. For the west we found $g_{wa} = 0.86 \pm 0.01$, also consistent with the expected value of 0.850

6.4 Mismatching and misalignment

A cavity is said to be *misaligned* when the beam axis is tilted or shifted with respect to its axis. Small misalignment produces higher order modes whose amplitude with respect to the fundamental one depends on the level of misalignment. It can be shown that to the first order the power transferred on the first order HG modes respectively by a tilt $\Delta\theta$ and a shift $\Delta\alpha$ is [79]:

$$\frac{P_{HG_{10,01}}}{P_{00}} \sim \left(\frac{\Delta\theta}{\theta_0} \right)^2 \quad (6.28)$$

$$\frac{P_{HG_{10,01}}}{P_{00}} \sim \frac{\Delta\alpha^2}{w_0} \quad (6.29)$$

where $\theta_0 = \frac{\lambda}{\pi w_0}$ is the beam divergence and w_0 is the beam waist (See App. A). If the gaussian parameters (position and size of the waist) of the incoming beam are slightly different from those of the cavity eigenmode, the cavity and the beam are said to be *mismatched*. In this case, at the first order, the power is transferred on the Laguerre-Gauss mode with $l = 0$ and $p = 1$. Respectively for a size deviation Δw and position deviation Δz we have [79]:

$$\frac{P_{LG_{10}}}{P_{00}} \sim \left(\frac{\Delta w}{w_0} \right)^2 \quad (6.30)$$

$$\frac{P_{LG_{10}}}{P_{00}} \sim \frac{\Delta z^2}{2z_R} \quad (6.31)$$

$z_R = \pi w^2 / \lambda$ is the Rayleigh range.

The amount of mismatching and misalignment is measured by comparing the height of the fundamental mode peak in transmission with those of the first and second order modes.³ An example of the measurement is shown in Fig. 6.10 where the transmitted power during a free swinging of the cavity has been plotted. We measured a mismatching of $\sim 9\%$ and a misalignment of $\sim 7\%$. In general the arm cavities can be aligned in order to make the first order mode completely disappear while

³The LG₁₀ mode resonates at the same frequency of the second order HG modes

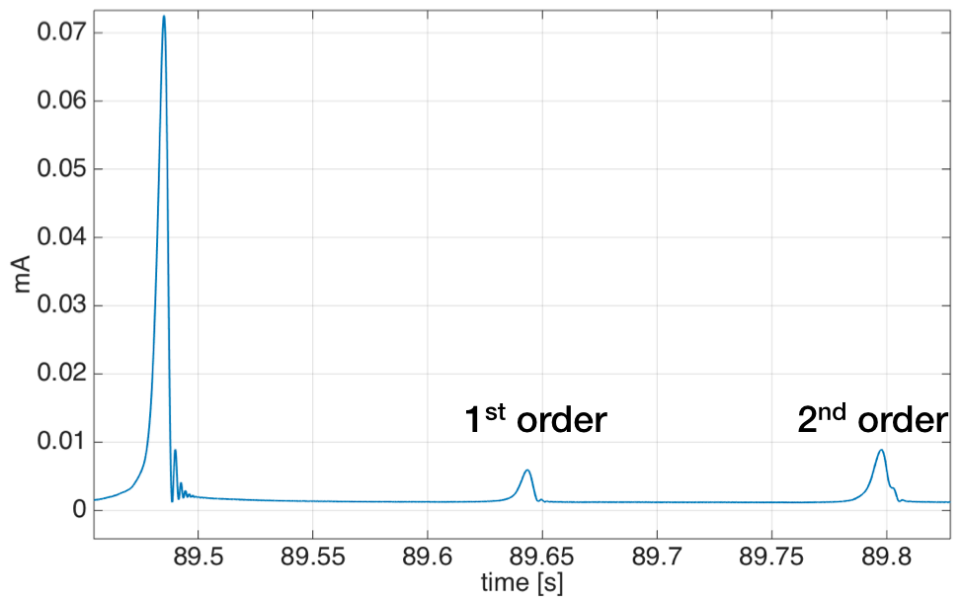


Figure 6.10: A part of the cavity spectrum in transmission, showing the fundamental model together with the first and second order modes. Cavity mismatching and misalignment are computed from peak relative heights.

the mismatching has been reduced up to $\sim 1.6\%$ by a fine tuning of the injection telescope.

Conclusions - Part II

In this part we have presented the work done in the context of Advanced Virgo commissioning. Such intense commissioning activity succeeded in making Advanced Virgo sensitivity good enough (~ 27 Mpc for BNS inspiral range) to join Advanced LIGO in its second observation run. The joint data taking culminated with the first three detector BBH merging observation and the first GW detection from a binary neutron star merger.

I contributed both to the laser noise analysis and to the arm cavities optical characterization. In the following I summarize the main results and lessons learnt.

Injection system frequency noise

As detailed in Chap. 5, laser frequency is pre-stabilized using as reference the input mode cleaner and a rigid reference cavity. My activity was focused on the identification and reduction of the noise limiting the frequency stability. The main steps and results of this activity can be summarized as follows:

- We have realized a complete noise budget for the reference cavity error signal.
- From this noise budget we have compute the frequency noise injected in the ITF.
- We have automated the noise budget computation in order to make it a useful tool for the noise hunting.
- This activity contributed to reduce the frequency noise level until it met the requirement of 1 Hz RMS, allowing a reliable lock of the arm cavities.
- Finally, we compared the estimated frequency with that measured by the arm cavity, finding a good agreement.

Arm cavities optical characterization

The goal of this activity was to study the optical performances of the arms cavities. Even if the cavity mirrors have already been characterized during their production, polishing and coating, is the "in situ" characterization which has the final word. The results of this activity can be can be summarized as follows:

- We have verified that the finesse, g-factor, roundtrip losses, mismatching and misalignment of the arm cavities were compliant with the requirements.
- Particular attention was dedicated to the measurement of round trip losses for two reasons. First, as it will be shown in the next part of the thesis, the measurement of cavity losses is extremely interesting in relation with the use of squeezed light for quantum noise reduction. Second, since a discrepancy of about a factor two has been observed in Advanced LIGO between measured and simulated losses, this suggested that some loss sources could have been neglected in the estimation. The results we obtain from Advanced Virgo confirmed this discrepancy.
- We used the cavity reflectivity to compute round trip losses and we present a technique to compensate the effects of mismatching and misalignment on the measurement.
- Discarding results from photodiodes considered not reliable, we found a value between 65-75 ppm for the round trip losses. Even if it is the double of what it is expected from simulations, this is, to our knowledge, among the lowest value of RTL per unity length ever measured.⁴

⁴We will see in Sec. 8.4 that the RTL per unity length is the relevant quantity to be consider for the estimation of the degrading effect of the losses on the squeezing.

Part III

Filter cavity for frequency dependent squeezing production

Context and motivations

As already observed in the previous chapters, quantum noise is limiting second generation gravitational-wave detectors in a large fraction of their spectrum.

In Sec. 2.2 we gave a description of the two manifestation of quantum noise i.e. shot noise and radiation pressure noise, in a semiclassical picture. In 1981, Caves pointed out that both of them are originated by vacuum fluctuations entering the interferometer by the beam splitter anti-symmetric port [24]. Caves also proposed the injection of squeezed vacuum from the dark port as a strategy to decrease quantum noise without modifying the interferometer configuration.

Following Caves' results, in the following section we introduce a completely quantum formalism to describe vacuum squeezed states: in such states the amplitude and phase uncertainty, equally distributed in an ordinary vacuum, are modified in order to reduce one at the expense of the other. A squeezed state can be intuitively represented as an ellipse in the quadrature plane and it is characterized by the ratio of its axes (squeezing magnitude) and by its orientation (squeezing angle). Both of these parameters are functions of the Fourier frequency. If the quadrature with the reduced uncertainty is aligned with the gravitational-wave signal, the SNR is improved with respect to that achievable with an ordinary vacuum. Since the optomechanical coupling of the laser light with the interferometer test masses induces a rotation of the squeezing ellipse, the injection of a squeezed vacuum with constant squeezing angle, referred to as *frequency-independent squeezed vacuum* can reduce quantum noise only in the part of the spectrum where the gravitational-wave signal is aligned with the quadrature with reduced uncertainty. Effectiveness of squeezing in reducing shot noise has been successfully tested on LIGO [111] and it is routinely used in GEO [112].

In Fig. 6.11, the quantum noise reduction achievable by injecting frequency independent and frequency dependent squeezing is shown. We observe that using phase quadrature squeezing we can only reduce the high frequency quantum noise, that is the one dominated by shot noise while we increase the noise in the radiation pressure region. This effect is similar to the one achievable by increasing the laser power.

A broadband quantum noise reduction can be obtained by injecting a squeezed vacuum with an angle that varies with frequency, in such a way that the signal and the reduced noise quadrature are always aligned. This frequency-dependent squeezing can be obtained by reflecting off a frequency-independent squeezed state by a detuned Fabry-Perot filter cavity. In order to obtain a high level of frequency-dependent squeezing two kinds of difficulties have to be tackled. First, the squeezing angle should undergo a rotation in the frequency region where quantum noise switches from radiation pressure noise to shot noise (usually below 100 Hz). We will see in the following that this requires a filter cavity with a very long storage time of the order of ~ 3 ms. Moreover, the presence of optical losses reduces the squeezing factor,

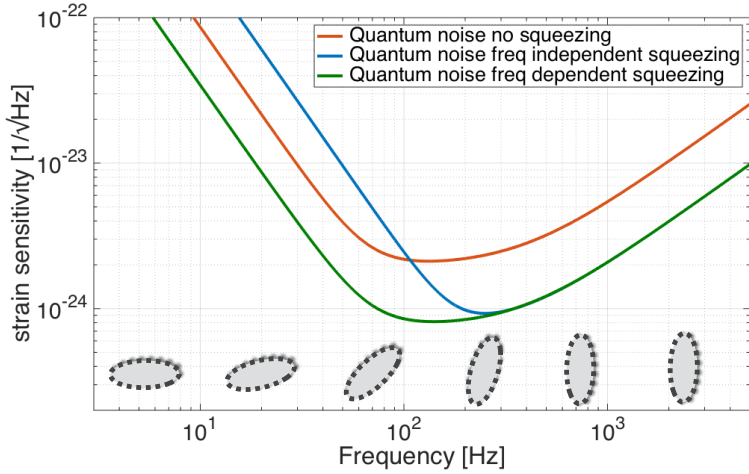


Figure 6.11: Quantum noise improvement achievable by injecting respectively 9 dB of frequency independent phase squeezing (blue line) and frequency dependent squeezing (green line). In the first case the improvement is only at high frequency while at low frequency noise is increased. In the second case a broadband noise reduction is achieved. In all the three cases the laser power is the same. In the bottom, it is shown the optimal squeezing ellipse rotation at the frequency region where the transition between radiation pressure and shot noise takes place.

since losses are associated with ordinary vacuum fluctuations that couple with the squeezed states reducing their squeezing level.

The rotation of the squeezing angle has been experimentally demonstrated in the MHz region [113] and, more recently, in the kHz region [114]. In the following chapters we present the work done on the development of a 300 m filter cavity at National Astronomical Observatory of Japan (NAOJ), using one arm of the former TAMA interferometer. The aim of the project is to demonstrate the feasibility of frequency dependent squeezing with rotation angle of ~ 70 Hz by using a 100 m scale filter cavity. In Chap. 7 we introduce the formalism necessary to describe squeezed states and compute quantum noise in the interferometer. Then we use it to show the improvement achievable by using frequency independent squeezing and compute the features of the filter cavity needed to obtain optimal results. In the following chapter we will discuss the optical design for the 300 m filter cavity at NAOJ. Since the project is mainly intended to test a technology to be implemented in a future upgrade of KAGRA,⁵ the filter cavity parameters are optimized for its features. Anyway the interest of this work goes beyond KAGRA, since a 100 m class filter cavity is also a possible solution for a medium-term upgrade of Advanced Virgo [115] and even

⁵The injection of frequency-dependent squeezing is particularly suitable in this context since increasing laser power to reduce shot noise can be difficult due to the cryogenic temperature of the detector. Moreover, since thermal noise is low enough to make quantum noise the main noise contribution in almost the whole spectrum, the reduction of quantum noise would have a direct and significant effect on the detector sensitivity.

longer filter cavities are planned for the third generation detector Einstein Telescope [116]. In Chap. 8, we present the study we have performed to design the cavity and in particular the simulation done in order to set requirements for the mirror quality, to avoid excessive squeezing degradation. This study is accompanied by an analysis of different mechanisms known to spoil squeezing in the system. We present a complete squeezing degradation budget based on the work of Kwee et al. [117]. On the basis of these results we discuss the advantages of using long filter cavities and show the expected improvement in KAGRA sensitivity. We also compare the performances of long filter cavity with those of a recently proposed technique which aims to exploit EPR entanglement to achieve a broadband quantum noise reduction. Finally, in Chap. 9 we present in detail the experiment design and the experimental work performed to integrate and lock the cavity.

CHAPTER 7

Frequency dependent squeezing in the two-photon formalism

In this chapter we present the proper formalism to give a completely quantum description of quantum noise. We will introduce two-photon formalism and use it to compute quantum noise in interferometer and its possible reduction using squeezed vacuum. Finally, again with this formalism, we describe the squeezing angle rotation produced on a squeezed state reflected by a filter cavity and the broadband quantum noise reduction achievable with such frequency dependent squeezed state.

7.1 Quantization of the electromagnetic field

Interferometric measurements are ultimately limited in a large fraction of the spectrum by the quantum nature of the light used to sense the mirror position¹. Therefore the starting point for developing the appropriate formalism to deal with this noise is the quantization of the electromagnetic field. This is achieved, as explained in detail in [119], by performing a Fourier expansion in terms of mode functions of the field and interpreting the coefficients of each term of such expansion as a quantum operator, thus imposing commutation relations on them. The resulting Hamiltonian for the electromagnetic field can be written as

$$H = \sum_k \hbar\omega_k \left(\hat{a}^\dagger \hat{a} + \frac{1}{2} \right) \quad (7.1)$$

where \hat{a}^\dagger and \hat{a} which are ladder operators for quantum harmonic oscillator, represent here the creation and annihilation operator of a photon with wave vector k . As for quantum harmonic oscillators we can introduce the quadrature operators \hat{p}_k and \hat{q}_k (which are simply the momentum and the position of the k -th oscillator). They are

¹It has been demonstrated by Braginsky et al. [118] that noise in gravitational-wave detectors is not influenced by quantization of the test masses.

non commuting observables defined as

$$\hat{p}_k = \frac{\hat{a}_k - \hat{a}_k^\dagger}{i\sqrt{2}} \quad \hat{q}_k = \frac{\hat{a}_k + \hat{a}_k^\dagger}{\sqrt{2}} \quad (7.2)$$

thus they are respectively proportional to the real and to the imaginary part of the complex operator \hat{a}

$$\hat{a}_k = \frac{1}{2}(\hat{q}_k + i\hat{p}_k) \quad (7.3)$$

Once we choose a phase reference, they can be regarded as the in-phase and out-of-phase components of the field amplitude.

7.2 Quantum states of light

Quantization of the electromagnetic field is responsible for the introduction of quantum noise as a direct consequence of the uncertainty principle. In the following we will present some different representations of quantum light states paying special attention to their quantum noise features.

7.2.1 Fock states

The Hamiltonian 7.1 is proportional to the number operator $\hat{N}_k = \hat{a}_k \hat{a}_k^\dagger$ which is the observable counting the photons with wavevector k . Fock states, or number states, are defined as eigenstates of the Hamiltonian.

$$H|n\rangle = \frac{1}{2} \sum_k \hbar\omega_k n_k |n\rangle \quad (7.4)$$

The vacuum state is defined as

$$\hat{a}_k |0\rangle = 0 \quad (7.5)$$

We are particularly interested in studying the noise features of the vacuum state $|0\rangle$ which can be deduced from the wave equation $\psi(q)$. Combing Eq. 7.1 and 7.2 we find the relation

$$\hat{a}|0\rangle = \left(q + \frac{\partial}{\partial q} \right) \phi(q) = 0 \quad (7.6)$$

which is verified by

$$\psi(q) = \frac{1}{\sqrt[4]{\pi}} \exp\left(-\frac{q^2}{2}\right) \quad (7.7)$$

An analogous relation holds for $\psi(p)$, using the momentum representation. The variance of the two quadrature operators, both with mean equal to zero, is

$$\Delta q^2 = \langle \psi | q^2 | \psi \rangle - \langle \psi | q | \psi \rangle^2 = \int \frac{1}{\sqrt{\pi}} q^2 \exp(-q^2) dq = \frac{1}{2} \quad (7.8)$$

$$\Delta q^2 = \langle \psi | p^2 | \psi \rangle - \langle \psi | p | \psi \rangle^2 = \int \frac{1}{\sqrt{\pi}} p^2 \exp(-p^2) dq = \frac{1}{2} \quad (7.9)$$

We see that even in a zero-photon state, there is a fluctuation in the quadratures of the vacuum field. Such fluctuation stems from the Heisenberg uncertainty principle for non-commuting operators and it is the smallest possible allowed:

$$\Delta q^2 \Delta p^2 = \frac{1}{4} \quad (7.10)$$

7.2.2 Coherent states

Coherent states are the most appropriate states to give a quantum description of laser light as their amplitude and phase are simultaneously defined as precisely as possible². We start by defining a displacement operator [119]

$$D(\alpha) = \exp(\alpha \hat{a}^\dagger - \alpha * \hat{a}) \quad (7.11)$$

where $\alpha = |\alpha| e^{i\theta}$ is a complex number. The displacement operator takes its name from the fact that it produces a displacement of the annihilation operator \hat{a} of a complex quantity α :

$$D^\dagger(\alpha) \hat{a} D(\alpha) = \hat{a} + \alpha \quad (7.12)$$

A coherent state $|\alpha\rangle$ is created applying the displacement operator to the vacuum state $|0\rangle$:

$$|\alpha\rangle = D(\alpha)|0\rangle \quad (7.13)$$

If we represent the vacuum state as an *error circle* centered in the origin of the quadrature space, a coherent state $|\alpha\rangle$ can be seen as a translation of such a state described by a vector with length $|\alpha|$ and direction θ . Since the translation does not modify the shape of the vacuum error circle, we can have an intuitive idea of the fact that a coherent state shares the same noise features of the vacuum state. Therefore it has equally distributed quadrature fluctuations whose product is the lowest possible allowed by Heisenberg principle. Fig. 7.1 shows a schematic representation in the quadrature planes of a coherent state obtained by applying the displacement operator to the vacuum state. Coherent states are eigenvalue of the annihilation operator \hat{a}

$$\hat{a}|\alpha\rangle = \alpha|\alpha\rangle \quad (7.14)$$

It is also interesting to see what happens if we project a coherent state in an eigenstate of the number operator $|n\rangle$

$$\langle n|\alpha\rangle = \frac{\alpha^n}{\sqrt{n!}} e^{-\frac{1}{2}|\alpha|^2} \quad (7.15)$$

²In a Fock state the number of photons is well defined but the phase is completely random.

from this we see that the probability distribution for the number of photons of a coherent state is a Poissonian with mean and variance equal to $|\alpha|^2$

$$P_n = \frac{|\alpha|^{2n}}{n!} e^{-\frac{1}{2}|\alpha|^2} \quad (7.16)$$

It can also be shown that the wave function for the two orthogonal quadrature of a coherent state is a Gaussian and that this is true for every state that has the product of their fluctuation in the two quadrature the lowest possible.

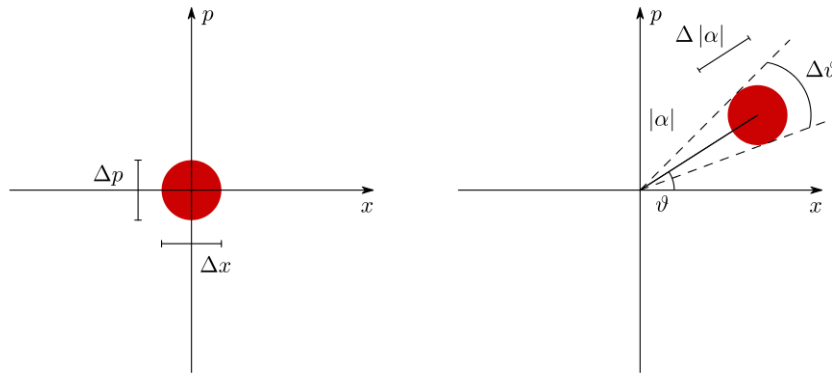


Figure 7.1: A coherent state in the optical phase space, obtained by applying the displacement operator to a vacuum state.

7.2.3 Squeezed state

So far we have treated coherent states, observing that they are minimum uncertainty state whose incertitude is equally distributed between their two quadratures. We can get rid of the last condition and consider a larger category of minimum uncertainty state allowing for the two uncertainties to be different.

It is clear that, in this case, a reduction of the noise in a quadrature will cause an enhancement of the noise in the other one, in order to be still compliant with Heisenberg limit. This asymmetry results in a *squeezing* of the error circle. Note that usually a squeezed state is defined as a state where fluctuations in one quadrature are lower than in coherent states. This does not necessarily mean that the uncertainty is the minimum possible. We define the squeezing operator as [119]:

$$S(\epsilon) = \exp \left(\frac{1}{2} \epsilon^* \hat{a}^2 - \frac{1}{2} \epsilon^* \hat{a}^\dagger 2 \right) \quad (7.17)$$

The squeezed state $|\alpha, \epsilon\rangle$ is obtained by applying the squeezing operator to the vacuum state and later the displacement operator

$$|\alpha, \epsilon\rangle = D(\alpha)S(\epsilon)|0\rangle \quad (7.18)$$

The squeezing parameter is defined as

$$\epsilon = re^{2i\phi} \quad (7.19)$$

where r accounts for the degree of squeezing and ϕ for its direction. Figure 7.2 shows a schematic representation in the quadrature planes of a squeezed state obtained by applying the displacement operator to a vacuum squeezed state.

The variance of a generic quadrature q_θ is

$$\Delta q_\theta^2 = \cosh(2r) - \sinh(2r) \cos[2(\phi - \theta)] \quad (7.20)$$

It is important to stress that the ellipse normally used to give an intuitive two-dimension representation of a squeezed state in the quadrature plane can be formally defined by introducing the Wigner function [119]. This is a quasi-probability distribution which can be used to derive separately the probability distributions of the two non-commuting quadratures (or a linear combination of them). The error circles (respectively a circle for coherent states and ellipses for squeezed one) are obtained by cutting the Wigner function surface with an horizontal plane at a half of the maximal height. Even if these representations are useful to picture intuitively the noise properties of these states, only distributions obtained by integrating the Wigner function with respect to one of the two variables can be regarded as probability distributions.

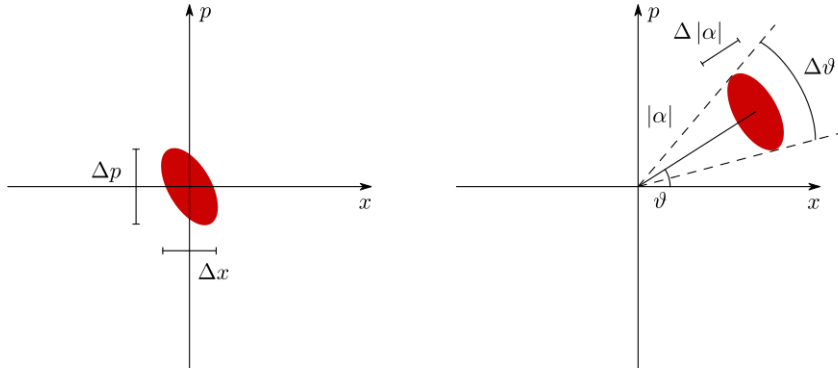


Figure 7.2: Representation of a squeezed state in the quadrature planes obtained by applying the displacement operator to a vacuum squeezed state.

7.3 Two-photon formalism

A laser beam can be described as a classical carrier at frequency ω_0 surrounded by small quantum fluctuations. In a vacuum state the classical field is zero and only the fluctuations are left. The positive-frequency part of the electric field can be written

as [120]:

$$E^+ = \sqrt{\frac{2\pi\hbar\omega_0}{Ac}} \int_0^\infty (\hat{a}_\omega e^{-i\omega t}) \frac{d\omega}{2\pi} \quad (7.21)$$

where A is the effective area of the beam and \hat{a}_ω is the annihilation operator of each mode, which verifies the following commutation relations

$$[\hat{a}_\omega, \hat{a}_{\omega'}] = 0 \quad [\hat{a}_\omega, \hat{a}_{\omega'}^\dagger] = 2\pi\delta(\omega - \omega') \quad (7.22)$$

In order to express the field as a sum of sidebands at a distance Ω from the carrier much smaller than ω_0 we can define the operators

$$\hat{a}_+ \equiv \hat{a}_{\omega_0+\Omega} \quad \hat{a}_- \equiv \hat{a}_{\omega_0-\Omega} \quad (7.23)$$

and the relative commutation relations

$$[\hat{a}_+, \hat{a}_{+'}^\dagger] = 2\pi\delta(\Omega - \Omega') \quad [\hat{a}_-, \hat{a}_{-'}^\dagger] = 2\pi\delta(\Omega - \Omega') \quad (7.24)$$

In terms of these sidebands operators the electric field writes

$$E^+ = \sqrt{\frac{2\pi\hbar\omega_0}{Ac}} e^{-i\omega_0 t} \int_0^\infty (\hat{a}_+ e^{-i\Omega t} + \hat{a}_- e^{+i\Omega t}) \frac{d\omega}{2\pi} \quad (7.25)$$

Interactions of the field with squeezers or suspended cavities, which are central in our work, produce correlations between upper and lower sidebands. For this reason it is useful to describe the field in terms of two-photon modes instead of single-photon modes. It also allows us to interpret these fluctuations in terms of phase and amplitude quadratures uncertainty. The annihilation and creation operators of these two-photon, introduced for the first time by Caves and Shoemaker in [121, 122] are defined as

$$\hat{a}_1 = \frac{\hat{a}_+ + \hat{a}_-^\dagger}{\sqrt{2}} \quad \hat{a}_2 = \frac{\hat{a}_+ - \hat{a}_-^\dagger}{\sqrt{2i}} \quad (7.26)$$

and satisfy the following commutation relations (with the approximation $\frac{\Omega}{\omega_0} \simeq 0$)

$$[\hat{a}_1, \hat{a}_{2'}^\dagger] = -[\hat{a}_2, \hat{a}_{1'}^\dagger] = i2\pi\delta(\Omega - \Omega') \quad (7.27)$$

$$[\hat{a}_1, \hat{a}_{1'}] = [\hat{a}_1, \hat{a}_{1'}^\dagger] = [\hat{a}_{1'}^\dagger, \hat{a}_{1'}^\dagger] = [\hat{a}_1^\dagger, \hat{a}_{2'}^\dagger] = [\hat{a}_1, \hat{a}_{2'}] = 0 \quad (7.28)$$

We can rewrite the electric field $E(t)$ in terms of these two-photon operators:

$$E = \sqrt{\frac{2\pi\hbar\omega}{Ac}} \left[\cos(\omega_0 t) \int_0^\infty (\hat{a}_1 e^{-i\Omega_0 t} + \hat{a}_1^\dagger e^{+i\Omega_0 t}) \frac{d\omega}{2\pi} \right. \quad (7.29)$$

$$\left. + \sin(\omega_0 t) \int_0^\infty (\hat{a}_2 e^{-i\Omega_0 t} + \hat{a}_2^\dagger e^{+i\Omega_0 t}) \frac{d\omega}{2\pi} \right] \quad (7.30)$$

We observe that \hat{a}_1 and \hat{a}_2 are the field amplitude of the $\cos(\omega_0 t)$ quadrature and $\sin(\omega_0 t)$ quadrature respectively. Electric field in terms of quadratures writes

$$E(\hat{a}_{1,2}, t) = \cos(\omega_0 t)E_1(a_1, t) + \sin(\omega_0 t)E_2(a_2, t) \quad (7.31)$$

with

$$E_{1,2} = \sqrt{\frac{2\pi\hbar\omega}{Ac}} \int_0^\infty (\hat{a}_{1,2} e^{-i\Omega_0 t} + \hat{a}_{1,2}^\dagger e^{+i\Omega_0 t}) \frac{d\Omega}{2\pi} \quad (7.32)$$

7.4 Homodyne detection of squeezed states of light

In order to characterize squeezed states, measuring their noise at different quadratures, the balanced homodyne detection technique is currently used. Application of this technique to squeezed states has been proposed for the first time in 1983 by Yuen and Chan [123]. It uses a 50:50 beamsplitter to make the squeezed beam interfere with a reference beam, called *local oscillator*, which has the same frequency and tunable phase shift ϕ .

The two beams entering the beamsplitter can be respectively written

$$\hat{a} = \alpha + \delta\hat{a} \quad \hat{b} = (\beta + \delta\hat{b})e^{i\phi} \quad (7.33)$$

where α and β represent the carrier and $\delta\hat{a}$ and $\delta\hat{b}$ represent the continuum of fluctuating modes surrounding it. Here we used a *linearized approach*, since the fluctuations are supposed to be small enough to allow neglecting those of second order and above. Here the beam quadratures are defined as $\delta\hat{X}_1^a = \delta\hat{a}^\dagger + \delta\hat{a}$ and $\delta\hat{X}_2^a = i(\delta\hat{a}^\dagger + \delta\hat{a})$.

The beams at the beamsplitter output

$$\hat{c} = \frac{1}{\sqrt{2}}(\hat{a} + \hat{b}) \quad \hat{d} = \frac{1}{\sqrt{2}}(\hat{a} - \hat{b}) \quad (7.34)$$

are sensed by two photodiodes producing the photo-currents $I_1 \propto \hat{c}^\dagger \hat{c}$ and $I_2 \propto \hat{d}^\dagger \hat{d}$. If we compute the difference between the two photocurrents $I_1 - I_2$, neglecting higher order fluctuations and assuming that the local oscillator (LO) is much brighter than the signal field (thus neglecting terms containing α), we find

$$I_1 - I_2 \simeq \beta(\cos(\phi)\delta\hat{X}_1^a + \sin(\phi)\delta\hat{X}_2^a) = \beta\delta\hat{X}_\phi^a \quad (7.35)$$

We see that the signal fluctuation in the quadrature \hat{X}_ϕ^a are amplified proportionally to the amplitude of the LO and at the same time the LO noise is suppressed. Moreover by shifting the additional phase of the LO it is possible to select the quadrature to measure.

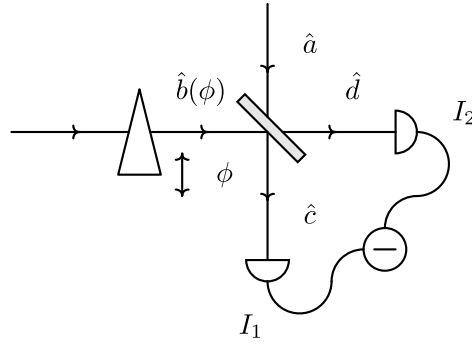


Figure 7.3: Scheme of the homodyne detection.

7.5 Input output relations

The two-photon formalism is particularly effective to describe the propagation of electromagnetic fields and relative quantum fluctuations in optical systems [124]. The two quadrature fields $\hat{a}_1(\Omega)$ and $\hat{a}_2(\Omega)$ are chosen as basis vector

$$\bar{\mathbf{i}} = \begin{pmatrix} \hat{a}_1(\Omega) \\ \hat{a}_2(\Omega) \end{pmatrix} \quad (7.36)$$

Optical elements such as movable mirrors, beam splitters, squeezers and free space propagation are described by appropriate matrices which applied to the input quadrature vector will produce an output quadrature vector encoding the effect of the interaction with each element. More optical elements can be combined in order to describe complex systems. This formalism has been extensively used to compute quantum noise of the interferometer in different configurations [120, 125, 126]. Noise spectral density S_h can be obtained from the input-output relation connecting the input fields and the gravitational-wave signal to the output field:

$$\bar{\mathbf{o}} = \mathbf{T}\bar{\mathbf{i}} + \mathbf{s}h \quad (7.37)$$

Where $\bar{\mathbf{s}}$ is the signal transfer function connecting a gravitational wave strain h to the output (also know as interferometer response) and \mathbf{T} is the transfer function for the input vacuum field $\bar{\mathbf{i}}$. In this simple case we have only considered the vacuum field entering the beam-splitter dark port. The (single sided) noise spectral density is [125, 127]

$$S_h = \frac{\begin{pmatrix} \cos \zeta & \sin \zeta \end{pmatrix} \mathbf{T} \mathbf{S} \mathbf{T}^\dagger \begin{pmatrix} \cos \zeta \\ \sin \zeta \end{pmatrix}}{\begin{pmatrix} \cos \zeta & \sin \zeta \end{pmatrix} \bar{\mathbf{s}} \bar{\mathbf{s}}^\dagger \begin{pmatrix} \cos \zeta \\ \sin \zeta \end{pmatrix}} \quad (7.38)$$

where the output field is projected on the homodyne field vector $(\cos \zeta \sin \zeta)$ and where \mathbf{S} is the noise spectral-density matrix for the input amplitude and phase quadratures \hat{a}_1 and \hat{a}_2 defined by the relation [120]

$$\langle \hat{a}_i(\Omega) \hat{a}_j^\dagger(\Omega') \rangle_{\text{sym}} = \pi S_{ij}(\Omega) \delta(\Omega - \Omega') \quad i, j = 1, 2 \quad (7.39)$$

For non-squeezed input vacuum, where amplitude and phase noise are uncorrelated, \mathbf{S} is the identity matrix.

Two-photon squeezing operator

The effect of a squeezer on a vacuum field expressed in the two-photon formalism can be described by a squeezing operator $\mathbf{S}(\mathbf{r}, \phi)$, providing the following input-output relation:

$$\bar{\mathbf{o}} = \mathbf{S}(\mathbf{r}, \phi) \bar{\mathbf{i}} = \mathbf{R}(-\phi) \mathbf{S}(\mathbf{r}, \mathbf{0}) \mathbf{R}(\phi) \bar{\mathbf{i}} \quad (7.40)$$

where

$$R(\phi) = \begin{pmatrix} \cos \phi & \sin \phi \\ -\sin \phi & \cos \phi \end{pmatrix} \quad S(r) = \begin{pmatrix} e^r & 0 \\ 0 & e^{-r} \end{pmatrix} \quad (7.41)$$

The quadrature at angle ϕ is squeezed by a factor e^{-r} and the orthogonal one is antisqueezed by a factor e^r .

Interferometer transfer matrix

Optomechanical coupling of vacuum fluctuations with the interferometer test masses induces correlations between phase and amplitude quadrature. The transfer matrix has the form [126]

$$\mathbf{T}_{\text{itf}} = \begin{pmatrix} 1 & 0 \\ -K(\Omega) & 1 \end{pmatrix} \quad (7.42)$$

The parameter $K(\Omega)$, which characterizes such coupling, is defined as

$$K(\Omega) = \left(\frac{\Omega_{\text{SQL}}}{\Omega} \right)^2 \frac{\gamma_{\text{itf}}^2}{\Omega^2 + \gamma_{\text{itf}}^2} \quad (7.43)$$

where γ_{itf} is the interferometer bandwidth with signal recycling and Ω_{SQL} is the approximate frequency at which radiation pressure noise switches to shot noise.

$$\Omega_{\text{SQL}} = \left[\frac{t_{\text{sr}}}{1 + r_{\text{sr}}} \right] \frac{8}{c} \sqrt{\frac{P_{\text{arm}} \omega_0}{m T_{\text{arm}}}} \quad (7.44)$$

$$\gamma_{\text{ifo}} = \left[\frac{1 + r_{\text{sr}}}{1 - r_{\text{sr}}} \right] \frac{T_{\text{arm}} c}{4 L_{\text{arm}}} \quad (7.45)$$

where t_{sr} and r_{sr} are the signal recycling mirror amplitude transmissivity and reflectivity, P_{arm} is the intracavity power, T_{arm} is the arm cavity input mirror power transmissivity, ω_0 is the angular frequency of the carrier field, m is the mirror mass.

It is interesting to notice that the interferometer transfer matrix can be written as a combination of squeezing and rotation operators:

$$\mathbf{T}_{\text{itf}} = \mathbf{S}(\mathbf{r}_{\text{itf}}, \phi_{\text{itf}}) \mathbf{R}(\theta_{\text{itf}}) \quad (7.46)$$

with

$$\begin{aligned} r_{\text{itf}} &= -\operatorname{arcsinh}(K/2) \\ \phi_{\text{itf}} &= \frac{1}{2} \operatorname{arccot}(K/2) \\ \theta_{\text{itf}} &= -\operatorname{arctan}(K/2) \end{aligned}$$

The input output relation for a broadband, tuned dual-recycled interferometer is given by [126]:

$$\begin{pmatrix} \hat{o}_1 \\ \hat{o}_2 \end{pmatrix} = e^{2i\phi} \begin{pmatrix} 1 & 0 \\ -K(\Omega) & 0 \end{pmatrix} \begin{pmatrix} \hat{a}_1 \\ \hat{a}_2 \end{pmatrix} + e^{i\phi} \begin{pmatrix} 0 \\ \sqrt{2K(\Omega)} \end{pmatrix} \frac{h(\Omega)}{h_{\text{SQL}}} \quad (7.47)$$

which can be used with Eq. 7.38 to find the quantum noise spectral density:

$$S_h = \frac{h_{\text{SQL}}^2}{2} \left[K(\Omega) + \frac{1}{K(\Omega)} \right] \geq h_{\text{SQL}}^2 = \frac{8\hbar}{m\Omega^2 L^2} \quad (7.48)$$

The first term, coming from the fluctuation of the input amplitude quadrature \hat{a}_1 , represents the radiation pressure component which is directly proportional to the optical power. The second term, coming from the fluctuation of the input phase quadrature \hat{a}_2 , represents the shot noise part of the quantum noise which is inversely proportional to the optical power.

If we assume to inject a squeezed state at the beam splitter dark port, we find the following input-output relation

$$\bar{\mathbf{o}} = \mathbf{S}(\mathbf{r}_{\text{itf}}, \phi_{\text{itf}}) \mathbf{R}(\theta_{\text{itf}}) \mathbf{S}(\mathbf{r}, \phi) \bar{\mathbf{i}} + \bar{\mathbf{s}} h$$

which corresponds to a noise spectral density

$$S_h = \frac{\begin{pmatrix} \cos \zeta & \sin \zeta \end{pmatrix} \mathbf{T}_{\text{itf}}(K) \mathbf{R}(-\phi) \mathbf{S}(2r, 0) \mathbf{R}(\phi) \mathbf{T}_{\text{itf}}^\dagger(K) \begin{pmatrix} \cos \zeta \\ \sin \zeta \end{pmatrix}}{\begin{pmatrix} \cos \zeta & \sin \zeta \end{pmatrix} \bar{\mathbf{s}} \bar{\mathbf{s}}^\dagger \begin{pmatrix} \cos \zeta \\ \sin \zeta \end{pmatrix}} \quad (7.49)$$

It can be shown that the minimum noise is achieved by tuning the frequency dependence of the squeezing angle in order to select always the quadrature with the

minimum noise. In this case we have

$$S_h = e^{-2r} \frac{\sum_n \begin{pmatrix} \cos \zeta & \sin \zeta \end{pmatrix} \mathbf{T} \mathbf{T}^\dagger \begin{pmatrix} \cos \zeta \\ \sin \zeta \end{pmatrix}}{\begin{pmatrix} \cos \zeta & \sin \zeta \end{pmatrix} \bar{\mathbf{s}} \bar{\mathbf{s}}^\dagger \begin{pmatrix} \cos \zeta \\ \sin \zeta \end{pmatrix}} \quad (7.50)$$

which corresponds to an overall reduction of the quantum noise without squeezing of a factor e^{-2r} . The required frequency dependence for the squeezing angle is

$$\phi = \arctan(K) - \cot(\zeta) \quad (7.51)$$

This means that since input field quadratures are rotated (and squeezed) by the interferometer, the squeezing angle of the injected squeezed vacuum should also rotate in order to counteract this effect, keeping the reduced noise quadrature always aligned with the gravitational-wave signal.

7.5.1 Filter cavity in the two-photon formalism

In the previous section we have shown that an optimal quantum noise reduction is achievable by injecting frequency dependent squeezed state with a proper rotation angle to compensate that induced by the reflection from the ITF.

Kimble et al. in 2001 [120] proposed for the first time to impress such frequency dependence by filtering the standard frequency-independent squeezed state using a detuned high-finesse Fabry-Perot cavity. In this case, only quantum fluctuations which lie in the cavity bandwidth enter the cavity and experience a dephasing, those outside are promptly reflected and are not affected by it. In order to impart a proper quadrature rotation, the cavity has to be kept detuned from the resonance. This produces an asymmetry for the reflectivity seen by upper and lower sidebands which results in a frequency dependent quadrature rotation. The effect of such a rotation depends only on the pole γ_{fc} and on the detuning $\Delta\omega_{\text{fc}}$ of the cavity. It can be obtained from the formula of the reflectivity in a Fabry-Perot cavity (Eq. 2.50) and in the two photon formalism, assuming a lossless cavity, it reads [120, 125]

$$\bar{\mathbf{o}} = e^{i\alpha_m} \mathbf{R}(\alpha_p) \bar{\mathbf{i}} \quad (7.52)$$

where the rotation angle is

$$\alpha_p = \arctan \left(\frac{2\gamma_{\text{fc}}\Delta\omega_{\text{fc}}}{\gamma_{\text{fc}}^2 - \Delta\omega_{\text{fc}}^2 + \Omega^2} \right) \quad (7.53)$$

In the frequency region interested by the rotation we have $\Omega \ll \gamma_{\text{itf}}$, and we can approximate the optomechanical parameter of Eq. 7.43 as $K \simeq \left(\frac{\Omega_{\text{SQL}}}{\Omega} \right)^2$. With this approximation, cavity pole and detuning have to be chosen in order to satisfy Eq.

7.51 are:

$$\Delta\omega_{\text{fc}} = \gamma_{\text{fc}} = \frac{\Omega_{\text{SQL}}}{\sqrt{2}} \quad (7.54)$$

For second generation gravitational-wave detectors the transition frequency between radiation pressure noise and shot noise is typically of the order of $2\pi \cdot 70$ Hz. The correspondent storage time is ³

$$t_{\text{st}} = \frac{1}{\gamma_{\text{fc}}} = \frac{\sqrt{2}}{\Omega_{\text{SQL}}} \simeq 3 \text{ ms} \quad (7.55)$$

As discussed in [114], this is an extremely long storage time, comparable with the longest ever achieved [114, 128].

7.5.2 Squeezing degradation due to optical losses

In a quantum description of an optical system, quantum fluctuations are expected to enter even unused ports (as in the case of the beam splitter dark port in the interferometer). Moreover, every time that the beam experiences a loss in the system, we have to take into account a vacuum fluctuation entering at the lossy point. We can conveniently model the loss as the effect of a beam splitter. We see that taking into account the vacuum fluctuation is the only way to preserve commutation relations. In fact if we imagine to write a naive input-output relation for a state experiencing a loss (with power attenuation η) as

$$\hat{a}_{\text{out}} = \sqrt{\eta} \hat{a}_{\text{in}} \quad (7.56)$$

we see that commutation relations cannot be verified:

$$[\hat{a}_{\text{out}}, \hat{a}_{\text{out}}^\dagger] = \eta [\hat{a}_{\text{in}}, \hat{a}_{\text{in}}^\dagger] \neq 1 \quad (7.57)$$

By modeling the process with a beam splitter where one of the two input is a vacuum field \hat{w}_{in} (see figure 7.4) we find

$$\begin{pmatrix} \hat{a}_{\text{out}} \\ \hat{w}_{\text{out}} \end{pmatrix} = \begin{pmatrix} \sqrt{\eta} & -\sqrt{(1-\eta)} \\ \sqrt{(1-\eta)} & \sqrt{\eta} \end{pmatrix} \begin{pmatrix} \hat{a}_{\text{in}} \\ \hat{w}_{\text{in}} \end{pmatrix} \quad (7.58)$$

and the commutation relations are now verified:

$$[\hat{a}_{\text{out}}, \hat{a}_{\text{out}}^\dagger] = \eta [\hat{a}_{\text{in}}, \hat{a}_{\text{in}}^\dagger] + (1-\eta)[\hat{a}_{\text{in}}, \hat{a}_{\text{in}}^\dagger] = 1 \quad (7.59)$$

If the beam experiencing loss is a squeezed one, the recombination with standard coherent vacuum causes a degradation of the squeezing feature of the beam. A realistic estimation of the quantum noise improvement achievable by injecting vacuum

³Here the cavity pole γ_{fc} is expressed in radians, i.e with an additional factor of 2π with respect to the definition in 2.56.

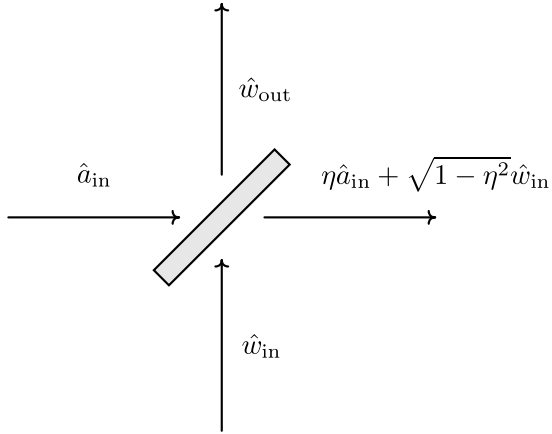


Figure 7.4: The loss process represented by a beam splitter where coherent vacuum fluctuations recombines with fluctuations of the beam experiencing the loss.

squeezing has to take into account the effect of losses on its path. For each loss, a coherent vacuum field has to be considered. The propagation of each of them through the system to the detector output is described by an appropriate transfer matrix. The input-output relation 7.37 will assume the more general form [129]

$$\bar{\mathbf{o}} = \sum_n \mathbf{T}_n \bar{\mathbf{i}}_n + \bar{s} h \quad (7.60)$$

where $\bar{\mathbf{i}}_n$ are the coherent vacuum fluctuations entering the dark port and those associated to each loss in the path and \mathbf{T}_n are the respective transfer matrices. This relation can be used in Eq. 7.38 to compute the quantum noise spectral density.

In the following there is a summary of the main points presented in this chapter:

- We defined vacuum squeezed states and introduced the two-photon formalism to describe amplitude and phase fluctuations and their modifications induced by interaction with optical systems. Such modifications are conveniently expressed in terms of linear input-output relations. Each part of the optical system is modeled by a two-photon operator (or transfer matrix) that has to be applied to the quadrature vector representing amplitude and phase fluctuation.
- From the input-output relations which connect vacuum fluctuations entering the beam splitter dark port to the detector output, it is possible to compute the quantum noise spectrum of the interferometer.
- A description of squeezing in terms of two-photon operator is given. We observed that injecting a squeezed vacuum in the beam splitter dark port we can modify quantum noise spectrum. In particular, it can be minimized imposing a specific frequency dependence of the squeezing angle, which is a function of

the interferometer parameters.

- We observed that such frequency dependence can be impressed by reflecting the squeezed vacuum off a filter cavity with a bandwidth which depends on the interferometer parameters. The cavity has to be operated in a detuned configuration (at half of the cavity bandwidth).
- The physical insight of this mechanism is presented: interferometer produces a rotation of the vacuum quadrature fluctuations entering the dark port, which becomes evident when they are no more equally distributed, as in the case of a squeezed state. Because of this rotation, the noise reduced quadrature of a frequency independent squeezed state is not always aligned with the signal. Filter cavity can be used to impress a counter-rotation to the squeezed state, allowing to have it optimally oriented at all frequencies.

CHAPTER 8

Filter cavity optical design

Frequency rotation of the squeezing angle by means of a filter cavity has been demonstrated in the MHz region, for the first time by Chelkowski et al in 2005. [113]. They used a filter cavity of 0.5 m with a linewidth of 1.47 MHz. In 2015 Oelker et al. [114] achieved a lower rotation frequency of about 1.2 kHz using a 2 m long cavity with a Finesse of about 30000. The filter cavity project a NAOJ aims to further reduce the rotation frequency up to about 70 Hz, which is the frequency required for optimal quantum noise reduction in second generation gravitational wave detectors. This is particularly challenging as it requires to achieve a very long cavity storage time (~ 3 s). The project, started in 2015, makes use of the south arms of former TAMA interferometer at NAOJ to accommodate a 300 m filter cavity. It also aims to demonstrate for the first time the operation of a 100 m scale filter cavity.

In this chapter we presented the design of the filter cavity. Since squeezing is easily degraded by losses, the cavity design has to be studied in order to reduce them as much as possible. One of the main loss sources is due to the light scattered by mirror surface imperfections. We present the study done in order to set requirement for the mirror quality, based on real mirror maps, used in Virgo. Moreover, a crucial point is to compare the squeezing degradation from the filter cavity optical losses with that originated by other mechanisms. Thus, we present a complete squeezing degradation budget for the 300 m cavity, based on the work by Kwee et al. [117]. We discuss the advantages of using long filter cavities and the expected improvement of KAGRA sensitivity produced by the implementation of this technology. Recently a new technique relying on EPR entanglement has been proposed to obtain of frequency dependent squeezing using the interferometer itself as a filter cavity. We briefly present it and compare their performance with those of a long filter cavity.

8.1 Choice of cavity parameters

As pointed out in Sec. 7.5.1, the main filter cavity features (linewidth and detuning) have to be determined in order to provide an angular frequency dependence given by

$$\theta_{fc}(\Omega) = \arctan(K(\Omega)) \quad (8.1)$$

with K being the frequency dependent optomechanical coupling defined in 7.43. K depends on the interferometer bandwidth γ_{itf}^2 and on Ω_{SQL} , the frequency marking the transition between radiation pressure noise and shot noise. As we have already seen in Eq. 7.44, in a dual recycled interferometer, with a tuned signal-recycling cavity, these two terms write:

$$\Omega_{SQL} = \left[\frac{t_{sr}}{1 + r_{sr}} \right] \frac{8}{c} \sqrt{\frac{P_{arm}\omega_0}{mT_{arm}}} \quad (8.2)$$

$$\gamma_{ifo} = \left[\frac{1 + r_{sr}}{1 - r_{sr}} \right] \frac{T_{arm}c}{4L_{arm}} \quad (8.3)$$

where t_{sr} and r_{sr} are the signal recycling mirror amplitude transmissivity and reflectivity, P_{arm} is the intracavity power, T_{arm} is the arm cavity input mirror power transmissivity, ω_0 is the angular frequency of the carrier field, m is the mirror mass. For KAGRA, using the parameters shown in Tab. 8.1, we have:

$$\Omega_{SQL} \simeq 2\pi \times 76.4 \text{ Hz} \quad (8.4)$$

and

$$\gamma_{ifo} = 2\pi \times 382 \text{ Hz} \quad (8.5)$$

We observed that in the region interested by the rotation $\Omega \ll \gamma_{ifo}$ and Eq. 7.43 can be simplified to obtain:

$$\theta_{fc}(\Omega) = \arctan \left(\frac{\Omega_{SQL}}{\Omega} \right)^2 \quad (8.6)$$

Parameter	Symbol	Value
Carrier field frequency	ω_0	$2\pi \times 282 \text{ THz}$
Standard quantum limit frequency	Ω_{SQL}	$2\pi \times 76.4 \text{ Hz}$
Arm input mirror transmissivity	T_{arm}	0.004
Signal recycling input transmissivity	t_{sr}^2	0.1536
Intracavity power	P_{arm}	400 kW
Mirror mass	m	22.8 kg

Table 8.1: Values and symbols for KAGRA interferometer parameters.

The required the bandwidth γ_{fc} and the detuning $\Delta\omega_{fc}$ of a lossless filter cavity

are those already found in Eq. 7.54. In the presence of losses, the bandwidth and the detuning can be optimized as [117]

$$\gamma_{\text{fc}} = \sqrt{\frac{2}{(2-\epsilon)\sqrt{1-\epsilon}}} \frac{\Omega_{\text{SQL}}}{\sqrt{2}} \quad (8.7)$$

$$\Delta\omega_{\text{fc}} = \gamma_{\text{fc}} \sqrt{1-\epsilon} \quad (8.8)$$

where ϵ is a function of the filter cavity round trip losses Λ_{rt}^2 , the free spectral range $f_{\text{FSR}} = c/2L_{\text{fc}}$ and Ω_{SQL} :

$$\epsilon = \frac{4}{2 + \sqrt{2 + 2\sqrt{1 + \left(\frac{2\Omega_{\text{SQL}}}{f_{\text{FSR}}\Lambda_{rt}^2}\right)^4}}} \quad (8.9)$$

Given a filter cavity with fixed length and losses, we can compute the parameter ϵ using Eq. 8.9. Then, using Eq. 8.7 and 8.8, we obtain the optimal bandwidth and detuning. Finally, in order to compute the cavity finesse, we can write the bandwidth γ_{fc} of a Fabry-Perot cavity in terms of the losses, length and input mirror transmissivity t_{in}^2 :

$$\gamma_{\text{fc}} = \frac{t_{\text{in}}^2 + \Lambda_{rt}^2}{2} f_{\text{FSR}} \quad (8.10)$$

Inverting the previous equation, we can finally compute t_{in}^2 which determines the cavity finesse. Considering losses Λ_{rt}^2 of 80 ppm (a value which will be justified in the following section), we found $\epsilon = 0.111$ and $\gamma_{\text{fc}} = 2\pi \times 57.3$. The optimal detuning will be $\Delta\omega_{\text{fc}} = 2\pi \times 54 \text{ Hz}$ and $t_{\text{in}}^2 = 0.0014$, corresponding to a finesse of 4480. We highlight the fact that for Λ_{rt}^2 up to ~ 700 ppm, the value of the finesse is almost independent of the cavity losses.

Mirrors dimension and radius of curvature (RoC)

In order to reduce the losses due to the finite size of the mirrors, known as *clipping losses*, we require the size of the beam to be as small as possible. As shown in [103], this is also the best way to reduce the effects of large-scale mirror defects. The smallest beam radius on the mirrors is obtained in the so called confocal configuration, where radii of curvature are equal to the cavity length. Nevertheless this configuration is marginally stable. We choose radii $\sim 400 \text{ m}$, reasonably larger than 300 m , to avoid cavity instability. The exact value of the RoC has been determined using numerical simulations, described in the following section, in order to minimize the losses. For a 300 m cavity with two mirrors with a RoC of 400 m , the beam diameter at the waist and on the mirrors is respectively 0.0162 m and 0.0205 m . In order to be able to reuse the mirror suspension developed for TAMA, we have chosen mirrors with a diameter of 0.1 m (as done in TAMA). They are roughly five time bigger than

the beam radius and the resulting clipping losses are completely negligible. The filter cavity parameters are reported in Tab. 8.2

Parameter	Symbol	Value
Length	L	300 m
Radius of curvature	RoC	variable
Mirror diameter	d	0.1 m
Input mirror transmissivity	t_{in}^2	0.0014
Finesse	F	4480
Beam diameter at waist(RoC 400 m)		0.0162 m
Beam diameter at the mirror(RoC 400 m)		0.0205 m

Table 8.2: Filter cavity parameters.

8.2 Requirements on mirror quality

Mirror defects, namely deviations of the mirror surface from a perfect spherical one, are described by the *mirror map*, which is a square matrix of n elements with $n = l_{\text{mir}}/\text{res}$, where l_{mir} is the length of the surface described, and res is the resolution of the map. Each matrix element, corresponding to a pixel with area res^2 , contains a measure of the mirror surface height h (with respect to a perfect spherical one).

We can associate to each mirror map (or to a part of it) the Root Mean Square (RMS) of the height, defined as:

$$\sigma_{\text{RMS}} = \sqrt{\frac{1}{n} \sum_{i=1}^n (h_i - \bar{h})^2} \quad \text{with} \quad \bar{h} = \sum_{i=1}^n h_i \quad (8.11)$$

Another useful number to quantify surface flatness is the peak-to-valley value (PV): a measure of the difference between the highest and the lowest point.

Mirror defects can be studied in the spatial frequency domain by applying a 2D Fourier transform to the mirror map. The lowest spatial frequency f_{\min} coincides with the inverse of l_{mir} , while the maximum spatial frequency f_{\max} is given by $1/(2 \cdot \text{res})$. A 1D Power spectral density (PSD) can be associated with the 2D Fourier transform map [130]. For such a 1D PSD we have the relation:

$$\sigma_{\text{RMS}}^2 = \int_{f_{\min}}^{f_{\max}} \text{PSD}(f) df \quad (8.12)$$

The low frequency defects, those which have a spatial frequency up to 10^3 m^{-1} , contribute to the so-called *mirror flatness* while higher frequency defects are associated with the *mirror roughness*. This distinction has no fundamental physical motivation,

but it is simply due to different techniques used to measure spatial defects in the two cases [131].

The scattering angle for light at normal incidence of wavelength λ can be written as a function of the frequency of spatial defects as [132]:

$$\theta = \lambda \times f \quad (8.13)$$

This equation means that a defect at spatial frequency f will scatter a fraction of the light at angles θ or larger. As a consequence, the amount of light reflected back at normal incidence will be reduced by the same amount. This fraction is given by $(4\pi \times \sigma(f)/\lambda)^2$ where $\sigma(f)$ is the amplitude of the defect at spatial frequency f .

For a given cavity length L and mirror diameter d , there is a maximum scattering angle θ_{limit} above which light is scattered out of the cavity:

$$\theta_{\text{limit}} = \frac{d}{2L} \quad (8.14)$$

Using Eq. 8.13 and 8.14 we can then find a spatial frequency f_{limit} for the mirror defects above which the light is scattered out of the cavity:

$$f_{\text{limit}} = \frac{d}{2L \times \lambda} \quad (8.15)$$

From the equation above, the losses due to defects with spatial frequency above f_{limit} can be estimated as [132]:

$$\text{losses}_{(f > f_{\text{limit}})} = \left(\frac{4\pi \times \sigma}{\lambda} \right)^2 \quad (8.16)$$

where σ is the RMS for frequencies above f_{limit} . For the filter cavity we are considering $f_{\text{limit}} = 157 \text{ m}^{-1}$.

It is important to note that the RMS for frequencies lower than f_{limit} also contributes to losses. In fact, even if light is not immediately scattered out of the cavity, it is likely to be transferred on higher order modes and eventually exit the cavity. Our goal is to estimate the amount of loss induced by mirror with a known flatness in order to set specifications on flatness needed to keep losses below a desired threshold. The round trip losses in a Fabry-Perot cavity are defined as [102]:

$$\Lambda_{rt}^2 = \frac{P_{in} - P_r - P_t}{P_{circ}} \quad (8.17)$$

where P_{in} is the input power (which is assumed to be a fundamental mode), P_{circ} , P_t , P_r are the powers circulating in the cavity, transmitted and reflected, respectively. Since we can only take advantage of the light reflected on the fundamental mode,

the definition of Eq. 8.17 has been modified to:

$$\Lambda_{rt}^2 = \frac{P_{in} - P_r^{00}}{P_{circ}} \quad (8.18)$$

where P_r^{00} is the fraction of the reflected power which is on the fundamental mode. We used the MATLAB package OSCAR [133] to perform a FFT simulation of the cavity (where we used real mirror maps) to compute the values of P_{circ} and P_r^{00} to be used in Eq. 8.18. We ran the simulation using five different measured mirror maps, for mirrors used in Virgo. Four of these mirrors were produced for the initial Virgo with a standard polishing technology. The fifth has been produced for Advanced Virgo and is by using an ion beam polishing technique. The Virgo maps have a resolution of about $350\text{ }\mu\text{m}$, while the Advanced Virgo map has a resolution of $378.4\text{ }\mu\text{m}$. One example of the Virgo maps and the Advanced Virgo map are shown in Fig. 8.1 along with their relative PSD. The cavity parameters used in the simulation are those reported in Tab. 8.2. The maps were only applied to the end mirror, while the input mirror has been considered perfect. We checked that the round trip losses for a cavity where both the mirrors have defects can be obtained by simply multiplying by two the previous result. Results presented here have already been multiplied by two.

Each surface has been characterized by its RMS and its PV over different diameters. The measured values are reported in Tab. 8.3. Round trip losses for the various mirrors have been calculated as a function of the radius of curvature and are reported in Fig. 8.2. The losses floor for each mirror has also been reported in the last column of Tab. 8.3 in order to be directly compared with the mirror flatness.

The presence of peaks in the plots of Fig. 8.2 is due to power transferred to higher order modes which are partially resonant along with the fundamental mode for certain values of the curvature radius.

Maps used in the simulation account for mirror defects with spatial frequency going from $10\text{ }m^{-1}$ to $2 \cdot 10^3\text{ }m^{-1}$. This means that losses caused by mirror roughness are not included in this estimation. A map of the roughness has been measured with an optical profilometer for the Advanced Virgo mirror [131]. This map, obtained by scanning an area of $0.3\text{ mm} \times 0.3\text{ mm}$ with a resolution of $1.28\text{ }\mu\text{m}$, scans frequencies from $3.3 \cdot 10^3$ to $3.9 \cdot 10^5\text{ }m^{-1}$. From its RMS, under the assumption that it is uniform on the surface, we can estimate additional losses due to roughness, which should be added to those already estimated using the flatness measurement. The RMS is 0.08 nm, which corresponds to 0.89 ppm of additional losses for a single reflection. For the initial Virgo mirrors, the specification on the roughness RMS was 0.1 nm which corresponds to 1.4 ppm of additional losses for a single reflection. In both cases the losses are dominated by flatness defects. The roughness map for Advanced Virgo and the relative PSD are shown in Fig. 8.3. The measurement of the light scattered at angles larger than a few degrees gives losses of the order of 5 ppm [134]. These

	diameter 0.10 m		diameter 0.05 m		diameter 0.02 m		diameter 0.01 m		
Mirror	RMS (nm)	PV (nm)	RMS (nm)	PV (nm)	RMS (nm)	PV (nm)	RMS (nm)	PV (nm)	Losses (ppm)
V1	2.617	15.95	1.424	9.46	0.687	6.04	0.558	5.38	57.8
V2	1.875	15.64	1.234	8.56	0.682	6.29	0.812	5.92	80.6
V3	2.499	15.34	1.360	10.51	0.754	4.31	0.430	3.31	39.8
V4	1.752	45.61	0.984	12.12	0.509	4.46	0.531	4.46	42.6
ADV	0.319	2.99	0.274	2.09	0.192	1.18	0.142	0.97	5.6

Table 8.3: RMS and PV (over different diameters) and the round trip losses floor for each mirror map. The values indicated for the losses correspond to the floor of Fig. 8.4.

include both the losses due to the roughness discussed above and those due to point defects. The corresponding additional round-trip losses will be $2 \cdot 5 = 10$ ppm. As observed in Sec. 6.2, even including all these effects, still a difference exists between the measured losses in Advanced LIGO and Advanced Virgo and simulation results. Hypothetical losses due to scattering at angles between mrad and a few degrees (proposed as a possible explanation) are not included in this budget.

The conclusions of this study are that, for our filter cavity (length 300 m, mirror diameter 10 cm, RoC ~ 400 m):

- An Advanced Virgo-class mirror will produce floor losses < 10 ppm and a Virgo-class mirror will produce losses $\sim 40 - 80$ ppm. In order to determine the final specifications on the mirror flatness, the squeezing degradation given by the cavity losses has to be compared to the other degradation mechanisms. This analysis is performed in the following section.
- The accidental degeneracy can amplify the losses by more than an order of magnitude. The simulation gives the *safe* regions, where the losses are at the floor level.
- The precise RoC value should be chosen in some of the floor losses regions for the RoC value.
- A precision on the RoC of $\sim 1\%$ is necessary to guarantee the RoC to be in these regions.

obt

Mirror dimensions

Choosing the best mirror dimension is not as straightforward as it may seem to be. The scattering mechanisms described in the previous paragraph show that bigger mirrors have lower levels of losses. In fact, we see from Eq. 8.15 that by increasing

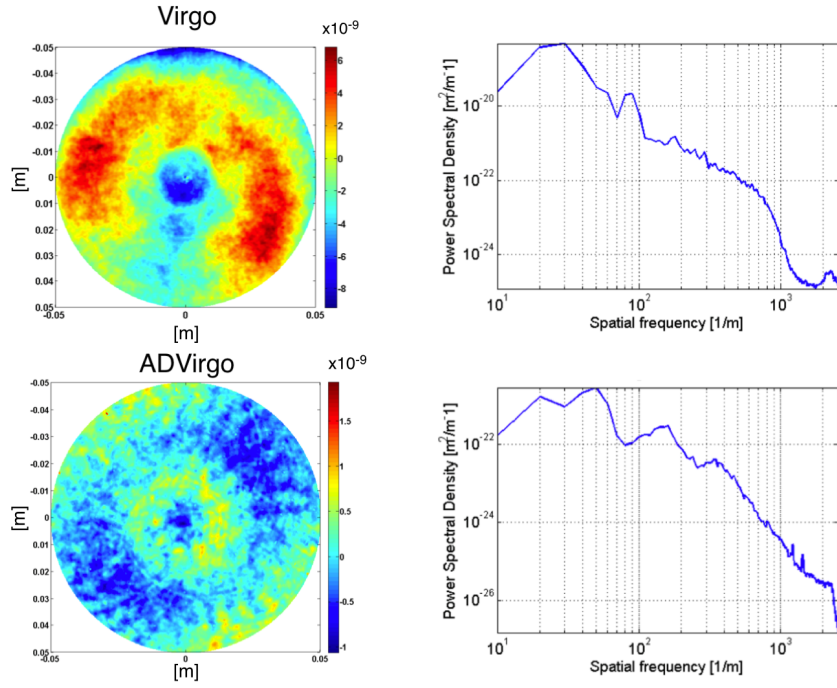


Figure 8.1: Initial Virgo map (top) and Advanced Virgo map (bottom). Mirrors maps (left), PSD (right).

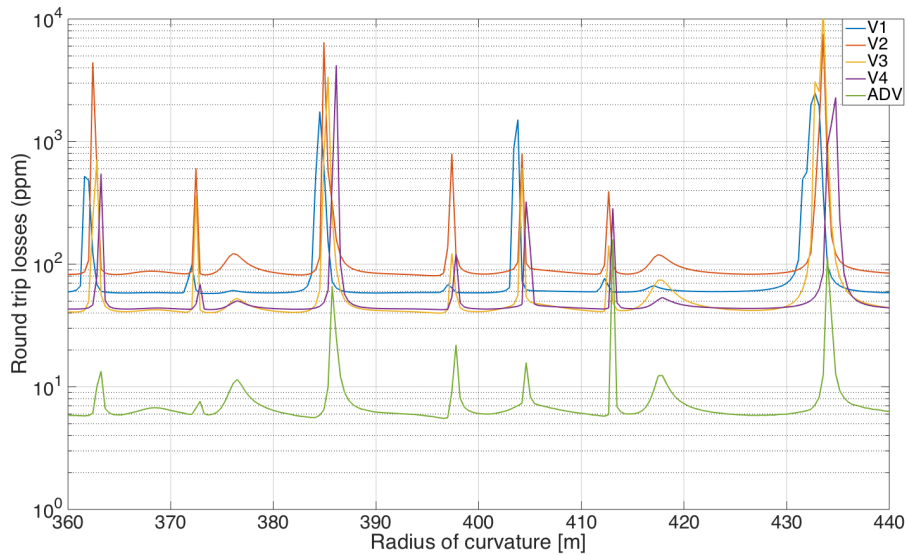


Figure 8.2: Round trip losses as a function of the radius of curvature. Peaks correspond to values of RoC for which the cavity is quasi-degenerate.

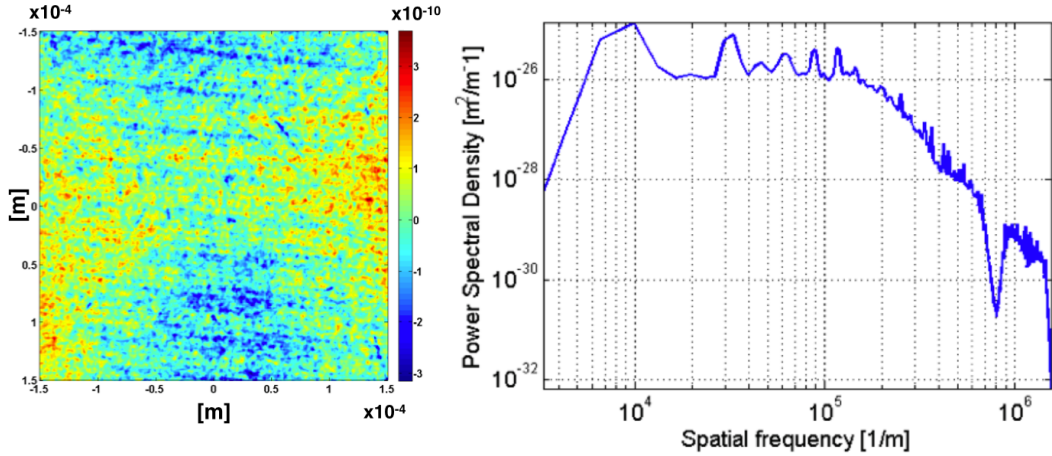


Figure 8.3: Roughness maps for the Advanced Virgo configuration. Mirror map (left), PSD (right).

the mirror diameter d , the minimum spatial frequency f_{limit} of defects which scatter light out of the cavity is higher. Consequently, the RMS for frequencies above f_{limit} in Eq. 8.16 is reduced and, consequently, the losses. However this is not the only effect to be taken into account. We have already observed that for certain values of the curvature radius, the cavity can be degenerate. This means that the separation between the resonance frequency of the fundamental mode and that of a higher order mode is small enough to make it partially resonant. If it happens, some power of the fundamental mode is then transferred to this higher order mode, and losses in the fundamental mode are remarkably increased. Critical RoC values are highlighted by simulation and correspond to the peak observed in Fig. 8.2. Mirror dimensions also have a strong impact on the appearance of such peaks.

In Fig. 8.4, round trip losses for a virgo mirror (V3) are shown as a function of the RoC for different values of the mirror diameter. We see that for bigger diameters more peaks are observed, i.e. there are more RoC values which make the cavity degenerated. This number is reduced for smaller mirrors. This effect can be possibly explained by considering the intensity profile of higher order modes. In fact, the power of higher mode is spread on a bigger surface than the fundamental mode. Generally, the *width* of a mode increases with its order, and then, a reduction of the mirror dimension prevents the build-up of wider modes. This explanation is confirmed by the fact that a gradual reduction of mirror dimension first eliminates resonances of the modes with higher n .

Using smaller mirrors will reduce the number of peaks, while increasing the floor losses level since f_{limit} in Eq. 8.15 is reduced. Therefore mirror dimensions should be chosen in order to strike the best balance between low floor losses and the presence of a safe zone for the RoC reasonably far from degeneracies. Using smaller mirrors allows us relaxing accuracy requirements on the RoC value. We can see from Fig. 8.4 that a mirror diameter of 0.075 m allows us to pick a RoC, for example of 420, for

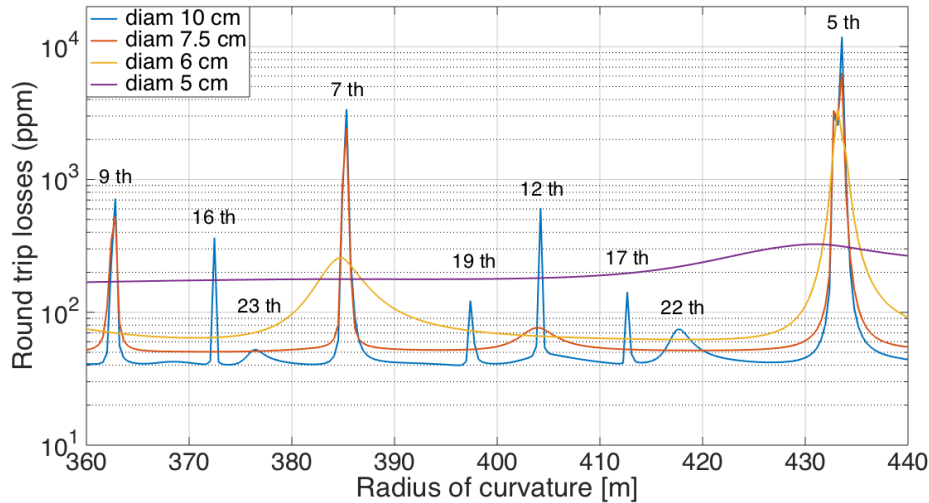


Figure 8.4: Round trip losses as a function of RoC for different values of the mirror diameter. Peaks which correspond to cavity degeneracies are reduced for smaller mirrors while the floor of round trip losses increases.

which losses remain basically constant in a range of ~ 20 m. Therefore the required precision on the RoC is $\sim 5\%$. For such a mirror dimension the contribution of clipping losses to cavity losses are still negligible. We decided to keep the value of 0.1 m for the mirror diameter in order to be compliant with the TAMA suspension system. If needed, diaphragms can be placed in front of the mirror to reduce their diameter according to what we have observed.

Simple round trip simulation

Since complete FFT simulation measuring losses as a function of the RoC can require up to few hours, we have tested a quicker method to assess losses, assuming that the cavity is not degenerate.

A complete simulation of the cavity has been used to compute fields in our system and then to evaluate round trip losses, according to Eq. 8.18. This simulation allows us to take into account the effect of higher order mode resonance. In this case, light does not exit the cavity but is partially transferred to a higher order mode. This effect is observable by comparing the round trip losses on the fundamental mode with those in all modes (i.e the total amount of light exiting the cavity). Coinciding with resonance, the curves relative to the two cases show a discrepancy accounting for the light which is still in the cavity but not on the fundamental mode. On the other hand, when the cavity is not degenerate, the total amount of light exiting the cavity coincides with the light lost on the fundamental mode. This quantity corresponds to the floor losses level reported in Tab. 8.4 and has been compared with that obtained by simply computing the power escaping the mirror aperture after a single roundtrip [reflection from a mirror with real map, propagation for 300 m, then reflection again

from a perfect mirror (as in the simulated cavity) and propagating again for 300 m]. In practice, we measure the lost power after a cavity round trip of the beam. The comparison between losses obtained with the complete simulation and those found with the simple round trip are shown in Tab. 8.4 for different mirrors maps and for different values of the diameter and shows a good agreement. Even if the second method is less accurate and cannot be used in the case of degeneracy, it is much faster and can be employed to obtain a rough estimation of the floor level of the round trip losses in the cavity. A plot of the light power exiting cavity after the first reflection is shown in Fig. 8.5.

Mirror	Diameter	RTL - full sim	RTL - quick sim
V1	10 cm	57.8 ppm	57.6 ppm
V2	10 cm	80.6 ppm	79.4 ppm
V4	10 cm	42.6 ppm	40.4 ppm
ADV	10 cm	5.6 ppm	5.6 ppm
V3	10 cm	39.8 ppm	38.8 ppm
V3	7.5 cm	50.4 ppm	50.0 ppm
V3	6.0 cm	62.4 ppm	62.0 ppm
V3	5.0 cm	168.6 ppm	165.4 ppm

Table 8.4: Comparison between losses obtained with the complete simulation and those found with simple round method for different mirrors maps and for different value of the diameter. Results of the quick simulation have been multiplied by two as in the previous case.

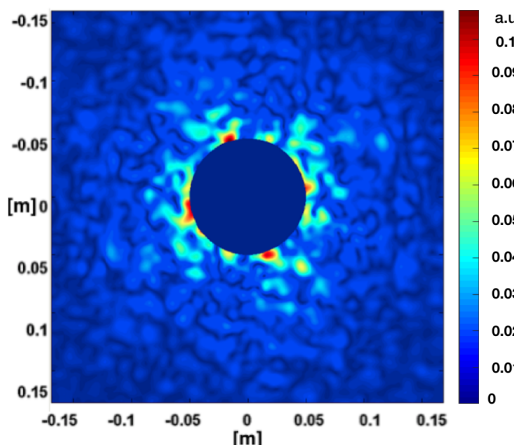


Figure 8.5: Amplitude of the field scattered out of the cavity by high spatial frequency defects. The field is observed after being reflected from a mirror with a real map and then propagated for 300 m.

Mirror	diameter 0.05 m		diameter 0.02 m	
	RMS (nm)	PV (nm)	RMS (nm)	PV (nm)
#1	1.96	11.5	0.52	3.28
#2	2.09	12.2	0.52	3.28
#3	1.5	8.3	0.48	3.36
#4	1.94	14.8	0.48	3.28

Table 8.5: RMS and PV (over different diameters) and the round trip losses floor for each mirror map. The values indicated for the losses correspond to the floor of Fig. 8.4.

8.2.1 Cavity mirror specification and results

We set the specification on the mirror peak-valley (PV) to be less than 12.7 nm on a diameter of 0.05 m and less than 6.3 nm on a diameter of 0.02 m. These values should comfortably allow for RTL below 80 ppm. The requirement of 80 ppm for the RTL has been set after performing a complete squeezing degradation budget, as it will be explained in details in the following section.

Four mirrors have been purchased for the filter cavity and they have been coated and characterized by LMA in Lyon. The results of this characterization are reported in Tab. 8.5 and show that the mirror flatness is compliant with our requirements. In Fig. 8.6 we show a plot of the four mirror maps. RTL computations using the measured mirror maps are reported in Sec. 9.8. The losses floor is ~ 40 ppm, a factor two below our threshold.

8.3 Squeezing degradation budget

From Eq. 7.48 we can see that quantum noise in an interferometer, normalized with respect to shot noise, can be simply expressed as

$$N(\Omega) = 1 + K^2(\Omega) \quad (8.19)$$

where K is the optomechanical coupling defined in Eq. 7.43. In an ideal system, the injection of a frequency dependent squeezed vacuum from the interferometer dark port will reduce the quantum noise to

$$N(\Omega) = e^{-2\sigma}(1 + K^2(\Omega)) \quad (8.20)$$

where σ is connected with the squeezing magnitude usually expressed in decibel by $\sigma_{\text{dB}} = -20\sigma \times \log_{10} e$.

In a real setup, two factors prevent this optimal noise reduction: first, optical losses will decrease the squeezing level, introducing a non-squeezed vacuum; second, fluctu-

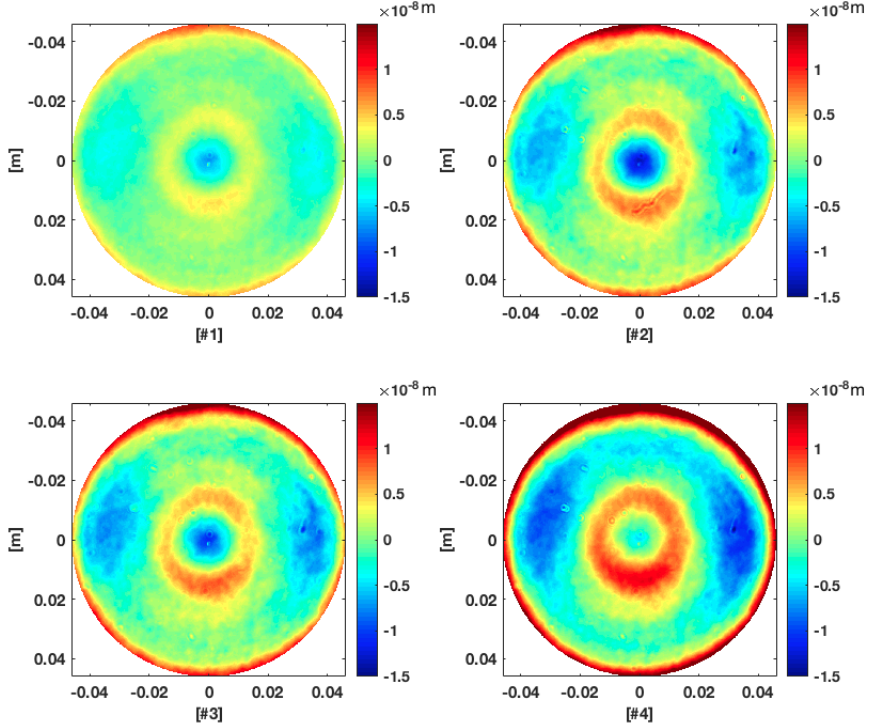


Figure 8.6: Maps of the four filter cavity mirrors. Mirror #1 and #4 have been installed.

ations of the squeezing angle will preclude an optimal rotation of the squeezed state. In [117] a detailed analysis of several of these mechanisms has been applied to a 16 m filter cavity, with round trip losses of 1 ppm/m, which is considered a possible short-term solution for Advanced LIGO [129].

The same analysis is performed here for the 300 m filter cavity, with round trip losses of 80 ppm, corresponding to a conservative estimate for Virgo-class quality mirrors. To ease the comparisons between the two cases, the numerical values for other sources of squeezing degradation are exactly the same of [117], as reported in Tab. 8.6. Fig. 8.8 shows the *squeezing degradation budget* for the 300 m filter cavity with losses 80 ppm (0.25 ppm/m) compared with that of 16 m filter cavity with loss 16 ppm (1 ppm/m) from [117]). It shows the ratio between the quantum noise of a dual recycled Fabry-Perot Michelson interferometer without squeezing and the quantum noise in the presence of frequency dependent-squeezing. An initial realistic squeezing level of 9 dB has been considered and the various degradation mechanisms have been taken into account separately and combined (black curve). In this analysis, as for [117], the contribution of the interferometer losses has been neglected. The quantum noise computation has been done propagating three different vacuum fields in the system. The first, is the one entering the squeezer and then injected in the filter cavity. The second includes vacuum fluctuations associated to losses experienced by the squeezed vacuum before entering the interferometer. The third accounts for readout losses,

taking place after the beam exit the interferometer. For each of this three fields $\bar{\mathbf{i}}_n$ the associated transfer functions \mathbf{T}_n are computed in order to find input output relations of the form of Eq. 7.60 which can be used together with Eq. 7.38 to compute the quantum noise. In the following the main degradation mechanisms taken into account are discussed. Details of the transfer matrices computation can be found in [117])

The expected frequency dependent squeezing achievable with a 300 m filter cavity is ~ 4 dB below 100 Hz and ~ 6 dB above.

Filter cavity losses

The optical losses in the filter cavity spoil the squeezing in two ways: firstly, they corrupt squeezing with anti-squeezing by mixing the quadratures. As reported in [117]), this mechanism is independent of the non squeezed vacuum fluctuations and it is caused by a difference in the cavity reflection magnitude for the upper and lower audio sidebands. Secondly, as usual, squeezed vacuum is recombined with ordinary vacuum introduced by losses. For a 16 m cavity, the filter cavity losses represent the main contribution to squeezing degradation up to 100-200 Hz, that is the frequency region where sidebands vacuum enter filter cavity. Since this effect depends on the round trip losses per meter¹ [135], it is considerably reduced in a 300 m cavity with round trip losses of 80 ppm, and at low frequencies becomes comparable with that of the mode mismatching. For this reason it is not extremely useful to further reduce filter cavity losses by increasing the mirror quality (for example using Advanced Virgo-class mirrors), unless mode matching is substantially improved.

Injection and readout losses

Injection losses, Λ_{inj}^2 , (caused by scattering, absorption and imperfections in the optics) and readout losses, Λ_{ro}^2 , (from the interferometer to the readout, including the photodetector quantum efficiency) cause a squeezing degradation by mixing ordinary vacuum with squeezed vacuum. Being independent of the cavity length, their impact does not change with a longer cavity. This mechanism is the dominating source above 100-200 Hz, assuming a losses value of 5% both for injection and readout losses. In this region, quantum noise is by far the limiting noise: a reduction in injection/readout losses will lead to a consistent improvement of present and future detector sensitivity.

Mode mismatching

Following the analysis shown in [117], a squeezing degradation is also determined by an imperfect mode matching between the squeezed field and the cavity mode

¹This statement will be justify in the following section.

$(\Lambda_{\text{mmFC}}^2)$, and between the cavity mode and the local oscillator (Λ_{mmLO}^2). This mismatching allows part of the field to bypass the cavity without experiencing frequency rotation, and is also a source of losses.

The magnitude of the mode mismatching can be easily measured. Nevertheless, the amplitude of the squeezing degradation depends of an arbitrary phase which is difficult to quantify (see [117] for a detailed explanation). For this reason, in Fig. 8.2 we have shown the worst case scenario.

As in the case of injection and readout losses, this effect does not depend on the filter cavity length and, for a 300 m filter cavity with a RTL of about 80 ppm, it is comparable with the degradation due to filter cavity losses. The estimation is done assuming a mismatch of 2% between squeezed injected field and filter cavity modes and a mismatch of 5% between injected field and the local oscillator.

Phase Noise

The level of measured squeezing can be reduced in the presence of fluctuations between the squeezed and measured quadratures. Fast fluctuations of the squeezed quadrature, usually referred to as phase noise, can be either frequency dependent or independent. The frequency independent ones are those generated for example by length fluctuation of the injection path or fluctuation of the relative phase of the local oscillator and the squeezed field. Assuming a realistic RMS of 30 mrad for this noise we can neglect its effect in the squeezing degradation budget.

Frequency dependent phase noise is generated by detuning fluctuations which are determined by the lock accuracy. Being originated inside the filter cavity, they mostly affect Fourier frequencies within its bandwidth. In a 300 m cavity, assuming a residual length noise of about 0.3 pm (RMS), also this effect becomes completely negligible with respect to other mechanisms.

Losses inside the interferometers

In the analysis above we have not considered the losses experience by the squeezed vacuum, when it propagates inside the ITF. The source losses to be taken into account are those inside the arm cavities and those in the signal extraction cavity (SEC). For what concern KAGRA, arm round trip losses Λ_{arm}^2 are assumed to be around 100 ppm.². The fraction of power lost at the reflection from the arms cavities, assuming KAGRA reflectivity is

$$\epsilon_{\text{arm}} = \frac{2\Lambda_{\text{arm}}^2}{T_{\text{arm}}} \simeq 5\% \quad (8.21)$$

Since the SEC loss (excluding arm cavities) are estimated to be 2000 ppm [136], that is only 0.2%, we would expected these losses to have a smaller impact with respect to those of the arm cavities. This is not what we found by simulating squeezing

²We have seen that slightly lower values have been measured in Advanced Virgo and Advanced LIGO.

degradation induced by ITF loss with GWINC, as shown in Fig. 8.7.

This is due to the effect of the signal recycling. We have seen that it forms, for a beam entering the dark port, a double resonant cavity together with arm cavity input and end mirrors. We can consider the cavity formed by SR and input mirror as an equivalent mirror. In the broadband configuration, such cavity is resonant and the equivalent mirror reflectivity is lower than that of the input mirror alone. This results in an increased arm bandwidth (and a reduced finesse) which reduces the effect of arm cavity RTL. The overall conclusion is that for the arm and SEC loss value considered, the degradation effect is below 1.5 dB, thus it is negligible with respect to other degradation sources.

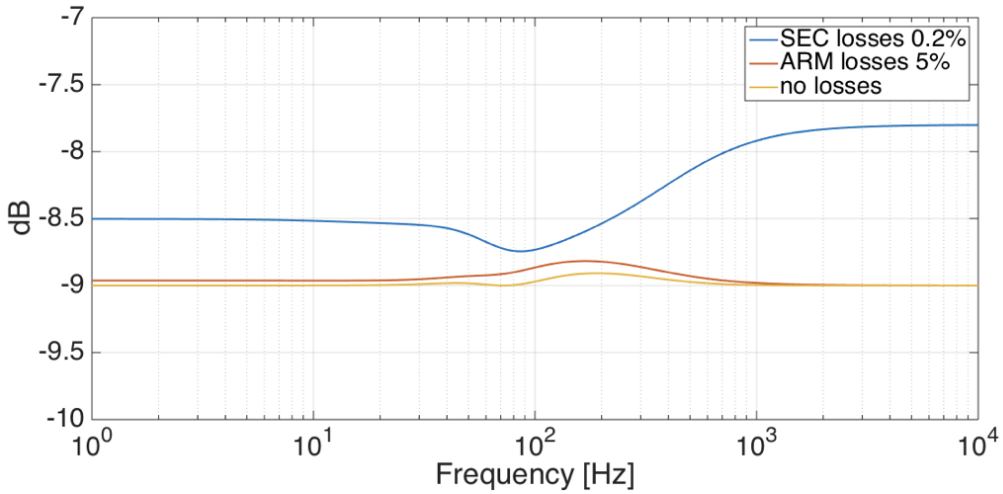


Figure 8.7: Squeezing degradation induced by losses inside the ITF in the arm cavities and in the signal recycling cavity respectively.

Parameter	Symbol	Value
Filter cavity losses	Λ_{rt}^2	80 ppm
Injection losses	Λ_{inj}^2	5%
Readout losses	Λ_{ro}^2	5%
Mode-mismatch squeezer-filter cavity	Λ_{mmFC}^2	2%
Mode-mismatch squeezer-local oscillator	Λ_{mmLO}^2	5%
Filter cavity length noise (RMS)	δL_{fc}	0.3 pm
Injected squeezing	σ_{dB}^2	9 dB

Table 8.6: Parameters used in the estimation of squeezing degradation.

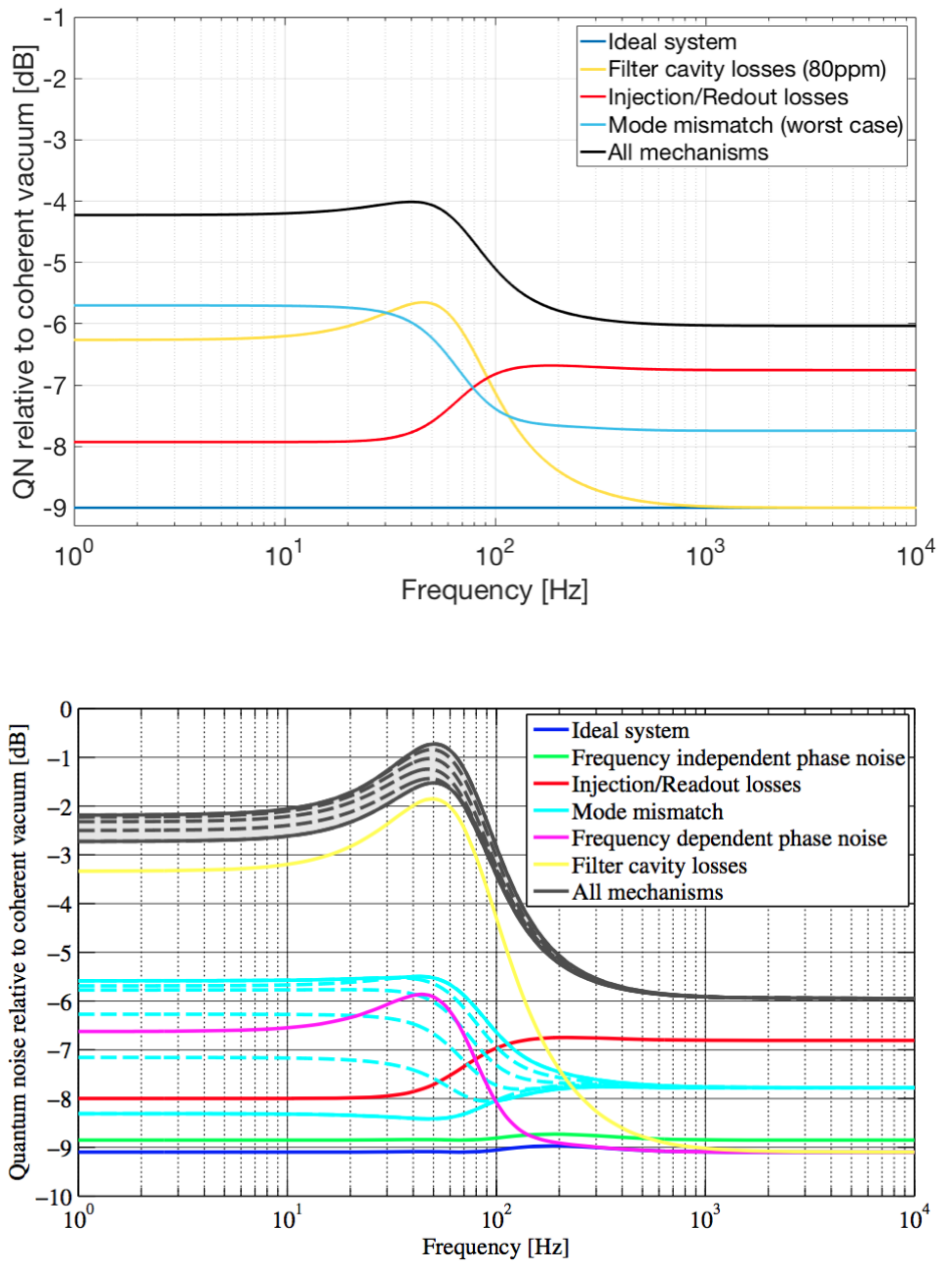


Figure 8.8: *Squeezing degradation budget* for a 300 m filter cavity with losses 80 ppm (0.25 ppm/m) (top plot) and a 16 m filter cavity with loss 16 ppm (1 ppm/m) (bottom plot from [117]). Quantum noise relative to coherent vacuum in the signal quadrature for an ideal system (blue curve) is compared with the one obtained taking into account degradation mechanisms (one by one).

8.4 Motivations for using long filter cavities

In this section we will present the motivation for using long (100 m scale) filter cavities. To do that we will show first that the relevant quantity affecting the squeezing degradation is the round trip losses per unity length and that such quantity is reduced for longer cavities. Then, we will see also that a long filter cavity, using best quality optics available, allows for frequency dependent squeezing levels, limited by mismatching and input output losses. This can reduce quantum noise also at low frequency, where it is dominated by radiation pressure noise.

Losses per unit length

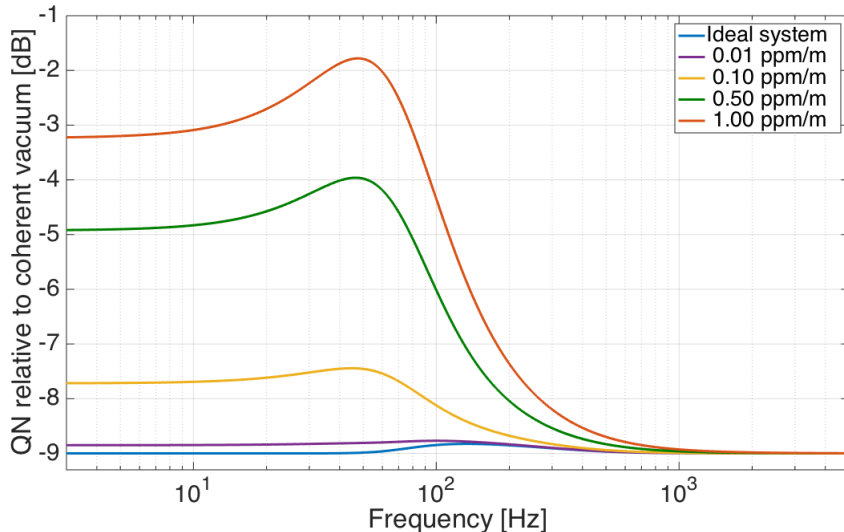


Figure 8.9: Squeezing performances achievable with different values of losses per unit length are plotted. 300 meter filter cavity with the best mirror quality presently available, brings to a squeezing degradation lower than the yellow curve.

The performances of the filter cavity are ultimately affected by their total losses \mathcal{E} . These depend on the round trip losses Λ_{rt}^2 multiplied by the equivalent number of round trips N . Assuming an end mirror transmission close to 1, we have $N \simeq 1/T_{\text{in}}$ and for the total losses we find

$$\mathcal{E} \simeq \frac{\Lambda_{\text{rt}}^2}{t_{\text{in}}^2} \quad (8.22)$$

We have seen in Sec. 3.3 that t_{in}^2 has to be chosen in order to have the bandwidth of the filter cavity similar to that of the interferometer: $\gamma_{\text{fc}} = ct_{\text{in}}^2/(4L) = \gamma_{\text{itf}}$. This means

$$t_{\text{in}}^2 \simeq \frac{4\gamma_{\text{itf}}L}{c} \quad (8.23)$$

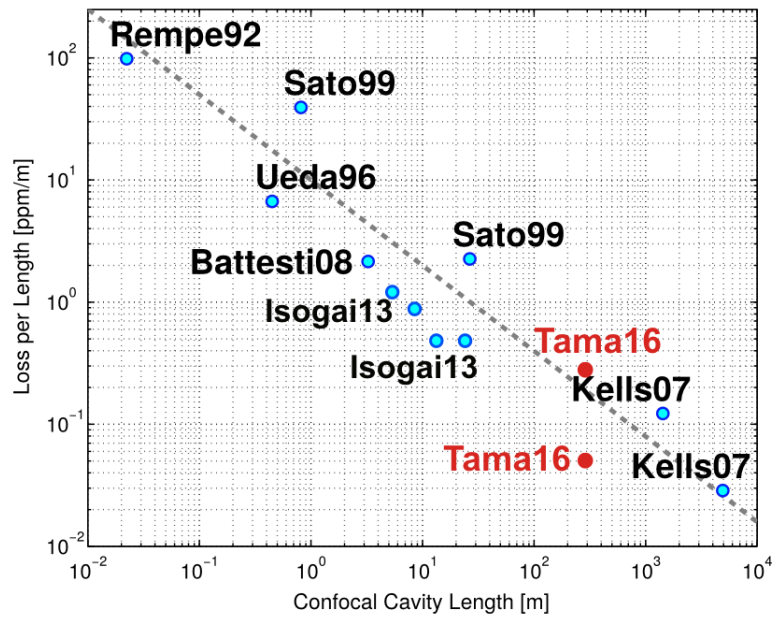


Figure 8.10: The plot shows some measured round-trip loss per unit length from the literature. It was originally published in [129], than update with measurements by Isogai et al in [100]. We added the simulated losses for filter cavity in TAMA, with both Virgo (top point) and advanced Virgo (bottom point) mirror quality. To remove any dependence on the choice of cavity geometry the plots are done in function of the confocal length, i.e the length of the confocal cavity which has the same beam dimension on the mirror as the cavity whose losses are reported. References for the measurements in literature can be found in [129]

by substituting this in 8.22 we find

$$\mathcal{E} \simeq \frac{c\Lambda_{rt}^2}{4\gamma_{itf}L} \propto \frac{\Lambda_{rt}^2}{L} \quad (8.24)$$

This means that the important quantity is the loss per unit length, as observed for the first time in [135]. In Fig. 8.9 squeezing performances achievable with different values of losses per unit length are plotted and it confirms that the degradation effect (mostly affecting low frequencies) is strongly dependent on this quantity. Therefore, it is interesting to study how this quantity depends on the length. In Fig. 8.10 some values of round trip losses per unit length from literature are reported, also including the simulated losses for the filter cavity in TAMA (with Virgo and advanced Virgo mirror quality). It is evident that this quantity decreases for longer cavities, but it is not inversely proportional to it. An empirical scaling law obtained in [100] by fitting the data is:

$$\Lambda_{rt}^2 \simeq 10 \text{ ppm} \cdot \left(\frac{L_{conf}}{1 \text{ m}} \right)^{0.3} \quad (8.25)$$

which means that

$$\mathcal{E} \propto \frac{\Lambda_{rt}^2}{L_{conf}} \simeq 10 \frac{\text{ppm}}{m} \cdot \left(\frac{L_{conf}}{1 \text{ m}} \right)^{-0.7} \quad (8.26)$$

To remove any dependence on the choice of cavity geometry the plots are done in function of the confocal length, i.e the length of the confocal cavity which has the same beam dimension on the mirror as the cavity whose losses are reported.

Eq. 8.25 shows that round trip losses increases with length, an effect that is likely due to the increasing of the beam dimension which makes it more affected by mirror defects. Since this dependence is not linear with the length, but weaker, the overall result is that round trip losses per unit length are reduced by increasing the cavity length.

For optimal quantum noise reduction, filter cavity length has to be chosen in order to have total losses causing a squeezing degradation lower than that induced by other mechanisms. This is not the case for 16 m cavity in LIGO, anyway in this case the goal is not to reduce quantum noise as much as possible but only not to exceed thermal noise (which is limiting sensitivity at low frequency) as it would happen in case of frequency independent squeezing injection [129].

We have seen that in a 300 m filter cavity using the best mirror available the squeezing degradation induced by cavity losses becomes completely negligible. Moreover, since the requirement is set on the cavity linewidth (depending on the product of the finesse and the cavity length) a longer filter cavity allows for lower level of finesse, making easier the control.

8.5 Frequency dependent squeezing with EPR entanglement

In 2016 Y.Ma et al. [137] proposed an alternative way for benefit from frequency dependent squeezing without the need of a filter cavity. The main idea behind this new technique is to inject a pair of EPR-entangled beams from the ITF dark port. If one of the two beams is detuned from the carrier, it will see the reflection from the ITF as that of a detuned cavity, thus it will experience frequency dependent squeezing. Measuring a fixed quadrature (by homodyne detection) of the detuned beam will allow to conditionally squeeze the other beam in a frequency dependent way.

The production of two EPR entangled beams is realized by detuning the pumping frequency of the Optical Parametric Amplifier (OPA). Normally the OPA is pumped at a frequency $\omega_p = 2\omega_0$ where ω_0 is the ITF carrier frequency. The OPA will create correlated sidebands at a distance $\pm\Omega$ from half of the pump frequency. If now the pump frequency is shifted of a quantity Δ , correlations will be created between upper and lower symmetric sidebands around half of the pumping frequency $\omega_p/2 = \omega_0 + \Delta/2$ (within the squeezing bandwidth). If we refer these sidebands to the frequencies ω_0 and $\omega_0 + \Delta$ respectively denoted as *signal* and *idler* beam, we see that the upper sideband of the signal beam at a frequency $\omega_0 + \Delta$ is correlated to the lower sideband of the idler beam at a frequency $\omega_0 + \Delta - \Omega$ while the lower sideband of the signal $\omega_0 - \Omega$ is correlated with the upper sideband of the idler $\omega_0 + \Delta$. In terms of quadrature picture we have two beams entering the interferometer dark port whose quadratures are EPR entangled between each other as shown in Fig. 8.11. It means that if we denote signal and idler quadratures with $\hat{a}_{1,2}$ and $\hat{b}_{1,2}$ respectively, combinations of these quadratures will show fluctuation below quantum noise and we can infer $\hat{a}_{-\theta}$ by measuring \hat{b}_θ .

The signal beam which exits the ITF verifies the standard input-output relations of Eq. 7.47. We have seen that the optimal noise reduction is obtained by squeezing the quadrature $\hat{a}_{-\arctan(1/K)}$, that, in our case means detecting $\hat{b}_{\arctan(1/K)}$. Once the two beams exit the interferometer we can separate them and we can detect a fixed quadrature of the idler beam. As we have anticipated, since the idler beam is detuned, it undergoes a frequency dependent rotation that can be optimized (by tweaking the OPA pumping frequency, signal recycling and arm cavity length) in order to make the detected output quadrature to be $\hat{b}_2^{\text{out}} = \hat{b}_{\arctan(1/K)}$. The optimal quantum noise reduction without taking into account any optical losses will be:

$$S_h = \frac{h^2}{2 \cosh 2r} \left(K + \frac{1}{K} \right) \quad (8.27)$$

If we compare it to that achievable with standard frequency independent squeezing injection in Eq. 7.50, we see that we loose 3 dB of squeezing with respect to it, even

in the ideal lossless case.

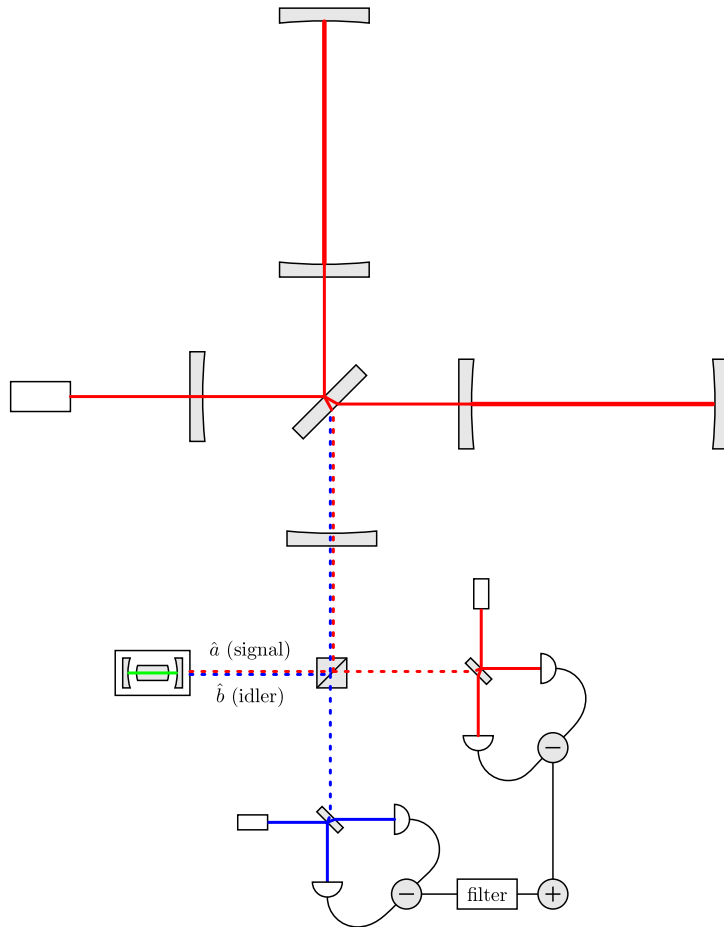


Figure 8.11: Scheme of the EPR entanglement technique for quantum noise reduction. The two EPR entangled beams are injected from the ITF dark port. Their reflection are separated and detected. By measuring a fixed quadrature of the detuned beam, which experienced frequency dependent quadrature rotation, it is possible to conditionally squeezing the other beam in a frequency dependent way.

Pros and cons with respect to filter cavities

The main advantage of the EPR entanglement technique is undoubtedly the possibility to avoid using an auxiliary filter cavity, which in addition to the construction of the infrastructure brings potential control and mode matching issues. The price to pay, in addition to a 3 dB reduction already mentioned, is an increased effect of the input and output losses which, in this configuration, count twice as they affect both beams. Simulations reported in [137] shows that arm and signal recycling losses (assumed respectively to be 100 ppm and 2000 ppm) are reducing the quantum noise improvement of ~ 1 dB. Even if this effect is much lower than that expected assuming a filter cavity with RTL of 1 ppm/m, we have shown that using a 100 m scale

filter cavity and the best mirror quality available, the effect of cavity losses becomes negligible with respect to other loss mechanisms.

Assuming an initial level of squeezing of 15 dB and an optimistic level of input ad readout losses of 5% (as we did for the filter cavity), we expected an overall quantum noise reduction between 5-6 dB, which is comparable with what we expected from a 300 m filter cavity (with 9 dB of initial squeezing).

Practical implementations of this technique are already planned: a table top experiment to demonstrate entanglement with a simple cavity and a test on GEO has been recently presented [138, 139]. In the case of GEO, which is not limited by radiation pressure noise at low frequency, the goal will be to use frequency dependent squeezing for adapting quantum noise reduction to a detuned configuration of the signal recycling cavity. These experiments will allow to tackle some technical difficulties such as the separation of the entangled beams at the output, the realization of the conditional measurement and the fine tuning of the detuning frequency and SR and arms length to obtain the proper frequency dependence.

8.6 Improvement in KAGRA sensitivity

We can quantify the expected improvement in KAGRA sensitivity by using the estimation of the achievable level of frequency-dependent squeezing using a 300 m filter cavity. In Fig. 8.12 the quantum noise for KAGRA, without squeezing, is compared with the quantum noise obtained using 9 dB of frequency-dependent squeezed light, when all degradation mechanisms previously described are taken into account. We considered both the case of a filter cavity with round trip losses of 80 ppm and that of a perfect filter cavity. The comparison shows that no major improvements can be obtained by reducing round trip losses under the level of ~ 80 ppm since their effect becomes comparable with that of other degradation mechanisms.

Fig. 8.13 shows the improvement in KAGRA sensitivity using 9 dB frequency-dependent squeezing, considering a filter cavity with round trip losses of 80 ppm and other degradation mechanisms. We remark that the use of squeezing allows us to reach a sensitivity beyond the standard quantum limit around 70 Hz. In Fig. 8.14 the quantum noise of a realistic lossy system is shown along with other KAGRA noise sources. We observe how a reduction in the only quantum noise will result in an improvement in almost the whole KAGRA observation bandwidth.

We also remark that:

- In the frequency region below 100 Hz, thermal noise is close to quantum noise and there is little to be gained from a further significant reduction in quantum noise (obtainable by improving mismatching, injection/readout losses and decreasing losses in the filter cavity).
- In the frequency region above 100 Hz, which is dominated by quantum noise,

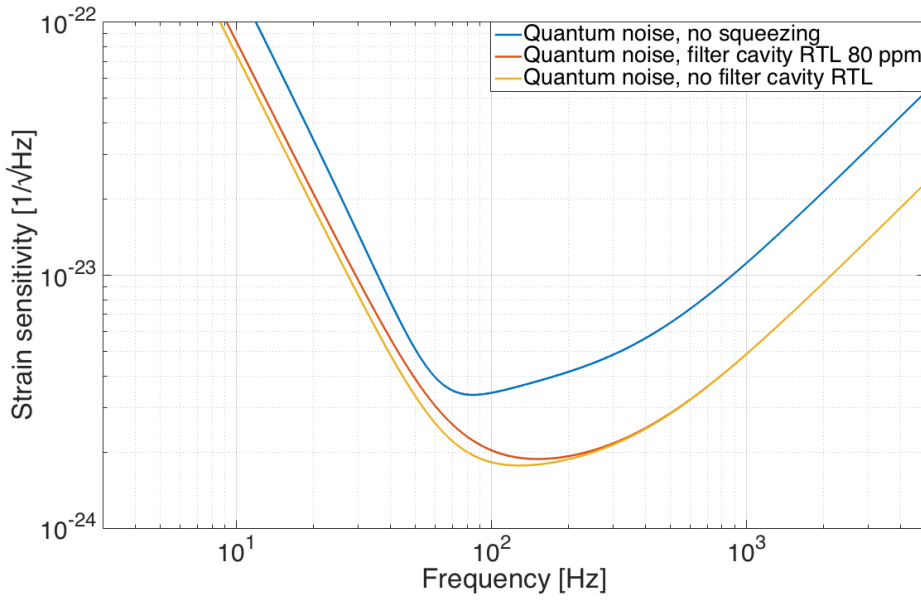


Figure 8.12: Quantum noise for KAGRA without squeezing, compared with the quantum noise using 9 dB frequency-dependent squeezing, both in the ideal system and when all the degradation mechanisms are taken into account. We remark that quantum noise without squeezing is relative to official KAGRA sensitivity using a configuration with a homodyne detection angle of 121.8° , while quantum noise in the presence of squeezing uses a standard homodyne angle of 90° .

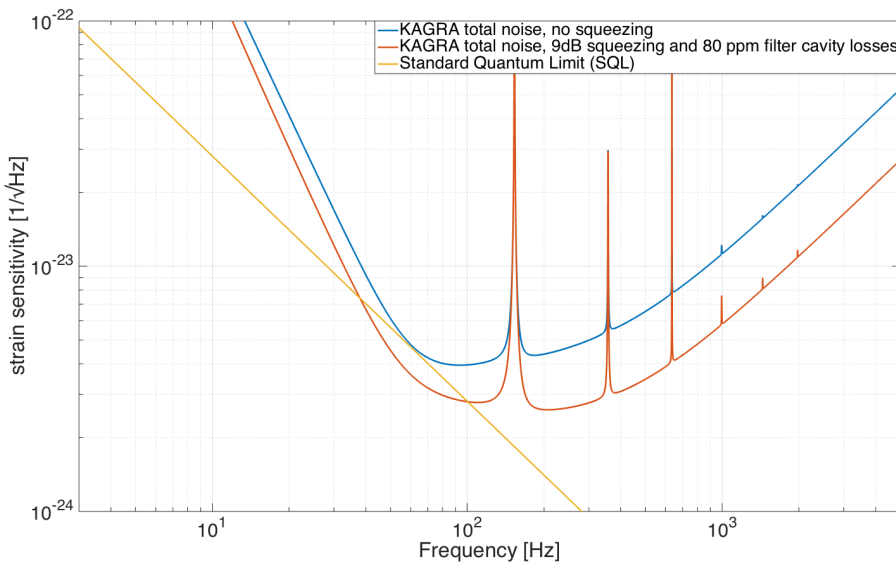


Figure 8.13: Improvement in KAGRA sensitivity using 9 dB frequency-dependent squeezing, considering lossy cavity and other degradation mechanisms.

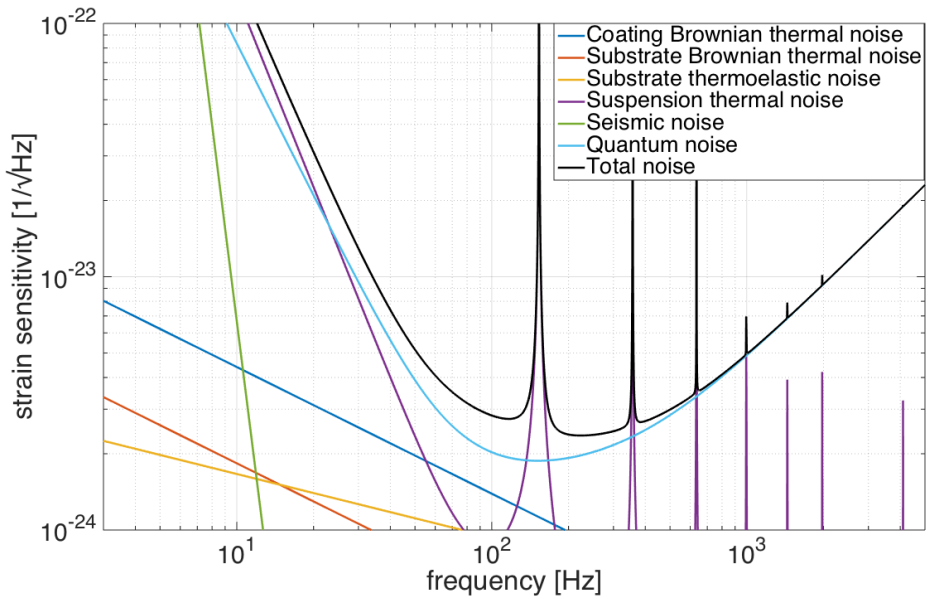


Figure 8.14: The quantum noise in the presence of 9 dB of squeezing and lossy system (filter cavity RTL 80 ppm) is compared with the other noise sources. Note that below 100 Hz, the contribution from thermal noise would prevent an improvement in the total sensitivity even in case a further reduction of quantum noise.

there is much more room for improvements. However, a reduction of the filter cavity optical losses would not provide a higher squeezing level, since in this region the squeezing degradation is mainly caused by injection and readout losses.

This suggests that a further reduction of the filter cavity losses would not be necessary, while a major benefit can be obtained by protecting squeezing from losses due to injection, detection and mismatching.

CHAPTER 9

Filter cavity experiment integration

So far we have discussed the optical design of the filter cavity with particular attention to the requirement on mirror quality and to the analysis of different mechanisms competing to cause squeezing degradation. From the results of this analysis we could discuss and justify the choice of a long filter cavity and present the expected improvement in KAGRA sensitivity. In this chapter we focus on the experiment integration. We describe the optical setup for the production of frequency independent squeezing to be injected in the cavity, the design and integration of the mode matching injection telescope, the development of the suspended mirror local control, the preparation and suspension of the mirrors and finally the lock of the filter cavity. A scheme of the filter cavity integration in TAMA infrastructure is shown in Fig. 9.1.

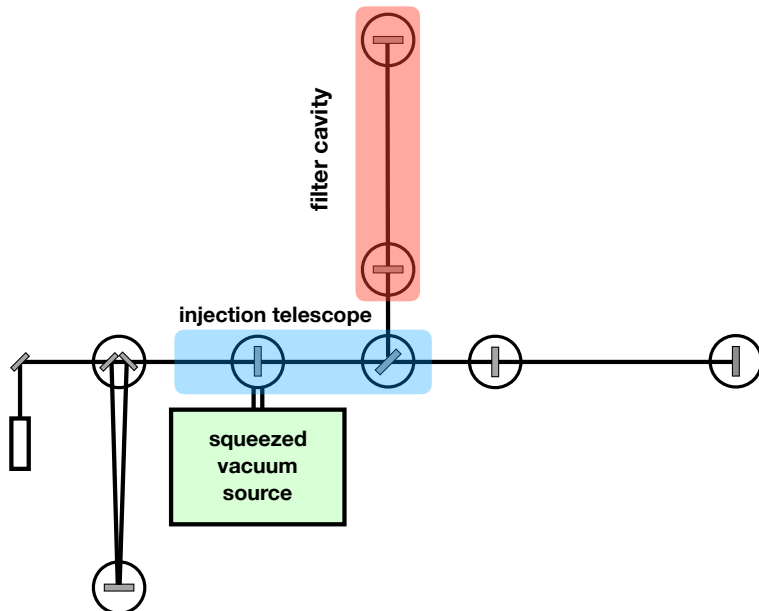


Figure 9.1: Scheme of the filter cavity integration in TAMA infrastructure.

9.1 Production of frequency independent squeezing

The production of frequency independent squeezing will be the starting point in order to impress and measure a rotation of the squeezing ellipse. The generation of frequency independent squeezing is a well-established technology developed in the gravitational-wave community for the purpose of reducing quantum noise at high frequency (in the region where it is dominated by shot noise). It has been successfully tested in GEO [112] and in LIGO Hanford observatory [111]. The technique has been refined over the years and recently up to 15 dB of squeezing have been observed [140]. In Fig. 9.3 the schematic setup for producing frequency independent squeezing in TAMA is shown. It is based on the design of GEO squeezing group [141]. The main laser (a Mephisto by Innolight) is a solid state Nd:YAG laser emitting at 1064 nm up to a power of 2 W. A piezoelectric actuator on the crystal allows to modify the frequency of the emitted light in a range of ± 65 MHz, with a gain of ~ 1 MHz/V and a bandwidth of 100 kHz. For a larger dynamics a thermal control on the crystal temperature is also available.

The beam exiting the laser is divided in two by a beam splitter. One side is used to feed the SHG cavity, which doubles the laser frequency producing green light at 532 nm. In our scheme this light is used both to pump the optical parametric oscillation cavity (OPO) for squeezing vacuum production and for the lock of the filter cavity. As shown in Sec. 8.1 the filter cavity should have a finesse of ~ 4500 for the infrared light. In order to ease the cavity control, we decide to use green light for that purpose and set the cavity mirrors reflectivities in order to have a much lower finesse (about 270) for it.

Before being split, the beam exiting the SHG cavity is stabilized in power with a Mach-Zehnder interferometer (MZ). The part sent to the OPO passes through a triangular mode cleaner cavity which acts as a filter for higher order modes and reduces high frequency phase noise. The beam used for the control of the filter cavity passes through an acusto-optic modulator (AOM), which induces a tunable frequency shift and it is used to control the detuning of the infrared (squeezed) beam with respect to the cavity resonance. The infrared beam transmitted by the first beam splitter is filtered by a mode cleaner similar to the green one and it is used in part as local oscillator for the homodyne detection (HMD) and in part as a test beam to probe the filter cavity detuning. Two auxiliary lasers similar to the main one are used. The first auxiliary laser (AUX laser 1) provides the *coherent control* field used to stabilize the squeezed ellipse angle [141]. The second auxiliary laser (AUX laser 2) is used for the OPO length control. Two phase lock loops (PLL) are used to lock the phase of the two auxiliary lasers to the main laser with different shift. Three resonant electro-optic modulators (EOM) are used to provide error signals for the five cavities in the experiments: one just after the main laser with a modulation frequency of 15.2 MHz, used for the lock of SHG and IR mode cleaner. One after

the SHG at 78 MHz for the lock of the filter cavity and the green mode cleaner. The last one at 90 MHz for the OPO lock. At the time of writing the SHG has been assembled and locked, the mode cleaners has been assembled and tested. A part of the green beam has been successfully used to lock the filter cavity and the infrared light after the first beam splitter has been superposed to the green light and sent in the filter cavity. In the following we give a more detailed description of the SHG which has been already installed.

Second harmonic generator

The second harmonic generator (SHG) consists in a hemilitic cavity only resonant for the infrared light. It is composed by a $\text{MgO} : \text{LiNbO}_3$ non linear crystal of dimensions 2 mm x 2.5 mm x 6.5 mm and a meniscus mirror. The crystal surface towards the meniscus mirror is flat and treated with antireflected coating, the other has a RoC of 12 mm and has an high reflective coating with reflectivities respectively of 99.95% for IR and 99.8% for green. The meniscus mirror has an internal radius of curvature of 25 mm and reflectivities $\sim 92\%$ for IR and $< 2\%$ for green light. The FSR is ~ 4 GHz and the finesse for infrared light is about 75. In order to maximize the up-conversion process where two photons at pump frequency ω are absorbed and a photon at frequency 2ω is re-emitted, the conservation of momentum (usually referred to as *phase matching*) has to be satisfied. This is achieved changing the refractive index of the crystal by tuning its temperature. For this purpose a thermal control loop has been developed. The best conversion efficiency achieved is 45%. The cavity is kept resonant for the infrared light by using a piezoelectric actuator on the meniscus mirror. The lock is done with a standard PDH technique in transmission, at present the correction filter is provided by a Stanford research low-noise preamplifier.

9.2 Input telescope

The infrared squeezed beam and the auxiliary green beam used for the cavity lock need to be matched to the cavity eigenmode. The dimension and curvature of the beam at the input mirror has been set in Sec. 8.1. In particular the beam exiting the optical bench need to be magnified of a factor 10. For this purpose an afocal reflective telescope is used. It consists of two spherical mirrors: a concave one with RoC 6 m and a convex one with RoC 0.6 m. The afocal condition is achieved by positioning the mirrors at a distance $d = f_1 + f_2$. Were f_1 and f_2 are the focal length of the concave and the convex mirror which are respectively 3 m and -0.3 m. The nominal distance is then 2.7 m. In Fig. 9.4 is presented an overview of the optical scheme, including the telescope. In particular it shows the path of the green and the

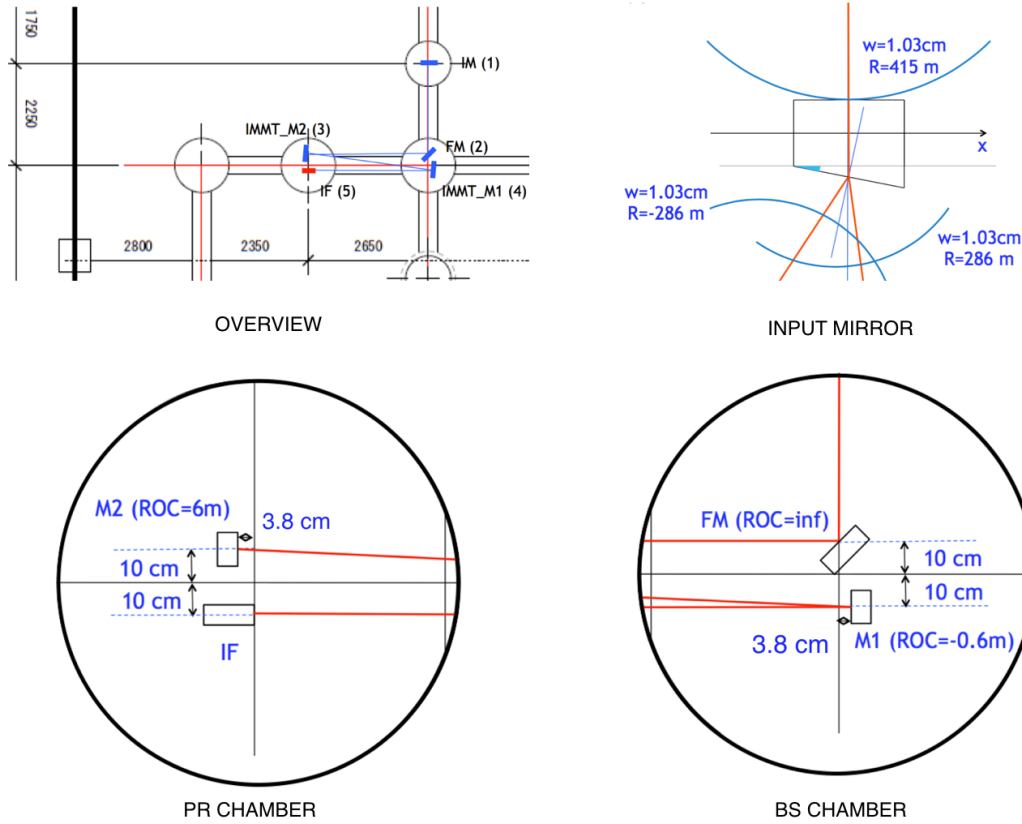


Figure 9.2: Injection telescope design

infrared beam and how they are superposed.¹

In Fig. 9.2 details of the disposition of injection telescope optics in the two chamber are shown. The infrared beam coming from the optical table enters the PR chambers² from a viewport, passes through a Faraday isolator (IF in figure) and it is sent in the BS chamber where it is reflected by the convex mirror (M1 in figure), which is a fixed 2" mirror. It goes back in the PR chamber where it is reflected by the concave mirror, which is a 4" suspended mirror. Finally, the beam re-enter the BS chamber where it impinges on a suspended steering mirror (FM in figure) and it is sent to the filter cavity input mirror.

In order to check the telescope design and find the proper beam dimension at the Faraday isolator we simulated the beam propagation using the ABCD matrix formalism (see App. A). Details on this study are reported in App. C. Results of the propagation (assuming astigmatism) done with ABCD matrices have been compared with those found simulating the system with the optical design software Zemax. The results are in agreement between each other.

¹As this picture is mainly intended to show the green and the infrared optical path, some simplification have been done. For example Faraday isolator on the infrared path in the first vacuum chamber is not shown.

²The name of the vacuum chambers refers to their former function in TAMA. The injection optics are accommodated in the former power recycling (PR) and beam splitter (BS) chamber.

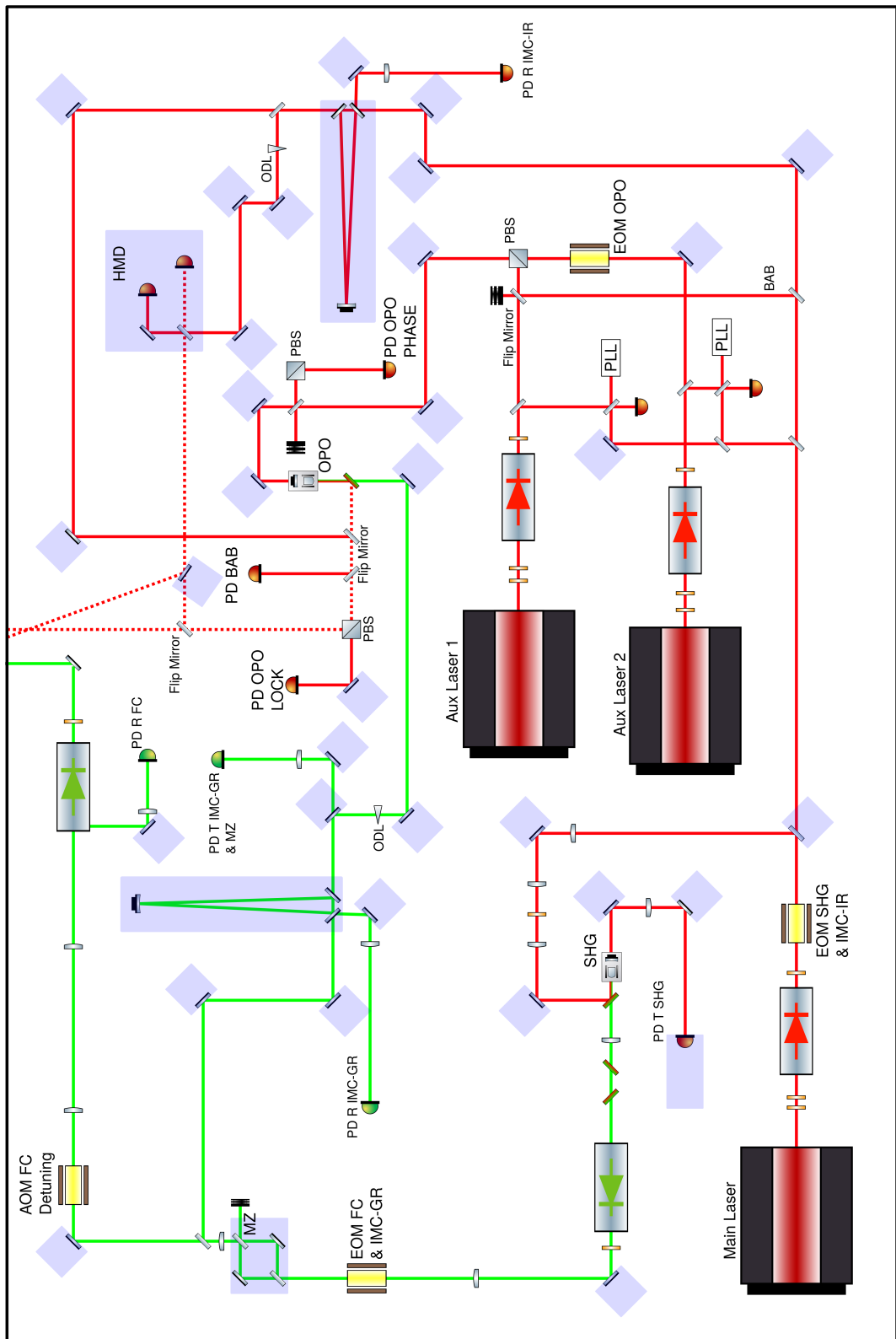


Figure 9.3: Optical scheme of the frequency independent vacuum squeezed source.

Telescope loss sources

Along its propagation through the injection telescope, the beam is affected by losses induced by different mechanisms. As seen in the previous section, they are critical as they degrade the achievable squeezing level. We considered each loss mechanism and tried to estimate the associate induced loss:

- **Astigmatism** - Non-normal incidence of the beam on the telescope mirrors introduces some astigmatism. This effect has been studied by propagating separately the beam on the x and on the y plane and using appropriate ABCD matrices for the mirror reflection which account for non normal incidence. The losses due to the astigmatism, calculated computing the overlap integral between the astigmatic beam and the closest TEM_{00} , are less then 0.3%. Details of this computation can be found in Sec. [C.1](#).
- **Spherical aberrations** - Gaussian beams have parabolic front waves, therefore they cannot perfectly match the surface of a spherical mirror. This causes the so-called spherical aberrations on the reflected beam. In Sec. [C.3](#) a computation of the magnitude of this effect has been done. The conclusion is that, due to the small ratio of the beam with respect to the mirrors, the associated losses are negligible.
- **Mirror defect scattering** - An estimation of the losses induced by scattering due to telescope mirrors defect has been done in [C.3](#). The results is that, assuming a peak-to-valley (PV) value of $\lambda/10 = 63.3$ nm, losses due to each reflection are less then 0.8%. Because of the small RoC of the telescope mirrors the PV specification cannot be much better than this one.

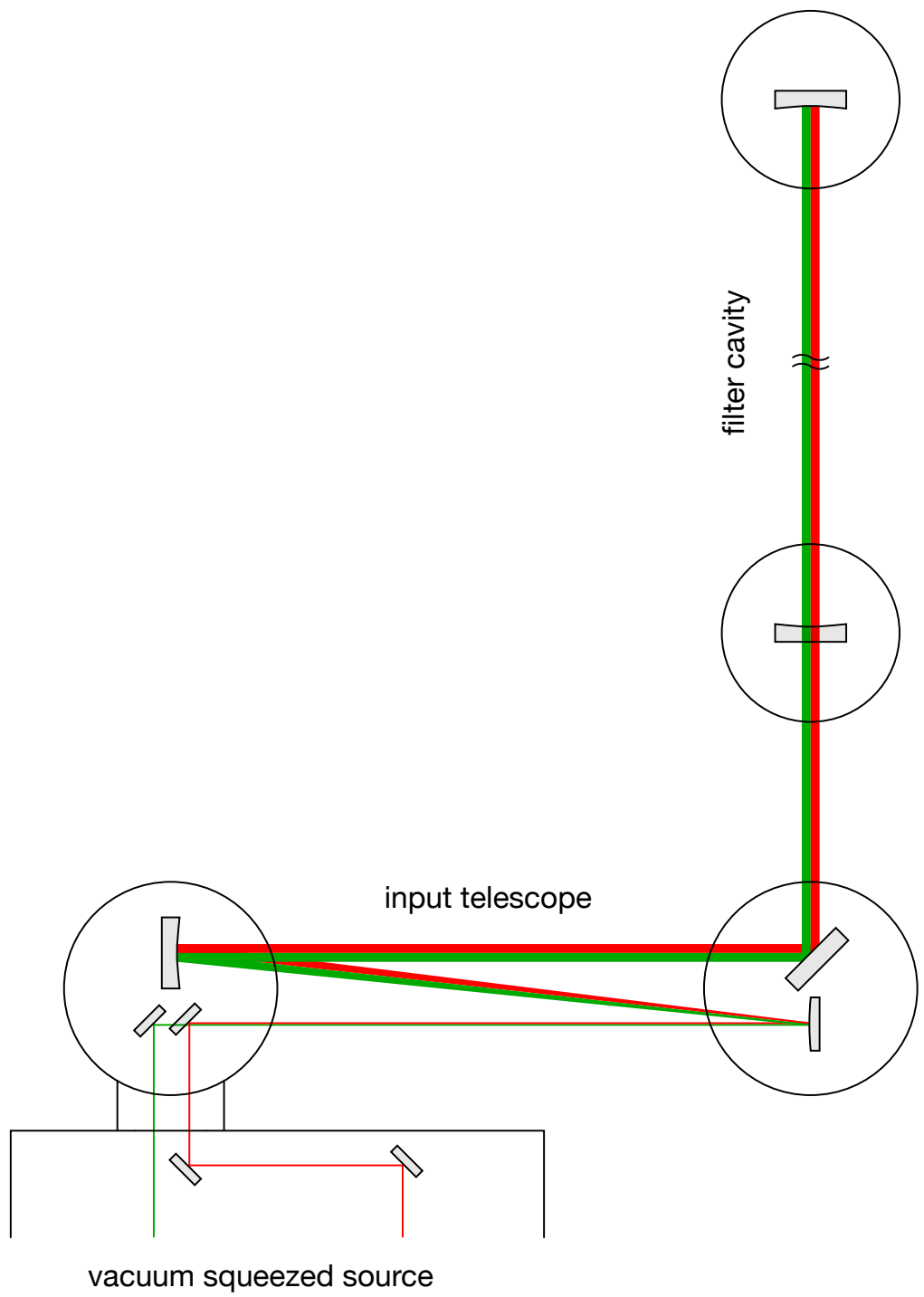


Figure 9.4: Overview of the optical scheme. Green beam and infrared beam coming from the optical table enter the first vacuum chamber where they are superposed on a dichroic mirror. Then they are magnified by the afocal telescope and injected in the cavity.

9.3 Mirrors control

In our experiment we make use of four suspended mirrors, two are part of the injection system described above and two are the mirrors constituting the filter cavity. All are suspended by using a double pendulum suspension shown in Fig. 9.5, originally developed for TAMA experiment. It is composed by a top stage to which four wires are attached and used to suspend an intermediate mass. A passive damping system consisting in a set of magnets placed around this mass is installed. The mirror, with a diameter of 10 cm, is suspended with 2 loop wires at the intermediate mass.³ Four magnets are glued to the mirror and can be pushed or pulled by controlling a current flow in the correspondent coil. The double pendulum is placed on a vibration isolation multilayer stack made of rubber and metal blocks [142].

After having installed the suspension in the vacuum chambers,⁴ we developed their *local controls*. As already mentioned in Sec. 5.7, they consist of a monitoring system which senses the mirror position with respect to a ground reference and a feedback control system which acts on the mirrors. This system is used for three main purposes:

- **Damp pendulum resonances** - As observed in Sec. 2.2.3, the use of suspended mirrors is mainly due the peculiar features of the pendulum transfer function. The pendulum filters the suspension point vibrations which are transmitted to the suspended mass with an attenuation $\sim 1/f^2$ where f is the Fourier frequency of the vibration. This is true only for frequency higher than the resonance frequency of the system. At the resonance frequency, on the contrary, ground motion displacement is amplified. An excitation of the system at the resonance frequency can induce large displacements of the mirrors affecting alignment and length control. Local controls are used to damp excess of motion at low frequency (below 10 Hz), where normally these resonances are located.
- **Displace the mirror** - Orientation of the mirrors has to be fine-tuned in order to make the cavity axis coincide with the beam direction. By adding an offset to the control loop it is possible to change the mirror position in a controlled and repeatable way, without exciting the mirror resonances and act on the cavity alignment.
- **Keep references of mirror position**- Local controls provide a way to monitor and record the mirror position. References can then be used to recover the

³The telescope folding mirror installed in the former BS suspension has a diameter of 15 cm and the suspension is slightly different.

⁴In the case of the input and end mirror (corresponding to TAMA test masses) an upgraded suspension system (TAMA SAS [143]) were used. Since these were too complex for our purpose we dismounted them and replaced them with the former double pendulum system.

alignment of the cavity. Of course this is effective only if the reference is more stable than the mirror position.

In the following we will detail the technique used to sense the mirror position and how to implement the feedback loop for the mirror control.

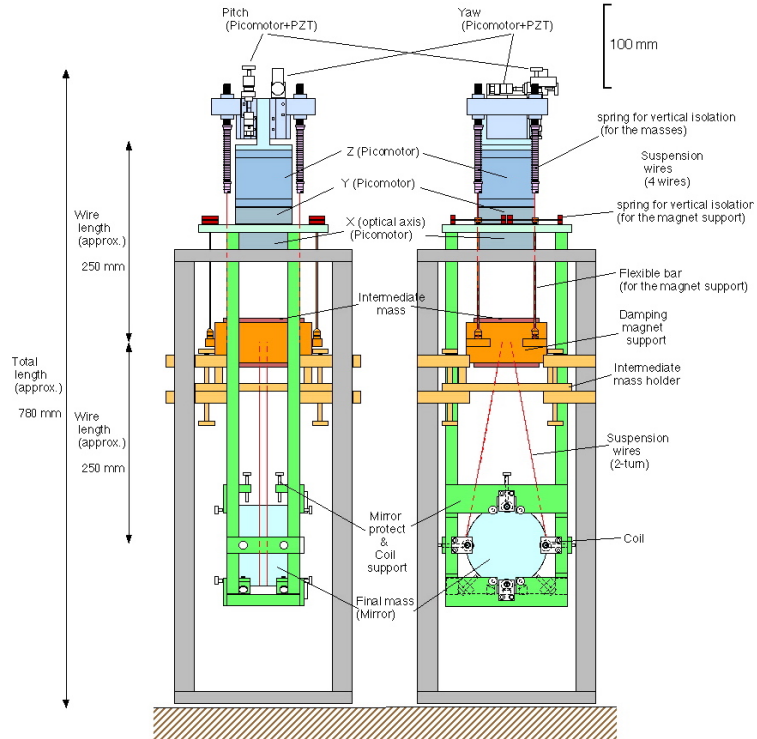


Figure 9.5: TAMA double pendulum suspension used for filter cavity mirrors. (Figure by A.Araya and K.Arai)

9.4 Mirror position readout

A suspended mirror can be regarded as a rigid body, with six degrees of freedom: three translation along the main axes and three rotation around them. (See Fig. 9.6.) The most relevant for us are the translation along the optical axis, referred to as *length*, as it changes the cavity length, and the *pitch* and *yaw* for the rotations as they change the direction of the cavity axis.⁵ The mirror motion is sensed by measuring the displacement of an auxiliary laser beam reflected by the mirror. A Position Sensor Device (PSD) is used for this purpose. As shown in Fig. 9.7 (for a 2D example), a displacement of the mirror along the beam axis of an amount d corresponds to a shift X_1 of the beam position on a PSD of

$$X_1 = 2d \sin \alpha \quad (9.1)$$

⁵Due to the large mirror RoC the two translations orthogonal to the beam correspond to small pitch and yaw angle and can be neglected.

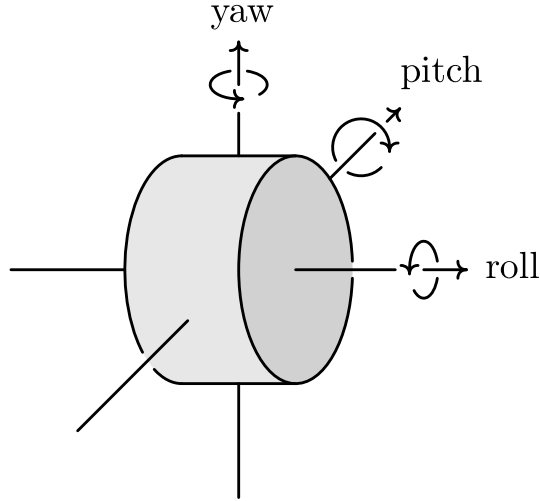


Figure 9.6: Degrees of freedom for the mirror rotation.

where α is the incidence angle of the laser on the mirror. An angular displacement

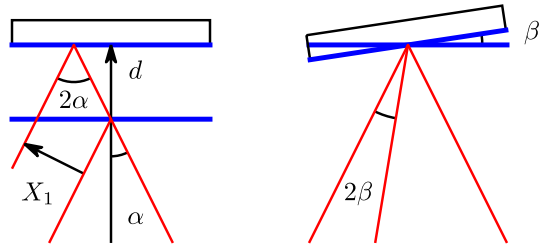


Figure 9.7: Displacement of the reflected beam induced by a shift and tilt of the mirror.

of the mirror of an angle β corresponds to an angular displacement of the reflected beam of

$$\theta = 2\beta \quad (9.2)$$

which produces a shift of the beam position on a PSD placed at a distance l from the mirror given by

$$X_\theta^y = l \tan 2\beta \simeq 2l\beta \quad (9.3)$$

Here we assumed that the rotation is around the vertical axis (yaw). In case we have a pitch, the relation 9.3 becomes

$$X_\theta^p \simeq 2l\beta \cos \alpha \quad (9.4)$$

This device to sense mirror displacement is referred to as *optical lever* and the distance l is called arm of the optical lever.

Decoupling of tilts and shift error signals

In this configuration the error signal in the PSD x-axis accounts both for a mirror displacement along the optical axis (length) and a rotation around the vertical axis (yaw). In order to distinguish them we can add a lens in the optical path of the

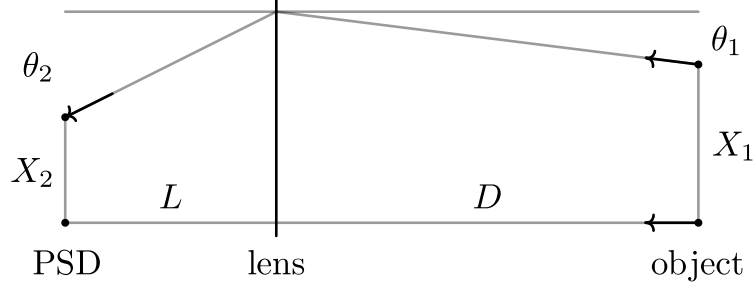


Figure 9.8: Optical scheme to decouple shift and tilt by using a lens.

beam between the mirror and the PSD, as shown in Fig. 9.8. The effect of the lens is easily computed by using ABCD matrix formalism [144]. If X_1 and θ_1 are respectively translation and rotation of the beam just after the reflection, the resulting translation and rotation at a distance D from a lens, with a focal f , placed at a distance L from the mirror, are (See Fig. 9.8.)

$$\begin{pmatrix} X_2 \\ \theta_2 \end{pmatrix} = \begin{pmatrix} 1 & D \\ 0 & 1 \end{pmatrix} \begin{pmatrix} 1 & 0 \\ -\frac{1}{f} & 1 \end{pmatrix} \begin{pmatrix} 1 & L \\ 0 & 1 \end{pmatrix} \cdot \begin{pmatrix} X_1 \\ \theta_1 \end{pmatrix} \quad (9.5)$$

$$= \begin{pmatrix} 1 - \frac{D}{f} & D + L(1 - \frac{D}{f}) \\ -\frac{1}{f} & 1 - \frac{1}{f} \end{pmatrix} \cdot \begin{pmatrix} X_1 \\ \theta_1 \end{pmatrix} \quad (9.6)$$

The displacement measured by a PSD along its x-axis will be thus

$$X_2 = \left(1 - \frac{D}{f}\right) \cdot X_1 + \left(L \left(1 - \frac{D}{f}\right) + D\right) \cdot \theta \quad (9.7)$$

We see that the distance D of the PSD from the lens can be opportunely chosen to make it sensitive only to tilts or to shift. In particular, if we place the PSD on the focal plane focal plane we are only sensible to tilts:

$$D_f = f \Rightarrow X_2 = \left(L \left(1 - \frac{D_f}{f}\right) + D_f\right) \cdot \theta_1 = f \cdot \theta_1 \quad (9.8)$$

While at the image plane we are only sensible to shifts:

$$D_i = \frac{Lf}{L-f} \Rightarrow X_2 = \left(1 - \frac{D_i}{f}\right) \cdot X_1 = \left(1 - \frac{L}{L-f}\right) \cdot X_1 \quad (9.9)$$

In Fig. 9.9 are shown the positions of the focal plane and the image plane with respect to the lens as a function of its focal length, given a configuration where the

mirror and the lens are at a distance $L = 0.63$ m, which is almost the value we expected in our system.

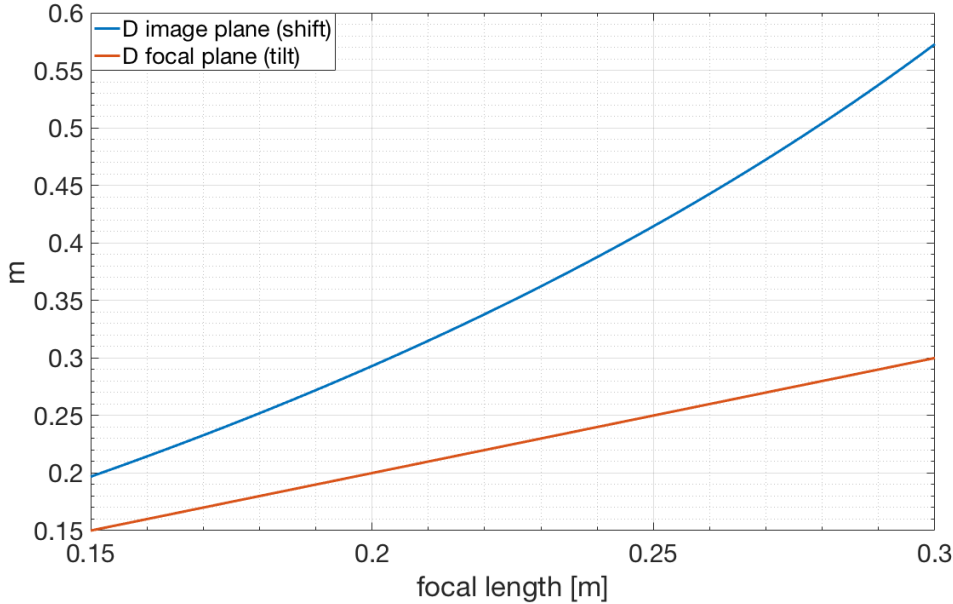


Figure 9.9: Distance of the focal plane and the image plane from the lens as a function of its focal length where the mirror and the lens are at a distance $L = 0.63$ m.

Combining Eq. 9.1 and Eq. 9.8 we find the relation between the beam displacement X_2 sensed by a PSD placed on the focal plane and the actual shift d of the mirror (i.e. the magnification factor)

$$X_2^{\text{shift}} = \left[2 \sin \alpha \left(1 - \frac{L}{L-f} \right) \right] d \quad (9.10)$$

The same can be done with Eq. 9.2 and Eq. 9.8: the relation between the beam displacement X_2 sensed by a PSD placed on the image plane and the actual tilt of an angle β of the mirror is

$$X_2^{\text{tilt}} = 2f \cdot \beta \quad (9.11)$$

In Fig. 9.10 the magnification factors are shown in function of the focal length assuming a distance $L = 0.63$ m between the mirror and the lens.

9.5 Optical levers implementation

The technique described above is routinely used for the control of suspended mirrors in GW interferometers [145]. With respect to former TAMA local controls, where only tilts were monitored and controlled, we decided to implement the decoupling

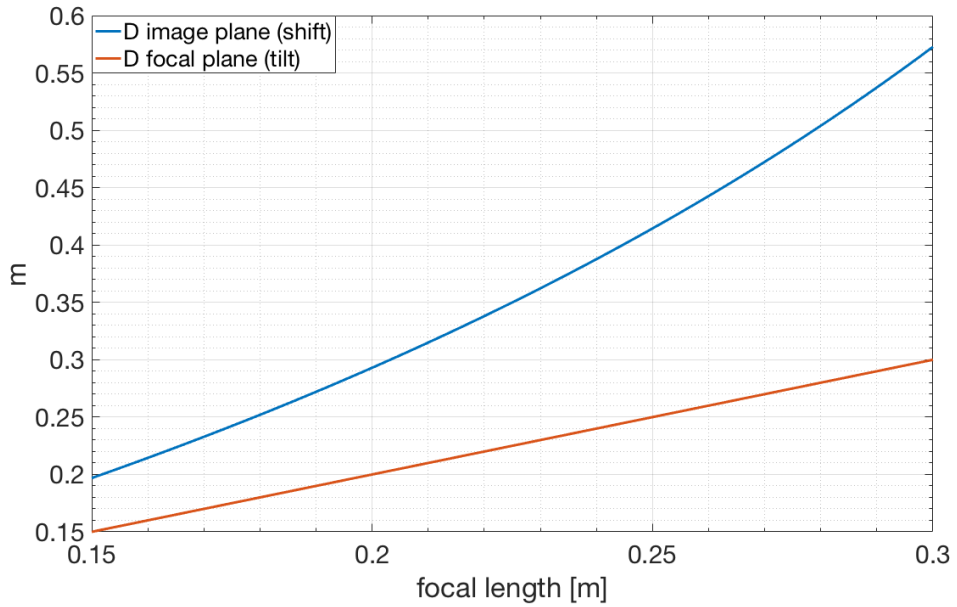


Figure 9.10: Magnification factors for tilt and shift as a function of the focal length assuming a distance $L = 0.63$ m between the mirror and the lens.

of shift and tilt error signal for the filter cavity mirrors. One of the main difficulties in its realization was represented by necessity to fit all the needed optics in small shelves (22.5 cm x 18 cm) under the viewports. Such shelves were previously used for TAMA and we decided to keep using them since their compactness and the fact that they are attached to the vacuum chamber would limit their vibrations.

A picture of the system is shown in Fig. 9.11 while the value of some relevant parameters is reported in Tab. 9.1.

Parameter	Symbol	Value
Distance mirror-lens	L	0.63 m
Focal length	f	0.2 m
Incidence angle	α	45°
PSD calibration	C	$184 \cdot V_{\text{sum}} [\frac{V}{m}]$

Table 9.1: Values of some parameters of the optical lever system

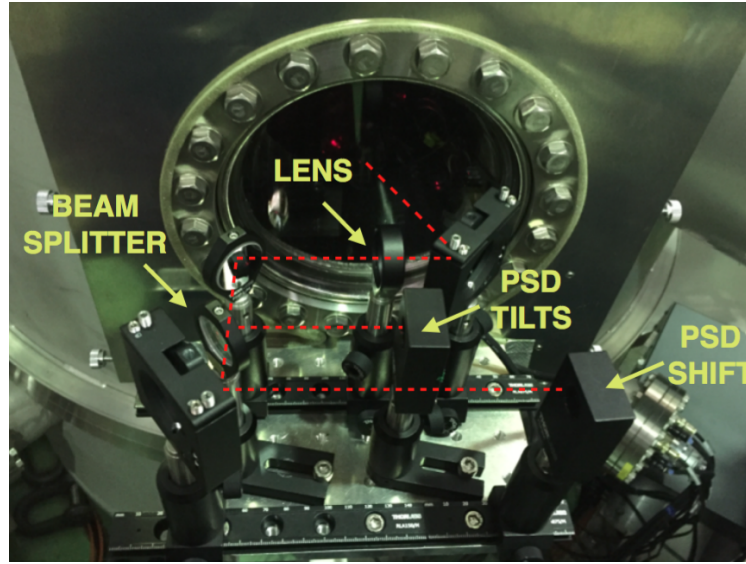


Figure 9.11: Picture of the optical lever implemented for the input mirror control. The dimension of the optics support is 22.5 cm x 18 cm.

By using these parameters we can compute the magnification factor of our system. According to them, an output voltage V_{tilt} of the PDS on the focal plane corresponds to an actual motion given by

$$V_{\text{shift}} = \left[2 \sin \alpha \left(1 - \frac{L}{L-f} \right) \cdot C \right] d \quad (9.12)$$

and for the PSD at the image plane⁶

$$V_{\text{tilt}} = 2Cf \cdot \beta \quad (9.13)$$

Where $C \left[\frac{\text{V}}{\text{m}} \right]$ is the PSD calibration which depends on the amount of power impinging on the sensor.

9.5.1 PSD position accuracy

A displacement of the PSDs from their nominal position will introduce a coupling between tilt and shift. The magnitude of such coupling for the PDS on the focal plane (sensitive to tilts) can be computed from Eq. 9.7

$$D_f = f + \delta D \Rightarrow X_2 = \left(-\frac{\delta D}{f} \right) \cdot X_1 + \left(f + \delta D \left(1 - \frac{L}{f} \right) \right) \cdot \theta_1 \quad (9.14)$$

⁶Even here, in the case of pitch a factor $\cos \alpha$ has to be taken into account.

while for the one on the image plane we find

$$D_i = \frac{Lf}{L-f} + \delta D \quad \Rightarrow \quad X_2 = \left(-\frac{f}{L-f} - \frac{\delta D}{f} \right) \cdot X_1 + \left(\delta D \left(1 - \frac{L}{f} \right) \right) \cdot \theta_1 \quad (9.15)$$

The coupling, defined as the ratio between the magnification factor of tilt and shift, are plotted in Fig. 9.12 and 9.13 as a function of the displacement δD from the nominal position for the PSD on the focal plane and that on the image plane, respectively. We see that in the first case an accuracy of ± 0.5 cm (which is a very reasonable target) allows for a decoupling of 10% while for the image plane we expect less than 0.4% of coupling.

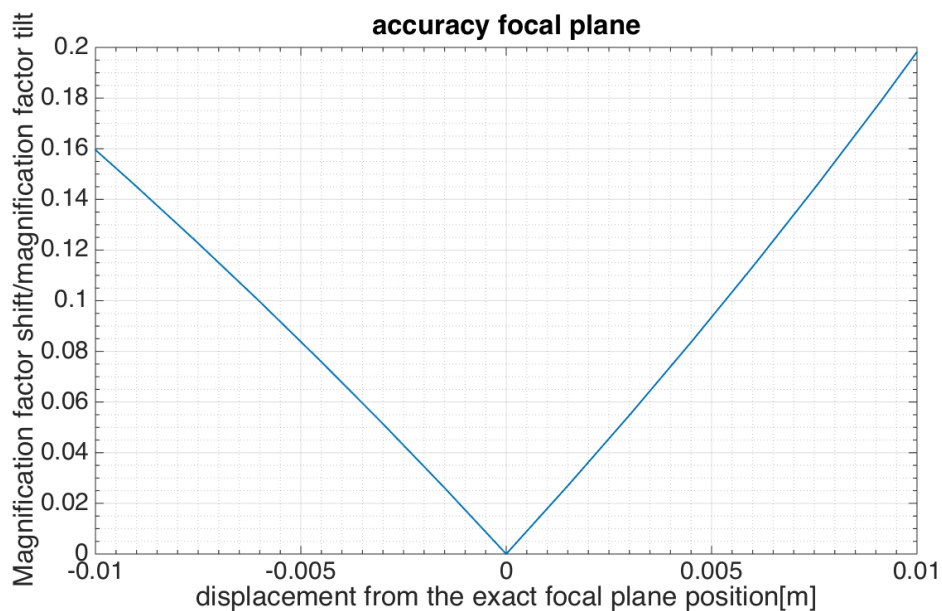


Figure 9.12: Ratio between the magnification factor of tilt and shift as a function of the displacement δD from the nominal position for the PSD on the focal plane

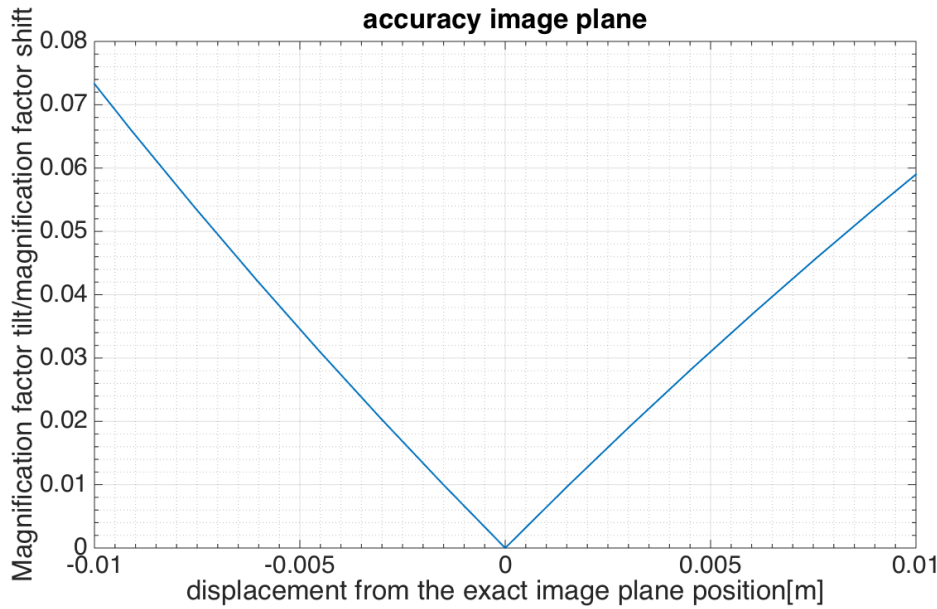


Figure 9.13: Ratio between the magnification factor of shift and tilt as a function of the displacement δD from the nominal position for the PSD on the image plane.

9.5.2 Optical lever tuning

An optimal decoupling of shift and tilt requires a high accuracy on the PSD position and it is not straightforward to understand from the signals how much residual coupling we have. The technique we used to fine-tune the position of the PSD consists at first in identifying the resonance frequencies relative to each degree of freedom and then exciting the resonance of a degree of freedom and move the PSD that should be insensitive to it, in order to minimize the amplitude of its signal. If the PSD on the focal plane is not perfectly horizontal, this can bring a coupling between tilt and yaw. This has been reduced by rotating the signal after the acquisition.

The mechanical transfer functions of the mirror showing the resonance for the three degrees of freedom are reported plotted in Fig. 9.15. They have been measured by means of white noise injection on the mirror and data have been fitted to find frequency and Q of each resonance. Since we have a double pendulum we expected to see a pair of poles and a zero between them but the transfer function of both yaw and length seems to have only one resonance. This is due to the magnet damping system on the intermediate mass which acts broadening the poles and zero. Since for yaw and length they are closely located, their effects merge and the resulting transfer function looks like a single resonant system. Transfer function has been fitted with the following poles and zeros:

- Yaw: One double pole at 1.48 Hz with a Q of 5.
- Pitch: Two double pole at 2 Hz and 6 Hz with a Q of 2 and 6 respectively.
One double zero at 6 Hz with a Q of 3.

-
- Length: One double pole at 0.94 Hz with a Q of 4.

After having diagonalized the sensing, we optimized the driving matrix trying to minimize the excitation of the resonance of each degree of freedom when injecting noise on another one. A scheme of this procedure is shown in Fig. 9.14

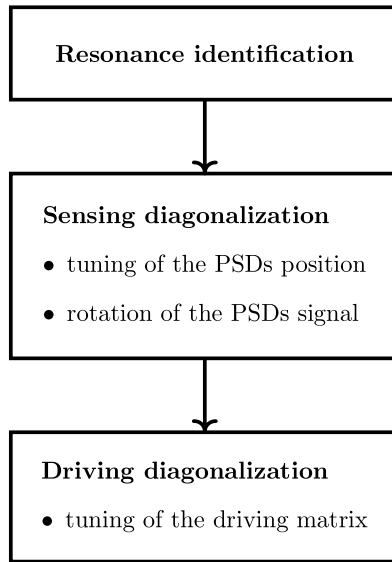


Figure 9.14: Scheme of the procedure used to tune the local controls.

The major difficulties in this procedure were due to the fact that most of the resonance are very damped therefore it is not easy to observe free oscillations of the mirrors at the resonant frequency. Figures 9.18, 9.19 and 9.20 show the mechanical transfer functions in the three degrees of freedom when white noise was injected on one degree of freedom at time. In the first one, for example, we injected noise in yaw and measured the mechanical transfer function and coherence in the three degrees of freedom. In the ideal case, we should observe a perfect coherence in yaw and no coherence in the other two degrees of freedom. We see that this is not exactly the case since a residual coherence is present in length. The fact that resonance of yaw at 1.5 Hz appears in the length transfer function suggests that we have a residual coupling in the sensing (conversely excitation of the length resonance would have meant a coupling in the driving). By comparing the magnitude of the peaks, this coupling has been estimated to be $\sim 0.25\%$, which, according to what computed in Eq. 9.14, corresponds to a displacement of the PSD from the optimal position of ~ 1.5 mm.

The level of decoupling achieved was proven to be sufficient to stably lock the cavity.

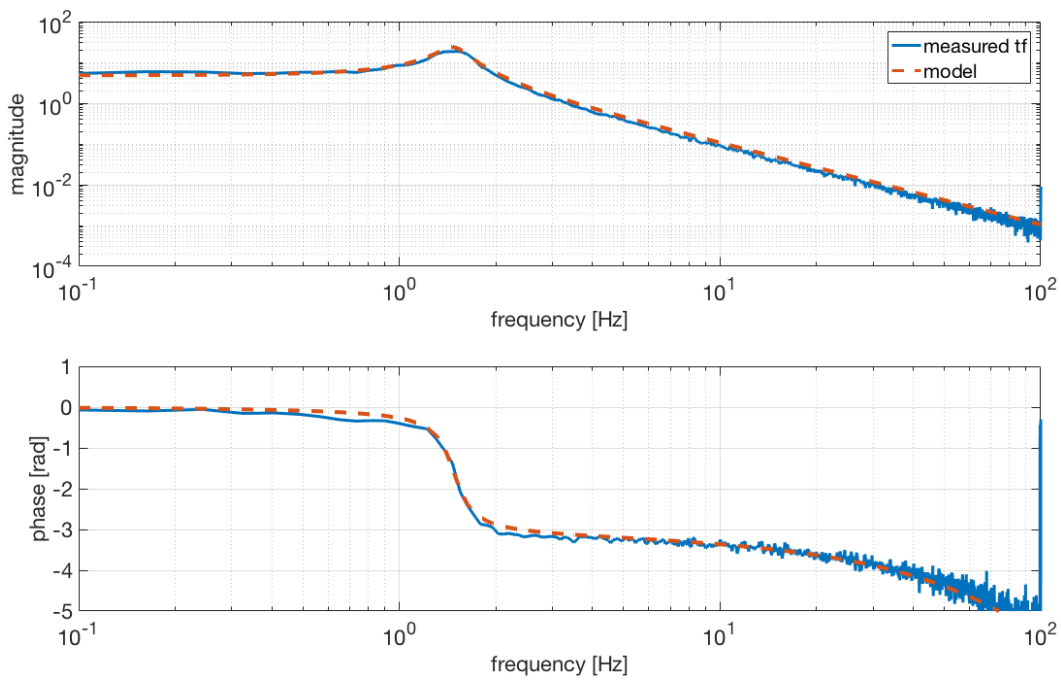


Figure 9.15: Mechanical transfer function of yaw. It is fitted by a double complex pole at 1.48 Hz with a Q of 5.

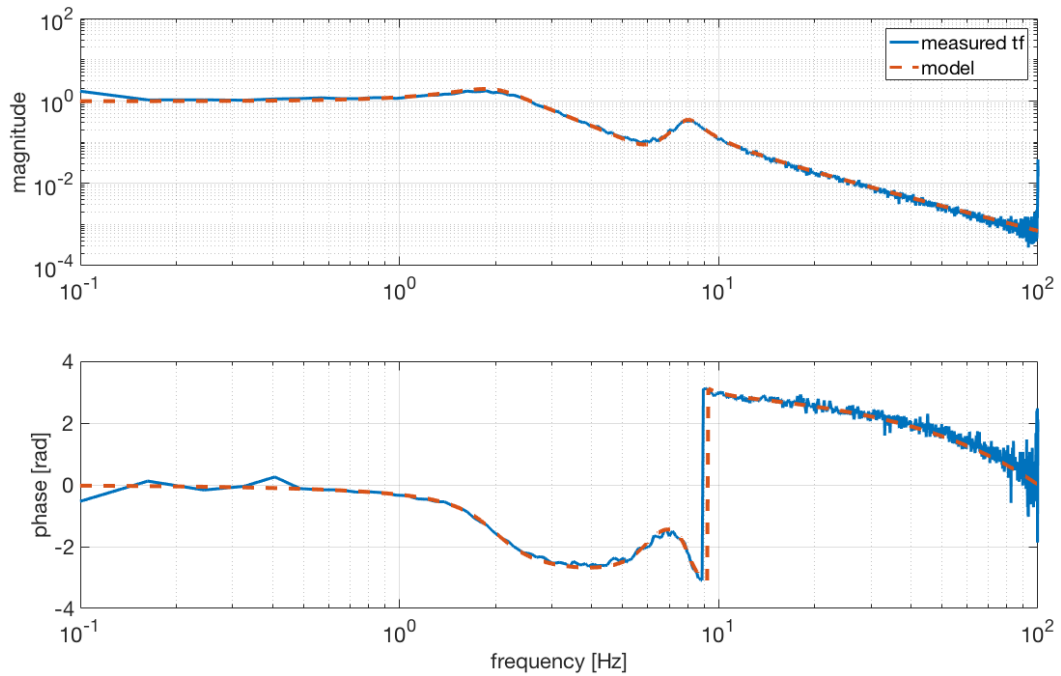


Figure 9.16: Mechanical transfer function of pitch. It is fitted two double complex pole at 2 Hz and 6 Hz with a Q of 2 and 6 respectively and a double zero at 6 Hz with a Q of 3.

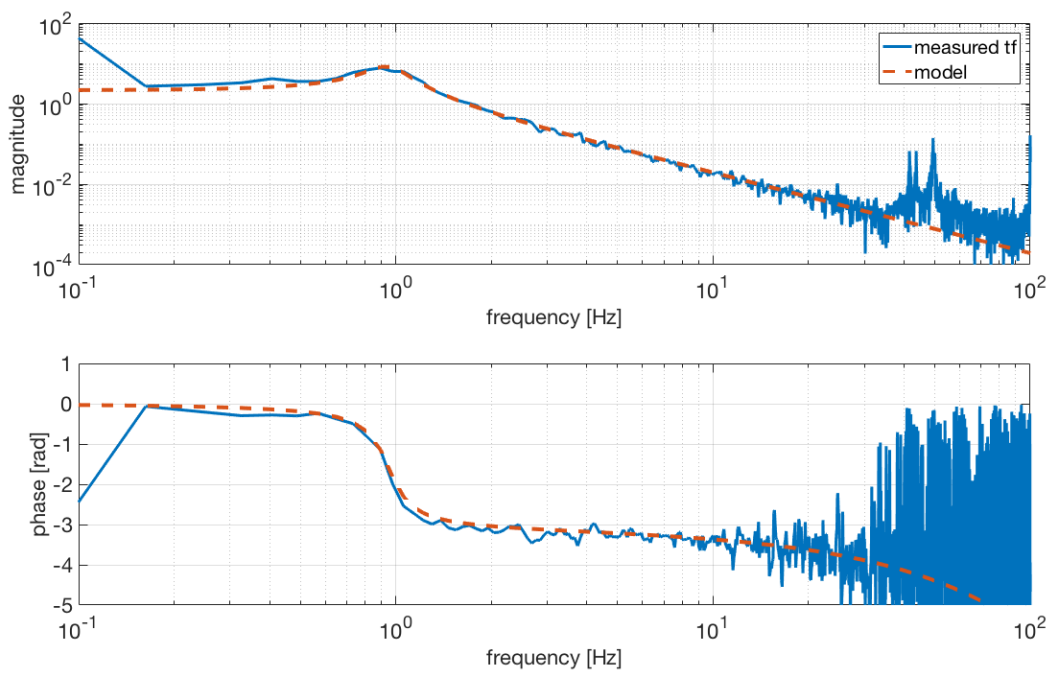


Figure 9.17: Mechanical transfer function of length. It is fitted by a double complex pole at 0.94 Hz with a Q of 4.

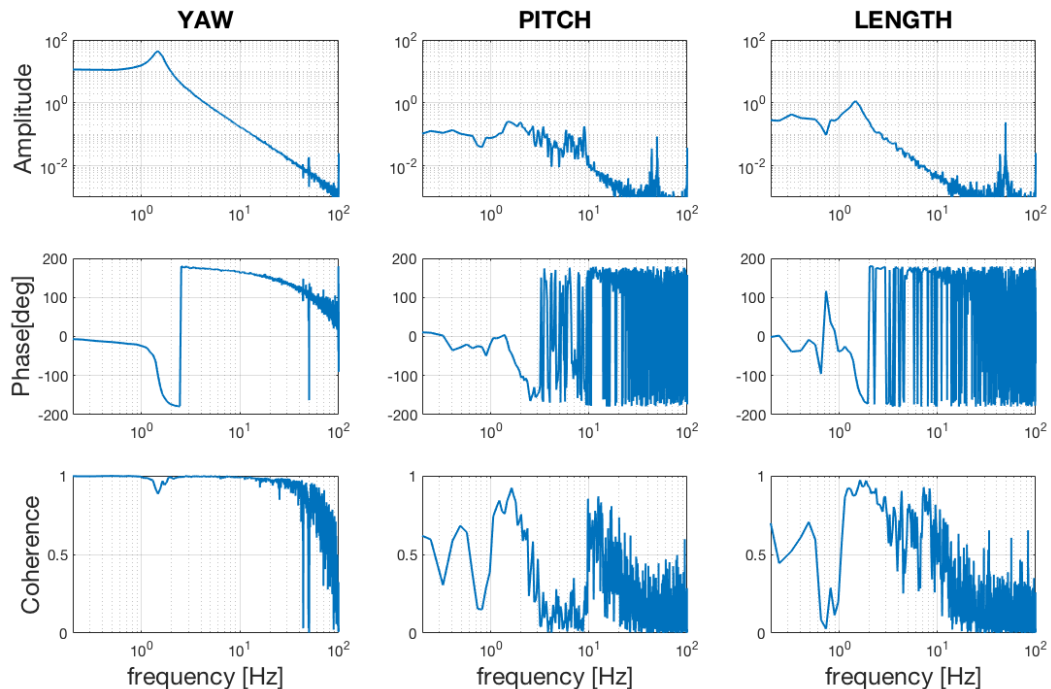


Figure 9.18: Transfer functions and coherence for the three degrees of freedom when injecting noise on yaw through mirror's coils.

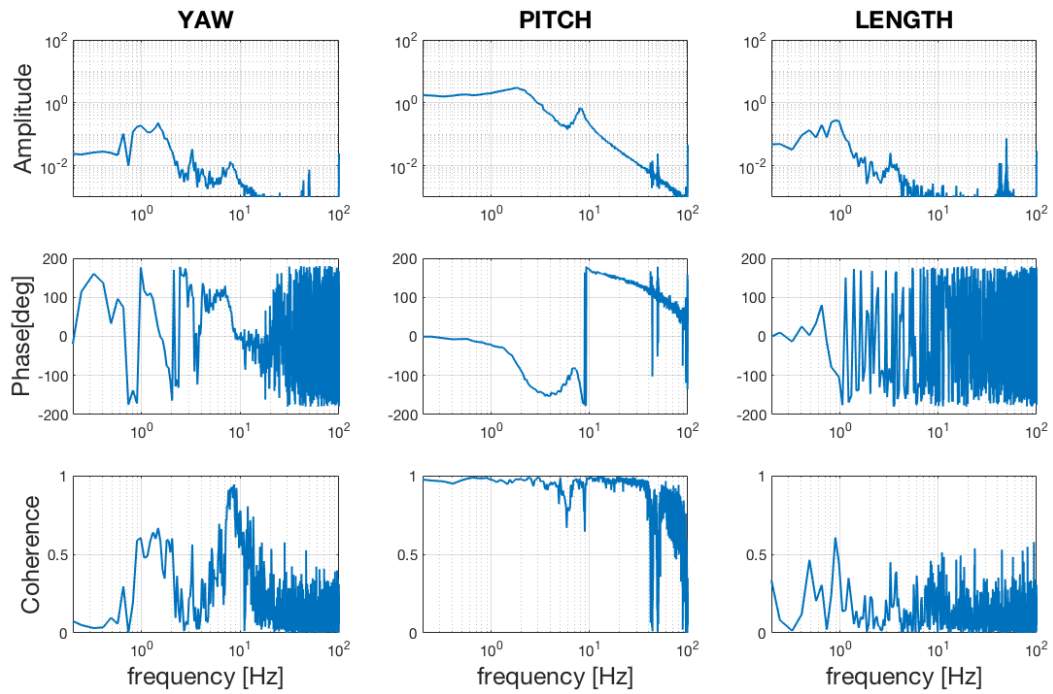


Figure 9.19: Transfer functions and coherence for the three degrees of freedom when injecting noise on pitch through mirror's coils.

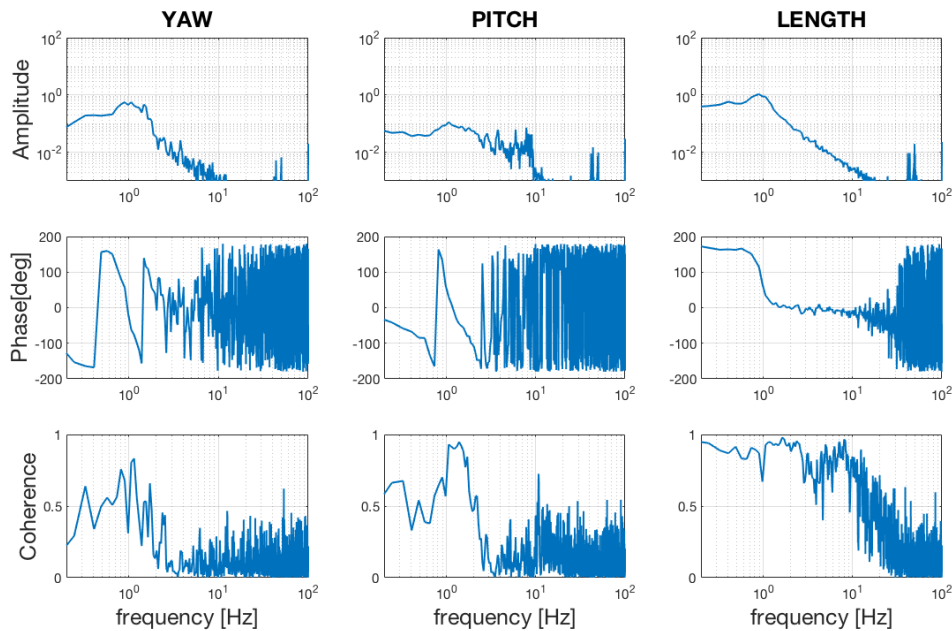


Figure 9.20: Transfer functions and coherence for the three degrees of freedom when injecting noise on length through mirror's coils.

9.6 Feedback loop implementation

The analog error signals relatives to the three degrees of freedom are converted into digital signals and processed by a digital control system. This digital control is programmed in LabVIEW and together with the ADC and the DAC was used in the past for the control of TAMA [146]. A major part of the work to implement the feedback loop consisted in re-programming such digital control for our purposes. Details on the system and the codes developed can be found in Sec. D.

Such system provides a correction signal, which is sent to an appropriate combinations of coils in order to move the mirror. The filter configuration is set by means of a user interface, the *filter bank*, specifying poles, zeros and Q factor of the filter transfer function in the s-domain. Then it is discretized and digital filter coefficient are computed.

In Fig. D.2 a scheme of the control loop implemented for each degrees of freedom of each suspension is shown. Two noise injection points and two switches have been added. By properly combining injection points, reading points and status of the switches it is possible to measure mechanical transfer functions, filters, open loop and close loop transfers functions.

Filters design

Filters are designed in order to maximize the gain and, at the same time, guarantee the stability of the feedback loop. It is important to stress that only a fraction of the error signal spectrum (below 20 Hz) accounts for a real motion of the mirrors and it is otherwise dominated by noise. Filters should also prevent to feed back such noise to the mirror avoiding actuators saturation.

We designed our filters starting from the suspension mechanical transfer functions. Among the four suspended mirrors for which we implemented local controls only those of the filter cavity have been equipped with an optical lever with a lens to decoupled tilt and shift. Those of the injection system have a simpler system which allows to control only the pitch and the yaw.

Our goal is to damp resonances of the pendulum and control its orientation. For this purpose, we put a simple pole (integrator) at low frequency (0.1Hz), a complex zero, with a $Q = 1$, at the first resonance frequency of each degree of freedom, and a complex pole at 15 Hz (20 Hz for pitch), with a $Q = 1$. The gain has been adjusted in order to have the unity gain frequency (UGF) just above the first resonance (around 3-4 Hz). At that frequency, the open loop transfer function has a slope of $1/f$ and the phase is above 180° (as required for the stability). The measured open loop transfer function for the three degrees of freedom are shown in Fig. 9.21. We see that for pitch, due to the presence of a second resonance, the unity gain is crossed again at about 9 Hz. The open loop transfer functions for the three degrees of freedom are shown in Fig. 9.21.

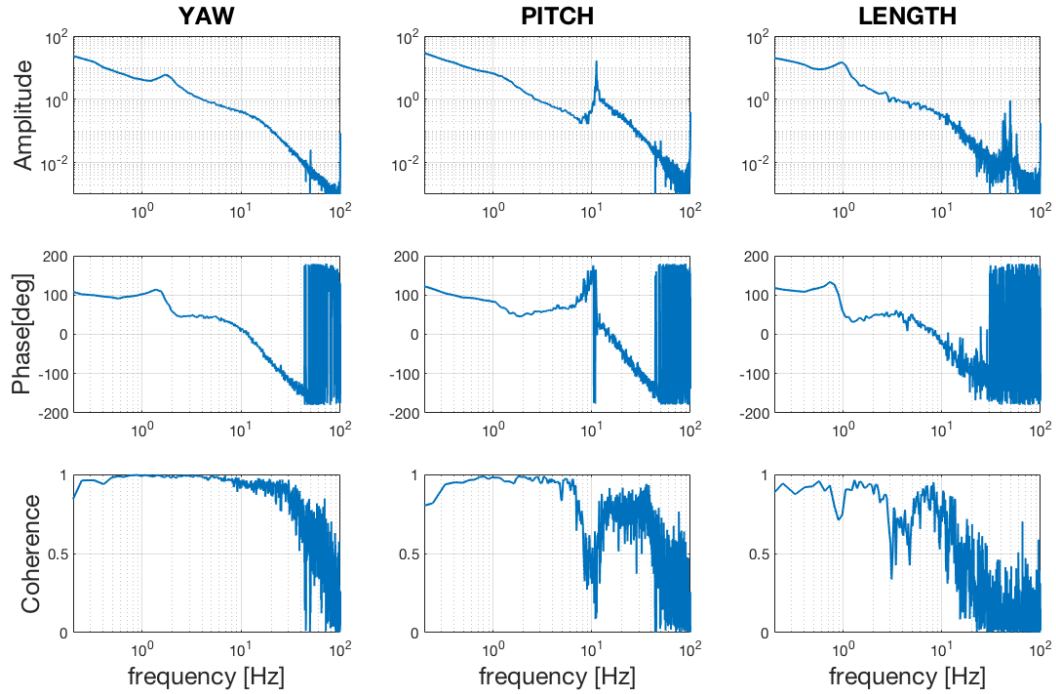


Figure 9.21: Open loop transfer function for the three degrees of freedom.

9.7 Local controls performance

The integrator in the control loop of pitch and yaw allows to keep the mirror in a certain position by adding an offset to the loop. Alternatively to obtain the same result it is possible to apply an out-of-loop DC signal to the coils and use a filter without integrator only to damp double pendulum resonances below 10 Hz. The choice of one system with respect to the other depends on if the suspension is more or less stable than the sensor. We implemented both type of controls and by comparing the performances we decided to use the first one. With these controls we managed to keep the cavity aligned and locked for a maximum of ~ 1 hour.

In Fig. 9.22, the comparison between open loop and closed loop spectra for the three degrees of freedom are shown. Generally, the open loop RMS angular motion when the mirrors are not excited is about few μrad which is close to the value needed for a stable lock of the cavity. Such threshold is found from Eq. 6.28, imposing that the total angular motion θ_{RMS} is much lower than the beam divergence $\theta_0 = \frac{\lambda}{\pi w_0} \sim 60\mu\text{rad}$. The control loop reduces the RMS motion below $1\mu\text{rad}$. Anyway at some point an excess of motion in the suspended telescope mirrors was observed. RMS for the pitch angular motion reaches about $10\mu\text{rad}$ and it was due to a resonance at about 7.5 Hz probably excited by the intermediate mass touching damping magnets. At the same time, we observed a remarkable vertical jitter of the beam at 300 m ($\sim 3\text{-}4$ mm). By taking a spectrum of the vertical motion after propagating the beam for 300 m we could identify the peak at 7.5 Hz as the cause of the jitter. We decided

to change the filter shape in order to increase the correction in the resonance region. To do that we moved the complex zero and pole at 3 Hz and 50 Hz respectively. This operation was successful in reducing the pitch RMS angular motion below 2 Hz RMS, decreasing the beam jitter accordingly.

Even if the performances of local controls were sufficiently good to allow the lock of the cavity, the labVIEW digital control system, which is more than 10 years old, is sometimes affected by spikes which prevent to keep a good alignment. The installation of a new, more reliable control system is planned for the next future.

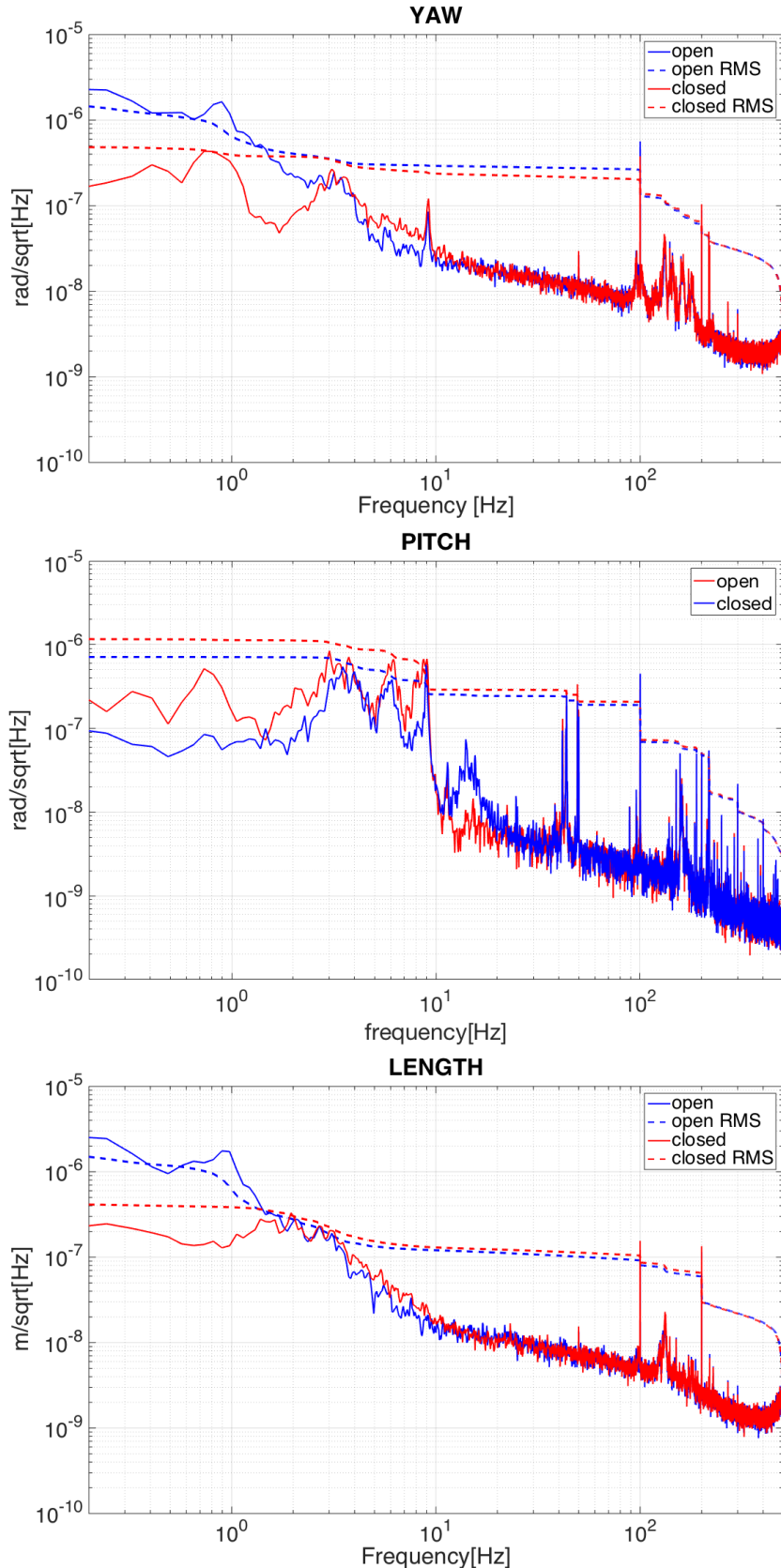


Figure 9.22: Comparison between open loop and closed loop spectra for the three degrees of freedom.

9.8 Mirrors preparation and installation

Choice of the mirrors

As anticipated in Sec. 8.2.1, four mirrors have been purchased, polished and coated for the filter cavity. The choice of which of them to install has been done performing FFT simulations of the cavity using measured mirror maps. The RTL for the four combinations are plotted in Fig. 9.23 as a function of the deviation from the nominal RoCs. They all show a RTL bottom level of about 40 ppm which is compliant with our requirement. We choose the combination for which the peaks in the losses due to higher order mode resonances were more distant from the nominal RoC value. It corresponds to input number 4 and output number 1 (orange line in the plot). Table 8.5 in Sec. 8.2.1 reports the flatness measured at LMA in Lyon, where the mirrors have also been coated.

Measurement of the wedge

In order to separate the two reflected beams, filter cavity mirrors have a wedge of $400 \mu\text{rad}$. Since the wedge was not marked on the edge of the mirrors, as it happens usually, we had to measured it by using an autocollimator. This tool works by projecting an image (a cross) onto the mirror and measuring the deflection of the reflected image against a screen with a grid. If the mirror has a wedge, the reflection of the first and second surface are not superposed, resulting in two crosses on the screen. The line joining the crosses' center indicates the wedge direction (i.e the diameter with the maximum slope).

Magnets and standoff glueing

Once individuated the wedge, we glued the magnets and stand-offs in order to have it on the horizontal plane by using Master Bond EP30-2 epoxy [147] and a custom glueing jig developed expressly for TAMA mirrors. For each mirror we use four cylindrical magnets with diameter 2 mm and hight 5 mm. In Fig. 9.24 are shown some details of the glueing process.

Mirrors installation

Local controls have been developed and tested on dummy mirrors already installed in the suspensions. Once the final mirrors have been coated and characterized, we have suspended them in place of the dummy ones. This activity required quite a lot of time and attention as the suspension wires are tiny (between 50 and 100 μm) and easy to break. The mirror replacing procedure consists at first in blocking the mirror and the intermediate mass by using the earthquake stops and a support plate,

respectively. After that we lower suspension points of the top wires which hold the intermediate mass. Once it is done it is possible to lower the intermediate mass and loosen the wires which suspend the mirror. At this point the dummy mirror can be removed and the good one can be installed. Finally the suspension points and the intermediate mass are raised to their original position and the earthquake stops are unscrew so that the mirror is actually suspended.

Vacuum restoration

The cavity has to operate in vacuum in order to be stably locked. TAMA has a vacuum system [148] equipped with different gate valves that allow to separate vacuum chambers and the ducts. During the installation of the suspensions the gate valves were closed in order to preserve the vacuum still present in the ducts since TAMA was operational. Such gates have small (~ 10 cm) windows in their middle, which let the beam pass through and allowed us to perform a pre-alignment of the cavity. However we found out that these windows were causing major aberrations on the beam, which was strongly astigmatic after propagating for 300 m. Since it was not straightforward to identify the windows as the cause of such astigmatism, we spent a lot of time trying to improve the beam shape by tuning lensing configuration on the optical table without success. After installing the mirrors, the vacuum pumps have been started in order to evacuate the vacuum chambers and improve the vacuum in the duct. The final level vacuum we reached was about $8 \cdot 10^{-8}$ mbar.

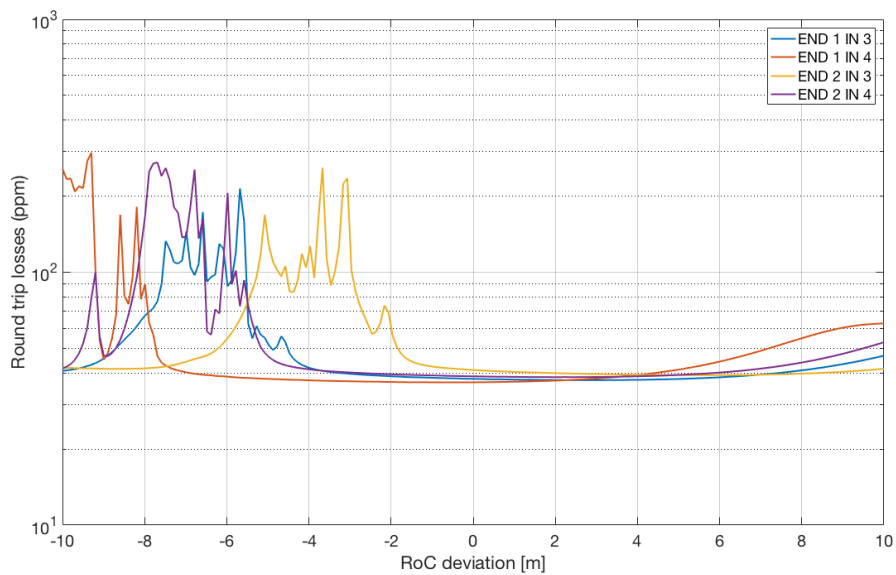


Figure 9.23: Round trip losses for different combination of filter cavity mirrors as a function of the deviation from the measured RoC.

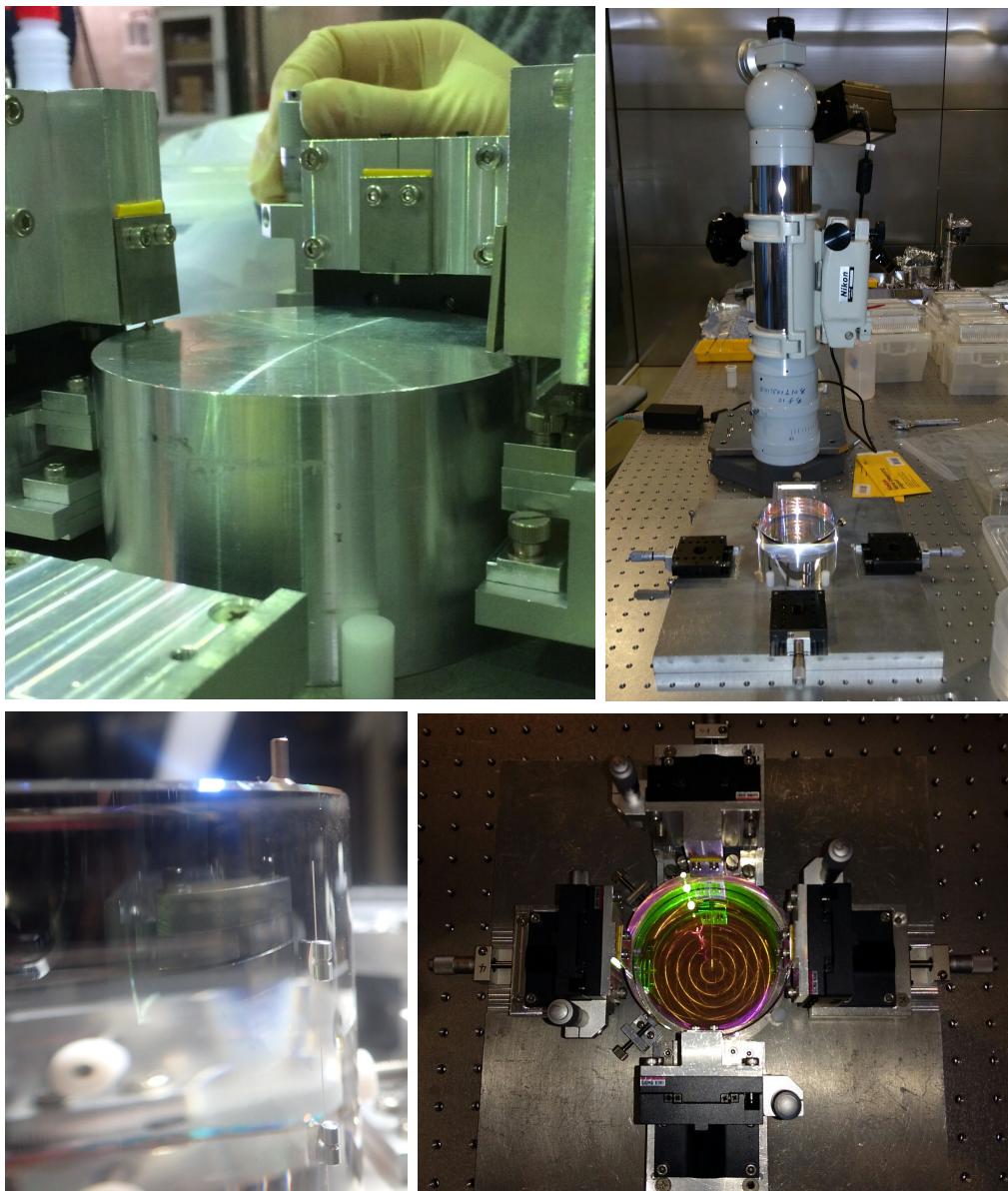


Figure 9.24: From top right clockwise: autocollimator used to find the wedge direction, top view of the glueing jig, glued magnet and stand-offs, test of magnet glueing on a dummy mirror

9.9 Cavity alignment

The cavity has been aligned in order to make both the green and the infrared beam flashing at the same time. A pre-alignment has been done before closing the vacuum chambers by moving the suspension with picomotors to center two movable targets placed inside the pipe at 10 m and 290 m. In the standard alignment procedure we use local controls to move the mirrors. In order to align the green beam, we start by completely misaligning the input mirror and we move the suspended mirrors of the

injection system (the concave telescope mirror and the last folding mirror, see Fig. 9.4) in order to center the beam on the end mirror. We put a camera on an external bench after the end mirror and use it as reference. Then we align the input mirror in order to have the beam reflected by the cavity superposed to the injected one. At that point we are able to see flashes on the camera in transmission and we tweak the position of both input and end cavity mirrors to get rid of higher order HG modes as much as possible. After that, we superpose the infrared beam on the green one by moving the two steering mirrors on the IR path on the squeezing optical table and a dichroic mirror inside the first vacuum chamber where green beam and infrared beam get superposed (See Fig. 9.4).

In Fig. 9.25 (top line) some flashes of the green beam recorded by the camera in transmission are showed. When we cut the green beam, infrared flashes becomes visible on the camera⁷ (bottom line of Fig. 9.25). Flashes have been recorded when the cavity was not optimally aligned, anyway the TEM₀₀ is resonating from time to time for both beams. It is shown in the first column Fig. 9.25.

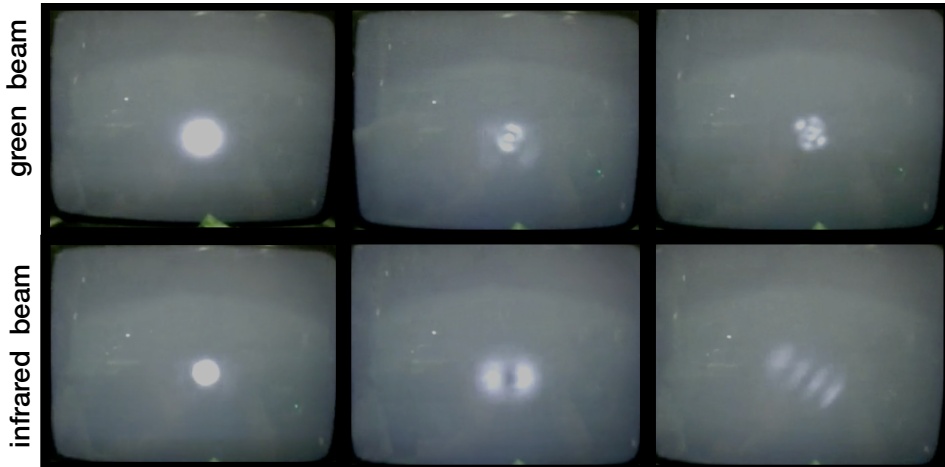


Figure 9.25: Flashes recorded by a camera in transmission, for the green beam (top line) and infrared beam (bottom line). The TEM00 of both beams is shown in the first column.

9.10 Lock and optical characterization

The filter cavity is kept resonant by locking the laser frequency on the cavity length using a standard Pound-Drever-Hall scheme in reflection [149]. The laser frequency is phase-modulated using an EOM driven with a RF signal at 78 MHz. This produces a pair of sidebands at a distance from the carrier given by the modulation frequency, which are not resonant in the cavity. The reflected beat pattern of the carrier and

⁷The dichroic coating of cavity mirrors is such that on resonance the transmitted green light is much powerful than the infrared one.

the sidebands depends on the phase of the carrier and contains the information of its deviation from the resonance. In order to provide a suitable correction signal, the error signal is demodulated by mixing this signal with a local oscillator at the modulation frequency and extracting the DC part with a low-pass filter. The error signal is then filtered by an analog servo, which produces a correction sent to the laser. The low frequency part of the signal (up to 72 mHz) is sent to the laser thermal controller acting on the temperature of the laser crystal, higher frequency correction are sent to the piezo actuator which modifies the laser cavity length.

The main preliminary activity in order to achieve the lock has been the preparation of the analog servo which is described in the following.

9.10.1 Servo preparation

The open loop transfer function G_{OL} of the lock feedback loop, shown in Fig. 9.26, is the product of different transfer functions:

$$G_{OL} \left[\frac{V}{V} \right] = G_{opt} \left[\frac{W}{Hz} \right] \cdot G_{PD} \left[\frac{V}{W} \right] \cdot G_{MIX} \left[\frac{V}{V} \right] \cdot G_{servo} \left[\frac{V}{V} \right] \cdot G_{piezo} \left[\frac{Hz}{V} \right] \cdot G_{SHG} \left[\frac{Hz}{Hz} \right]$$

G_{opt} is the optical transfer function which transduces a detuning between the cavity length and laser frequency into an optical signal. It has a frequency dependence determined by the cavity pole. G_{PD} and G_{MIX} are the gain of the photodiode and mixer used in the demodulation chain, which can be considered flat in the region of interest. G_{piezo} is the piezo transfer function which has pole about 100 kHz. G_{SHG} accounts for the doubling of the frequency operated by the second harmonic generator. The analog circuit providing G_{servo} was originally used at APC to lock the frequency of a NG:YAG laser (same model of that used in our experiment) to a 30 cm mode cleaner cavity with $F = 100$ [150]. Some modifications were needed to adapt it to our purposes: we need to compensate the pole of the filter cavity at 1.45 kHz to preserve the stability of the feedback and to modify the electronic gain to accounts for different value of the optical gain and photodiode gain. The computations done in order to estimate these values are reported in Sec. E. In Tab. 9.2 are reported some relevant parameters for the green light. The servo allows to switch between two different filters, resulting in different G_{OL} frequency dependence. Servo gain has been set in order to have a tunable unity gain frequency with a mean value about 8 kHz for the "1/ f^4 filter" and 14 kHz for the "1/ f filter" while the phase margins are about 45° and 52° respectively. The amplitude and phase of the two open loop transfer functions are plotted in Fig. 9.26. The modification to the servo has been done at APC and before to ship it to NAOJ we have test it. We have used a Stanford Research to simulate the effect of the cavity pole and we have measured the open loop transfer function verifying that it has the expected UGF and phase margin.

Parameter	Symbol	Value
Length	L	300 m
Free spectral range	FSR	500 kHz
Input mirror transmission	t_1^2	0.7%
End mirror transmission	t_2^2	2.9%
Finesse	F	172
Linewidth (FSR/Finesse)	$\Delta\nu$	2.9 kHz
Cavity pole		1.45 kHz
modulation depth	m	0.1 rad
Modulation frequency	Ω	$2\pi \cdot 78$ Hz
Input Power	P_0	0.25 mW

Table 9.2: Filter cavity parameters for green light.

	"1/f filter"	"1/ f^4 filter"
$DC < f < 145\text{Hz}$	$G_{OL} \propto 1/f^2$	$G_{OL} \propto 1/f^5$
$145\text{ Hz} < f < 1.54\text{kHz}$	$G_{OL} \propto 1/f$	$G_{OL} \propto 1/f^4$
$1.54\text{kHz} < f < 30\text{kHz}$	$G_{OL} \propto 1/f$	$G_{OL} \propto 1/f$

9.10.2 Lock characterization

The servo has different points where it is possible read signals and to inject noise in order to monitor the lock and measure transfer functions. In Sec.E a detailed description of these injection/reading points is given together with the combinations needed to measure the different transfer functions.

In the following some characterization measurements performed on the lock are reported.

Error signal calibration

The PDH filter cavity signal has been calibrated injecting a line at 28 kHz (well above the UGF which is at 10 kHz) on an injection point summed to the piezo correction signal. The amplitude of the 28 kHz line in Hz is obtained using the formula:

$$S_{\text{Hz}} = V_{\text{RMS}}(V) \cdot \sqrt{2} \cdot 100 \cdot 2 \cdot 10^6 \text{Hz/V} = 353\text{Hz} \quad (9.16)$$

where $V_{\text{RMS}} = 1.25 \cdot 10^{-6}$ has been measured with a spectrum analyzer. The factor $\sqrt{2}$ is needed to pass from V_{RMS} to the line amplitude. The factor 100 accounts for the attenuation of the monitoring channel "PZTmon" and $2 \cdot 10^6$ Hz/V is the piezo gain after the SHG.

Measuring the line at 28 kHz in the error signal and compensating for the cavity frequency pole it is possible to find the calibration factor K in V/Hz. The formula

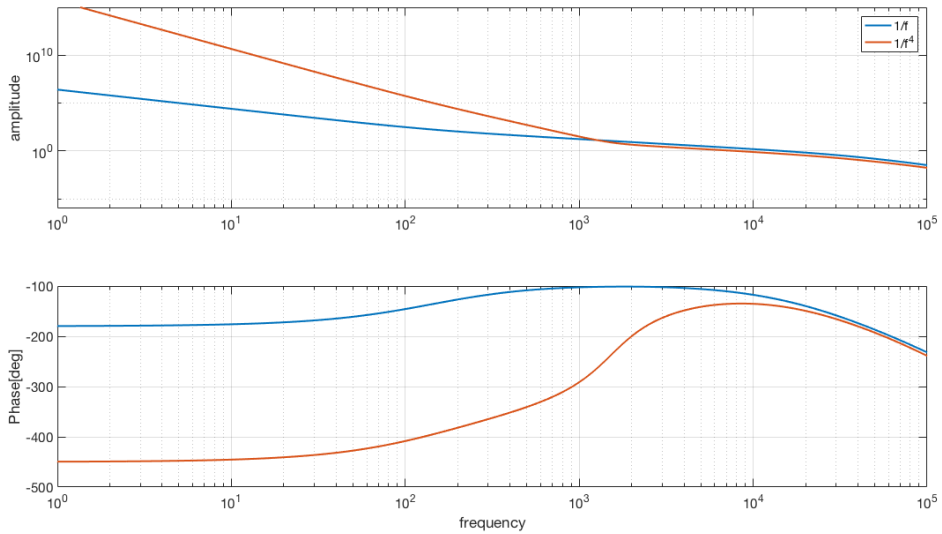


Figure 9.26: Simulated open loop transfer functions of the feedback loop for the filter cavity control.

used is :

$$S_V = \frac{K(\text{V/Hz})}{15.9} \cdot \frac{S_{\text{Hz}}}{\sqrt{1 + f_0^2}} \quad (9.17)$$

where the factor 15.9 accounts for the gain of the error signal monitor channel and $f_0 = 1.45$ kHz. Having measured $S_V = \sqrt{2} \cdot 38.9 \cdot 10^{-3}$ V we found

$$K = 1.8 \cdot 10^{-4} \left[\frac{\text{V}}{\text{Hz}} \right] \quad (9.18)$$

which seems to be in agreement with the calibration obtained looking the PDH signal when the cavity is freely swinging. In that case we measure a peak-to-peak value of ~ 4 V for a cavity line of 2.9 kHz, which corresponds to a $K = 1.7 \cdot 10^{-4}$ V/Hz . Note that when the cavity is freely swinging ringing effects can perturb this measurement. We have also checked that reducing the frequency of the line sent to the piezo (with the same amplitude) to 14 kHz, the amplitude of the line of the error signal is multiplied by 2, as expected because of the cavity pole. Then we tried to increase the amplitude of the line at first by a factor 10, thus having a line with amplitude of 3 kHz (comparable with cavity linewidth). The cavity stays locked and the calibration factor measured is the same measured before. Increasing further the amplitude to ~ 7 kHz (more than twice the cavity linewidth) makes the lock less stable.

Correction signal spectrum: free running laser noise estimation

The spectrum of the PZT correction signal sent to the laser when the cavity is locked is plotted in Fig 9.27 between 1 and 200 Hz. Since in this region the gain of the loop

is very high, the signal is proportional to the laser frequency noise. The spectrum above 5 Hz is well fitted by the curve

$$S_{\text{laser}} \simeq \frac{7.5 \cdot 10^3}{f} \left[\frac{\text{Hz}}{\sqrt{\text{Hz}}} \right] \quad (9.19)$$

which is compatible with the expected free running laser noise. For $f < 5$ Hz the spectrum is likely to be limited by mirror control noise and seismic noise. Another measurement taken at higher frequency than above 4 kHz the spectrum is limited by a flat noise, which is compatible with the noise of the 100 kΩ resistor at the output of the PZT monitoring signal.

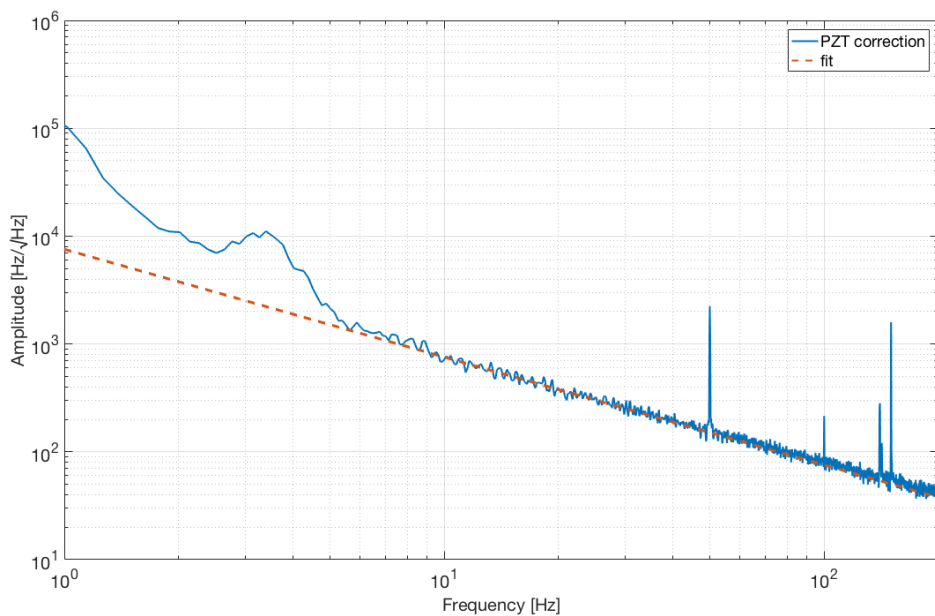


Figure 9.27: PZT correction signal spectrum from which the free running laser noise has been estimated (dotted orange line).

Error signal RMS: measurement of the lock accuracy

PDH error signal accounts for the laser frequency deviation from the resonance and its RMS estimates the accuracy of the lock. The time series of the calibrated error signal is shown in Fig. 9.28, together with the relative histogram. The RMS is ~ 100 Hz. Fig. 9.29 shows a plot of the error signal spectrum and its RMS which is consistent with that computed using data in time.

Open loop transfer function

We measured the open loop transfer function by injecting noise (swept sine with amplitude 50 mV) on "perturb" channel which is summed to the error signal. (See

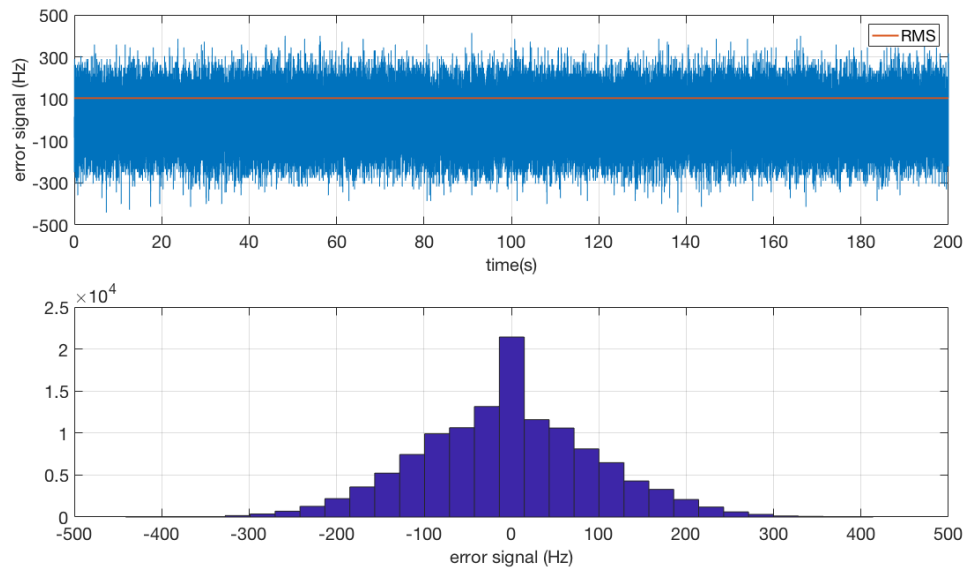


Figure 9.28: Calibrated error signal in time together with the relative histogram. The residual RMS is about 100 Hz.

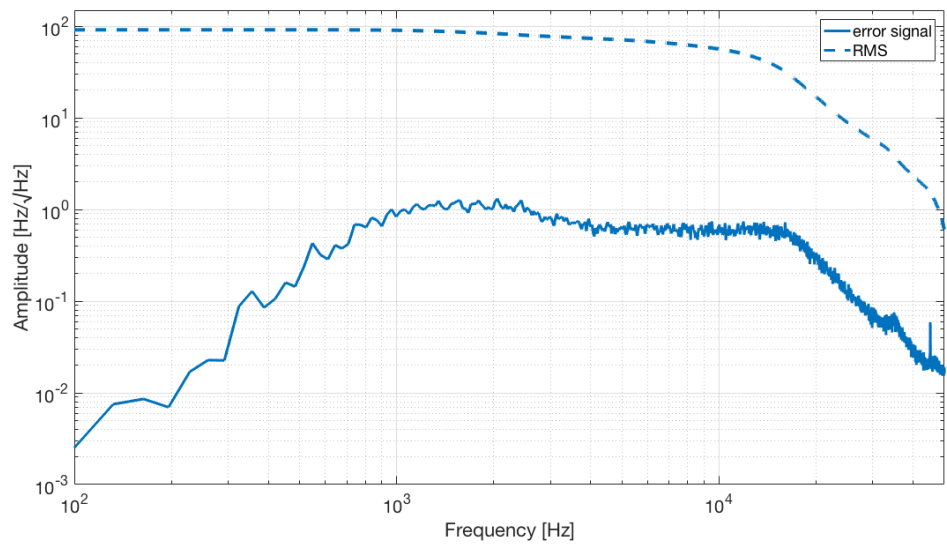


Figure 9.29: Error signal spectrum and the relative RMS.

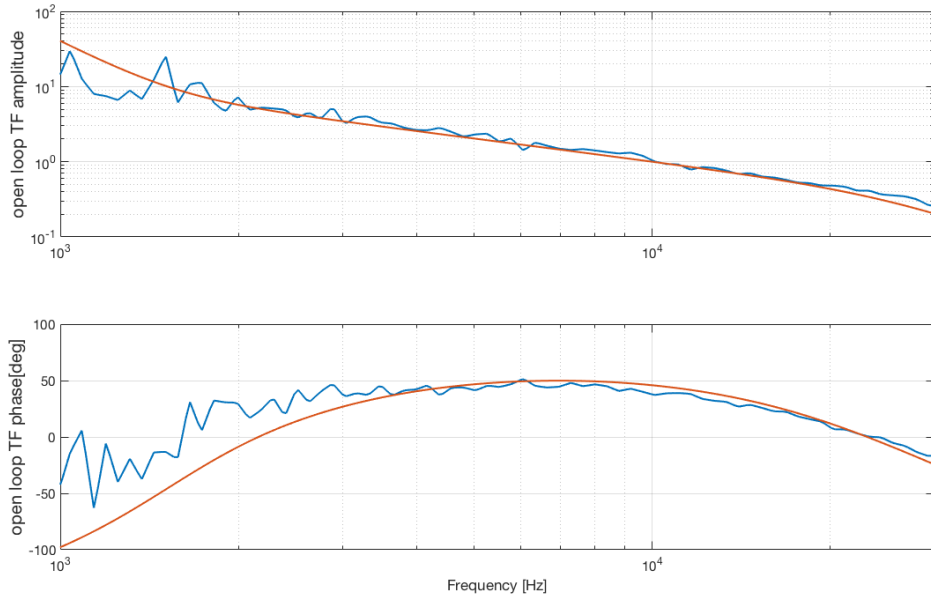


Figure 9.30: Measurement of the open loop lock transfer function (blue line) which has been fitted (orange line) with the poles and zeros reported in Tab. 9.10.2

Sec. E) The UGF is at ~ 10 Hz as expected and the phase margin is 42° degree. The transfer function, shown in Fig. 9.30 has been fitted by the following set of poles and zeroes.

zeros	Q	quantity	origin
145 Hz	simple	1	servo
1.54 kHz	simple	4	servo
poles	Q	quantity	origin
0.0001 Hz	simple	5	servo
1.45 kHz	simple	1	cavity
27 kHz	simple	1	piezo
36.2 kHz	simple	1	cavity
145 kHz	simple	1	servo
154 kHz	simple	1	servo
118 kHz	0.79	1	servo

Cavity transmitted power

The power exiting the SHG is supposed to be stabilized by using a Mach-Zehnder interferometer. Since it has not been installed yet, cavity input power suffers from large power fluctuation. Plot in Fig. 9.31 compares the transmitted power and the input power measured at the reflection of a temporary beam splitter which is installed at the place of Mach-Zehnder interferometer. As expected, the two fluctuations are

correlated.

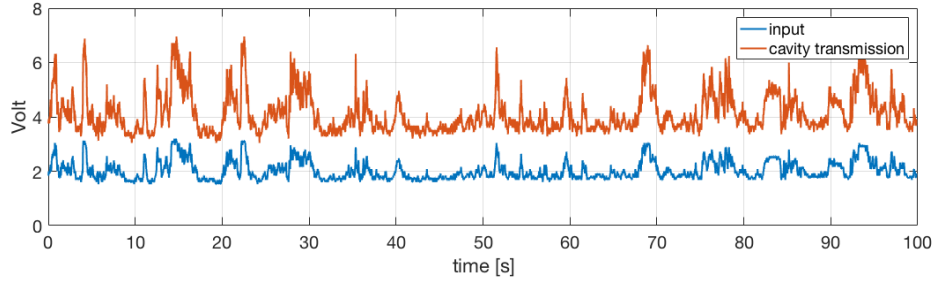


Figure 9.31: Top plot: power fluctuations of the input and transmitted beam. Bottom plot: coherence between the two measurements.

9.10.3 Conclusion and future plans

The results of the presented work on the integration and commissioning of the filter cavity can be summarized as follows:

- Cavity mirrors have been suspended and controlled.
- Injection optics have been installed and the injection mode-matching telescope have been tuned.
- The SHG is working and a part of the green light produced have been used for the cavity control.
- The cavity has been stably locked on the laser frequency with green light.
- The infrared beam used to characterize the cavity has been superposed to the green beam.
- AOM used for shifting the relative frequency of green and infrared beam has been installed.⁸

The lock accuracy achievable with the actual compensation filter is about 100 Hz. Since it is larger then cavity linewidth of the IR beam (~ 100 Hz), we have planned to modify the filter shape, increasing the gain at high frequency where most of the RMS is accumulated. The possibility to use an EOM to increase the loop bandwidth is being studied. The goal will be to increase the lock accuracy below 1Hz RMS in order to make negligible its effect on the squeezing degradation induced by frequency dependent phase noise (described in Sec. 8.3). The next step for what concern the filter cavity will be to tune the AOM frequency shift to make also the IR beam resonate. In this condition we will be able to characterize the cavity and measure

⁸In the final configuration the squeezed IR beam should be detuned at half of its bandwidth, to obtain the proper frequency dependance.

its round trip losses. For what concern the assembly of the squeezed vacuum source the main milestones will be the realization of the OPO cavity for the squeezing production and the of homodyne detection to measure it. Finally we will inject squeezed vacuum into the filter cavity to impress a frequency dependance on the angle of the squeezing ellipse.

Conclusions - Part III

This last part of the thesis was described the design and realization of a 300 m filter cavity for the production of frequency dependent squeezing. The goal of this experiment is to demonstrate for the first time the effectiveness of such a device in producing squeezed vacuum state with rotation angle ~ 70 Hz, to reduce quantum noise in the whole detector bandwidth. We studied the optical design of the cavity and its integration in the TAMA infrastructure. In the following we summarized our main results obtained:

- We studied the effect of optical losses by performing simulations with real mirror maps and in parallel we produced a squeezing degradation budget taking into account all the mechanisms responsible for reducing the squeezing level. From the results of these two studies we set the round trip losses threshold to 80 ppm (corresponding to Virgo quality mirrors). We found that in this condition (starting from 9 dB of squeezing) the available squeezing is limited to 4 dB by realistic mismatching losses (7%) below 100 Hz and to 6 dB by realistic input output losses (5% each) above 100 Hz. This results together with the expected improvement in KAGRA sensitivity have been published in [151].
- We also studied the degradation induced by losses inside the ITF. We have found out that their contribution (mainly due to signal recycling cavity losses) is below 1.5 dB for the expected losses values (arm RTL of 100 ppm and signal recycling of 2000 ppm) and it doesn't compromise the results obtained for the squeezing degradation budget, where they have not been considered.
- We discussed the opportunity to use long (100 m scale) filter cavities for producing frequency dependent squeezing demonstrating that their use, combined with the best mirrors available at present, brings to a negligible squeezing degradation by cavity round trip losses.

We have also compared the performances of long filter cavities with that of the recently proposed EPR-entanglement technique observing that major advantages can be obtain from the latter only reducing input and output losses below 5%

- In the last chapter we have described the experimental work performed both on the realization of the frequency independent vacuum squeezed source and on the filter cavity integration. A second harmonic generator has been assembled and the 300 m filter cavity has been locked by using green light. The completion of squeezed vacuum source as well as some improvements on the lock accuracy and cavity characterization are planned for the next future. Once this will be achieved, the two components will be combined to obtain frequency dependent squeezed vacuum.

CHAPTER 10

Conclusions and perspectives

Second generation gravitational waves detectors have ushered in gravitational-wave astronomy. The first and successive detections of binary black hole mergers and the first detection of a binary neutron star merger have already produced dramatic results for astrophysics and cosmology.

The role of Advanced Virgo, as a part of this network, has already proven to be crucial for contributing to the sky-localization and it is expected to contribute to parameter estimation of the sources. With these strong motivations, a huge effort has been done to speed-up Advanced Virgo commissioning and join Advanced LIGO during O2, participating to the first detection of a BBH merger by three detector and to the first detection of a binary neutron star merger.

My contribution to this commissioning activity has been twofold. First I have realized (and automated) a complete noise budget for the pre-stabilized laser frequency noise. This activity contributed to the reduction of the frequency noise below the requirement necessary for a stable lock of the arm cavities.

Second, I have performed the optical characterization of the arm cavities in order to verify that optical parameters corresponds to the ones expected. A special attention has been payed to the measurement of round trip losses, which have been found to be the lower ever measured with this mirror size (among 65-75 ppm) although twice higher than what we expected from simulation.

The effort to improve second generation detector sensitivity is motivated by strong scientific interests in having more numerous and louder GW detections. This, in the case of BBH or BNS mergers, would allow a more precise estimation of the source parameters, investigation of the neutron star state equation, test GR and alternatives theories, increase precision on Hubble constant estimation and also the measurement of the astrophysical stochastic background.

The third part of this work is dedicated to test the production of frequency dependent squeezed vacuum as a strategy to mitigate quantum noise. In order to do that we have been implementing a frequency independent vacuum source and a 300 m filter

cavity designed to impress a frequency dependence with a rotation of the squeezed angle of ~ 70 Hz. This is the frequency required to reduce quantum noise in the whole detector bandwidth and it have never been achieved before. We presented a design for the cavity. In particular we have performed FFT simulations to estimate round trip losses due to mirrors defect. These results combined with a squeezing degradation budget allowed to set a requirement for the round trip losses and consequently for the mirror quality. Thanks to this study we could demonstrate that using a long filter cavities, with best mirrors available, the contribution of round trip losses on the total squeezing degradation becomes negligible and the limiting loss sources are the mismatching and the losses in the input and output path. The necessity of a very low loss cavity was one of the motivations to accurately measure the round trip losses of Advanced Virgo arm cavities.

During this thesis I have contributed to the implementation and commissioning of a filter cavity prototype at TAMA. The experience acquired with this prototype will be valuable for the implementation of 100 m scale filter cavities already planned in second generation interferometers upgrades.

The injection of frequency dependent squeezed vacuum from ITF dark port is the most promising technique for reducing quantum noise so far. An alternative way to do that, which exploits the EPR entanglement, has been recently proposed. It has the remarkable advantage to use the ITF itself as a filter cavity, avoiding the use of an additional cavity. Also in this case the factor limiting its effectiveness is represented by losses, mostly by the input-output ones. Whatever the configuration chosen for frequency dependent squeezing implementation, the reduction of losses in the squeezing path (mainly by improving the matching and developing low loss optical components for the input/output path) will be a priority in order to take full advantage of such techniques.

APPENDIX A

Electromagnetic field in Fabry-Perot cavities

Laser beams differ from plane waves since they are confined in a spatial region around the propagation axis and they have slightly curved phase front. We start from a monochromatic beam which is a solution of the Helmholtz equation

$$(\nabla^2 + k^2) E(x, y, z) = 0 \quad (\text{A.1})$$

with $k = \omega/c$. and we look for solutions of the form

$$E(x, y, z) = \phi(x, y, z)e^{-ikz} \quad (\text{A.2})$$

It represents a wave propagating in the z direction, with $\phi(x, y, z)$ accounting for the changing intensity distribution in the transversal plane. The fact that the change in the beam profile varies very slowly with z allows us to neglect its second order derivatives $\partial^2\phi/\partial z^2$. Therefore by inserting Eq. A.2 in Eq. A.1 we obtain

$$\left(\frac{\partial^2}{\partial x^2} + \frac{\partial^2}{\partial y^2} - 2ik \frac{\partial}{\partial z} \right) \phi(x, y, z) = 0 \quad (\text{A.3})$$

which is known as *paraxial wave equation*.

The simplest solution with cylindrical symmetry is referred to as *Gaussian fundamental mode* and reads

$$E(r, z) = E_0 \frac{w_0}{w(z)} \exp \left(i\eta(z) - \frac{ikr^2}{2R(z)} - \frac{r^2}{w^2(z)} - ikz \right) \quad (\text{A.4})$$

In the following some relevant quantities are defined:

- **Beam radius w** - radius where the beam equals a fraction $1/e \simeq 0.368$ of the amplitude on the axis.
- **Radius of curvature R** - radius of curvature of the wavefront.
- **Beam waist w_0** - minimum radius of the beam.

- **Rayleigh range** - defined as

$$z_R = \frac{\pi w_0^2}{\lambda} \quad (\text{A.5})$$

is the distance along the propagation direction of a beam from the waist to the place where the radius has increased of a factor $\sqrt{2}$. It distinguish the *near field* region ($z \ll z_R$), where the wavefront is almost flat and the radius almost constant from the *far field* region ($z > z_R$), where the radius increases linearly and the wavefront curvature is equal to the distance from the waist. The evolution of the beam radius and radius of curvature can be written as:

$$w(z) = w_0 \sqrt{1 + (z/z_R)^2} \quad (\text{A.6})$$

$$R(z) = z(1 + (z/z_R)^2) \quad (\text{A.7})$$

- **Far field divergence** - defined as

$$\theta_0 = \frac{\lambda}{\pi w_0} \quad (\text{A.8})$$

from which is evident that the smaller the waist, the bigger the divergence experienced by the beam.

- **Gouy phase η** - defined as

$$\eta(z) = \arctan \frac{z}{z_R} \quad (\text{A.9})$$

it is an additional phase shift acquired by gaussian beams with respect to plane waves with the same frequency. As we will see in the following, this phase is particularly interesting when we are dealing with Higher Order Modes.

- **Complex Gaussian parameter** - (or **complex radius of curvature**), defined as

$$\frac{1}{q(z)} = \frac{1}{R(z)} - \frac{i}{z_R} \quad (\text{A.10})$$

encodes the beam information and it will proven to be useful to compute its propagation through optical systems. Its free evolution is described by the equation:

$$q(z) = iz_R + z \quad (\text{A.11})$$

More general solutions of the paraxial wave equation can be found both in cartesian or cylindrical coordinates. In the first case we have higher-order Hermite-Gaussian

(HG) modes, defined as

$$E(x, y, z)_{m,n} = E_0 \frac{w_0}{w(z)} H_m \left(\frac{\sqrt{2}x}{w(z)} \right) H_n \left(\frac{\sqrt{2}y}{w(z)} \right). \quad (\text{A.12})$$

$$\exp \left(i\eta(z)(m+n+1) - \frac{ikr^2}{2q(z)} - ikz \right) \quad (\text{A.13})$$

Where H_m are the Hermite polynomials. The horizontal index m and the vertical index n identifies each HG mode and determine its intensity distribution on the transversal plane. Also the Gouy phase depends of the mode order. The transverse power profiles of the first modes is shown in Fig. A.2. Solutions in cylindrical coordinates are known as Laguerre-Gauss (LG) modes and are defined by:

$$E(x, y, z)_{m,n} = E_0 \frac{w_0}{w(z)} \left(\frac{\sqrt{2}r}{w(z)} \right)^{|l|} L_p^{(|l|)} \left(\frac{2r^2}{w^2(z)} \right). \quad (\text{A.14})$$

$$\exp \left(i\eta(z)(2p+l+1) - \frac{ikr^2}{2q(z)} + il\phi - ikz \right) \quad (\text{A.15})$$

Where L_m are the generalized Laguerre polynomials. The radial index p and the azimuthal index l identifies each LG mode. Also in this case the Gouy phase depends on the mode order.

It is easy to verify that the fundamental modes is recovered when $m = n = 0$ for HG modes and $p = l = 0$ for LG modes.

Beam propagation and cavity modes

We have seen that the complex parameter q defined in Eq. A.10 contains all the information about the beam. In order to propagate it through an optical system, it is possible to associate a 2×2 matrix, called *ray transfer matrix*, to any optical component and use it to compute the relation between q parameters of the beam at the input and at the output of each of them. If $M = \begin{bmatrix} A & B \\ C & D \end{bmatrix}$ is the ray transferred matrix of an optical system (usually also referred to as ABCD matrix). The relation has the form

$$q_{\text{out}} = \frac{Aq_{\text{in}} + B}{Cq_{\text{in}} + D} \quad (\text{A.16})$$

For what concern a Fabry-Perot cavity, the most relevant are the ones describing the free propagation over a distance d and that describing the reflection from a mirror with RoC R . They write respectively

$$M_p = \begin{bmatrix} 1 & d \\ 0 & 1 \end{bmatrix} \quad M_m = \begin{bmatrix} 1 & 0 \\ -\frac{2}{R} & 1 \end{bmatrix} \quad (\text{A.17})$$

The ABCD matrix associated with a round trip in a Fabry-Perot cavity is then $M^{RT} = M_m(R_2)M_p(d)M_m(R_1)M_p(d)$.

Eigenmodes of the cavity are self-consistent field configurations which reproduce themselves after one round trip. The associated q parameter is solution of the equation

$$q = \frac{M_{11}^{RT} q_{\text{in}} + M_{12}^{RT}}{M_{21}^{RT} q_{\text{in}} + M_{22}^{RT}} \quad (\text{A.18})$$

If equation is solvable the cavity is said to be stable and it verifies the stability condition:

$$0 < \left(1 - \frac{d}{R_1}\right) \left(1 - \frac{d}{R_2}\right) < 1 \quad (\text{A.19})$$

From q we can compute the value of the waist w_0 and its distances d_1 and d_2 from the mirrors (see Fig. A.1) which determine univocally a basis of HG or LG modes matching the cavity geometry. The waist parameters are related to the cavity parameters by the following relations:

$$w_0 = \left(\frac{\lambda}{\pi}\right)^2 \frac{d(R_1 - d)(R_2 - d)(R_1 + R_2 - d)}{(R_1 + R_2 - 2d)^2} \quad (\text{A.20})$$

$$d_1 = \frac{d(R_2 - d)}{R_1 + R_2 - 2d} \quad (\text{A.21})$$

$$d_2 = \frac{d(R_1 - d)}{R_1 + R_2 - 2d} \quad (\text{A.22})$$

We also remark that self-consistency condition implies that wavefront radius of curvature of the beam at the mirrors equals the RoC of mirrors itself.

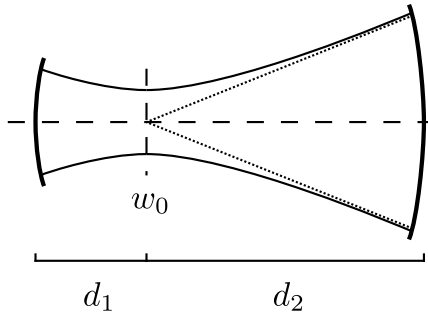


Figure A.1: Matched Gaussian beam profile.

Since the Gouy phase varies with the mode order, different HOMs accumulate different phase shifts during a cavity round trip thus they have different resonance frequencies. The resonance condition reads

$$\nu_\chi = \frac{\text{FSR}}{\pi} \arccos \left(1 - \frac{d}{R_1}\right) \left(1 - \frac{d}{R_2}\right) (\chi + 1) \quad (\text{A.23})$$

Where $\chi = m + n$ for HG modes and $2p + l$ for LG modes.

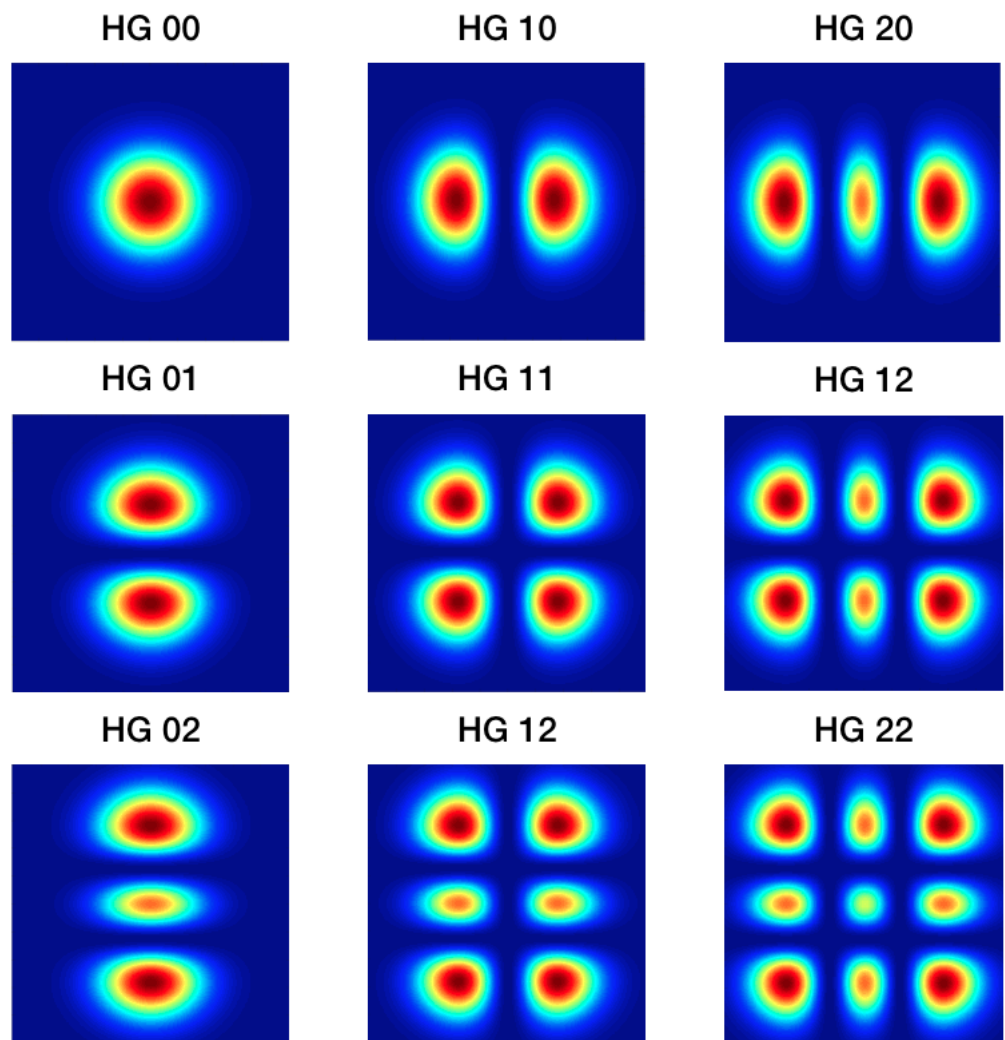


Figure A.2: Transversal power pattern of Hermite-Gauss modes for $m = 0, 1, 2$ and $n = 0, 1, 2$.

APPENDIX B

Round trip losses from reflectivity

Here we present the derivation of the formula used for computing round trip losses from the cavity reflectivity.

The normalized power (assuming P_{in}) reflected by a cavity at the resonance reads:

$$P_{\text{res}} = \left[\frac{r_1 - r_2}{1 - r_1 r_2} \right]^2$$

In our case the end mirror is almost completely reflecting. We can consider the losses as an increased end mirror transmissivity and we have

$$r_2 = \sqrt{1 - T_2 - L} \simeq \sqrt{1 - T_2}$$

So the cavity reflectivity becomes

$$\begin{aligned} P_{\text{res}} &= \left[\frac{r_1 - \sqrt{1 - L}}{1 - r_1 \sqrt{1 - L}} \right]^2 \\ &= \frac{r_1^2 - 2r_1 \sqrt{1 - L} + 1 - L}{1 - 2r_1 \sqrt{1 - L} + r_1^2(1 - L)} \\ &\sim \frac{r_1^2 - r_1(2 - L) + 1 - L}{1 - r_1(2 - L) + r_1^2(1 - L)} \\ &= \frac{(1 - r_1)^2 - (1 - r_1)L}{(1 - r_1)^2 + (1 - r_1)r_1L} \\ &= \frac{(1 - r_1) - L}{(1 - r_1) + r_1L} \end{aligned}$$

where from second to third line we used $\sqrt{1 - L} = 1 - L/2$.

Therefore

$$P_{\text{res}}(1 - r_1 + r_1L) = 1 - r_1 - L,$$

which means

$$L = (1 - r_1) \frac{1 - P_{\text{res}}}{1 + P_{\text{res}} r_1}.$$

With the approximation

$$r_1 = \sqrt{1 - T_1} \sim 1 - \frac{T_1}{2}$$

we get

$$\begin{aligned} L &= \frac{T_1}{2} \frac{1 - P_{\text{res}}}{1 + P_{\text{res}} - \frac{T_1}{2} P_{\text{res}}} \\ &\simeq \frac{T_1}{2} \frac{1 - P_{\text{res}}}{1 + P_{\text{res}}} \end{aligned}$$

APPENDIX C

Injection telescope design

We have computed the beam parameters at each point of the injection optical path by using ABCD matrices. Since the beam parameters on the input mirror are determined by the cavity geometry we have done the computation backwards to find the beam parameters needed at the input of the Faraday isolator. The results (assuming a normal incidence for the beam on the mirror) are reported in Tab. C.1, such parameters for the main beam on the various optics of the system are shown.

C.1 Beam astigmatism

In order to quantify the astigmatism induced on the beam from the non-normal incidence, the beam has also been propagated separately on the x and on y plane. The ABCD matrix describing the reflection from a mirror with radius of curvature R for a beam with incidence angle θ on the x and on y plane is respectively

$$M_x = \begin{pmatrix} 1 & 0 \\ \frac{-2}{R \cos \theta} & 1 \end{pmatrix} \quad (\text{C.1})$$

	x [mm]	x' [mrad]	R [m]	w [mm]	w_0 [mm]	Z [m]
IM	0.0	0.1800	286.2069	10.2850	6.9485	155.5722
FM	0.3816	0.1800	286.5707	10.3614	6.9485	157.6922
$M_2(\text{in})$	0.86544	0.1800	287.0986	10.4590	6.9485	160.3802
$M_2(\text{out})$	0.86544	-0.10848	-3.0317	10.4590	0.0982	-3.0314
$M_1(\text{in})$	0.56893	-0.10848	-0.3008	1.0331	0.0982	-0.2981
$M_1(\text{out})$	0.56893	1.7879	113.0578	1.0331	1.0327	0.0878
IF	5.3749	1.7879	6.3475	1.3766	1.0327	2.7758

Table C.1: Propagation for the main beam through the telescope without taking into account non-normal incidence on the mirrors.

$$M_y = \begin{pmatrix} 1 & 0 \\ \frac{-2}{R/\cos\theta} & 1 \end{pmatrix} \quad (\text{C.2})$$

The results of the propagation for the main beam are shown in Tab. C.2

	R _x [m]	R _y [m]	w _x [mm]	w _y [mm]	w _{0x} [mm]	w _{0y} [mm]	Z _x [m]	Z _y [m]
IM	268.2069	268.2069	10.2850	10.2850	6.9485	6.9485	155.5722	155.5722
FM	286.5707	286.5707	10.3614	10.3614	6.9485	6.9485	157.6922	157.6922
M ₂ (in)	287.0986	287.0986	10.4590	10.4590	6.9485	6.9485	160.3802	160.3802
M ₂ (out)	-3.0296	-3.0338	10.4590	10.4590	0.0981	0.0982	-3.0293	-3.0335
M ₁ (in)	-0.2987	-0.3029	1.0266	1.0396	0.0981	0.0982	-0.2960	-0.3002
M ₁ (out)	60.3079	33.6877	1.0266	1.0396	1.0252	1.0350	-0.1601	0.2996
IF	6.3382	6.3362	1.3223	1.4237	1.0252	1.0350	2.5279	2.9876

Table C.2: Propagation for the main beam through the telescope taking into account non-normal incidence on the mirrors.

Overlap integral

The losses due to the astigmatism can be quantified calculating the overlap integral between the astigmatic beam and the closest TEM₀₀. A generic astigmatic beam at a distance z from the waist can always be written as:

$$E_a(z) = N_a \exp \left[i\eta_a(z) - ik \left(\frac{x^2}{2q_x(z)} + \frac{y^2}{2q_y(z)} \right) \right] \quad (\text{C.3})$$

where η_a is the Gouy phase and the normalization factor is

$$N_a = \sqrt{\frac{k\sqrt{z_{Rx}z_{Ry}}}{\pi q_{x(z)}q_{y(z)}}} \quad (\text{C.4})$$

with

$$q_{x,y}(z) = z - iz_{Rx,y} \quad (\text{C.5})$$

where

$$z_{Rx,y} = \frac{\pi\omega_{0x,y}^2}{\lambda} \quad (\text{C.6})$$

The non-astigmatic fundamental mode E_b is recovered assuming $q_x = q_y = q$. The overlap integral is defined as

$$O = \iint E_a^* E_b dx dy \quad (\text{C.7})$$

and its square modulus is

$$|O|^2 = \left(\frac{z_R}{|q(z)|^2} \frac{\sqrt{z_{Rx}z_{Ry}}}{|q(z)_x q(z)_y|} \right)^2 \left| \frac{1}{(\frac{1}{2q_x(z)} - \frac{1}{2q})(\frac{1}{2q_y(z)} - \frac{1}{2q})} \right|^2 \quad (\text{C.8})$$

This is a complex function with real values which can be maximize to find the best possible coupling. For our system we find a coupling of 99.73%. The parameters of the fundamental mode which maximize the coupling correspond to the mean value between x and y of the waist position and radius of curvature.

C.2 Spherical aberrations

The beam phase change due to a reflection by a spherical mirror is $4\pi z(x, y)/\lambda$ where z is the mirror surface equation $z(x, y) = R - \sqrt{R^2 - (x^2 + y^2)}$ which after an expansion to the second order becomes [152]:

$$z(x, y) = \frac{x^2 + y^2}{2R} \left(1 + \frac{x^2 + y^2}{4R} \right) \quad (\text{C.9})$$

The first fraction represents the usual paraboloidal approximation for the phase change while the second fraction is the correction due to the actual spherical shape of the mirror. Such a correction is negligible if $\omega^2/R^2 \ll 1$ where ω is the typical size of the beam on the mirror. This is the case for all the mirrors in the injection path, thus we can neglect the effect of spherical aberrations.

C.3 Losses due to mirror defects

Defects of the mirror make not all the incident light be reflected on the fundamental mode. This light is considered lost for our scopes. An estimation of the amount of lost light has been done in simulation by reflecting a beam from a mirror with a realistic mirror map and computing the overlap integral between the reflected and the transmitted beam. Because of the small radius of curvature of the mirrors composing the telescope, specification on the mirror flatness can not be too good. A peak-valley value of $\frac{\lambda}{10}$ is assumed, where $\lambda = 633$ nm. Mirror maps from Virgo are generally better than that. To perform the simulation we re-scaled the maps values in order to have a PV value of $\frac{\lambda}{10}$ on a diameter of 4 cm. The beam dimension assumed in the calculation is 0.01 m. The result for different maps are shown in Tab. C.3 where we also reported the RMS obtained after the rescaling. The same has been done for a pick-valley value of $\frac{\lambda}{20} = 31.65$ nm. The relative results are shown in Tab. C.4.

mirror	pv_initial [nm]	rms [nm]	rms_res [nm]	coupling
VEM01	8.26	1.28	9.80	0.9906
VEM04	7.34	1.06	9.13	0.9899
ADV1	6.90	0.26	2.37	0.9983
VEM09	6.97	1.11	10.18	0.9929
VEM10	6.27	0.74	7.47	0.9922

Table C.3: Losses due to reflection of a telescope mirror assuming a peak-to-valley value of $\frac{\lambda}{10} = 63.3$ nm.

mirror	pv_initial [nm]	rms [nm]	rms_res [nm]	coupling
VEM01	8.26	1.28	4.90	0.9977
VEM04	7.34	1.06	4.57	0.995
ADV1	6.90	0.26	1.18	0.9996
VEM09	6.97	1.11	5.05	0.9982
VEM10	6.27	0.74	3.73	0.9980

Table C.4: Losses due to reflection of a telescope mirror assuming a peak-to-valley value of $\frac{\lambda}{20} = 31.65$ nm.

APPENDIX D

Local control: transfer functions computation

The digital control system is programmed in labVIEW. Programs developed for the control, named VIs (virtual instruments), are all part of a single project. Some of them run on remote realtime targets and others on a supervisor PC. VIs running on the remote target use a *timed loop* structure that runs synchronously with a clock. The loop rate is set to 1 kHz. The ADC and DAC are read and written at the beginning and end of the loop, respectively. The delay caused by the digital system has been measured looking at the phase of the transfer function between the input and the output of the system and it is shown in Fig. D.1. Digital filter coefficients

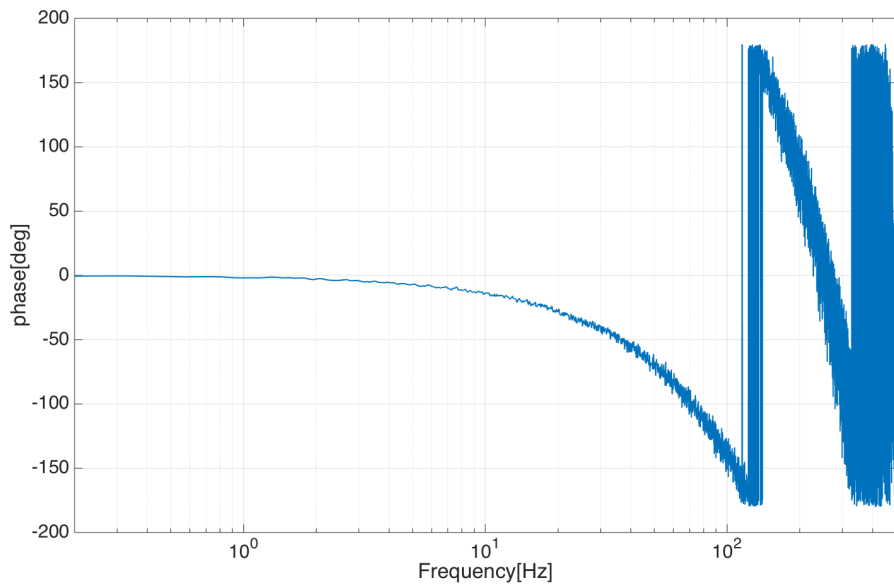


Figure D.1: Delay of the digital system

are calculated on the supervisor PC and saved in *global variable* which is passed to the realtime target. The main VIs of the project are:

- **IM_control.vi:** It is the core control where data coming from ADC (input

data) are filtered and passed to DAC (output data). It has the possibility to inject noise at different point in the data path. Injected noise, input and output data are saved in *shared variable* which are recalled from other VIs to compute spectra or transfer functions. It is also possible to add offset to the input data and to open the loop in different points. A scheme of the data path for each degree of freedom is show in Fig. D.2.

- `spectrum.vi`: It computes the spectrum of the input data between 0.08 Hz and 500 Hz. Default data length is 12288 points.
- `transfer_function.vi`: It can perform transfer functions between the injected noise and either input or output data. According to the scheme in Fig. D.2, with a proper combination of open switches and injected noise we can measure mechanical transfer functions of the mirrors, open loop transfer function and close loop transfer function.
- `my_filter_bank.vi`: This code run on the supervisor PC. It has an interface to set filters for each degree of freedom. it is possible to save filter parameters in a .txt file in order to recall them. Filter values can be changed online. The code computes filter coefficients and store them in a global variable which is read from the control VI.

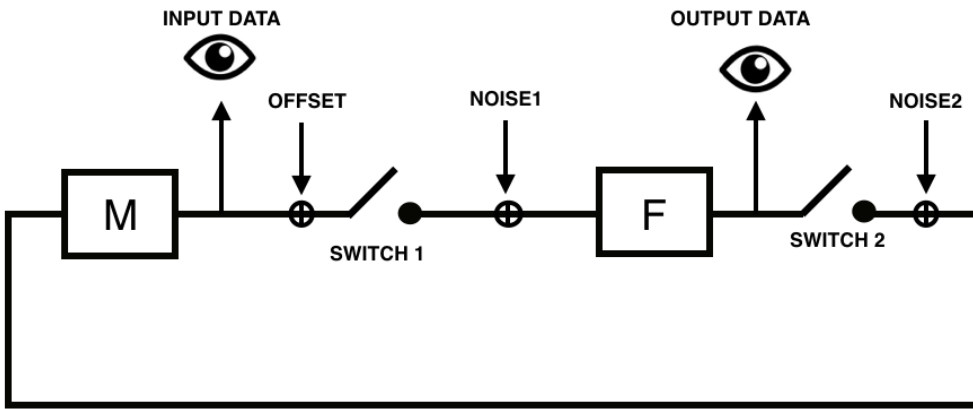


Figure D.2: Scheme of the control loop for the three degree of freedom

Transfer functions recap

From the scheme in Fig. D.2 we can find the configuration of switches and noise and the channels to use in `transfer_function.vi` to measure the desired transfer function:

Mechanical transfer function

- Switch 1 → open
- Switch 2 → open
- Noise → n_2

$$M = \frac{IN}{n_2} \quad (D.1)$$

Filter transfer function

- Switch 1 → open
- Switch 2 → open
- Noise → n_1

$$F = \frac{OUT}{n_1} \quad (D.2)$$

Open loop transfer function

- Switch 1 → closed
- Switch 2 → open
- Noise → n_2

$$\frac{OUT}{n_2} = -FM \quad (D.3)$$

Closed loop transfer function

- Switch 1 → closed
- Switch 2 → closed
- Noise → n_2

$$OUT = -MF(OUT + n_2)$$

$$OUT(1 + MF) = -MF \cdot n_2$$

$$\frac{OUT}{n_2} = \frac{-FM}{1 + FM}$$

APPENDIX D. LOCAL CONTROL: TRANSFER FUNCTIONS
COMPUTATION

APPENDIX E

Filter cavity optical gain and transfer functions

The filter cavity input beam is modulated by using a resonant electro-optic phase modulator (EOM) driven at 78MHz. Such a device is composed by a crystal, whose change in the refraction index is linearly dependent by the presence on an electric field (Pockel effect). The electric field, perpendicular to the direction of the laser beam propagation, is proportional to the applied voltage V divided by the crystal thickness d . The induced change in the reflection index is

$$\Delta n = \frac{n_e^3 r_{eo}}{2d} V$$

where n_e is the unperturbed refraction index and r_{eo} is the opportune component of the electro-optic tensor of the crystal. The phase shift generated by this change is

$$m = \frac{2\pi}{\lambda} l \Delta n = \frac{\pi l n_e^3 r_{eo}}{\lambda d} V$$

If we apply a sinusoidal driving voltage $V \sin(\Omega t)$, the beam exiting the EOM has the form

$$E_{in} = E e^{i\omega t + m \sin \omega t}$$

which can be expanded in terms of Bessel functions of the first kind as ¹

$$E_{in} = E [J_0(m) e^{i\omega t} + J_1(m) e^{i(\omega + \Omega)t} - J_1(m) e^{i(\omega - \Omega)t}]$$

This shows that the phase modulation has created two sidebands at a distance Ω from the carrier, whose amplitude depends on the modulation depth. The reflectivity of the filter cavity for the green light can be written as

¹ According to Jacobi-Anger expansion $E e^{i(\omega t + m \sin \omega t)} = E e^{i\omega t} \sum_{n=-\infty}^{n=+\infty} J_k(m) e^{i n \Omega t}$. Since the amplitude of the Bessel function decreases with k , if $m \ll 1$ we can keep only the first term of the expansion.

$$R_{cav} = \frac{-r_1 + r_2 \exp(i\frac{\omega}{FSR})}{1 - r_1 r_2 \exp(i\frac{\omega}{FSR})}$$

and the beam reflected from the cavity is

$$E_{ref} = E[R_{cav}(\omega)J_0(m)e^{i\omega t} + R_{cav}(\omega+\Omega)J_1(m)e^{i(\omega+\Omega)t} - R_{cav}(\omega-\Omega)J_1(m)e^{i(\omega-\Omega)t}]$$

from that we can compute the power impinging on the photodiode

$$\begin{aligned} P_{ref} = & P_c |R_{cav}(\omega)|^2 + P_s (|R_{cav}(\omega+\Omega)|^2 + |R_{cav}(\omega-\Omega)|^2) \\ & + 2\sqrt{P_c P_s} [\Re[R_{phs}] \cos \Omega t + \Im[R_{phs}] \sin \Omega t] \end{aligned}$$

with $P_c = P_0 J_0^2(m)$, $P_s = P_0 J_1^2(m)$ and $R_{phs} = R_{cav}(\omega)R_{cav}^*(\omega+\Omega) - R_{cav}^*(\omega)R_{cav}(\omega-\Omega)$.

The reflected power is composed by a DC part and two terms oscillating at the modulation frequency, whose amplitude is proportional respectively to the imaginary and real part of the function R_{phs} and thus keep the important information on the phase of the reflected beam. These terms arise from the beating of the carriers and the sidebands. We neglect the beating of each sidebands with the others. In order to extract the phase information contained in the oscillating terms, the signal, recorded by a photodiode with a bandwidth up to 100 MHz, is demodulated by mixing it with a local oscillator at the modulation frequency, with the phase opportunely tuned in order to select one of the two oscillating terms. If the modulation frequency is higher then the cavity linewidth ($\Omega > FSR/F$), as in our case,² near the resonance $R_{cav}(\omega \pm \Omega) \simeq -1$ thus $R_{phs} = i2\Im(R_{cav}(\omega))$ is purely imaginary and only the part proportional to the sine survives. The error signal, after the demodulation, will be

$$\text{Err} = G_{PD} G_{MIX} 2\sqrt{P_c P_s} \Im(R_{phs}) \simeq G_{PD} G_{MIX} 2P_0 m \Im(R_{cav}(\omega))$$

where G_{PD} , G_{MIX} G_{LPF} are respectively, the gain of the photodiode, the gain of the mixer and the gain of the low pass filter. The last equality holds in the region where sidebands are not resonant, as can be seen in picture E.3 and we made the approximation $\sqrt{P_0 P_1} \simeq P_0 m/2$. As expected the error signal is linear around the region where it crosses the zero. Once the lock is acquired, the frequency of the laser will be controlled in order to be always about the resonance. The linear coefficient of the error signal about the zero point, also known as optical gain, will tell us how many Watt correspond to a shift of 1 Hz of the laser frequency from the resonance. Around $\omega = 0$ we have

$$\Im(R_{cav}) = \frac{r_2(1 - r_1^2)}{FSR \cdot (1 - r_1 r_2)^2} \cdot \omega$$

²In this case the modulation frequency is higher than the FSR, in order not to have resonant sidebands it should be $\Omega \bmod FSR > dv$.

switching to $f = \omega/2\pi$ the linearised error signal will be

$$\text{Err} = G_{\text{PD}} G_{\text{MIX}} \underbrace{\frac{4mP_0}{\text{FSR}} \frac{\pi r_2(1 - r_1^2)}{(1 - r_1 r_2)^2} f}_{G_{\text{OPT}}[\text{W/Hz}]}$$

We remark that if $r_2 = r_1 \simeq 1$ the optical gain assumes the simpler form

$$G_{\text{OPT}}[\text{W/Hz}] = 4mP_0 \frac{\text{finesse}}{\text{FSR}} = \frac{4mP_0}{dv}$$

The peak of the error signal occurs at half hight of the transmitted power curve at a frequency $dv/2$. It can be observed that the value at the maximum is roughly half of the value of the linearized error signal at the same frequency detuning. The peak-to-peak (PP) error signal value can be calculated from the optical gain by multiplying it by $dv/2$ ³ Using $dv = \text{FSR}/\text{finesse}$ it can be written as

$$\text{Err}_{\text{PP}}[\text{V}] = 2mP_0 \frac{\pi}{\text{Finesse}} \frac{r_2(1 - r_1^2)}{(1 - r_1 r_2)^2} \cdot G_{\text{PD}} G_{\text{MIX}} = 1665 \cdot m \cdot P_0 \text{ V}$$

In order to have an error signal of 200 mV (a tentative value needed for a correct operation of the servo), the modulation depth m and the input power P_0 should combine as shown in Fig. E.1. It is useful to remark that the RF max power impinging on the photodiode is

$$P_{\text{RF}}^{\text{max}}[\text{W}] = mP_0 \frac{\pi}{\text{Finesse}} \frac{r_2(1 - r_1^2)}{(1 - r_1 r_2)^2} = 0.39 \cdot m \cdot P_0 \text{ W}$$

Parameter	Value
PD amplifier gain	$16 \cdot 10^3 \text{ [V/A]}$
PD photosensitivity	0.27 [A/V]
G_{SHG}	2 [Hz/Hz]
G_{PD}	$4.3 \cdot 10^3 \text{ [V/W]}$
G_{OPT}	$1.3 \cdot 10^{-8} \text{ [W/Hz]}$
G_{MIX}	0.5 [V/V]

Table E.1: Filter cavity gains summary.

Loop scheme

A scheme of the cavity lock feedback loop is sketched in Fig. E.4. Different blocks are detailed in Sec. 9.10.1 If we define $G = G_1 \cdot G_2 \cdot G_3 \cdot G_4$ the open loop transfer function is simply $H \cdot G$. The scheme shows points where we can read signals and points

³The factor 2 accounting for the difference from the error signal and its linearization is compensated by the factor 2 needed to pass from the peak to the peak-to-peak value.

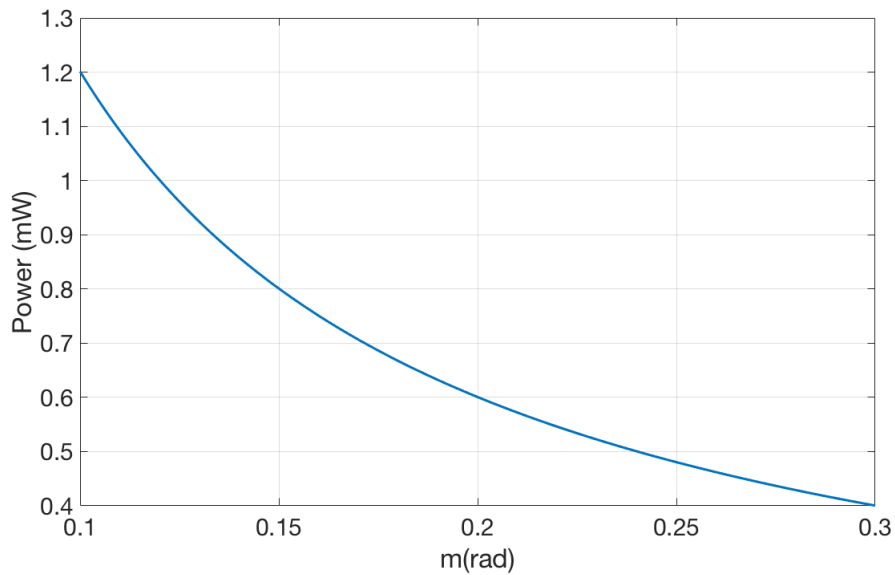


Figure E.1: The points on the curves show the relation between m and P_0 needed to have $\text{Err}_{pp} = 200 \text{ mV}$.

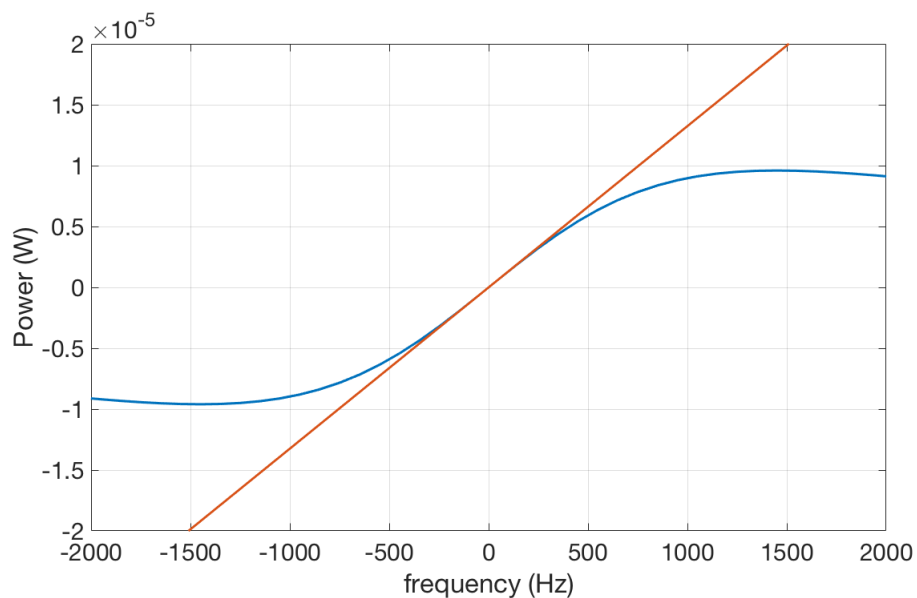


Figure E.2: Comparison between the PDH error signal and its linearisation around zero.

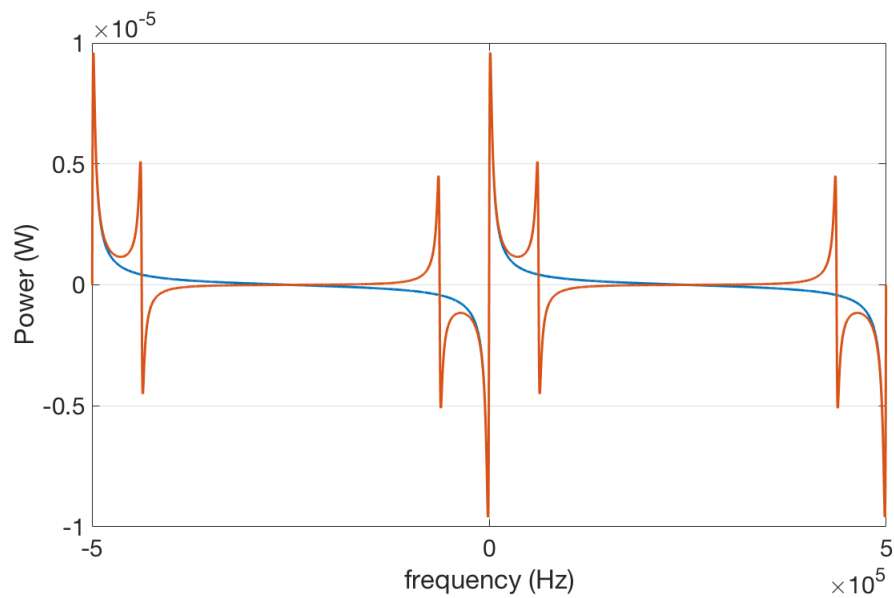


Figure E.3: Comparison between the PDH error signal (orange line) and its approximation (blue line) assuming $R_{\text{cav}}(\omega \pm \Omega) \simeq -1$ that, as can be seen, is valid only in the regions where the sidebands are not resonant.

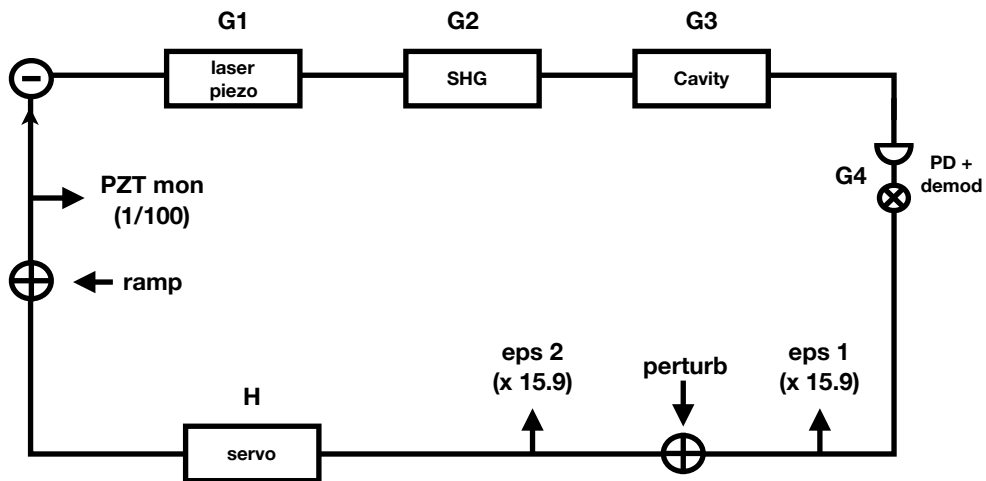


Figure E.4: Scheme of the cavity lock feedback loop.

where we can inject noise. By choosing the appropriate combination of observation and injection points we can measure different parts of the loop transfer function. In particular:

- $H \cdot G \rightarrow$ OPEN LOOP TF

Injection point: perturb

TF channels: EPS1/EPS2

Note: Open loop transfer function is show in Fig. 9.30. It allows to measure the UGF and the phase margin. The measurement is not good at low frequency where the gain of the loop is higher. At these frequency we are not able to inject enough noise to dominate the error signal without unlocking.

- $H \rightarrow$ SERVO TF

Injection point: perturb

TF channel: PZTmon/EPS2

Note: The measurement, shown in Fig. E.5, was performed with a swept sine and no information on the coherence is available. Even though the measurement is not very good, it seems to show the correct slope and it becomes flat in the UGF region, as expected.

- $G \rightarrow$ OPTICAL TF

Injection point: ramp

TF channel: EPS2/PZTmon

Note: The blocks composing G should frequency independent up to few tens of kHz except for the cavity which i supposed a pole at 1.45 KHz. Being able to fit the pole frequency would allow a measurement of the cavity finesse. Also in this case, the amount of noise we could inject without unlocking was not high enough to provide a clear measurement. The TF shown in Fig. E.6 seems to decrease at 1/f in the UGF frequency as expected, but the phase's measurement is very bad and it is not possible to extrapolate a value for the cavity pole.

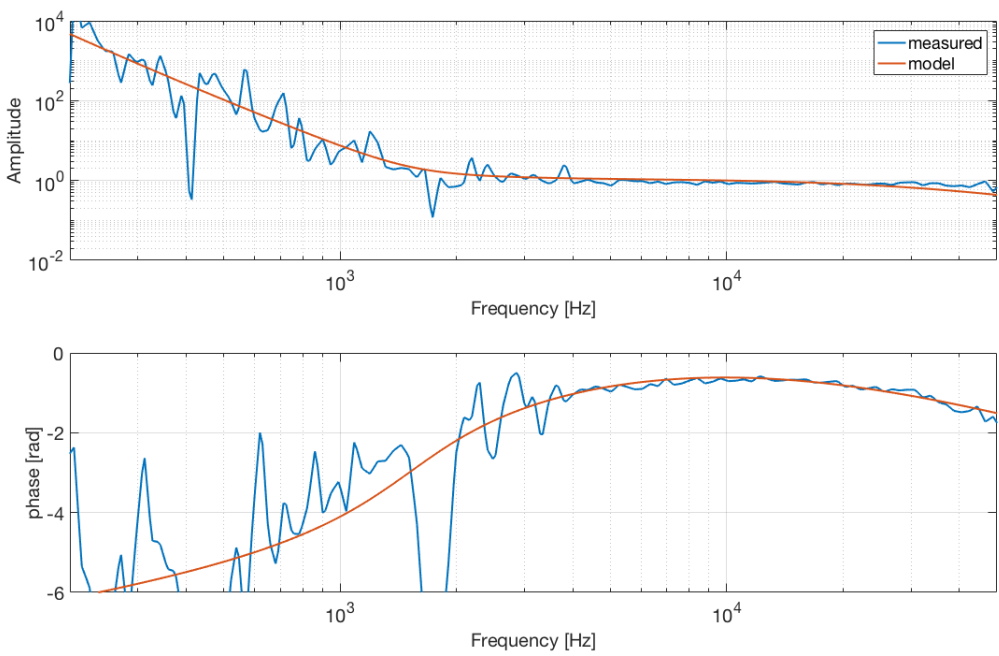


Figure E.5: Electronic transfer function.

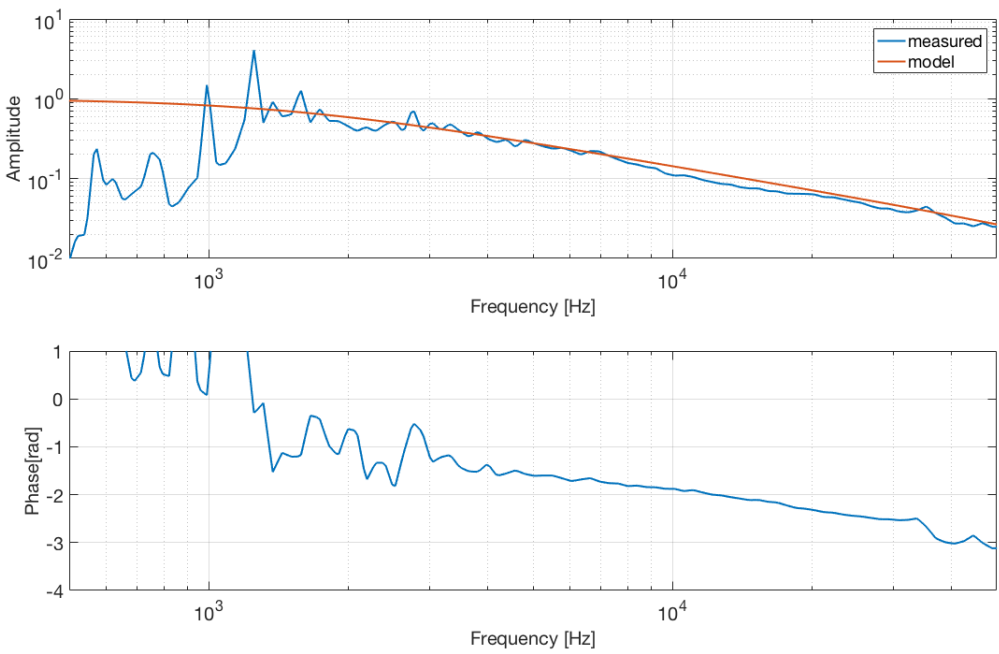


Figure E.6: Optical transfer function. The frequency dependence should be given by the cavity pole. The amplitude is compared with a model given by a simple pole at 1.45 kHz.

Bibliography

- [1] A. Einstein, “Zur Elektrodynamik bewegter Körper”, *Annalen der Physik* **322** no. 10, (1905) 891–921.
- [2] A. Einstein, “Die Grundlage der allgemeinen Relativitätstheorie”, *Annalen der Physik* **354** no. 7, (1916) 769–822.
- [3] M. Maggiore, *Gravitational Waves: Volume 1: Theory and Experiments*. Oxford University Press, 2007.
- [4] P. Saulson, *Fundamentals of Interferometric Gravitational Wave Detectors*. World Scientific, 1994.
- [5] **LIGO Scientific Collaboration and Virgo Collaboration**, B. P. Abbott *et al.*, “GW170817: Observation of Gravitational Waves from a Binary Neutron Star Inspiral”, *Phys. Rev. Lett.* **119** (Oct, 2017) 161101.
- [6] S. E. Gossan, P. Sutton, A. Stuver, M. Zanolin, K. Gill, and C. D. Ott, “Observing gravitational waves from core-collapse supernovae in the advanced detector era”, *Phys. Rev. D* **93** (Feb, 2016) 042002.
- [7] S. J. Bell and A. Hewish, “Angular Size and Flux Density of the Small Source in the Crab Nebula at 81.5 Mc/s”, *Nature* **213** no. 5082, (03, 1967) 1214–1216.
- [8] N. Andersson, V. Ferrari, D. I. Jones, K. D. Kokkotas, B. Krishnan, J. S. Read, L. Rezzolla, and B. Zink, “Gravitational waves from neutron stars: promises and challenges”, *General Relativity and Gravitation* **43** no. 2, (2011) 409–436.
- [9] **LIGO Scientific Collaboration and Virgo Collaboration**, B. P. Abbott *et al.*, “Searches for Gravitational Waves from Known Pulsars with Science Run 5 LIGO Data”, *The Astrophysical Journal* **713** no. 1, (2010) 671.
- [10] **LIGO Scientific Collaboration and Virgo Collaboration**, J. Abadie *et al.*, “Beating the Spin-down Limit on Gravitational Wave Emission from the Vela Pulsar”, *The Astrophysical Journal* **737** no. 2, (2011) 93.

- [11] **LIGO Scientific Collaboration and Virgo Collaboration**, J. Aasi *et al.*, “Narrow-band search of continuous gravitational-wave signals from Crab and Vela pulsars in Virgo VSR4 data”, *Phys. Rev. D* **91** (Jan, 2015) 022004.
- [12] T. Regimbau, “The astrophysical gravitational wave stochastic background”, *Research in Astronomy and Astrophysics* **11** no. 4, (2011) 369.
- [13] J. D. Romano and N. J. Cornish, “Detection methods for stochastic gravitational-wave backgrounds: a unified treatment”, *Living Reviews in Relativity* **20** no. 1, (Apr, 2017) 2.
- [14] **LIGO Scientific Collaboration and Virgo Collaboration**, B. P. Abbott *et al.*, “Binary Black Hole Mergers in the First Advanced LIGO Observing Run”, *Phys. Rev. X* **6** (Oct, 2016) 041015.
- [15] T. G. F. Li, W. Del Pozzo, S. Vitale, C. Van Den Broeck, M. Agathos, J. Veitch, K. Grover, T. Sidery, R. Sturani, and A. Vecchio, “Towards a generic test of the strong field dynamics of general relativity using compact binary coalescence”, *Phys. Rev. D* **85** (Apr, 2012) 082003.
- [16] B. D. Lackey and L. Wade, “Reconstructing the neutron-star equation of state with gravitational-wave detectors from a realistic population of inspiralling binary neutron stars”, *Phys. Rev. D* **91** (Feb, 2015) 043002.
- [17] B. F. Schutz, “Determining the Hubble constant from gravitational wave observations”, *Nature* **323** no. 6086, (09, 1986) 310–311.
- [18] **LIGO Scientific Collaboration, Virgo Collaboration, 1M2H Collaboration, Dark Energy Camera GW-EM Collaboration, DES Collaboration, DLT40 Collaboration, Las Cumbres Observatory Collaboration, VINROUGE Collaboration, and MASTER Collaboration**, “A gravitational-wave standard siren measurement of the Hubble constant”, *Nature* (10, 2017) .
- [19] W. Del Pozzo, “Inference of cosmological parameters from gravitational waves: Applications to second generation interferometers”, *Phys. Rev. D* **86** (Aug, 2012) 043011.
- [20] C. Messenger and J. Read, “Measuring a Cosmological Distance-Redshift Relationship Using Only Gravitational Wave Observations of Binary Neutron Star Coalescences”, *Phys. Rev. Lett.* **108** (Feb, 2012) 091101.
- [21] C. Messenger, K. Takami, S. Gossan, L. Rezzolla, and B. S. Sathyaprakash, “Source Redshifts from Gravitational-Wave Observations of Binary Neutron Star Mergers”, *Phys. Rev. X* **4** (Oct, 2014) 041004.

-
- [22] S. R. Taylor, J. R. Gair, and I. Mandel, “Cosmology using advanced gravitational-wave detectors alone”, *Phys. Rev. D* **85** (Jan, 2012) 023535.
 - [23] M. Maggiore, “Gravitational wave experiments and early universe cosmology”, *Physics Reports* **331** no. 6, (2000) 283 – 367.
 - [24] C. M. Caves, “Quantum-mechanical noise in an interferometer”, *Phys. Rev. D* **23** (Apr, 1981) 1693–1708.
 - [25] F. Arduin, E. Stutzmann, M. Schimmel, and A. Mangeney, “Ocean wave sources of seismic noise”, *Journal of Geophysical Research: Oceans* **116** no. C9, (2011) C09004.
 - [26] **Virgo Collaboration**, F. Acernese *et al.*, “Properties of seismic noise at the Virgo site”, *Classical and Quantum Gravity* **21** no. 5, (2004) S433.
 - [27] P. R. Saulson, “Terrestrial gravitational noise on a gravitational wave antenna”, *Phys. Rev. D* **30** (Aug, 1984) 732–736.
 - [28] T. Creighton, “Tumbleweeds and airborne gravitational noise sources for LIGO”, *Classical and Quantum Gravity* **25** no. 12, (2008) 125011.
 - [29] J. C. Driggers, M. Evans, K. Pepper, and R. Adhikari, “Active noise cancellation in a suspended interferometer”, *Review of Scientific Instruments* **83** no. 2, (2012) 024501.
 - [30] H. B. Callen and R. F. Greene, “On a Theorem of Irreversible Thermodynamics”, *Phys. Rev.* **86** (Jun, 1952) 702–710.
 - [31] P. R. Saulson, “Thermal noise in mechanical experiments”, *Phys. Rev. D* **42** (Oct, 1990) 2437–2445.
 - [32] Y. Levin, “Internal thermal noise in the LIGO test masses: A direct approach”, *Phys. Rev. D* **57** (Jan, 1998) 659–663.
 - [33] T. Chalermsongsak, F. Seifert, E. D. Hall, K. Arai, E. K. Gustafson, and R. X. Adhikari, “Broadband measurement of coating thermal noise in rigid Fabry–Pérot cavities”, *Metrologia* **52** no. 1, (2015) 17.
 - [34] K. Yamamoto, H. Hayakawa, A. Okada, T. Uchiyama, S. Miyoki, M. Ohashi, K. Kuroda, N. Kanda, D. Tatsumi, and Y. Tsunesada, “Effect of energy deposited by cosmic-ray particles on interferometric gravitational wave detectors”, *Phys. Rev. D* **78** (Jul, 2008) 022004.
 - [35] B. J. Meers, “Recycling in laser-interferometric gravitational-wave detectors”, *Phys. Rev. D* **38** (Oct, 1988) 2317–2326.

- [36] M. Bassan, *Advanced Interferometers and the Search for Gravitational Waves: Lectures from the First VESF School on Advanced Detectors for Gravitational Waves*. Springer International Publishing, 2014.
- [37] J. Weber, “Detection and Generation of Gravitational Waves”, *Phys. Rev.* **117** (Jan, 1960) 306–313.
- [38] A. Abramovici, W. E. Althouse, R. W. P. Drever, Y. Gürsel, S. Kawamura, F. J. Raab, D. Shoemaker, L. Sievers, R. E. Spero, K. S. Thorne, R. E. Vogt, R. Weiss, S. E. Whitcomb, and M. E. Zucker, “LIGO: The Laser Interferometer Gravitational-Wave Observatory”, *Science* **256** no. 5055, (1992) 325–333.
- [39] R. X. Adhikari, “Gravitational radiation detection with laser interferometry”, *Rev. Mod. Phys.* **86** (Feb, 2014) 121–151.
- [40] H. Grote, A. Freise, M. Malec, G. Heinzel, B. Willke, H. Lück, K. A. Strain, J. Hough, and K. Danzmann, “Dual recycling for GEO 600”, *Classical and Quantum Gravity* **21** no. 5, (2004) S473.
- [41] **LIGO Scientific Collaboration and Virgo Collaboration**, J. Abadie *et al.*, “Search for gravitational waves from low mass compact binary coalescence in LIGO’s sixth science run and Virgo’s science runs 2 and 3”, *Phys. Rev. D* **85** (Apr, 2012) 082002.
- [42] **LIGO Scientific Collaboration and Virgo Collaboration**, J. Aasi, “Search for gravitational waves from binary black hole inspiral, merger, and ringdown in LIGO-Virgo data from 2009–2010”, *Phys. Rev. D* **87** (Jan, 2013) 022002.
- [43] **LIGO Scientific Collaboration and Virgo Collaboration**, J. Abadie *et al.*, “All-sky search for gravitational-wave bursts in the second joint LIGO-Virgo run”, *Phys. Rev. D* **85** (Jun, 2012) 122007.
- [44] B. Abbott, R. Abbott, R. Adhikari, J. Agresti, P. Ajith, B. Allen, R. Amin, and N. Lockerbie, “Implications for the origin of GRB 070201 from LIGO observations”, *Astrophysical Journal* **681** no. 2, (12, 2008) 1419–1430.
- [45] **LIGO Scientific Collaboration and Virgo Collaboration**, B. P. Abbott *et al.*, “An upper limit on the stochastic gravitational-wave background of cosmological origin”, *Nature* **460** no. 7258, (08, 2009) 990–994.
- [46] **LIGO Scientific Collaboration**, Martynov *et al.*, “Sensitivity of the Advanced LIGO detectors at the beginning of gravitational wave astronomy”, *Phys. Rev. D* **93** (Jun, 2016) 112004.

-
- [47] T. Uchiyama, S. Miyoki, S. Telada, K. Yamamoto, M. Ohashi, K. Agatsuma, K. Arai, M.-K. Fujimoto, T. Haruyama, S. Kawamura, O. Miyakawa, N. Ohishi, T. Saito, T. Shintomi, T. Suzuki, R. Takahashi, and D. Tatsumi, “Reduction of Thermal Fluctuations in a Cryogenic Laser Interferometric Gravitational Wave Detector”, *Phys. Rev. Lett.* **108** (Apr, 2012) 141101.
 - [48] B. F. Schutz, “Networks of gravitational wave detectors and three figures of merit”, *Classical and Quantum Gravity* **28** no. 12, (2011) 125023.
 - [49] **LIGO Scientific Collaboration and Virgo Collaboration**, B. P. Abbott *et al.*, “Prospects for Observing and Localizing Gravitational-Wave Transients with Advanced LIGO and Advanced Virgo”, *Living Reviews in Relativity* **19** no. 1, (Feb, 2016) 1.
 - [50] **Virgo Collaboration**, F. Acernese *et al.*, “Advanced Virgo: a second-generation interferometric gravitational wave detector”, *Classical and Quantum Gravity* **32** no. 2, (2015) 024001.
 - [51] L. Pinard, C. Michel, B. Sassolas, L. Balzarini, J. Degallaix, V. Dolique, R. Flaminio, D. Forest, M. Granata, B. Lagrange, N. Straniero, J. Teillon, and G. Cagnoli, “Mirrors used in the LIGO interferometers for first detection of gravitational waves”, *Appl. Opt.* **56** no. 4, (Feb, 2017) C11–C15.
 - [52] **Virgo Collaboration**, M. Lorenzini *et al.*, “The monolithic suspension for the Virgo interferometer”, *Classical and Quantum Gravity* **27** no. 8, (2010) 084021.
 - [53] R. Abbott, R. Adhikari, G. Allen, S. Cowley, E. Daw, D. DeBra, J. Giaime, G. Hammond, M. Hammond, C. Hardham, J. How, W. Hua, W. Johnson, B. Lantz, K. Mason, R. Mittleman, J. Nichol, S. Richman, J. Rollins, D. Shoemaker, G. Stappfer, and R. Stebbins, “Seismic isolation for Advanced LIGO”, *Classical and Quantum Gravity* **19** no. 7, (2002) 1591.
 - [54] **LIGO Scientific Collaboration and Virgo Collaboration**, B. P. Abbott *et al.*, “Observation of Gravitational Waves from a Binary Black Hole Merger”, *Phys. Rev. Lett.* **116** (Feb, 2016) 061102.
 - [55] **LIGO Scientific Collaboration and Virgo Collaboration**, B. P. Abbott *et al.*, “Properties of the Binary Black Hole Merger GW150914”, *Phys. Rev. Lett.* **116** (Jun, 2016) 241102.
 - [56] D. Keitel, X. J. Forteza, S. Husa, L. London, S. Bernuzzi, E. Harms, A. Nagar, M. Hannam, S. Khan, M. Pürrer, G. Pratten, and V. Chaurasia, “The most powerful astrophysical events: Gravitational-wave peak luminosity of binary black holes as predicted by numerical relativity”, *Phys. Rev. D* **96** (Jul, 2017) 024006.

- [57] **LIGO Scientific Collaboration and Virgo Collaboration**, B. P. Abbott *et al.*, “GW170814: A Three-Detector Observation of Gravitational Waves from a Binary Black Hole Coalescence”, *Phys. Rev. Lett.* **119** (Oct, 2017) 141101.
- [58] S. Fairhurst, “Source localization with an advanced gravitational wave detector network”, *Classical and Quantum Gravity* **28** no. 10, (2011) 105021.
- [59] L. P. Singer, L. R. Price, B. Farr, A. L. Urban, C. Pankow, S. Vitale, J. Veitch, W. M. Farr, C. Hanna, K. Cannon, T. Downes, P. Graff, C.-J. Haster, I. Mandel, T. Sidery, and A. Vecchio, “The First Two Years of Electromagnetic Follow-up with Advanced LIGO and Virgo”, *The Astrophysical Journal* **795** no. 2, (2014) 105.
- [60] **LIGO Scientific Collaboration and Virgo Collaboration**, B. P. Abbott *et al.*, “Tests of General Relativity with GW150914”, *Phys. Rev. Lett.* **116** (May, 2016) 221101.
- [61] M. Isi, M. Pitkin, and A. J. Weinstein, “Probing dynamical gravity with the polarization of continuous gravitational waves”, *Phys. Rev. D* **96** (Aug, 2017) 042001.
- [62] **LIGO Scientific Collaboration and Virgo Collaboration**, J. Abadie *et al.*, “Predictions for the rates of compact binary coalescences observable by ground-based gravitational-wave detectors”, *Classical and Quantum Gravity* **27** no. 17, (2010) 173001.
- [63] M. Zevin, C. Pankow, C. L. Rodriguez, L. Sampson, E. Chase, V. Kalogera, and F. A. Rasio, “Constraining Formation Models of Binary Black Holes with Gravitational-wave Observations”, *The Astrophysical Journal* **846** no. 1, (2017) 82.
- [64] **LIGO Scientific Collaboration and Virgo Collaboration**, B. P. Abbott *et al.*, “Astrophysical Implications of the Binary Black-hole Merger GW150914”, *The Astrophysical Journal Letters* **818** no. 2, (2016) L22.
- [65] **LIGO Scientific Collaboration and Virgo Collaboration**, B. P. Abbott *et al.*, “GW170104: Observation of a 50-Solar-Mass Binary Black Hole Coalescence at Redshift 0.2”, *Phys. Rev. Lett.* **118** (Jun, 2017) 221101.
- [66] L. Rezzolla, B. Giacomazzo, L. Baiotti, J. Granot, C. Kouveliotou, and M. A. Aloy, “The Missing Link: Merging Neutron Stars Naturally Produce Jet-like Structures and Can Power Short Gamma-ray Bursts”, *The Astrophysical Journal Letters* **732** no. 1, (2011) L6.

-
- [67] LIGO Scientific Collaboration and Virgo Collaboration, *Fermi* Gamma-ray Burst Monitor, INTEGRAL, B. P. Abbott *et al.*, “Gravitational Waves and Gamma-Rays from a Binary Neutron Star Merger: GW170817 and GRB 170817A”, *The Astrophysical Journal Letters* **848** no. 2, (2017) L13.
- [68] LIGO Scientific Collaboration and Virgo Collaboration, Fermi GBM, INTEGRAL, IceCube Collaboration, AstroSat Cadmium Zinc Telluride Imager Team, IPN Collaboration, The Insight-Hxmt Collaboration, ANTARES Collaboration, The Swift Collaboration, AGILE Team, The 1M2H Team, The Dark Energy Camera GW-EM Collaboration and the DES Collaboration, The DLT40 Collaboration, GRAWITA: GRAvitational Wave Inaf TeAm, The Fermi Large Area Telescope Collaboration, ATCA: Australia Telescope Compact Array, ASKAP: Australian SKA Pathfinder, Las Cumbres Observatory Group, OzGrav, DWF (Deeper, Wider, Faster Program), AST3, and CAASTRO Collaborations, The VINROUGE Collaboration, MASTER Collaboration, J-GEM, GROWTH, JAGWAR, CaltechNRAO, TTU-NRAO, and NuSTAR Collaborations, Pan-STARRS, The MAXI Team, TZAC Consortium, KU Collaboration, Nordic Optical Telescope, ePESSTO, GROND, Texas Tech University, SALT Group, TOROS: Transient Robotic Observatory of the South Collaboration, The BOOTES Collaboration, MWA: Murchison Widefield Array, The CALET Collaboration, IKI-GW Follow-up Collaboration, H.E.S.S. Collaboration, LOFAR Collaboration, LWA: Long Wavelength Array, HAWC Collaboration, The Pierre Auger Collaboration, ALMA Collaboration, Euro VLBI Team, Pi of the Sky Collaboration, The Chandra Team at McGill University, DFN: Desert Fireball Network, ATLAS, High Time Resolution Universe Survey, RIMAS and RATIR, and SKA South Africa/MeerKAT, B. P. Abbott *et al.*, “Multi-messenger Observations of a Binary Neutron Star Merger”, *The Astrophysical Journal Letters* **848** no. 2, (2017) L12.
- [69] LIGO Scientific Collaboration and Virgo Collaboration, “Estimating the Contribution of Dynamical Ejecta in the Kilonova Associated with GW170817”. Accepted by *Astrophys. J. Lett.*
<https://dcc.ligo.org/public/0145/P1700309/006/LIGO-P1700309.pdf>.
- [70] S. J. Smartt, T.-W. Chen, A. Jerkstrand, M. Coughlin, E. Kankare, S. A. Sim, M. Fraser, C. Inserra, K. Maguire, K. C. Chambers, M. E. Huber, T. Krühler, G. Leloudas, M. Magee, L. J. Shingles, K. W. Smith, D. R.

- Young, J. Tonry, R. Kotak, A. Gal-Yam, J. D. Lyman, D. S. Homan, C. Agliozzo, J. P. Anderson, C. R. Angus, C. Ashall, C. Barbarino, F. E. Bauer, M. Berton, M. T. Botticella, M. Bulla, J. Bulger, G. Cannizzaro, Z. Cano, R. Cartier, A. Cikota, P. Clark, A. De Cia, M. Della Valle, L. Denneau, M. Dennefeld, L. Dessart, G. Dimitriadis, N. Elias-Rosa, R. E. Firth, H. Flewelling, A. Flörs, A. Franckowiak, C. Frohmaier, L. Galbany, S. González-Gaitán, J. Greiner, M. Gromadzki, A. N. Guelbenzu, C. P. Gutiérrez, A. Hamanowicz, L. Hanlon, J. Harmanen, K. E. Heintz, A. Heinze, M.-S. Hernandez, S. T. Hodgkin, I. M. Hook, L. Izzo, P. A. James, P. G. Jonker, W. E. Kerzendorf, S. Klose, Z. Kostrzewska-Rutkowska, M. Kowalski, M. Kromer, H. Kuncarayakti, A. Lawrence, T. B. Lowe, E. A. Magnier, I. Manulis, A. Martin-Carrillo, S. Mattila, O. McBrien, A. Müller, J. Nordin, D. O'Neill, F. Onori, J. T. Palmerio, A. Pastorello, F. Patat, G. Pignata, P. Podsiadlowski, M. L. Pumo, S. J. Prentice, A. Rau, A. Razza, A. Rest, T. Reynolds, R. Roy, A. J. Ruiter, K. A. Rybicki, L. Salmon, P. Schady, A. S. B. Schultz, T. Schweyer, I. R. Seitenzahl, M. Smith, J. Sollerman, B. Stalder, C. W. Stubbs, M. Sullivan, H. Szegedi, F. Taddia, S. Taubenberger, G. Terreran, B. van Soelen, J. Vos, R. J. Wainscoat, N. A. Walton, C. Waters, H. Weiland, M. Willman, P. Wiseman, D. E. Wright, Ł. Wyrzykowski, and O. Yaron, “A kilonova as the electromagnetic counterpart to a gravitational-wave source”, *Nature* (Oct, 2017) .
- [71] E. Pian, P. D’Avanzo, S. Benetti, M. Branchesi, E. Brocato, S. Campana, E. Cappellaro, S. Covino, V. D’Elia, J. P. U. Fynbo, F. Getman, G. Ghirlanda, G. Ghisellini, A. Grado, G. Greco, J. Hjorth, C. Kouveliotou, A. Levan, L. Limatola, D. Malesani, P. A. Mazzali, A. Melandri, P. Møller, L. Nicastro, E. Palazzi, S. Piranomonte, A. Rossi, O. S. Salafia, J. Selsing, G. Stratta, M. Tanaka, N. R. Tanvir, L. Tomasella, D. Watson, S. Yang, L. Amati, L. A. Antonelli, S. Ascenzi, M. G. Bernardini, M. Boér, F. Bufano, A. Bulgarelli, M. Capaccioli, P. Casella, A. J. Castro-Tirado, E. Chassande-Mottin, R. Ciolfi, C. M. Copperwheat, M. Dadina, G. De Cesare, A. Di Paola, Y. Z. Fan, B. Gendre, G. Giuffrida, A. Giunta, L. K. Hunt, G. L. Israel, Z.-P. Jin, M. M. Kasliwal, S. Klose, M. Lisi, F. Longo, E. Maiorano, M. Mapelli, N. Masetti, L. Nava, B. Patricelli, D. Perley, A. Pescalli, T. Piran, A. Possenti, L. Pulone, M. Razzano, R. Salvaterra, P. Schipani, M. Spera, A. Stamerra, L. Stella, G. Tagliaferri, V. Testa, E. Troja, M. Turatto, S. D. Vergani, and D. Vergani, “Spectroscopic identification of r-process nucleosynthesis in a double neutron-star merger”, *Nature* (Oct, 2017) .
- [72] I. Arcavi, G. Hosseinzadeh, D. A. Howell, C. McCully, D. Poznanski, D. Kasen, J. Barnes, M. Zaltzman, S. Vasylyev, D. Maoz, and S. Valenti,

“Optical emission from a kilonova following a gravitational-wave-detected neutron-star merger”, *Nature* (Oct, 2017) .

- [73] **ANTARES Collaboration, IceCube Collaboration, Pierre Auger Collaboration, LIGO Scientific Collaboration and Virgo Collaboration**, A. Albert *et al.*, “Search for High-energy Neutrinos from Binary Neutron Star Merger GW170817 with ANTARES, IceCube, and the Pierre Auger Observatory”. Submitted to *Astrophys. J. Lett.* https://dcc.ligo.org/public/0146/P1700344/006/GW170817_neutrinos.pdf.
- [74] **LIGO Scientific Collaboration and Virgo Collaboration**, “Search for post-merger gravitational waves from the remnant of the binary neutron star merger GW170817”. in preparation.
<https://dcc.ligo.org/DocDB/0145/P1700318/006/remnant.pdf>.
- [75] L. S. Collaboration and V. Collaboration, “W170817: Implications for the Stochastic Gravitational-Wave Background from Compact Binary Coalescences”. Submitted to *Phys. Rev. Lett.*
<https://dcc.ligo.org/public/0145/P1700272/007/LIGO-P1700272.pdf>.
- [76] **Virgo Collaboration**, “Advanced Virgo Technical Design Report”. Technical report, VIR-0128A-12, 2012. <https://tds.virgo-gw.eu/ql/?c=8940>.
- [77] R. Barellet, A. Brillet, R. Chiche, F. Cleva, L. Latrach, and C. N. Man, “An injection-locked Nd:YAG laser for the interferometric detection of gravitational waves”, *Measurement Science and Technology* **7** no. 2, (1996) 162.
- [78] E. Genin for INJ subsystem, “AdV INJ status talk@ LVC meeting, Pasadena, March 2015”. Presentation, VIR-0100A-15, 2015.
<https://tds.virgo-gw.eu/ql/?c=10817>.
- [79] D. Z. Anderson, “Alignment of resonant optical cavities”, *Appl. Opt.* **23** no. 17, (Sep, 1984) 2944–2949.
- [80] B. Canuel, E. Genin, J. Marque, and P. Benoit, “Reference Cavity characterization”. Scientific & Technical note, VIR-0231A-13, 2013.
<https://tds.virgo-gw.eu/ql/?c=9577>.
- [81] G. Ballardin, L. Bracci, S. Braccini, C. Bradaschia, C. Casciano, G. Calamai, R. Cavalieri, R. Cecchi, G. Celli, E. Cuoco, E. D’Ambrosio, V. Dattilo, A. D. Virgilio, L. Fabbroni, F. Fidecaro, F. Frasconi, A. Gaddi, A. Gennai, G. Gennaro, A. Giazotto, G. Losurdo, L. Holloway, P. L. Penna, F. Lelli, E. Majorana, M. Mazzoni, F. Paoletti, M. Pasotti, A. Pasqualetti, R. Passaquieti, D. Passuello, R. Poggiani, P. Puppo, F. Raffaelli,

- P. Rapagnani, F. Ricci, P. Ruggi, R. Stanga, R. Taddei, F. Vetrano, A. Vicerè, and Z. Zhang, “Measurement of the VIRGO superattenuator performance for seismic noise suppression”, *Review of Scientific Instruments* **72** no. 9, (2001) 3643–3652.
- [82] G. Losurdo, M. Bernardini, S. Braccini, C. Bradaschia, C. Casciano, V. Dattilo, R. D. Salvo, A. D. Virgilio, F. Frasconi, A. Gaddi, A. Gennai, A. Giazotto, H. B. Pan, F. Paoletti, A. Pasqualetti, R. Passaquieti, D. Passuello, R. Taddei, Z. Zhang, G. Cella, E. Cuoco, E. D’Ambrosio, F. Fidecaro, S. Gaggero, P. L. Penna, S. Mancini, R. Poggiani, A. Vicerè, M. Mazzoni, R. Stanga, L. Holloway, and J. Winterflood, “An inverted pendulum preisolator stage for the VIRGO suspension system”, *Review of Scientific Instruments* **70** no. 5, (1999) 2507–2515.
- [83] G. Losurdo, G. Calamai, E. Cuoco, L. Fabbroni, G. Guidi, M. Mazzoni, R. Stanga, F. Vetrano, L. Holloway, D. Passuello, G. Ballardin, S. Braccini, C. Bradaschia, R. Cavalieri, R. Cecchi, G. Cella, V. Dattilo, A. D. Virgilio, F. Fidecaro, F. Frasconi, A. Gennai, A. Giazotto, I. Ferrante, P. L. Penna, F. Lelli, T. Lomtadze, A. Marin, S. Mancini, F. Paoletti, A. Pasqualetti, R. Passaquieti, R. Poggiani, R. Taddei, A. Vicerè, and Z. Zhang, “Inertial control of the mirror suspensions of the VIRGO interferometer for gravitational wave detection”, *Review of Scientific Instruments* **72** no. 9, (2001) 3653–3661.
- [84] M. Was, “Advanced Virgo noise budget”. Advanced Virgo activity report, VIR-0655A-17, 2017. <https://tds.virgo-gw.eu/ql/?c=12587>.
- [85] E. Calloni and G. Vajente, “Conceptual design of the second stage of frequency stabilization for Advanced Virgo”. Virgo note, VIR-0013C-12, 2012. <https://tds.virgo-gw.eu/ql/?c=8815>.
- [86] F. Bondu, *L’interféromètre Virgo : propriétés optiques, stabilisation en fréquence du laser*. Habilitation à diriger des recherches, Université Nice Sophia Antipolis, June, 2008. <https://tel.archives-ouvertes.fr/tel-00284986>.
- [87] B. Swinkels, “Requirements on sensing noise for the Pound-Drever-Hall technique for the lock of the arm-cavities”. Virgo note, VIR-0467A-12, 2012. <https://tds.virgo-gw.eu/ql/?c=9290>.
- [88] E. Genin on behalf of the INJ team, “INJ status @ July 2015 coll. meeting”. Presentation, VIR-0311A-15, 2015. <https://tds.virgo-gw.eu/ql/?c=11034>.

-
- [89] K. Numata, A. Kemery, and J. Camp, “Thermal-Noise Limit in the Frequency Stabilization of Lasers with Rigid Cavities”, *Phys. Rev. Lett.* **93** (Dec, 2004) 250602.
 - [90] **Virgo Collaboration**, F. Acernese *et al.*, “The Virgo automatic alignment system”, *Classical and Quantum Gravity* **23** no. 8, (2006) S91.
 - [91] B. Canuel, E. Genin, M. Mantovani, J. Marque, P. Ruggi, and M. Tacca, “Sub-nanoradiant beam pointing monitoring and stabilization system for controlling input beam jitter in gravitational wave interferometers”, *Appl. Opt.* **53** no. 13, (May, 2014) 2906–2916.
 - [92] E. Capocasa, M. Barsuglia, I. Fiori, M. Mantovani, E. Genin, P. Ruggi, B. Swinkels, and M. Tacca, “AdVirgo injection system frequency noise”. Presentation, VIR-0212A-16, 2016.
<https://tds.virgo-gw.eu/ql/?c=11520>.
 - [93] F. Carbognani, “Metatron: state machine-based automation for Virgo @ Aug 2017 LVC Meeting in Geneva”. Presentation, VIR-0659A-17, 2017.
<https://tds.virgo-gw.eu/ql/?c=12591>.
 - [94] J. G. Rollins, “Advanced LIGO Guardian: Overview and Coder’s Introduction”. LIGO Document G1400016-v7.
<https://dcc.ligo.org/LIGO-G1400016>.
 - [95] L. Pinard, “Advanced Virgo Input Mirror Characterization report- IM04 (coatings C14081+C14087)”. Specification/Characterisation, VIR-0544A-14, 2014. <https://tds.virgo-gw.eu/ql/?c=10650>.
 - [96] L. Pinard, “Advanced Virgo End Mirror Characterization report- EM01 (coatings C14042/10 + C14035/10)”. Specification/Characterisation, VIR-0269A-15, 2015. <https://tds.virgo-gw.eu/ql/?c=10990>.
 - [97] L. Pinard, “Advanced Virgo Input Mirror Characterization report- IM02 (coatings C14081+C14087)”. Specification/Characterisation, VIR-0543A-14, 2014. <https://tds.virgo-gw.eu/ql/?c=10649>.
 - [98] L. Pinard, “Advanced Virgo End Mirror Characterization report- EM03 (coatings C14042/20 + C14035/20)”. Virgo Internal Note, VIR-0270A-15, 2015. <https://tds.virgo-gw.eu/ql/?c=10991>.
 - [99] L. Matone, M. Barsuglia, F. Bondi, F. Cavalier, H. Heitmann, and N. Man, “Finesse and mirror speed measurement for a suspended Fabry–Perot cavity using the ringing effect”, *Physics Letters A* **271** no. 5, (2000) 314 – 318.

- [100] T. Isogai, J. Miller, P. Kwee, L. Barsotti, and M. Evans, “Loss in long-storage-time optical cavities”, *Opt. Express* **21** no. 24, (Dec, 2013) 30114–30125.
- [101] M. Rakhmanov, *Dynamics of Laser Interferometric Gravitational Wave Detectors*. PhD thesis, California Institute of Technology, 2000.
- [102] J. Degallaix, M. Galimberti, R. Bonnand, and Q. Benoit, “Defining the arm cavity loss for Advanced Virgo”. Scientific & Technical note, VIR-0706A-10, 2010. <https://tds.virgo-gw.eu/ql/?c=8044>.
- [103] F. Magaña-Sandoval, R. X. Adhikari, V. Frolov, J. Harms, J. Lee, S. Sankar, P. R. Saulson, and J. R. Smith, “Large-angle scattered light measurements for quantum-noise filter cavity design studies”, *J. Opt. Soc. Am. A* **29** no. 8, (Aug, 2012) 1722–1727.
- [104] R. Bonnand and J. Degallaix, “Advanced Virgo arm mirror flatness specification, RTL or RTL00?”. Presentation, VIR-0032A-12, 2012. <https://tds.virgo-gw.eu/ql/?c=8834>.
- [105] **Virgo Collaboration**, “Measurement of the optical parameters of the Virgo interferometer”, *Appl. Opt.* **46** no. 17, (Jun, 2007) 3466–3484.
- [106] F. Bondu, M. Laval, and J.-Y. Vinet, “From mirror maps to TEM00 model: evaluation of effective losses”. Un-classified, VIR-0054B-07, 2007. <https://tds.virgo-gw.eu/ql/?c=1939>.
- [107] E. Capocasa, “Optical characterization for the arm cavities: ideas and first results”. Advanced Virgo activity report, VIR-0290A-16, 2016. <https://tds.virgo-gw.eu/ql/?c=11601>.
- [108] E. Capocasa, A. Chiummo, and D. Hoak, “North arm optical characterization and North input scattering”. Presentation, VIR-0424A-16, 2016. <https://tds.virgo-gw.eu/?content=3&r=12616>.
- [109] H. Yamamoto. Personal Communication.
- [110] H. Kogelnik and T. Li, “Laser Beams and Resonators”, *Appl. Opt.* **5** no. 10, (Oct, 1966) 1550–1567.
- [111] **LIGO Scientific Collaboration**, J. Aasi *et al.*, “Enhanced sensitivity of the LIGO gravitational wave detector by using squeezed states of light”, *Nat Photon* **7** no. 8, (Aug, 2013) 613–619.
- [112] **LIGO Scientific Collaboration**, “A gravitational wave observatory operating beyond the quantum shot-noise limit”, *Nat Phys* **7** no. 12, (Dec, 2011) 962–965.

-
- [113] S. Chelkowski, H. Vahlbruch, B. Hage, A. Franzen, N. Lastzka, K. Danzmann, and R. Schnabel, “Experimental characterization of frequency-dependent squeezed light”, *Phys. Rev. A* **71** (Jan, 2005) 013806.
 - [114] E. Oelker, T. Isogai, J. Miller, M. Tse, L. Barsotti, N. Mavalvala, and M. Evans, “Audio-Band Frequency-Dependent Squeezing for Gravitational-Wave Detectors”, *Phys. Rev. Lett.* **116** (Jan, 2016) 041102.
 - [115] F. Ricci for the Virgo collaboration, “Vision document on the future of Advanced Virgo”. Official documents, VIR-0136B-16, 2016.
<https://tds.virgo-gw.eu/ql/?c=11441>.
 - [116] M. Abernathy *et al.*, “Einstein gravitational wave Telescope Conceptual Design Study”. ET Design Study, ET-0106C-10.
<http://www.et-gw.eu/index.php/etdsdocument>.
 - [117] P. Kwee, J. Miller, T. Isogai, L. Barsotti, and M. Evans, “Decoherence and degradation of squeezed states in quantum filter cavities”, *Phys. Rev. D* **90** (Sep, 2014) 062006.
 - [118] V. B. Braginsky, M. L. Gorodetsky, F. Y. Khalili, A. B. Matsko, K. S. Thorne, and S. P. Vyatchanin, “Noise in gravitational-wave detectors and other classical-force measurements is not influenced by test-mass quantization”, *Phys. Rev. D* **67** (Apr, 2003) 082001.
 - [119] D. F. Walls and G. J. Milburn, *Quantum Optics*. Springer Berlin Heidelberg, 2008.
 - [120] H. J. Kimble, Y. Levin, A. B. Matsko, K. S. Thorne, and S. P. Vyatchanin, “Conversion of conventional gravitational-wave interferometers into quantum nondemolition interferometers by modifying their input and/or output optics”, *Phys. Rev. D* **65** (Dec, 2001) 022002.
 - [121] C. M. Caves and B. L. Schumaker, “New formalism for two-photon quantum optics. I. Quadrature phases and squeezed states”, *Phys. Rev. A* **31** (May, 1985) 3068–3092.
 - [122] B. L. Schumaker and C. M. Caves, “New formalism for two-photon quantum optics. II. Mathematical foundation and compact notation”, *Phys. Rev. A* **31** (May, 1985) 3093–3111.
 - [123] H. P. Yuen and V. W. S. Chan, “Noise in homodyne and heterodyne detection”, *Opt. Lett.* **8** no. 3, (Mar, 1983) 177–179.
 - [124] T. Corbitt, Y. Chen, and N. Mavalvala, “Mathematical framework for simulation of quantum fields in complex interferometers using the two-photon formalism”, *Phys. Rev. A* **72** (Jul, 2005) 013818.

- [125] J. Harms, Y. Chen, S. Chelkowski, A. Franzen, H. Vahlbruch, K. Danzmann, and R. Schnabel, “Squeezed-input, optical-spring, signal-recycled gravitational-wave detectors”, *Phys. Rev. D* **68** (Aug, 2003) 042001.
- [126] A. Buonanno and Y. Chen, “Quantum noise in second generation, signal-recycled laser interferometric gravitational-wave detectors”, *Phys. Rev. D* **64** (Jul, 2001) 042006.
- [127] H. Miao, H. Yang, R. X. Adhikari, and Y. Chen, “Quantum limits of interferometer topologies for gravitational radiation detection”, *Classical and Quantum Gravity* **31** no. 16, (2014) 165010.
- [128] F. D. Valle, E. Milotti, A. Ejlli, U. Gastaldi, G. Messineo, L. Piemontese, G. Zavattini, R. Pengo, and G. Ruoso, “Extremely long decay time optical cavity”, *Opt. Express* **22** no. 10, (May, 2014) 11570–11577.
- [129] M. Evans, L. Barsotti, P. Kwee, J. Harms, and H. Miao, “Realistic filter cavities for advanced gravitational wave detectors”, *Phys. Rev. D* **88** (Jul, 2013) 022002.
- [130] H. Yamamoto, “1D PSD of mirror maps”. LIGO Document T1100353-v1.
<https://dcc.ligo.org/LIGO-T1100353>.
- [131] N. Straniero, J. Degallaix, R. Flaminio, L. Pinard, and G. Cagnoli, “Realistic loss estimation due to the mirror surfaces in a 10 meters-long high finesse Fabry-Perot filter-cavity”, *Optics express* **23** no. 16, (August, 2015) 21455—21476.
- [132] J. C. Stover, *Optical Scattering: Measurement and Analysis, Third Edition*. SPIE Press, 2012.
- [133] J. Degallaix, “OSCAR a Matlab based optical FFT code”, *Journal of Physics: Conference Series* **228** no. 1, (2010) 012021.
- [134] L. Pinard. Personal Communication.
- [135] F. Y. Khalili, “Optimal configurations of filter cavity in future gravitational-wave detectors”, *Phys. Rev. D* **81** (Jun, 2010) 122002.
- [136] L. Barsotti, J. Harms, and R. Schnabel, “Squeezed vacuum states of light for gravitational wave detectors”. LIGO Document P1600121-v8.
<https://dcc.ligo.org/cgi-bin/private/DocDB/ShowDocument?.submit=Identifier&docid=P1600121&version=8>.
- [137] Y. Ma, H. Miao, B. H. Pang, M. Evans, C. Zhao, J. Harms, R. Schnabel, and Y. Chen, “Proposal for gravitational-wave detection beyond the standard

-
- quantum limit through EPR entanglement”, *Nat Phys* **13** no. 8, (Aug, 2017) 776–780.
- [138] H. Miao, “Conditional frequency-dependent squeezing via EPR entanglement”. LIGO Document G1701715-v1.
<https://dcc.ligo.org/cgi-bin/private/DocDB>ShowDocument?submit=Identifier&docid=G1701715&version=1>.
- [139] D. D. Brown, H. Miao, C. Collins, C. Mow-Lowry, D. Töyrä, and A. Freise, “Broadband sensitivity enhancement of detuned dual-recycled Michelson interferometers with EPR entanglement”, *Phys. Rev. D* **96** (Sep, 2017) 062003.
- [140] H. Vahlbruch, M. Mehmet, K. Danzmann, and R. Schnabel, “Detection of 15 dB Squeezed States of Light and their Application for the Absolute Calibration of Photoelectric Quantum Efficiency”, *Phys. Rev. Lett.* **117** (Sep, 2016) 110801.
- [141] S. Chelkowski, H. Vahlbruch, K. Danzmann, and R. Schnabel, “Coherent control of broadband vacuum squeezing”, *Phys. Rev. A* **75** (Apr, 2007) 043814.
- [142] R. Takahashi, F. Kuwahara, E. Majorana, M. A. Barton, T. Uchiyama, K. Kuroda, A. Araya, K. Arai, A. Takamori, M. Ando, K. Tsubono, M. Fukushima, and Y. Saito, “Vacuum-compatible vibration isolation stack for an interferometric gravitational wave detector TAMA300”, *Review of Scientific Instruments* **73** no. 6, (2002) 2428–2433.
- [143] **TAMA Collaboration**, R. Takahashi, K. Arai, D. Tatsumi, M. Fukushima, T. Yamazaki, M.-K. Fujimoto, K. Agatsuma, Y. Arase, N. Nakagawa, A. Takamori, K. Tsubono, R. DeSalvo, A. Bertolini, S. Márka, and V. Sannibale, “Operational status of TAMA300 with the seismic attenuation system (SAS)”, *Classical and Quantum Gravity* **25** no. 11, (2008) 114036.
- [144] E. Majorana, “OpLev”. JGW-T1503946-v1. <http://gwdoc.icrr.u-tokyo.ac.jp/cgi-bin/private/DocDB>ShowDocument?docid=3946>.
- [145] **Virgo Collaboration**, F. Acernese *et al.*, “A local control system for the test masses of the Virgo gravitational wave detector”, *Astroparticle Physics* **20** no. 6, (2004) 617 – 628.
- [146] **TAMA Collaboration**, D. Tatsumi, “TAMA300 interferometer development”, *Journal of Physics: Conference Series* **120** no. 3, (2008) 032011.

BIBLIOGRAPHY

- [147] J. Romie, N. Robertson, K. Gushwa, C. Torrie, and M. Heintze, “Guidance on Gluing with EP30-2”. LIGO Document T1300322-v6.
<https://dcc.ligo.org/LIGO-T1300322>.
- [148] Y. Saito, Y. Ogawa, G. Horikoshi, N. Matuda, R. Takahashi, and M. Fukushima, “Vacuum system of the 300m gravitational wave laser interferometer in Japan (TAMA300)”, *Vacuum* **53** no. 1, (1999) 353 – 356.
- [149] E. D. Black, “An introduction to Pound–Drever–Hall laser frequency stabilization”, *American Journal of Physics* **69** no. 1, (2001) 79–87.
- [150] M. Granata, *Optical Development for Second- and Third-Generation Gravitational-Wave Detectors: Stable Recycling Cavities for Advanced Virgo and Higher-Order Laguerre-Gauss Modes*. PhD thesis, Université Paris Diderot, 2011.
- [151] E. Capocasa, M. Barsuglia, J. Degallaix, L. Pinard, N. Straniero, R. Schnabel, K. Somiya, Y. Aso, D. Tatsumi, and R. Flaminio, “Estimation of losses in a 300 m filter cavity and quantum noise reduction in the KAGRA gravitational-wave detector”, *Phys. Rev. D* **93** (Apr, 2016) 082004.
- [152] P. Hello and N. Man, “Design of a low-loss off-axis beam expander”. Virgo note, VIR-NOT-LAS-1390-12. <https://tds.virgo-gw.eu/ql/?c=304>.